

# Reference dosimetry of MRI-guided radiotherapy machines

by

Ilias Billas

A thesis submitted for the degree of Doctor of Philosophy

(Ph.D.)

The Institute of Cancer Research

The University of London

September 2021

I, Ilias Billas confirm that the work presented in this thesis is my own. Where information has been derived from other sources, I confirm that this has been indicated in the thesis.

## Abstract

A cutting-edge cancer treatment modality, that integrates MRI guidance and delivery of radiotherapy (MRIgRT), sets a new standard for personalised radiotherapy. There are, however, aspects around the accurate determination of absorbed dose in a magnetic field that need to be resolved. The influence of the Lorentz force on the secondary charged particles perturbs the detector dose response and this puts MRIgRT outside the scope of currently available protocols for reference dosimetry. The aim of this thesis is to investigate, clarify and resolve issues around traceable reference dosimetry for, and calibration of, MRIgRT systems. In this new context, I characterise the performance of suitable commercially available detectors in the presence of strong magnetic fields. Furthermore, potential routes to achieve traceability in dosimetry for MRIgRT, which are compatible with the existing standards and calibrations available for conventional radiotherapy, are identified and established. Finally, I propose guidelines for calibration and audit.

In this thesis I show that Gafchromic EBT-3 film and alanine are suitable detectors for dosimetry, with the inclusion of appropriate corrections, in MRIgRT. Based on this finding and with the inclusion of alanine as reference class detector, I demonstrate a route for the calibration of secondary standard ionisation chambers in MRIgRT, in terms of absorbed dose to water traceable to the NPL (National Physical Laboratory) primary standard. This methodology is applied to the currently commercial and in the under-development MRIgRT systems, and I show that the uncertainty is comparable to, if not quite matching, that of dosimetry for conventional radiotherapy. The application of work described in this thesis includes an alanine reference dosimetry service, for MRIgRT systems. This allows a dosimetry audit, provided by NPL, and the calibration of ionisation chambers (but also other dosimeters), either by a site visit to radiotherapy centres or as a postal dosimetry service.

## Acknowledgments

First of all, I would like to thank my PhD supervisors Dr Simon Duane (NPL), Professor Hugo Bouchard (UoM) and Professor Uwe Oelfke (ICR) for their continuous support throughout this project and for their constant source of inspiration. Simon has been more than a supervisor and a colleague to me. He has been my mentor and an example of a scientist that I would like to become. His calmness and his way of approaching and solving scientific problems, has transformed me as a scientist (but also as a person). Hugo, with his enthusiasm and passion for science, was the one to convince me to pursue a PhD. During these years, he has been a big influence on my research and has always been there to encourage and motivate me. Uwe gave me the opportunity to join ICR and study a degree of PhD. His insightful discussions and his key advices about the project, inspired me and gave me the confidence needed to deliver my PhD.

I would also have to thank my former teacher Fanis Kypriotis, who, back in the high school, trusted my skills and steer me in the right direction to continue with higher education.

I am grateful to my colleagues at NPL for their support and encouragement. You all supported me greatly and were always willing to help me. I would particularly like to thank Michael Homer and David Maughan for assisting with the on- and off-site measurements, David Shipley for teaching me Monte Carlo simulations, Clare Gouldstone for giving useful advice on alanine dosimetry, Thorsten Sander for reviewing some of my published papers and his useful advice on the uncertainty budget and Hugo Palmans for his useful comments on a manuscript [[\*Phys. Med. Biol.\* \*\*64\*\* \(2019\) 06NT03 \(9pp\)](#)].

I would also like to thank Thijs Perik and Jochem Kaas from NKI, Simeon Nill and Ian Hanson from The RMH/ICR, Geoff Budgell, Joe Berresford and James Agnew from The Christie, Jarrad Begg, Urszula Jelen, Bin Dong from Liverpool Cancer Therapy Centre, Australia, Carsten Brink, Hans L. Riis and Anders S. Bertelsen from Odense, Fau Pierre and Hugues Mailleux from IPC and Niall McAndrew and Ben George from GCUK Oxford for access into their MRI-linac machines and their help with measurements.

I also wish to acknowledge the financial support of the NPL which made this PhD project possible.

I am grateful to my parents, Marika and Vasilis, for their love and support throughout my life. Thank you for giving me the opportunities and experiences that have made me who I am. This journey would not have been possible if not for them.

Special thanks go to my wife, Maria, for her full supports during my PhD. All these years Maria has stood by me through all my efforts, my absence, my frustration and impatience.

The last word goes for Maximos, my son, who for the last two years has given me the extra strength and motivation to get things done. I want him to know that, this journey has been more than a marathon and a lesson on mental toughness. It is this lesson that I would like to impart to Maximos, to whom this thesis is dedicated.

## List of Publications

**Billas, I.**, Bouchard, H., Oelfke, U. & Duane, S. 2019. The effect of magnetic field strength on the response of Gafchromic EBT-3 film. *Physics in Medicine & Biology*, **64**, 06NT03.

i. This paper summarises work presented in Chapter 3.

**Billas, I.**, Bouchard, H., Oelfke, U., Shipley, D. R., Gouldstone, C. A. & Duane, S. 2020. Alanine dosimetry in strong magnetic fields: use as a transfer standard in MRI-guided radiotherapy. *Physics in Medicine & Biology*, **65**, 115001.

ii. This paper summarises work presented in Chapter 4.

**Billas, I.**, Bouchard, H., Oelfke, U. & Duane, S. 2021. Traceable reference dosimetry in MRI guided radiotherapy using alanine: calibration and magnetic field correction factors of ionisation chambers. *Physics in Medicine & Biology*, **66**, 165006.

iii. This paper summarises work presented in Chapter 5 and Chapter 6.

de Pooter, J., A., **Billas, I.**, de Prez, L. A., Duane, S., Kapsch, R.-P., Karger, C., van Asselen, B. & Wolthaus, J., W. H. 2021. Reference dosimetry in MRI-linacs: evaluation of available protocols and data to establish a code of practice. *Physics in Medicine & Biology*, **66**, 05TR02.

iv. This paper includes information generated by work described in Chapter 5.

## Technical reports

**Ilias Billas**, Michael Homer and Simon Duane 2018. Report on dose measurements on the MRI-linac at Liverpool Hospital (Australia) performed by NPL. NPL Report IR 46, National Physical Laboratory Hampton Road, Teddington.

(link: <http://eprintspublications.npl.co.uk/7731/1/IR46.pdf>)

v. This report summarises work presented in Chapter 2, Chapter 5 and Chapter 6.

**Ilias Billas** and Simon Duane 2018. Report on dose measurements on the Elekta Unity MR-linac at The Royal Marsden Hospital performed by NPL. NPL Report IR 49, National Physical Laboratory Hampton Road, Teddington.

(link: <http://eprintspublications.npl.co.uk/8117/1/IR49.pdf>)

vi. This report summarises work presented in Chapter 5 and Chapter 6.

**Ilias Billas** and Simon Duane 2018. Report on dose measurements on the MR-linac at Christie Hospital performed by NPL. NPL Report IR 50, National Physical Laboratory Hampton Road, Teddington.

(link: <http://eprintspublications.npl.co.uk/8116/1/IR50.pdf>)

vii. This report summarises work presented in Chapter 5 and Chapter 6.

## Table of Contents

Abstract .....	3
Acknowledgments.....	4
List of Publications .....	6
Technical reports .....	7
Table of Contents .....	8
List of tables .....	13
List of figures .....	14
List of acronyms.....	17
Chapter 1     Introduction .....	18
1.1     Radiotherapy .....	18
1.2     MRI in radiotherapy .....	19
1.2.1     MRI imaging .....	19
1.2.2     Advantages and challenges .....	20
1.3     MRI-guided Radiotherapy .....	21
1.3.1     Current MRIgRT systems .....	22
1.3.2     Effect of magnetic field on radiation dosimetry .....	23
1.4     Aims of the project .....	25
Chapter 2     Radiation dosimetry of photon beams with and without magnetic fields .	26
2.1     Radiation transport in matter .....	26
2.1.1     Interactions with matter.....	26
2.1.2     Magnetic field coupling to MV beams .....	28
2.1.3     Monte Carlo radiation transport simulations.....	31
2.2     Reference dosimetry of photon beams .....	32
2.2.1     Theory of absorbed dose measurement in photon beams .....	32
2.2.2     Determination of absorbed dose to water in reference conditions.....	33

2.3	Reference dosimetry in MRIgRT .....	35
2.3.1	Effect of magnetic field on absorbed dose to water.....	36
2.3.2	Effect of magnetic field on ionisation chamber response .....	40
2.3.3	Determination of absorbed dose to water in the presence of magnetic fields	
	42	
2.3.4	Beam quality characterisation in the presence of magnetic fields .....	44
2.4	Reference conditions in MRIgRT .....	45
Chapter 3	Experimental dosimetry with radiochromic film in magnetic fields .....	47
3.1	Introduction .....	47
3.2	Materials and methods.....	48
3.2.1	Experimental setup.....	48
3.2.2	Magnetic field uniformity .....	49
3.2.3	Dose output measurements .....	50
3.2.4	Effect of magnetic field on absorbed dose to water at $^{60}\text{Co}$ beam quality	51
3.2.5	Film response curve .....	51
3.2.6	Film digitisation .....	52
3.2.7	Film uncertainty .....	52
3.3	Results .....	53
3.3.1	Validation of the $^{60}\text{Co}$ beam model.....	53
3.3.2	Effect of magnetic field on absorbed dose to water at $^{60}\text{Co}$ beam quality	54
3.3.3	Beam uniformity at measurement plane .....	55
3.3.4	Effect of magnetic field on EBT-3 signal .....	55
3.3.5	Effect of magnetic fields on dose determined with EBT-3 film .....	58
3.3.6	Film uncertainty .....	59
3.4	Discussion .....	60
3.4.1	Comparison with different studies .....	61
3.5	Summary .....	64

Chapter 4	Alanine dosimetry in strong magnetic fields .....	65
4.1	Introduction .....	65
4.1.1	Electron paramagnetic resonance spectroscopy .....	65
4.1.2	EPR spectrometry system .....	67
4.1.3	Alanine/EPR dosimetry .....	69
4.2	Materials and Methods .....	72
4.2.1	Alanine dosimetry at NPL .....	72
4.2.2	Alanine reference dosimetry in a magnetic field .....	73
4.2.3	Experimental setup .....	75
4.2.4	Air gaps on the farmer compatible alanine holder .....	79
4.2.5	Monte Carlo simulations .....	80
4.3	Results .....	83
4.3.1	Validation of the beam models .....	83
4.3.2	Alanine model and experimental setup validation in a magnetic field .....	85
4.3.3	Effect of air gaps on alanine in a magnetic field .....	85
4.3.4	Effect of the magnetic field on absorbed dose to water .....	87
4.3.5	Alanine response in a magnetic field .....	87
4.3.6	Quality correction factor for the presence of a magnetic field on alanine .....	90
4.3.7	The effect of the magnetic field on alanine response .....	91
4.3.8	Uncertainties .....	92
4.4	Discussion .....	95
4.4.1	MC simulations and air gap effects .....	95
4.4.2	Quality correction factor for the presence of a magnetic field on alanine .....	96
4.4.3	The effect of the magnetic field on alanine response .....	97
4.5	Summary .....	98
Chapter 5	Experimental reference dosimetry measurements in MRIgRT using alanine: calibration and magnetic field correction factors of ionisation chambers .....	99

5.1	Introduction .....	99
5.2	Materials and Methods .....	103
5.2.1	Traceable measurements of absorbed dose to water in magnetic fields .	103
5.2.2	Ionisation chamber calibration coefficient in magnetic fields .....	104
5.2.3	Determination of the quality correction factor for the presence of a magnetic field on a radiation detector .....	105
5.2.4	Alanine magnetic field correction factor.....	112
5.3	Results .....	116
5.3.1	Alanine magnetic field correction factor.....	116
5.3.2	Output stability of MRI-linacs .....	122
5.3.3	TPR <sub>20,10</sub> of MRI-linacs .....	123
5.3.4	Ion recombination correction factors .....	124
5.3.5	Volume averaging correction factors .....	126
5.3.6	Reference dosimetry measurements and calibration coefficients of Farmer-type chambers .....	126
5.3.7	Farmer-type chamber magnetic field correction factors .....	128
5.3.8	Uncertainty budget .....	130
5.4	Discussion .....	133
5.4.1	MC simulations .....	134
5.4.2	Measurements and influence quantities on the detectors' signals .....	134
5.4.3	Validation of alanine as a transfer standard in zero magnetic field and Farmer-type chamber calibration coefficients .....	136
5.4.4	Farmer-type chamber magnetic field correction factors .....	136
5.4.5	Uncertainties .....	137
5.5	Summary .....	138
Chapter 6	Validation of alanine-based reference dosimetry on MRIgRT .....	139
6.1	Dose comparison with VSL .....	139

6.2	Comparison with other studies .....	142
6.3	Pilot study of alanine postal dosimetry service for MRI-linac machines.....	146
6.4	Comparison .....	146
6.5	Summary .....	147
Chapter 7	General discussion and conclusion, and future work.....	148
7.1	Future work .....	151
Appendix A	Summary of magnetic field correction factors of ionisation chambers .	153
Appendix B	Work instructions for user's chamber calibration in an MRI-linac.....	157
B.1	Summary .....	157
B.2	Equipment provided by NPL.....	157
B.3	Equipment provided by the user.....	157
B.4	Materials and Methods .....	157
B.5	Result.....	158
References	.....	160

## List of tables

Table 1.1: Differences in the MRI-linac concepts .....	23
Table 2.1: Reference conditions for the determination of the absorbed dose to water in the MRI-linac systems .....	46
Table 3.1. Average absolute difference for red, green and blue channel.....	56
Table 4.1: Alanine quality correction factors for the presence of a magnetic field .....	91
Table 4.2: Alanine relative intrinsic sensitivity .....	92
Table 4.3: Uncertainty budget for the determination of the quality correction factor for the presence of magnetic field on alanine .....	92
Table 5.1: The radiotherapy treatment centres that I visted .....	108
Table 5.2: Alanine magnetic field correction factors.....	117
Table 5.3: Statistics of the absolute value of the difference between the measured and MC normalised depth doses for the ViewRay MRIdian™ .....	118
Table 5.4: Measured TPR <sub>20,10</sub> .....	124
Table 5.5: Ion recombination correction factors .....	125
Table 5.6: <i>kvol</i> values for alanine and Farmer-type chamber .....	126
Table 5.7: Indirect and direct Farmer-type chamber magnetic field correction factors	129
Table 5.8. Uncertainty budget for the Farmer-type chamber calibration coefficient in the presence of a magnetic field.....	132
Table 6.1: Ratios, R, on measured dose outputs .....	140
Table 6.2: Magnetic field correction factors of the studies from van Asselen et al. (2018) and de Prez et al. (2019b) and of this study .....	143
Table 6.3: Magnetic field correction factors of the study from Krauss et al. (2020) and and of this study .....	143
Table 6.4: Magnetic field correction factors determined from the inline MRI-linac configuartion .....	145
Table 6.5: Calibration coefficients of two ionisation chambers and TPR <sub>20,10</sub> -Odense ..	146
Table 6.6: Calibration coefficients of an ionisation chamber and TPR <sub>20,10</sub> -Christie ....	147
Table A.1: Indirect magnetic field correction factor at MRIdian™ and Unity™.....	154
Table A.2: Direct magnetic field correction factor at MRIdian™ and Unity™ .....	155
Table A.3: Indirect magnetic field correction factor at the Australian MRI-linac.....	156

## List of figures

Figure 1.1: Different MRI-linac designs .....	23
Figure 2.1: The dominant interaction type as a function of photon energy .....	27
Figure 2.2: MC calculated path-tracks of electrons in a homogeneous medium.....	30
Figure 2.3: MC calculated path-tracks of electrons in a heterogeneous medium .....	30
Figure 2.4: Schematic illustration of a typical electron track, with and without the effect of a transverse magnetic field .....	37
Figure 2.5: Depth doses without and with 1.5 T magnetic field.....	38
Figure 2.6: Measured 1 T depth dose in the Australian MRI-linac .....	39
Figure 2.7: Dependence of the electron tracks due to magnetic field strengths and energy beams.....	41
Figure 3.1: Schematic front view of the experimental setup .....	49
Figure 3.2: Magnetic field uniformity .....	50
Figure 3.3: Measured and MC calculated lateral profiles a $^{60}\text{Co}$ beam .....	53
Figure 3.4: MC calculated $^{60}\text{Co}$ depth doses for 0 T and 1.5 T .....	54
Figure 3.5: MC calculated beam profiles, for 0 T and 1.5 T .....	55
Figure 3.6: EBT-3 film response curve for all magnetic fields for the red channel .....	56
Figure 3.7: $\Delta\text{netOD}$ for each magnetic field strength as a function of dose .....	57
Figure 3.8. $\Delta\text{netOD}_{\text{DBDallas}}$ a function of magnetic field strength .....	58
Figure 3.9: Ratios of dose, with combined standard uncertainties .....	59
Figure 3.10: Relative uncertainties of netOD and dose values .....	60
Figure 4.1: Irradiation of the alanine a-amino acid produces free radicals.....	65
Figure 4.2: Energy levels of an electron spin.....	67
Figure 4.3: Block diagram of a typical EPR spectrometer. ....	68
Figure 4.4: Absortption curve converted to first derivative .....	69
Figure 4.5: Alanine EPR spectrum. ....	70
Figure 4.6: Typical NPL's alanine pellets. ....	73
Figure 4.7: NPL alanine holder.....	75
Figure 4.8: Front schematic view (cross-section) of the experimental setup.....	76
Figure 4.9: Inline and crossline profiles with 1.5 T and without magnetic .....	77
Figure 4.10: Measured magnetic field uniformity at different strengths .....	78
Figure 4.11: Alanine bevel-air-gap of 0.052 cm .....	79

Figure 4.12: Alanine holder filled with pellets .....	81
Figure 4.13: MC models for the investigation of the effect of the air gaps .....	82
Figure 4.14: MC models to evaluate uncertainties due to air gaps .....	83
Figure 4.15: Validation of the MC models. ....	84
Figure 4.16: Comparison between MC and measurement results.....	86
Figure 4.17: MC results of the effect of the air gaps .....	86
Figure 4.18: a) Depth doses, of the 8 MV energy beam, for 0 T and 1.5 T .....	87
Figure 4.19: Normalised alanine dose as a function of alanine pellet position.....	88
Figure 4.20: Box plots presenting the ratio between the alanine/EPR signal .....	89
Figure 4.21: Alanine quality correction factors for the presence of magnetic field .....	90
Figure 4.22: Alanine relative intrinsic sensitivity .....	91
Figure 4.23: MC simulations to investigate the uncertainty estimation due to the random position of the alanine pellets inside the PEEK holder .....	94
Figure 5.1: Block diagrams of traceability routes for measurement of the absorbed dose to water in the presence of a magnetic field.....	100
Figure 5.2: Traceability route for measurement of the absorbed dose to water in the presence of a magnetic field using alanine as a transfer standard.....	104
Figure 5.3: Farmer-type chamber calibration coefficients as a function of TPR <sub>20,10</sub> ....	107
Figure 5.4: Orientations of a Farmer-type chamber and an alanine holder with respect to the magnetic field and the radiation beam .....	109
Figure 5.5: NPL designed water tank.....	110
Figure 5.6: Experimental setup on the MRI-linac machines .....	111
Figure 5.7: Accelerator head model of the ViewRay MRIdian™ MRI-linac system ..	115
Figure 5.8: Measured and MC calculated lateral dose profiles MRI-linacs .....	119
Figure 5.9: Comparison between MC and measurement results.....	120
Figure 5.10: Normalised MC calculated dose to alanine, when pellets are shifted in four different positions inside the alanine holder .....	122
Figure 5.11: Box plots presenting the normalised chamber signal to the signal of the first measurement of data acquired in MRI-linacs .....	123
Figure 5.12: Ratios of <i>k<sub>ion</sub></i> values with and without magnetic field. ....	125
Figure 5.13. Jaffé plots for a PTW 30013 and an IBA FC65-G chambers .....	125
Figure 5.14: Measured lateral inline profiles of the MRI-linacs.....	127
Figure 5.15: Calibration coefficients of PTW 30013 and IBA FC65-G .....	128

Figure 5.16: Indirect determination of the magnetic field correction factors .....	130
Figure 6.1. Comparison between NPL and VSL dose rate (cGy/MU) values .....	141

## **List of acronyms**

CoP: Code of Practice

CT: Computed Tomography

EPID: Electronic Portal Imaging Devices

ERE: electron return effect

GCUK: GenesisCare, Oxford, UK

ICR: The institute of Cancer Research

IGRT: image guided radiotherapy

IMRT: intensity modulated radiotherapy

IPC: Institute Paoli Calmettes, Marseille, France

linac: linear accelerator

MC: Monte Carlo

MRI: magnetic resonance imaging

MRigRT: MRI-guided radiotherapy

NKI: Netherlands Cancer Institute, The Netherlands

NPL: National Physical Laboratory

OD: optical density

Odense: Odense University Hospital, Denmark

PMMA: polymethyl methacrylate

QA: quality assurance

RF: radio-frequency

RMH/ICR: The Royal Marsden Hospital and The Institute of Cancer Research, UK

SDD: source to detector distance

SRS: stereotactic radiosurgery

SRT: stereotactic radiotherapy

TPS: Treatment planning system

UK: United Kingdom

UoM: University of Montreal

VMAT: volumetric modulated arc therapy

WHO: World Health Organisation

## Chapter 1 Introduction

### 1.1 Radiotherapy

In the United Kingdom (UK) has been reported 367,000 new cancer cases every year (2015 – 2017) and 166,000 cancer deaths<sup>4</sup>. Nevertheless, the cancer mortality rates has decreased by 17% since early 1970s and the five-year survival rates have improved from 24% to 50% over the last 40 years (Cancer Research UK, 2020). Radiotherapy has played a major role in health care and its evolution and improvement over time have allowed for more precise and personalised treatment.

Radiotherapy is the most effective non-surgical treatment that uses high energy ionising radiation to cure the cancer completely (curative radiotherapy) or to reduce the symptoms of cancer (palliative radiotherapy). Radiotherapy can be given externally by a machine (e.g.,  $^{60}\text{Co}$ , linear accelerator, protons) or internally by introducing a radiation source into the body in different ways (e.g., brachytherapy and molecular radiotherapy). The aim of any irradiation technique is to increase the probability of cure and minimise the risk of toxicity to healthy tissues. This can be achieved by a radiotherapy modality that can maximise the dose to the target tumour and minimise the incidental dose in surrounding normal tissues. Modern radiation techniques have greatly improved the risk-benefit ratio in radiotherapy.

Advances in radiation physics and computer technology allows tumours to be visualised directly prior to or even during treatment and ensures that the delivered treatment is comparable with the planned treatment, making it possible to deliver radiation dose more precisely. This is what we call image guided radiotherapy (IGRT), which has a goal to improve the accuracy on delivering the radiation dose to the tumour while minimising the risk to healthy tissues. IGRT was initially performed using planar kV x-ray images, from a radiographic film, combined with skin marks on the external anatomy in order to position the patient with respect to the treatment machine (Haus *et al.*, 1970). Progressive imaging methods, such as Electronic Portal Imaging Devices (EPID) (Herman *et al.*,

---

<sup>4</sup>Worldwide, there were more than 18 million new cases of cancer in 2018 (expected to rise to 27.5 million each year by 2040) with more than 9.5 million deaths: World Health Organization 2020. *Global Cancer Observatory*. <https://gco.iarc.fr/>. Accessed December 2020.

2001, Cremers *et al.*, 2004), diagnostic X-ray source combined with advanced detector systems (Munro and Bouius, 1998, Berbeco *et al.*, 2004), diagnostic Computed Tomography (CT) scanners (Court *et al.*, 2003, Kuriyama *et al.*, 2003), ultrasound devices (Western *et al.*, 2015), etc., can be used for treatment set-up verification. Such technology provides from 2D to 4D (3D + time) information to improve target localisation and determine the delivered dose to the tumour more accurately. The combination or the integration of these imaging devices with a dose delivery system has also helped the implementation of advanced radiotherapy modalities, such as stereotactic radiosurgery (SRS) (Antypas and Pantelis, 2008) or stereotactic radiotherapy (SRT) (Uematsu *et al.*, 2001), intensity modulated radiotherapy (IMRT) (Boyer *et al.*, 2001) and volumetric modulated arc therapy (VMAT) (Popescu *et al.*, 2010).

## 1.2 MRI in radiotherapy

### 1.2.1 MRI imaging

In magnetic resonance imaging (MRI) systems, the philosophy of visualisation and digitisation of a medical image is based on signals received from tissue proton relaxation, which is stimulated by combining a magnetic field and radio waves. Single-proton nuclei, of hydrogen atoms in the body, have spin 1/2, which either aligns or anti-aligns with the magnetic field employed from the MRI scanner. In matter, the ratio of population for each state follows the Boltzmann distribution. The nuclei are excited by a radio-frequency (RF) pulse sequence having a particular frequency called the Larmor frequency, which is defined by the gyromagnetic ratio of the nuclear species of interest (i.e., typically nuclei with an odd number of protons) and the magnetic field strength. That frequency corresponds to the energy excess between the states and therefore allows spin state transitions via electromagnetic interactions (Banwell, 1983). The relaxation of those excited states can further be observed via a macroscopic quantity called the magnetisation which follows the Bloch equation. As the RF waves emitted during spin relaxation have a frequency determined by the magnetic field strength, the use of precise field gradients inside the bore of the scanner can differentiate the signal frequency and phase, which further allows localising the position where the signal is emitted, this way forming an image of signal intensity for a particular excited slice.

### 1.2.2 Advantages and challenges

Radiotherapy relies on contemporary medical imaging techniques to achieve an accurate target definition and dose verification. Imaging is an important ingredient for treatment delivery in radiotherapy planning. Currently, CT data are mainly used in radiotherapy treatment planning, as they provide tissue-specific attenuation values (quantitative Hounsfield Units, HU), which are converted into electron density and used for radiation dose calculations on treatment planning system (TPS) (Chandarana *et al.*, 2018). CT images, however, have limitations on distinguishing soft tissues, and introduces inaccuracy in the contour definition of tumour and organs at risk in radiotherapy. Often are registered into MRI planning scans, which provide superb soft-tissue image contrast. While CT provides geometrical information of dense-tissue and an electron density map, MRI allows better segmentation of the areas of interest.

The incorporation of MRI in treatment planning significantly improves the delineation of, and enables more precise delivery of radiation to, the target volume. Due to its non-ionising properties and the ability to differentiate soft tissue, MRI is an ideal imaging technique. MRI-only treatment planning is not yet a commercial product, but its benefits (i.e. avoiding the imaging dose and the uncertainties associated with the MRI to CT registration) and its independency from a CT have been highlighted in literature and reported in the review work by Owrange *et al.* (2018). Despite the advantages of MRI-only radiotherapy planning, there are several challenges, including lack of electron density information and geometric distortion.

It is challenging for MRI to provide the underlying image data needed for the accurate radiation transport required for radiotherapy planning. Currently it cannot compete with a CT, which dominates this area. CT scans are primarily generated from the detection of an attenuated photon beam, where information of the electron density for each pixelized tissue can be determined. The disadvantage of an MRI to provide such information has been addressed from several studies (Korhonen *et al.*, 2014, Prior *et al.*, 2016, Largent *et al.*, 2019, Leu *et al.*, 2020), where they have developed methods to convert MR pixel values into electron density maps (i.e. generate pseudo-CT from MRI) needed on radiotherapy planning dose calculations.

Another disadvantage of MRI is related to image distortion, such geometric effects leads to errors in spatial localisation. The geometric distortions in MR images arises from various sources, which are categorised as hardware- and tissue-related (Deming and David, 2005). In MRI hardware, these sources are mainly the nonuniformity of the main magnet and the gradient field nonlinearity (in which the distortion is more pronounced away from the scanner isocentre (Doran *et al.*, 2005)), and eddy currents (which are generated from gradient switching). The tissue-related sources include changes in local tissue magnetic susceptibility, which arise from variations in the magnetisation properties of different tissue types within the body. When the patient is placed into the scanner, tissues become magnetised to a degree which depends on the magnetic susceptibility of the tissue. This effect creates an opposing magnetic field which perturbs the main field. This opposing field cannot easily be quantified, as it depends on the position, size, shape, orientation and susceptibility of the tissues (Schenck, 1996). Large geometric distortions due to differences in susceptibility can occur at tissue-air interfaces. Distortions become more noticeable at high magnetic field strengths than at lower because the spatial resolution is improved (as is tissue contrast) while the positional error remains the same (for a given relative non-uniformity in the main magnetic field). In radiotherapy treatment planning it is crucial that images have acceptable quality and their distortion is minimised. Studies have characterised and proposed corrections for the geometric distortion of MRI scans used in radiotherapy treatment planning (Moerland *et al.*, 1995, Fransson *et al.*, 2001, Crijns *et al.*, 2010, Bhushan *et al.*, 2012, Shan *et al.*, 2020). The distortions generated by the MRI hardware are commonly quantified with the use of a phantom with a known geometry. Images of this phantom (reference images) are compared with MR images to create a distortion map across the field of view. Susceptibility artefacts (patient induced distortions), on the other hand, can be minimised by using shorter TE (time to echo) values and fast spin-echo instead of gradient-echo sequences. However, the detailed reasons why some imaging sequences are less affected by the susceptibility artefacts than others are beyond the scope of this introduction and are unrelated to the dosimetry issues investigated in this thesis.

### 1.3 MRI-guided Radiotherapy

During radiotherapy, the tumour and organs can change shape and move as the human body moves (e.g. breathing induced organ motion). Currently, wide margin of radiation

around the tumour is used to ensure that the tumour is always in the beam. Consequently, regions of the bodies are irradiated where no cancer exists to compensate for the movements. MRI-guided radiotherapy (MRIgRT), a state-of-the-art cancer treatment, addresses this issue. This new radiotherapy modality is delivered by an MRI-linac which combines a linac (linear accelerator) with an MRI scanner. Recently, MRIgRT was introduced in the community and the clinical proof-of-principle was delivered (Acharya *et al.*, 2016, Fischer-Valuck *et al.*, 2017, Raaymakers *et al.*, 2017), with the ViewRay MRIdian™ system treating the world's first patient in February 2014 (ViewRay™, 2014). An MRI-linac provides real-time images during a patient's treatment and greatly enhanced soft-tissue image contrast (as discussed previously), while completely avoiding the additional radiation dose associated with treatment integrated imaging x-ray systems. The advantage of high-quality images in an MRI-linac, will enable a radiotherapy beam to be targeted to a precise part of the cancerous tumour, that are the most malicious, and dramatically reduce side effects. MRIgRT is expected to facilitate real-time adaptive radiotherapy planned based on high contrast anatomical images, visualising anatomical changes of the patient, to explore the possibilities of an advanced personalised radiotherapy.

### 1.3.1 Current MRIgRT systems

Development and progress of MRIgRT has attracted the attention of several sites/companies aiming at integrating an MRI scanner with a radiotherapy treatment machine. Currently, there are four different concepts: the Elekta Unity™ from Elekta Instrument AB Stockholm, Sweden (Lagendijk *et al.*, 2008, Raaymakers *et al.*, 2009, Lagendijk *et al.*, 2014b), the ViewRay MRIdian™ from ViewRay Inc., Oakwood, USA (Mutic and Dempsey, 2014) and the Aurora RT™ from MagnetTx Oncology Solutions Ltd. Edmonton Alberta, Canada (Fallone, 2014) are already commercial, and the Australian MRI-linac from the Liverpool hospital, Australia (Keall *et al.*, 2014, Liney *et al.*, 2016) is in the development phase. Figure 1.1 shows the different designs of MRI-linacs and Table 1.1 presents some of their main differences, such as: the energy of the MV treatment beam, the orientation of the external magnetic field with respect to the radiation beam (parallel or perpendicular), the strength of the magnetic field ranging from 0.35 T to 1.5 T and how the patient is irradiated from different coplanar beam directions, either by a radiation source rotating around the patient or by static source with a 'rotating'

patient. For further details on differences between the MRI-linac designs, the reader is referred to the review articles by Lagendijk *et al.* (2014a) and Pollard *et al.* (2017).

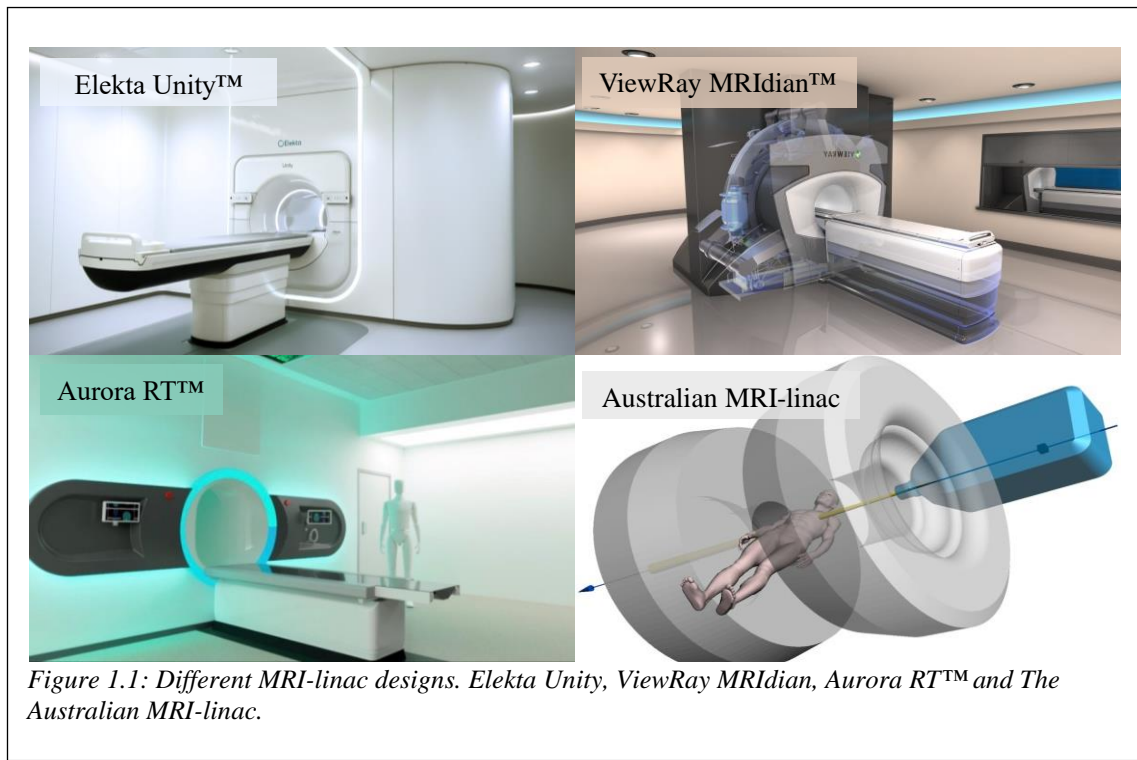


Table 1.1: Differences in the MRI-linac concepts

MRigRT System	MR design	Magnetic field (T)	Energy (MV)	Direction of beam to magnetic field
ViewRay MRIdian™	Split magnet	0.35	6	Perpendicular
Aurora RT™	Biplanar	0.5	6	Parallel <sup>†</sup>
Australian MRI-linac	Open bore	1.0	4 & 6	Parallel <sup>†</sup>
Elekta Unity™	Split bore	1.5	7	Perpendicular

<sup>†</sup>Also known as inline MRI-linac

### 1.3.2 Effect of magnetic field on radiation dosimetry

The main new feature of the MRI-linac technology, however, is the presence of the magnetic field within the patient during treatment and its impact on the central physical quantity of radiation therapy: *absorbed dose*. Naturally, the magnetic field exerts an additional Lorentz force on the energy-depositing electrons in the patient and therefore both key aspects – the calculation of dose required for treatment planning and the

measurement and verification of delivered doses – are affected. My thesis focuses on the effect of the magnetic field on radiation dosimetry. Measurements of the radiation dose in MRIgRT need to be performed in the presence of the constant magnetic field associated with the MRI scanner. Available dosimetry protocols – neglecting the additional Lorentz force – do not support any traceable reference dosimetry in MRIgRT nor do they provide guidance for the radiation field characteristics measurements. There is an urgent need for new radiation dosimetry concepts and strategies that enable the safe clinical practice of MRIgRT. My investigation will affect a large variety of essential processes in medical physics that ensures the safe delivery of dose to any patient. These include TPS commissioning and verification, output dose checks, dosimetry quality assurance (QA) and calibration of the linac dose output.

One essential requirement for the clinical practice of MRIgRT is that dose delivered to the clinical targets and organs at risk should be known with an uncertainty less or equal to the currently established dose uncertainty in conventional radiotherapy. To get to this end, accurate metrological capabilities for reference dosimetry need to be developed to support future dosimetry protocols and provide the users with reliable dosimetry traceable to primary standards. Furthermore, audit methods under reference standard conditions need to be established to ensure consistency in dosimetry between centres that employ MRIgRT.

Besides the aforementioned strategies that ensure the correctness of absolute dose values, the safe practice of MRIgRT relies on comparably high standards for relative dose profiles in all tissues of the patient. Radiotherapy treatments depend on the TPS, whose role is to accurately calculate the dose distribution in the patient’s anatomy. TPS dose calculation algorithms have been well characterised for conventional radiotherapy. However, MRIgRT presents a new challenge in predicting the dose in the patient due to the impact of the MRI static magnetic field on radiation transport. MRIgRT will also widely use small (on- and off-axis) and complex radiation fields to deliver optimized dose distributions to the patient. Unlike conventional small field dosimetry where a code of practice has recently been published (Palmans *et al.*, 2017) and dose can consistently be measured, small field dosimetry in the presence of a magnetic field is challenging. A magnetic field may additionally accentuate charged particle disequilibrium in the presence of medium heterogeneities (Bouchard *et al.*, 2015, de Pooter *et al.*, 2015).

Changes in density over a short space, such as air- and bone-tissue interfaces, and the lack of standardisation in small field dosimetry in MRIgRT, lead to greater uncertainties that must be addressed in dose calculation algorithms. It is of great importance that TPS that handle MRIgRT are supplied with accurate measured input data of absolute and relative (depth and lateral dose profiles) dose. In this context, a suitable detector needs to have the ability to capture electrons affected by the Lorentz force in a medium and consequently the distorted lateral beam profiles and depth dose curves. These data may then be used to evaluate the accuracy of present and future dose calculation algorithms.

## 1.4 Aims of the project

The aim of this PhD project is to investigate, clarify and resolve issues around traceable reference dosimetry for, and calibration of, machines that integrate MRI guidance and delivery of radiotherapy. In this new context, the performance of commercially suitable detectors under the influence of magnetic field strengths is characterised for absolute and relative dosimetry. Furthermore, potential routes to achieve traceability in dosimetry for MRI-linacs, which are compatible with the existing standards and calibrations available for conventional radiotherapy, are identified. Finally, guidelines for calibration and reference dosimetry audit are proposed.

The main issues I address in my thesis are:

1. The definition of reference conditions which are relevant for patient dosimetry (Chapter 2).
2. Assessment of available detector types for use in reference and relative dosimetry, taking into account MR safety, robustness, stability and dose response (Chapter 3 and Chapter 4).
3. Identification of potential routes to achieve traceability in dosimetry for MRI-linacs (Chapter 5).
4. Analysis of uncertainty, including the identification and quantification of the most significant influence quantities (Chapter 3, Chapter 4 and Chapter 5).
5. Draft guidelines for calibration and reference dosimetry audit services (Chapter 5 and Chapter 6).

## Chapter 2 Radiation dosimetry of photon beams with and without magnetic fields

### 2.1 Radiation transport in matter

In radiotherapy, the energy deposited by charged particles is the reason of killing cancer cells. In photon therapy, these particles are electrons, which ionise atoms in living cells leading with high likelihood to unrepairable damage, and finally cell death. Most of the ionisations that result from photon interactions originate from the interactions of secondary electrons. To get to this end, a sequence of interactions of photons and charged particles with a medium need to take place. As neutral particles photons undergo a small number of *discrete* interactions which can be sampled explicitly, it is feasible to simulate photon transport in a completely analogue way. On the other hand, electrons are charged, and in condensed media the number of interactions is too large to simulate in this analogue way. In the following, the sequence of photon and electron interactions is briefly explained.

#### 2.1.1 Interactions with matter

To treat cancer with radiotherapy, photons ( $\gamma$ -rays) are either created by a radioactive source or by thick-target bremsstrahlung interactions of a linac – accelerated electron beam. The photon beams are shaped (i.e., collimated or modulated) and combined in an optimal way to maximise the absorbed dose to targets (i.e., tumours) while minimising absorbed dose to organs at risk. A photon penetrating a medium may lose all, part or none of its energy. In the latter, the photon is transmitted through a medium without any interaction. In the first two, the photon is absorbed or scattered: it may undergo a single or multiple interactions transferring all or part of its energy to the medium and set electrons into motion. The important interaction processes of the photon with a medium in medical applications are the photoelectric process, the Compton scatter and the pair production. All three interactions transfer energy from the photon radiation field to electrons (and a positron in the pair production process). The probability of any of them to happen depends on the energy of the incident photon and the atomic number of the material (Figure 2.1). The photoelectric process dominates at low energies, the pair

production at high energies and at intermediate energies the Compton scatter is the most important process of photon-tissue interactions in megavoltage radiation therapy.

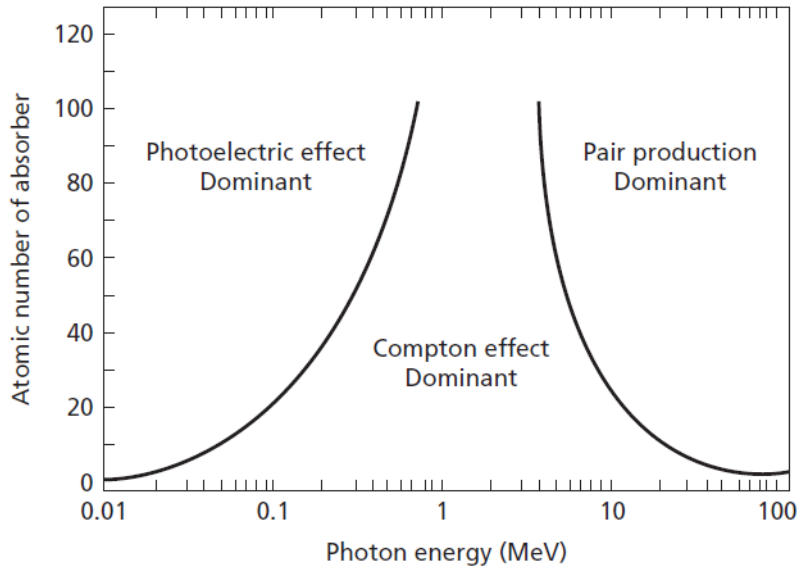


Figure 2.1: The dominant interaction type as a function of photon energy for different atomic number ( $Z$ ) of the absorber. Figure retrieved from Pawlicki et al. (2016).

The result of the photon interaction processes is the production of energetic secondary electrons. These electrons, when moving through a medium, experience multiple interactions and their kinetic energy is decreasing in a stochastic process, until they come at rest or they leave the medium. Their kinetic energy is given up by two different mechanisms: collision losses and radiation losses. In the first one, electrons lose energy through interactions with the orbit electrons of an atom, which leads to excitation of an atom or ionisation. Any scattered electron may be energetic enough to interact with another atomic electron (produce further excitation or ionisation along its own path) before it loses its energy and is captured by an atom. The excited and ionised atoms, with vacancies in their orbits, will relax via the emission of photons (characteristic x-rays). There is also the probability for an electron, when it is moving to an inner shell, to transfer its excitation energy to eject an electron from an outer shell: the Auger electron, instead of radiating an x-ray. This process results with two vacancies, which may be filled with the emission of further Auger electrons leading to multiple ionisation of the atom. The probability of an Auger electron to be emitted decreases with atomic number of the medium. In the radiation loss process, high energy electrons can also interact with the

electrostatic field of the atomic nucleus. When an electron passes close to a nucleus is decelerated, leaving in a different direction with reduced kinetic energy. The decrease in the electron's kinetic energy results in a photon being emitted (named bremsstrahlung photon). As in the scattered electron from the collision losses process, the deflected electron may also interact with another atom. The bremsstrahlung production is increasing with the atomic number of the medium and therefore is higher probability of this occurring in materials with larger atomic number. In megavoltage radiation therapy, this process is unusual, because human's tissues (soft tissues) have low atomic number. In this case collision losses predominates, and leads to a production of high-energy electron-photon cascade shower, which will stop when the energy of secondary electrons has been absorbed in the medium. During this process, electrons transfer their energy to medium, i.e. deposits absorbed dose.

### 2.1.2 Magnetic field coupling to MV beams

The key challenge of my thesis, in developing concepts of radiation dosimetry in the presence of a magnetic field, is the effect of the Lorentz force on the cascades of electrons set in motion by the original photon beam. Instead of traversing matter between successive interactions in a straight line, the electron follows a curved trajectory tending to spiral around the magnetic field direction. This modifies dosimeter response and the absorbed dose distribution in media.

#### 2.1.2.1 The Lorentz magnetic force

The Lorentz force,  $F$ , is the combined force on a particle of charge  $q$  with a velocity  $v$  from the electric field,  $E$ , and the magnetic field,  $B$ .

$$\vec{F} = q(\vec{E} + \vec{v} \times \vec{B}) \quad (2.1)$$

While an electric field can affect the kinetic energy of a charged particle, a magnetic field cannot, because it acts perpendicular to the direction of motion. In the absence of an electric field, the force reduces to:

$$F = |q\vec{v} \times \vec{B}| = q v B \sin(\theta) \quad (2.2)$$

where  $\theta$  is the angle between the direction of the velocity of the charge and the direction of the magnetic field. The motion of a charge particle in a magnetic field depends on the

initial angle  $\theta$ . Assuming a charged particle in a vacuum and in a uniform magnetic field, if  $\theta$  is:

- $0^\circ$  (parallel or antiparallel), the force will be zero and the charged particle continues to move along the same line with the same velocity in the same direction.
- $90^\circ$  (perpendicular), the charged particle experiences maximum magnetic force in direction perpendicular to the plane of the magnetic field and it will start moving in a uniform circular motion.
- at any other angle, it is only the component of the velocity which is perpendicular to the field which contributes to the force. The charged particle follows a helical path whose axis is aligned with the magnetic field.

#### **2.1.2.2 Effects on radiation transport**

The trajectories of electrons, transported in medium, in the presence of external electric and magnetic fields can be quite complicated, but may need to be considered in an analysis of the response of some detectors (for instance, the drift of ions in an air-filled ionisation chamber). For reference dosimetry in MRIgRT we can specialise to the case where the external field is purely magnetic. The electron loses kinetic energy through its interactions with the medium and the electron trajectory determines where this energy is absorbed by the medium. Those interactions are essentially unaffected by the external magnetic field, which only modifies the trajectories between interactions, and it is in this way that the magnetic field modifies the dose distribution arising from a given incident beam. Assuming that the energy loss by synchrotron radiation is negligible, the curved pathlength of the electron trajectory is independent of the magnetic field and will be the same with and without magnetic field.

A magnetic field modifies the electron trajectories in water, as shown in Figure 2.2, and the further effects of changes in density, such as between water and air, are shown in Figure 2.3.

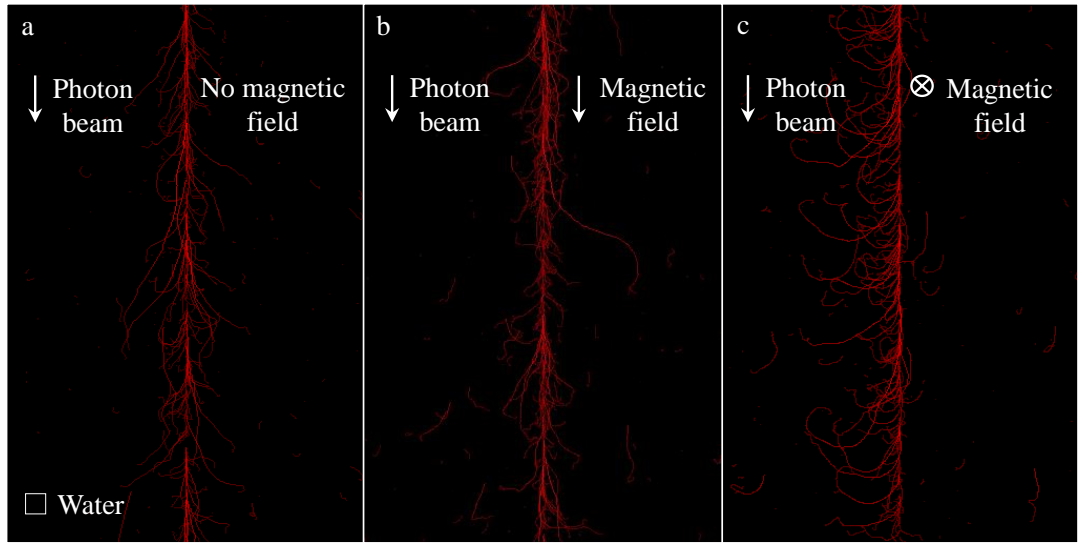


Figure 2.2: MC calculated path-tracks of electrons traversing a homogeneous medium of water, without magnetic field (a) and with magnetic field strength of 1.5 T, orientated either parallel (b) or perpendicular (c) to the direction of an 8 MV pencil photon beam. Symbol  $\otimes$  indicate magnetic field pointing into the plane.

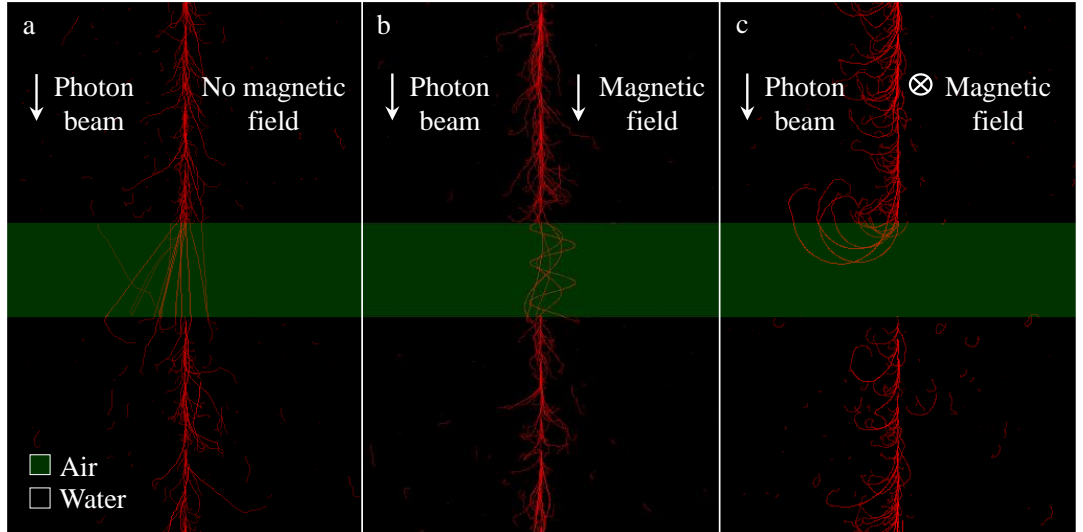


Figure 2.3: MC calculated path-tracks of electrons traversing a heterogeneous medium (water-air-water), without magnetic field (a) and with magnetic field strength of 1.5 T, orientated either parallel (b) or perpendicular (c) to the direction of an 8 MV pencil photon beam. Symbol  $\otimes$  indicate magnetic field pointing into the plane.

Figure 2.3 (c) shows a particular case, where the electrons travel in a heterogeneous medium, between high- and low-density regions (through water and air). In this case, the magnetic field noticeably changes the electron trajectories, forcing them to curve back and deposit their energy near the surface in the high-density region. This is an example

of the so-called electron return effect (ERE), which has been extensively discussed in the literature (Jette, 2000, Raaijmakers *et al.*, 2005, Raaijmakers *et al.*, 2007a, Kirkby *et al.*, 2008, Oborn *et al.*, 2010).

### 2.1.3 Monte Carlo radiation transport simulations

Monte Carlo (MC) simulations of detector response play a major and increasingly important role in accurate radiation dosimetry, including the characterisation of physical properties of beams and of radiation detectors. MC radiation transport codes, such as EGSnrc and PENELOPE have demonstrated a self-consistency test, by performing a Fano cavity test on MV beams, at a level of 0.1% (Seuntjens *et al.*, 2002, Sempau and Andreo, 2006). It has also been shown that the level of agreement with ionisation chamber experimental data, being the most difficult challenge for such a technique, is of the order of 0.3%, in  $^{60}\text{Co}$  and MV photon beams (McEwen *et al.*, 2014).

Accuracy in radiation transport is generally improved by reducing the energy thresholds for production of charged particles (AE) and photons (AP), which are defined when generating media, and reducing the cutoff energies (in MeV) for transport of charged particles (ECUT) and of photons (PCUT). In this way the simulation is closer to the physical processes, however, this makes it much more time consuming.

In the presence of the magnetic field, studies (Bouchard and Bielajew, 2015, Bouchard *et al.*, 2015, de Pooter *et al.*, 2015) have demonstrated that is necessary to define special conditions under which the Fano cavity test can be performed to check the consistency of MC transport algorithms. Accuracy in electron transport is generally improved by restricting the maximum step size. For instance, EGSnrc has a transport parameter ESTEPE, which is the maximum fractional kinetic energy loss per step. For transport in electromagnetic fields, the effect of the Lorentz force needs to be limited and the relevant parameter in EGSnrc is EM ESTEPE. This parameter implements an additional step size restriction: it is the maximum change in direction of motion, in radians per step, for charged particle transport in an electromagnetic field. Research undertaken in the EMPIR project of MR-guided radiotherapy (EMPIR 15HLT08 MRgRT), has shown that the EM ESTEPE parameter needs to be reduced from its default value (0.2) when the material density is low, e.g. for air, the parameter needs to be 0.01 in order to achieve the desired level of internal consistency of around 0.1% with EGSnrc (MRgRT, 2019).

## 2.2 Reference dosimetry of photon beams

The aim of reference dosimetry measurements is to calibrate the output of a linac, by following procedures from national or international Codes of Practice (CoPs), such as TRS 398 (Andreo *et al.*, 2000), TRS 483 (Palmans *et al.*, 2017), IPEM CoP (Lillicrap *et al.*, 1990, Eaton *et al.*, 2020), TG 51 (Almond *et al.*, 1999), etc. Measurements of the dose rate at a point are performed under reference conditions as described in CoPs: at a reference depth, in a water phantom for a nominal source to surface distance and with a reference field size (typically 10 cm × 10 cm) at the measurement point, which usually is at the isocentre of a linac. The output calibration is performed with radiation dosimeters by measuring the absorbed dose to water. The dosimeters must be traceably calibrated against a primary standard of absorbed dose to water, either directly or indirectly by intermediate steps, and corrected for quantities that will influence the true measured dose.

### 2.2.1 Theory of absorbed dose measurement in photon beams

Ionising radiation removes an orbital electron around the atomic nucleus producing electrical charges on atoms or molecules. One of the important effects of the ionising radiation is to damage DNA from a cell<sup>5</sup>. This happens directly or indirectly. In the first case, the atoms of the DNA molecule, or a neighbouring molecule, are ionised or excited and the ejected electron strikes and disrupts the DNA molecule (Sevilla *et al.*, 2016). In the second case, the reactions with water molecules surrounding the DNA (cellular fluid), lead to radiolysis and the production of free radicals ( $H^+$  and  $OH^-$ ). The free radicals may diffuse, reach to and react with the DNA molecules to restore a stable configuration of electrons. This will result with the disruption of the DNA molecule: causing the DNA to be ionised. It is estimated that the indirect processes account for two-thirds of the DNA damage (Reisz *et al.*, 2014). This is plausible, as the volume of the cellular fluid is much larger compared to the DNA.

The radiation damage to a tissue may be related to the energy absorbed by a tissue (or to the energy deposited to a tissue). The process of this absorbed energy is important as it

---

<sup>5</sup> DNA is critical for the reproduction of a cell, and ionising radiation would greatly affect cells that are rapidly reproduced, including most types of cancer. Thus, cancer cells are more sensitive to ionising radiation.

will be followed by complex physical, chemical and biological processes, as explained above.

The absorbed energy may be quantified by the absorbed dose  $D$ , which is defined as the mean energy  $d\bar{E}$  imparted by ionising radiation to a medium of mass  $dm$  (Hohlfeld *et al.*, 2001):

$$D = \frac{d\bar{E}}{dm} \quad (2.3)$$

and the SI unit of the absorbed dose is the gray (Gy):

$$1 \text{ Gy} = \frac{1 \text{ J}}{\text{kg}} \quad (2.4)$$

In radiotherapy, absorbed dose to water is the main quantity of interest as water is radiologically very similar to soft tissue. As a result, dose distributions in water are close to dose distributions in patient. This has driven the establishment of primary standards and the development of CoPs, protocols and recommendations for the measurement of the quantity of absorbed dose to water.

### **2.2.2 Determination of absorbed dose to water in reference conditions**

The absolute realisation of the absorbed dose to water is performed at primary standard laboratories. Based on the ICRU report 64 (Hohlfeld *et al.*, 2001) there are three fundamental methods: calorimetry (water- or graphite-based), chemical dosimetry and ionometry. The water absorbed dose calorimetry allows for the most direct realisation of the absorbed dose to water. The rest of the methods involve a number of steps and the application of conversion factor(s) is required. These fundamental methods will provide calibration coefficients for radiation detectors to allow the dissemination of the absorbed dose to water for radiotherapy purposes.

Traceability for measurements of the absorbed dose to water must be maintained to a primary standard. This is usually achieved through utilization of a transfer standard. This is a dosimetry device that is calibrated by comparison to a national standard, either directly or indirectly through intermediate calibrations. The intention of a transfer standard is to serve as a reference for calibrating secondary standards, which are radiation

detectors used to disseminate the absorbed dose to the end user. The calibration is performed under reference conditions (i.e. source to detector distance (SDD), depth in water, field size, environmental conditions, etc.), which are the same conditions as the absolute absorbed dose to water has been realised from a primary standard.

National (Lillicrap *et al.*, 1990, Almond *et al.*, 1999, Eaton *et al.*, 2020) and international (Andreо *et al.*, 2000, Palmans *et al.*, 2017) CoPs provide the methodology to ensure a high level of consistency in the determination of the absorbed dose to water in high energy photon beams among different external radiotherapy clinics (the user level). This involves the use of a calibrated detector (ionisation chamber is the most common detector used in everyday practice), which needs to be used in conditions that match those of calibration, in order for its calibration coefficient to be valid.

The reference measurement of the absorbed dose to water  $D_w$  for a reference beam quality  $Q_0$  is given by the relation:

$$D_{w,Q_0} = M_{Q_0} \cdot N_{D,w,Q_0} \quad (2.5)$$

where  $M_{Q_0}$  is the detector's signal (corrected to standard environmental conditions, i.e. temperature, pressure, humidity) at a reference beam quality  $Q_0$  and  $N_{D,w,Q_0}$  is the detector's calibration coefficient in terms of absorbed dose to water under the reference conditions used in a standard laboratory for a reference beam quality  $Q_0$ .

The determination of absorbed dose is subject to influence quantities, such as radiation energy, depth of the point of measurement, dose rate and radiation field size (Andreо *et al.*, 2000), all of which can affect the radiation quality and may change between calibration and measurement. The corrections which are then needed make up the overall quality dependent correction factor.

In most clinical situations, the measurement conditions of the absorbed dose to water using ionisation chambers do not match the reference conditions used in a standard laboratory and for which dosimetry CoPs apply. For instance, detectors are usually used in a different energy beam. Therefore, measurement at the user's beam quality  $Q$  different from the reference quality  $Q_0$  (where in most primary standard laboratories is  $^{60}\text{Co}$  gamma radiation) requires a beam quality correction factor, which is defined as:

$$k_{Q,Q_0} = \frac{N_{D,w,Q}}{N_{D,w,Q_0}} \quad (2.6)$$

where,  $N_{D,w,Q}$  is the calibration coefficient of the detector in terms of absorbed dose to water measured at a standard laboratory for the user's beam quality  $Q$ . Consequently, when a detector is used to measure the absorbed dose to water at radiation beam quality different from that it has been calibrated, the absorbed dose to water is given by:

$$D_{w,Q} = M_Q \cdot N_{D,w,Q_0} \cdot k_{Q,Q_0} \quad (2.7)$$

Modern radiotherapy modalities use complex and small radiation fields, and the dosimetry aspect in such conditions is not in line with conventional reference conditions. The recent published international CoP, TRS 483 (Palmans *et al.*, 2017), provides guidelines for reference dosimetry in small static field in external beam radiotherapy. Similarly to the beam quality, a departure from the reference radiation field size requires a correction factor to account for the change on the absorbed dose to water. To account for this change, a formalism was introduced by Alfonso *et al.* (2008), where a new set of machine specific reference field conditions are introduced for radiotherapy modalities that cannot achieve the conventional reference conditions.

## 2.3 Reference dosimetry in MRIgRT

Reference dosimetry for conventional radiotherapy is usually performed with ionisation chambers. In practice, secondary chambers are calibrated against a primary standard for absorbed dose to water (as explained in section 2.2.2) and then used to calibrate the output of radiotherapy machines following CoPs for clinical implementation of reference dosimetry.

At the current stage, the scope of existing high energy photon therapy dosimetry CoPs do not include dosimetry in MRIgRT. Although some reference conditions (i.e. SDD, depth in water, field size, etc.) for the realisation of the absorbed dose may be achieved in MRIgRT, the effects of the magnetic field on dosimetry are not considered, making these protocols invalid (unless and until those effects can be shown to be negligible).

A known effect, and one investigated extensively in the literature, is the influence of the constant magnetic field of the MRI scanner on radiation dosimetry. This field alters the

direction of motion of charged particles, due to the Lorentz force, and consequently affects the detector response and the dose to medium. Several studies have investigated the influence of the magnetic field on different detectors, such as: ionisation chambers (Reynolds *et al.*, 2013, O'Brien *et al.*, 2016, Spindeldreier *et al.*, 2017, Pojtinger *et al.*, 2018, Cervantes *et al.*, 2020), Gafchromic<sup>TM</sup> film (Reynoso *et al.*, 2016, Roed *et al.*, 2017, Barten *et al.*, 2018, Delfs *et al.*, 2018), Fricke dosimeters (Trachsel *et al.*, 2020) and Presage (Costa *et al.*, 2018). Other studies have quantified the effect of the magnetic field on the absorbed dose to water (Litzenberg *et al.*, 2001, Raaymakers *et al.*, 2004, Raaijmakers *et al.*, 2005, Raaijmakers *et al.*, 2007b, Oborn *et al.*, 2014, Gargett *et al.*, 2015, O'Brien *et al.*, 2016).

Several studies suggested a formalism (O'Brien *et al.*, 2016, van Asselen *et al.*, 2018, Malkov and Rogers, 2019, Cervantes *et al.*, 2020) that can be used for the determination of the absorbed dose to water. This formalism introduces a magnetic field strength-dependent correction factor to modify the detector calibration coefficient from zero magnetic field.

In the next two sections, the effect of the magnetic field on dose to water and to ionisation chamber response is explained. This will support the determination of the reference dosimetry and the detector quality correction factor under the presence of magnetic fields (section 2.3.3).

### 2.3.1 Effect of magnetic field on absorbed dose to water

As it is explained in section 2.1.2, the path of an electron trajectory moving in a medium is subject to the interactions with the atoms of the medium: the lower the density of a medium the larger the path length. In the presence of a magnetic field the path length is independent of the Lorentz force and it is analogous to the case without magnetic field. What the Lorentz force will change, is the direction of the electron trajectory. The force causes an angular change in the direction of the trajectory at a certain rate in radians per unit path length. In low density medium (i.e. air) this change would be more pronounced, as an electron will undergo less interactions, with the distance between each interaction being large, the trajectory is longer and the cumulative effect of the Lorentz force is a larger change in the direction. On the other hand, in a condensed medium (i.e. water) the distance between interactions is small, the electron path length is shorter, and the

cumulative effect of the Lorentz force is much smaller. Thus, magnetic fields effects are more pronounced in low density media.

To understand the effect of the magnetic field on dose to water in a photon beam, one can think in terms of the secondary electrons which are responsible for converting the energy, transferred at their depth of production, into absorbed dose over a range of depths. The magnetic field affects the secondary electrons, but not the photons that generate them: it modifies the transport of energy from the depth of production to where the energy is deposited. The interactions and rate of energy loss along the electron track are unaffected, but the tendency of the Lorentz force to make each electron track curl up means that, overall, the energy is carried a shorter distance and concentrated into a narrower range of depths (closer to the depth of production than when the field is zero).

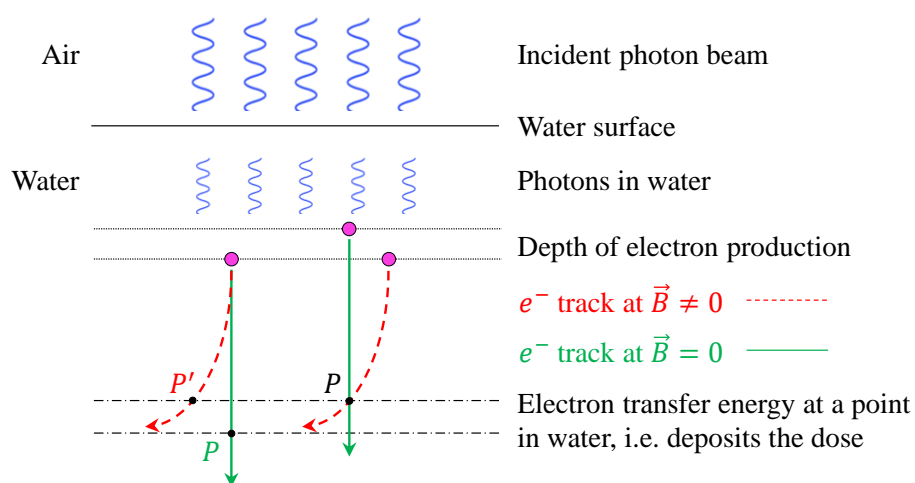
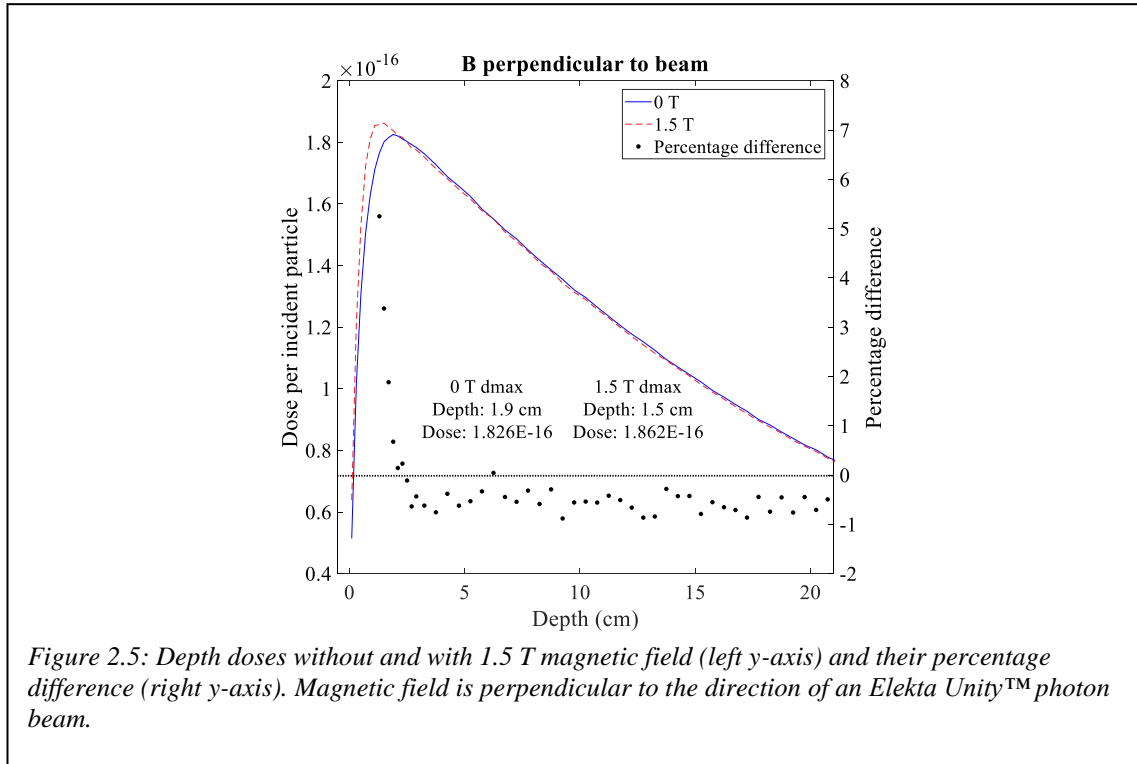


Figure 2.4: Schematic illustration of a typical electron track, with and without the effect of a transverse magnetic field. On the left, the effect is shown by aligning the tracks to have the same depth of electron production. On the right, the effect is shown by aligning the tracks to have the same depth of energy deposition

Figure 2.4 shows a schematic version of a typical electron track, with and without the effect of a transverse magnetic field. On the left, the effect is shown by aligning the tracks to have the same depth of electron production. In this case the electron will have the same energy and path length, but the corresponding points on their paths will be deposited at different depths ( $P$  for  $B = 0$  and  $P'$  for  $B \neq 0$ ). On the right, the effect is shown by aligning the tracks to have the same depth of energy deposition (of course, energy is deposited along the whole track, and this alignment varies according to whether one

considers energy deposited earlier or later along the electron track). The magnetic field has the effect of increasing the thickness of water through which the photon must travel, before producing the electron which makes this contribution to the dose at the depth of interest. The resulting increased photon attenuation accounts for the reduction in dose beyond the depth of dose maximum, as shown in Figure 2.5.



The effect of the magnetic field on dose to water is also seen in Figure 2.5, where MC calculated depth doses without and with 1.5 T magnetic field are shown in the left y-axis and their percentage difference in the right y-axis. In the build-up region, where an electronic equilibrium is being approached<sup>6</sup>, the electrons (generated in the water) are deflected by the Lorentz force and deposit their energy closer to the surface. In this case, the effect of the magnetic field is to increase the surface dose. In a way, this reduction in the depth over which electrons transport energy makes the depth dose curve look more like a depth collision kerma curve. As a result, the build-up is steeper and the  $d_{max}$  position is shifted closer to the surface by 0.4 cm for the 1.5 T compared to 0 T depth dose. When the magnetic field is on, the dose at  $d_{max}$  is increased by 2% and the surface

<sup>6</sup>As the depth in water increases, the electron fluence also increase, until is balanced by the upstream photon beam attenuation.

dose is enhanced by 24%. A separate effect, whereby the magnetic field deflects contaminant electrons as they approach the surface in air, tends to reduce surface dose and somewhat offsets this enhancement. At depths greater than  $d_{max}$ , where a transient electron equilibrium is established, the 1.5 T depth-dose curve is constantly lower by an average of 0.6%  $\pm 0.04\%$ .

In the case where the magnetic field is orientated parallel to the direction of the photon beam, a study by Bielajew (1993) demonstrated that, in broad parallel beams: under conditions of lateral electron equilibrium, the absorbed dose to water at the central axis of the beam is magnetic field independent. This simplifies the measurement of the absorbed dose in the presence of longitudinal magnetic fields, as the determination of the magnetic field correction factor (discussed in section 2.3.3) is subject to the effect of the magnetic field to the chamber signal only.

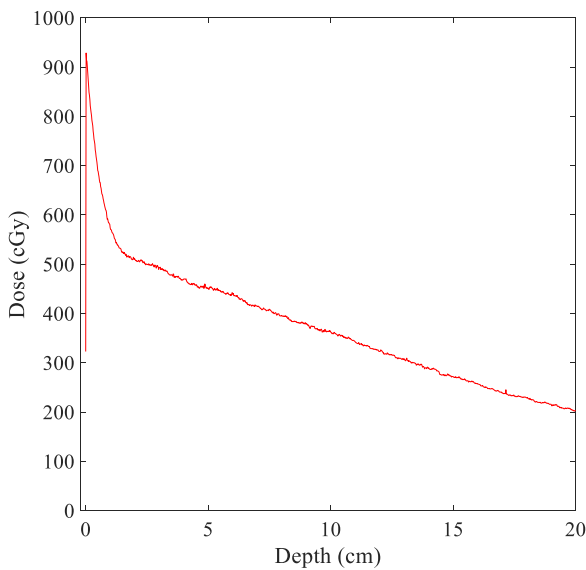


Figure 2.6: Measured 1 T depth dose in the Australian MRI-linac, where the magnetic field is parallel to the direction of the beam.

One of the deleterious effects of a longitudinal magnetic field on inline MRIGRT systems, is the surface dose enhancement, compared to the zero field. The fringe field from the magnet will collect and channel the contaminant electrons, generated in air and in the accelerator, on the surface of the water (or the patient's skin). This effect can be seen on Figure 2.6, where a measured depth dose of the Australian MRI-linac, that employs a 1 T magnet, is shown. Magnetic field in perpendicular orientation to the beam, has been used

in the past to eliminate the surface dose from the contaminant electrons Yorke *et al.* (1985).

### 2.3.2 Effect of magnetic field on ionisation chamber response

In the presence of a magnetic field, the charged particles traversing the air-cavity of an ionisation chamber experience the additional Lorentz force induced by the magnetic field, which strongly modifies the chamber's dose response and makes it challenging to perform beam output measurements in MRI-linacs. Recent works have shown that the uncertainty of ionisation chamber-based dosimetry is significantly increased by the presence of strong magnetic fields. Measurements and MC calculations have previously been made to characterise the response of different type of ionisation chambers (Meijsing *et al.*, 2009, Reynolds *et al.*, 2013, Smit *et al.*, 2013, O'Brien *et al.*, 2016, Spindeldreier *et al.*, 2017, Pojtinger *et al.*, 2018, Cervantes *et al.*, 2020). These works investigated the optimal chamber orientation with respect to magnetic field and radiation beam, parallel ( $\uparrow\uparrow$ ) or perpendicular ( $\perp$ ), as well as the magnetic field correction factor at different strengths. Considering the change of a Farmer-type chamber (mostly used as a reference detector) response in magnetic field strengths ranging from 0.35 T to 1.5 T relative to its response at 0 T, these studies found that when the long axis of the ionisation chamber is:

- i.  $\perp$  to the magnetic field and the radiation beam is  $\perp$  to the magnetic field the changes range from 4% - 11.3%.
- ii.  $\uparrow\uparrow$  to the magnetic field and the radiation beam is  $\perp$  to the magnetic field the change is  $\leq 1\%$ .
- iii.  $\uparrow\uparrow$  or  $\perp$  to the magnetic field and the radiation beam is  $\uparrow\uparrow$  to the magnetic field the change increases near to 2%.

When the magnetic field is switched on, the Lorentz force affects electron trajectories entering the chamber air cavity. This modifies the chamber response due to the ERE (electrons in the air cavity are curved back towards where they entered the cavity) and due to the change in the trajectories of the electrons scattered from the stem and from the chamber collecting electrode. Figure 2.7 (b) shows the response of a Farmer type chamber as a function of magnetic field strength for different energy beams. Data are from measurements that I performed at NPL (National Physical Laboratory, which is the UK Metrology Institute) by irradiating the chamber in a perpendicular orientation in an

electromagnet. Figure 2.7 (b) shows that the signal increases up to a certain magnetic field strength, beyond which it starts to decrease. The magnitude of the effect depends on the energy: the higher the energy the smaller the effect. The change in response of the chamber, in these different conditions, is due to the average effect on the electron path length, in the chamber cavity, of the magnetic field for a given energy beam. The stronger the magnetic field, the more the Lorentz force reduces the radius of curvature, tending to increase the average electron path length in the air cavity, as shown in Figure 2.7 (a). After a certain magnetic field strength, and also depending on the energy, the average path length in the air cavity starts to decrease. The extent of this effect, as it is reported on the three bullet points above, depends on the chamber orientation with respect to the magnetic field. In the perpendicular orientation of the chamber to the magnetic field (where electrons are pushed either towards the thimble tip or towards the stem of the chamber) the path length of electron tracks in the air cavity is greater compared to the parallel orientation. In this case, the magnetic field correction factor is stronger (i.e. further from unity), as the fractional change in the chamber signal is higher and consequently the calibration coefficient, for the effects of a magnetic field, needs to be stronger. All of these effects are more noticeable when the sensitive medium is air, compared to condensed media such as alanine etc., because the Lorentz force effect is cumulative and longer trajectories are affected more.

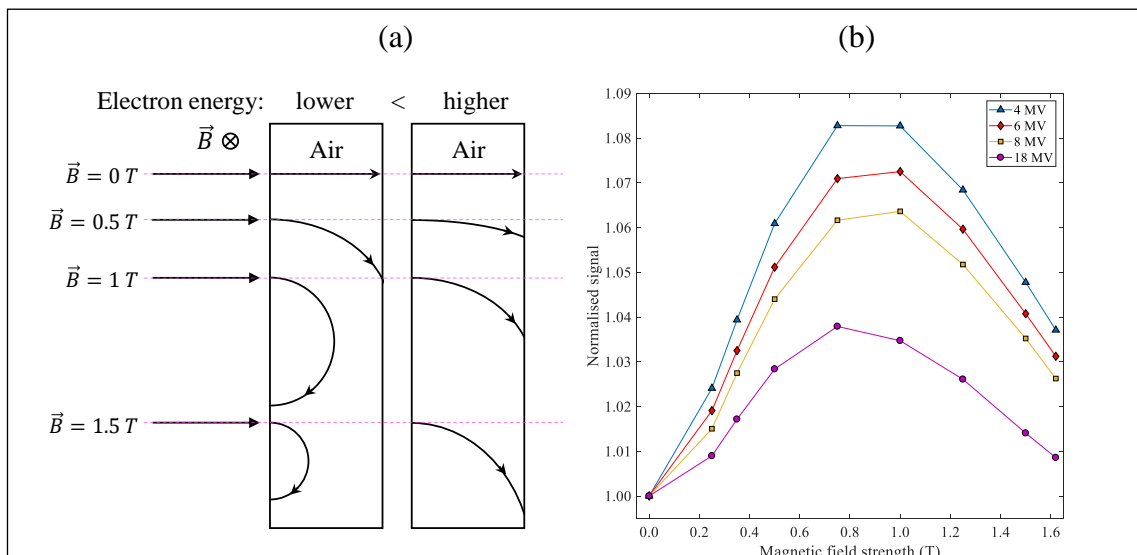


Figure 2.7: (a) Schematic illustration of the dependence of the electron tracks due to magnetic field strengths and energy beams, and (b) measured Farmer-type chamber response as a function of magnetic field strength, for different energy beams, when orientated perpendicular to magnetic field.

Among other effects of ionisation chambers in magnetic fields, which increase the uncertainty on dose measurement, are the air gaps around the cavity (Hackett *et al.*, 2016, Agnew *et al.*, 2017, O'Brien and Sawakuchi, 2017). This will restrict the use of ionisation chambers in water phantoms to avoid a significant signal variation, i.e. 3.8% for a Farmer-type chamber (Agnew *et al.*, 2017). It has also been shown (Malkov and Rogers, 2017, Spindeldreier *et al.*, 2017, Pojtinger *et al.*, 2019) that dead volumes (or the true sensitive volume) should be taken into account when performing MC simulations. Small changes in the collecting volumes can lead to a deviation of 1.4% between the simulated and the experimentally determined dose response in magnetic fields (Pojtinger *et al.*, 2019), on Farmer-type chambers. This, together with the intra-type chamber variation (i.e. non-radial symmetry), will result in significant disagreement with experimental data and will increase the uncertainty on future tabulated MC calculated quality correction factors for the presence of magnetic field for specific chambers.

### 2.3.3 Determination of absorbed dose to water in the presence of magnetic fields

The reference measurement of the absorbed dose to water in magnetic field  $B$  for a user beam quality  $Q_B$  and in the absence of the detector is given by:

$$D_{w,Q_B} = M_{Q_B} \cdot N_{D,w,Q_B} \quad (2.8)$$

where  $M_{Q_B}$  is the signal of the detector in a magnetic field at the user's beam quality  $Q_B$ , corrected for the reference values of influence quantities other than the quality correction factors of the beam and the presence of magnetic field, for which the calibration coefficient is valid.  $N_{D,w,Q_B}$  is the calibration coefficient of the detector in terms of absorbed dose to water in a magnetic field measured by a standard laboratory for the user's beam quality  $Q_B$ .

The user's beam quality  $Q_B$  is not available in standard laboratories and detectors are calibrated at a reference beam quality  $Q_0$  and in the absence of a magnetic field. As for the case of the beam quality and small field, the use of a magnetic field also indicates the departure from reference conditions. In that case, equation (2.8) is replaced by:

$$D_{w,Q_B} = M_{Q_B} \cdot N_{D,w,Q_0} \cdot k_{Q,Q_0} \cdot k_{Q,Q_B} \quad (2.9)$$

where  $N_{D,w,Q_0}$  is the calibration coefficient of the detector in terms of absorbed dose to water measured at a standard laboratory under reference conditions for a beam quality  $Q_0$ ,  $k_{Q,Q_0}$  and  $k_{Q,Q_B}$  are the beam quality correction factor, as defined in equation (2.6), and the magnetic field correction factor, respectively, that correct  $N_{D,w,Q_0}$  for the difference between the reference beam quality  $Q_0$  and the user quality in magnetic field  $Q_B$ .

The quality correction factor for the presence of the magnetic field  $k_{Q,Q_B}$  is defined, by analogy with the beam quality correction factor  $k_{Q,Q_0}$ , as:

$$k_{Q_B,Q} = \frac{N_{D,w,Q_B}}{N_{D,w,Q}} \quad (2.10)$$

where  $N_{D,w,Q}$  is the calibration coefficient of the detector in terms of absorbed dose to water and converted by the application of  $k_{Q,Q_0}$  from a beam quality  $Q_0$  to the user's beam quality  $Q$ , in the absence of a magnetic field.  $k_{Q_B,Q}$  will correct for the effect of the difference between the reference condition (no magnetic field) and the actual user condition (with magnetic field). In principle, it will also correct for the influence of the magnetic field on both the detector's signal and the absorbed dose to water.

Measured and calculated magnetic field correction factors, for different detectors, different orientations with respect to the magnetic field and different magnetic field strengths, have been reported in literature. However, it is apparent that few of the scientific articles (van Asselen *et al.*, 2018, de Prez *et al.*, 2019b, Krauss *et al.*, 2020) have adequately determined such factors for MRI-linac systems. Most of the articles (Meijsing *et al.*, 2009, Reynolds *et al.*, 2013, Smit *et al.*, 2013, O'Brien *et al.*, 2016, Spindeldreier *et al.*, 2017, Pojtinger *et al.*, 2018, Shipley *et al.*, 2019) reports correction factors that have been obtained in either a non-MRI-linac environment, or without considering the actual collection efficiency in MC simulations or wrongly expressing  $k_{Q_B,Q}$  as a ratio of detector readings with and without magnetic field, only. Comparison between the  $k_{Q_B,Q}$  values from these studies will introduce inconsistency. Nevertheless,

a review report by de Pooter *et al.* (2021) has made such attempt by applying some criteria for the selection of the  $k_{Q_B,Q}$  values.

### 2.3.4 Beam quality characterisation in the presence of magnetic fields

One important aspect in reference dosimetry for conventional MV photon beams, is the determination of the beam quality, which is usually specified based on either %dd(10)<sub>x</sub> (AAPM TG-51) or TPR<sub>20,10</sub> (TRS-398, TRS-483 and most national CoPs). %dd(10)<sub>x</sub> is defined as the percentage depth dose at 10 cm depth, in a 10 cm x 10 cm radiation field and at a source to surface distance (SSD) of 100 cm, for photons only and excluding electron contamination in the beam. On the other hand, TPR<sub>20,10</sub> is defined from the ratio of the measured absorbed doses (or the corrected ionisation chamber signals) at 20 cm and 10 cm depth in water, in a 10 cm x 10 cm radiation field. Although the definition of TPR<sub>20,10</sub> specifies an SSD of 100 cm, it turns out that the value TPR<sub>20,10</sub> is essentially independent of distance provided that the field size 10 cm x 10 cm is maintained.

TPR<sub>20,10</sub> is already independent of electron contamination, as measurements are determined at a depth beyond the build-up region, while %dd(10)<sub>x</sub> is defined to exclude such effects, by the application of a lead foil in the beam. The strong magnetic field in MRI-linac systems naturally tends to remove electron contamination from the beam. This has been shown by O'Brien *et al.* (2016), who calculated depth doses by MC simulation of an Elekta Unity™ MRI-linac, including a full head model with electron contamination, and a point source model without electron contamination (photons only), for 0 T and 1.5 T. This study found that the location of  $d_{max}$  and the value of %dd(10) were similar between the two models when the magnetic field was on, confirming that most of the contaminated electrons, in the full model, never reach the surface. However, in the absence of a magnetic field, the  $d_{max}$ , in the model including electron contamination, was closer to the surface by 1.7 mm, compared to the model without electron contamination. A 2% difference in %dd(10) values between the two models (with and without electron contamination) was reported from the authors. This difference is attributed to the contaminated electrons generated while the photon beam interacts with the cryostat of the MRI scanner, suggesting that the use of the %dd(10)<sub>x</sub> and the %dd(10) may not be considered similarly for MRI-linacs. In the case of photon only model and at 1.5 T, the position of  $d_{max}$  is shifted closer to the surface by 5.5 mm and

the  $\%dd(10)_x$  is changed by 2.4%, compared to zero magnetic field. This change must arise from the effects of the Lorentz force on secondary electrons produced in the phantom.

In the same study, however,  $TPR_{20,10}$  was shown to differ by less than 0.3% in the presence of a 1.5 T magnetic field strength compared to zero magnetic field. The authors state that this translates in a change of the beam quality correction factor of 0.03%, which makes the  $TPR_{20,10}$  a good candidate to specify the beam quality for reference dosimetry in magnetic field.

It should also be noted, that one of the technical difficulties in measuring  $\%dd(10)_x$  in an MRI-linac is the restricted range of possible SSD values, which would already make the direct use of AAPM's TG51 protocol for reference dosimetry more awkward. O'Brien *et al.* (2016) propose instead that  $\%dd(10)_x$ , without magnetic field, be obtained from a measurement of  $TPR_{20,10}$  using the conversion factors given by Kalach and Rogers (2003) for use with the AAPM's TG-51 protocol.

## 2.4 Reference conditions in MRIgRT

Reference conditions refer to those conditions (i.e. field size, depth in water, SSD, etc.) that the quantity of the absorbed dose to water is realised. These are also the conditions that dosimeters need to be calibrated to be traceable at a level of a national standard. A review paper by de Pooter *et al.* (2021) presents the reference conditions for the determination of the absorbed dose to water in MRI-linac systems. This study highlights the influence quantities that do not exist in current CoPs, i.e. chamber orientation with respect to the magnetic field and magnetic field strength. Table 2.1 shows the conditions recommended by IAEA's TRS-398 and IAEA's TRS-483 for high energy photon beams and those for MRI-linac systems, based on literature evaluation, as reported by de Pooter *et al.* (2021).

*Table 2.1: Reference conditions for the determination of the absorbed dose to water in the MRI-linac systems beam quality compared with the recommendation from TRS-398 (for MV photon beams) and TRS-483 for high energy photon beams. Influence quantities not used in existing CoPs are printed in bold italics. With permission from de Pooter et al. (2021).*

Influence quantity	Reference value		
	TRS-398	TRS-483	MRI-linac
Phantom material	Water	Water	Water
Chamber type	Cylindrical	Cylindrical	Cylindrical
<b><i>Chamber orientation to magnetic field</i></b>	n/a	n/a	Parallel
Chamber orientation to photon beam	Perpendicular	n/a	Perpendicular
<b><i>Magnetic field strength</i></b>	n/a For $\text{TPR}_{20,10} < 0.7$ , $10 \text{ g/cm}^2$ (or $5 \text{ g/cm}^2$ )	n/a	0.35 T, 1.5 T
Measurement depth ( $z_{\text{ref}}$ )		$10 \text{ g/cm}^2$	$10 \text{ g/cm}^2$
	For $\text{TPR}_{20,10} \geq 0.7$ , $10 \text{ g/cm}^2$		
Reference point of the chamber	On the central axis at the centre of the cavity volume	On the central axis at the centre of the cavity volume	On the central axis at the centre of the cavity volume
Position of the chamber reference point	At $z_{\text{ref}}$	At $z_{\text{ref}}$	At $z_{\text{ref}}$
SDD	100 cm	Isoc	Isoc
Field size at SDD	$10 \times 10 \text{ cm}^2$	$10 \times 10 \text{ cm}^2$ or size of the msr field	<sup>7</sup> $10 \times 10 \text{ cm}^2$
Gantry angle			90°

<sup>7</sup> Field size defined in the absence of magnetic field, i.e. by the photon fluence or kerma distribution.

## Chapter 3 Experimental dosimetry with radiochromic film in magnetic fields

This chapter investigates the effect of magnetic fields on the response of Gafchromic EBT-3 films and assess its suitability for dosimetry in MRI-linac systems. Moreover, results from this work contribute to clarifying the inconsistency of the results of recent published studies, on the effect of magnetic field on the sensitivity of Gafchromic films.

### 3.1 Introduction

Experimental techniques to measure the data required for TPS commissioning and verification need to be adapted for the context of MRIgRT. Indeed, detector specifications are crucial to correctly measure input data for TPS, such as absolute dose, beam profiles and depth doses, since the presence of a magnetic field is known to perturb the detector dose response (Meijsing *et al.*, 2009, Reynolds *et al.*, 2013, Smit *et al.*, 2013, O'Brien *et al.*, 2016). In this context, the performance of suitable detectors under the influence of a magnetic field needs to be characterised. Detector suitability will then be defined by the ability to capture electrons affected by the Lorentz force in a medium. Among available detectors that could fulfil such conditions, radiochromic film is a promising candidate.

Radiochromic film is a useful tool for relative dosimetry (measurements of the radiation field characteristics) and reference dosimetry (Girard *et al.*, 2012, Devic *et al.*, 2016, Billas *et al.*, 2017). It has high spatial resolution and a large measurement area suitable for validation of 2D dose maps. It is known to be almost water equivalent (Niroomand-Rad *et al.*, 1998) and shows small energy dependence (Devic *et al.*, 2004, Arjomandy *et al.*, 2010). Radiochromic film is used in advanced radiotherapy modalities (such as SRS (Palmer *et al.*, 2015b, Dimitriadis *et al.*, 2017), IMRT (Sankar *et al.*, 2006, Low *et al.*, 2011), etc.) that require complex QA and verification methods for radiation dosimetry. It is also used for end-to-end dosimetry audits where the whole treatment chain as experienced by a patient is considered (Clark *et al.*, 2015, Palmer *et al.*, 2015a). Radiochromic film has shown that it is a promising candidate for the detection of the affected lateral profiles and depth dose curves due to the magnetic field in MRIgRT systems (Crijns *et al.*, 2011, Crijns *et al.*, 2012, Smit *et al.*, 2014). It has also been demonstrated that radiochromic film is a good detector for capturing the electron return

effect (Raaijmakers *et al.*, 2005, Raaijmakers *et al.*, 2007a), which increases the dose at tissue-air interfaces.

Recent studies (Reynoso *et al.*, 2016, Roed *et al.*, 2017, Barten *et al.*, 2018, Delfs *et al.*, 2018) have investigated the performance of EBT-2 and EBT-3 films in different magnetic field strengths, at different orientation of the reference film edge with respect to the magnetic field, with and without real-time MR imaging and using different beam energies. Contradicting data were published by various authors and these will be covered in more detail in discussion. Briefly, the peer reviewed work by Reynoso *et al.* (2016) investigated the effect of a 0.35 T magnetic field strength on EBT-2 film, using a  $^{60}\text{Co}$  energy beam, and they found that the dose was changed by up to 15%. A study by Roed *et al.* (2017) examined the effect of a 1.5 T magnetic field strength on EBT-3 film using the same energy beam as Reynoso *et al.* (2016) ( $^{60}\text{Co}$ ) and their results show a change on dose ranging from 1% to 3%. Delfs *et al.* (2018) studied the effect of magnetic field strength (0.35 T and 1.42 T) on EBT-3 film. Although they used a different energy beam (6 MV) from Reynoso *et al.* (2016) and Roed *et al.* (2017), they report a dose change of 2.1%. A recent study by Barten *et al.* (2018) investigated the response of EBT-3 film sheets at different angles to a magnetic field in a  $^{60}\text{Co}$  unit with an integrated 0.35 T MRI system by ViewRay MRIdian<sup>TM</sup>. They compared to equivalent measurements at a 6 MV conventional linac (0 T) and they found a change of 0.9%.

The Gafchromic EBT-2 production has been discontinued and its next generation, EBT-3, differs in its structure (symmetrical polyester layers in order to eliminate errors on the scanning orientation) and the surface (matt surface to prevent Newton rings). However, both EBT-2 and EBT-3 films feature the same composition in the sensitive layer (Reinhardt *et al.*, 2012, Moylan *et al.*, 2013) and any change due to the magnetic field is expected to be similar.

## 3.2 Materials and methods

### 3.2.1 Experimental setup

The experimental setup (Figure 3.1) involved irradiation of Gafchromic EBT-3 film in an electromagnet (GMW type 3474-140) using a  $^{60}\text{Co}$  beam (Theratronics, Theratron 780c). The distance from the  $^{60}\text{Co}$  source to the centre of the magnetic poles (measurement point)

was 162 cm. An in-house polymethyl methacrylate (PMMA) phantom, 5 cm width and 26 cm height, was designed to fit inside the 5 cm gap between the two poles of the magnet (as shown in Figure 3.1), which provide a maximum magnetic field strength of 2 T. The phantom consisted of two symmetrical PMMA plates, each at a water equivalent depth of 1 cm, placed in front of and behind the film, and located so that the central axis of the film is placed in the centre of the two magnetic poles. The edge of the film was orientated parallel to magnetic field, along the x-axis, and perpendicular to radiation beam, in direction of the z-axis (Figure 3.1).

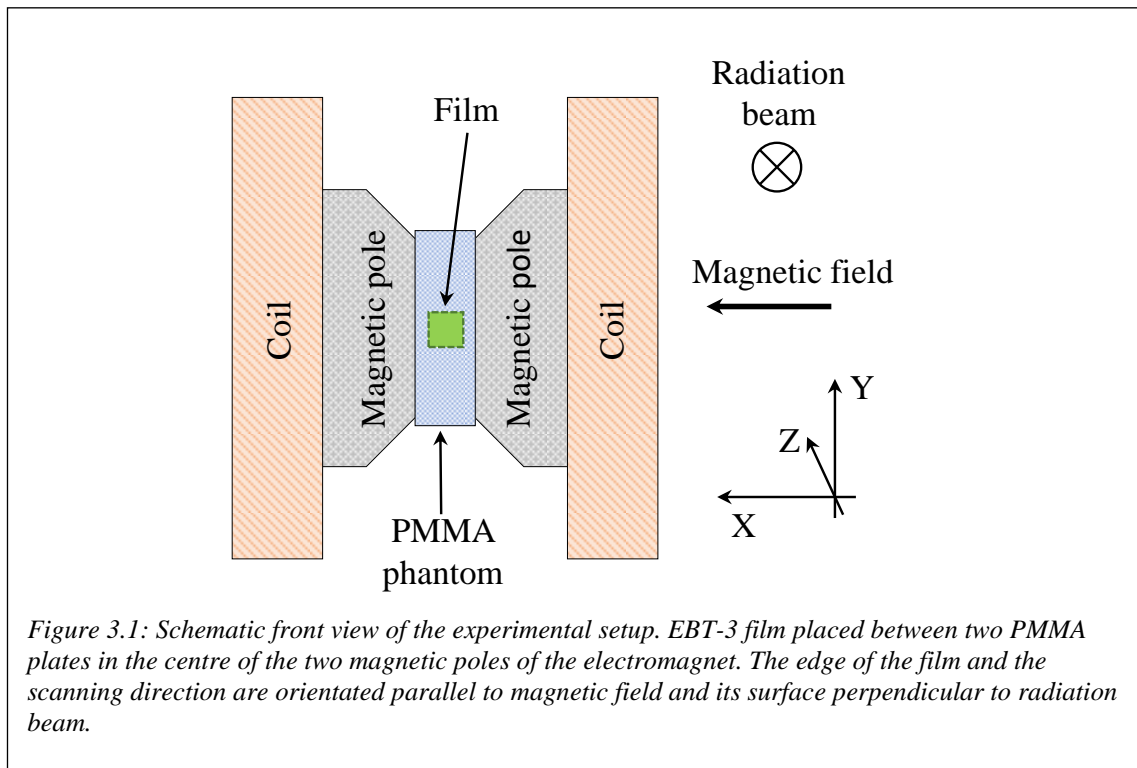


*Figure 3.1: Schematic front view of the experimental setup. EBT-3 film placed between two PMMA plates in the centre of the two magnetic poles of the electromagnet. The edge of the film and the scanning direction are orientated parallel to magnetic field and its surface perpendicular to radiation beam.*

### 3.2.2 Magnetic field uniformity

The magnetic field uniformity, for a pole gap of 5 cm, has been retrieved from the GMW electromagnet user manual (GMW, 2009). A plot of a normalised magnetic field as a function of position, from the front to the rear of the magnet (in z-axis as shown in Figure 3.1), is shown in Figure 3.2. The uniformity within  $\pm 2$  cm, which covers the ROI for film analysis (described in section 3.2.5), was found to be 99.97%.

In-house measurements of the magnetic field uniformity during these experiments were not achievable. However, the uniformity in the experimental setup, related with Chapter 4 and for pole gap of 7 cm, was assessed by measurements of the magnetic field,

at different magnetic field strengths, along the centre of the two magnetic poles (in z- and y-axis as shown in Figure 3.1). Measured data compare well with the one from GMW (2009) user manual, for 7 cm pole gap. Therefore, it is fair to use the GMW (2009) published data to assess the uniformity for a 5 cm pole gap.

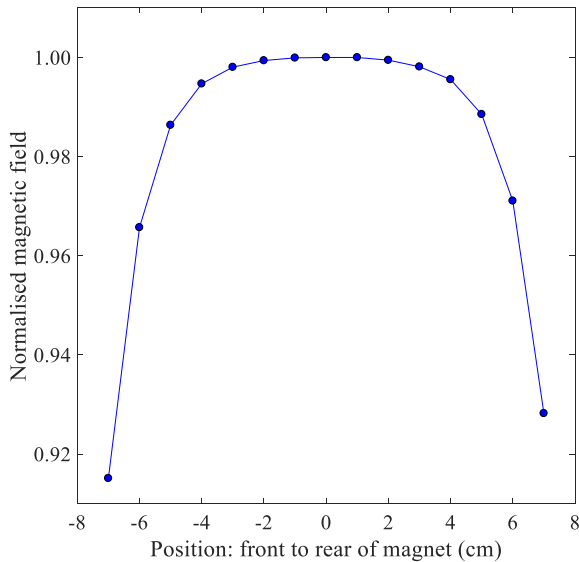


Figure 3.2: Magnetic field uniformity retrieved from the GMW electromagnet user manual (GMW, 2009), Filename: SC7955 Uniformity Plot 4.507. Pole gap: 5 cm. Plot shows normalised magnetic field as a function of position: front to rear of magnet. Note: magnet operated at 140 A and the magnetic field strength at 0 cm is 1.93 T.

### 3.2.3 Dose output measurements

Output measurements were made using alanine/EPR dosimetry, calibrated in terms of absorbed dose to water and traceable to the NPL primary standard, to determine the absorbed dose rate of the  $^{60}\text{Co}$  beam at zero magnetic field. Alanine pellets, approximately 2.3 mm height and 5 mm diameter, placed in a Farmer-type holder were used in a similar phantom to the one adopted for film dosimetry. Alanine was chosen due to non-standard condition of our experimental setup (such as field size and scatter conditions in the restricted space between the poles of the electromagnet). The phantom was built from a PMMA block, 2 cm  $\times$  5 cm  $\times$  26 cm, with a hole drilled into the insert to take an alanine Farmer-type holder which could be fitted perpendicular to the direction of the radiation beam. The film and alanine phantoms were constructed to place the film and alanine reference points at the same measurement point.

### 3.2.4 Effect of magnetic field on absorbed dose to water at $^{60}\text{Co}$ beam quality

The effect of the magnetic field on dose to water at a  $^{60}\text{Co}$  energy beam need to be determined and accounted on the dose values of the EBT-3 calibration curves. Isolating the effect on dose to water, will allow for the investigation of the effect of the magnetic field on the EBT-3 response, only.

MC simulations were performed to calculate  $^{60}\text{Co}$  absorbed dose to water in magnetic field strengths up to 2 T, using the user code *cavity* that forms part of the EGSnrc MC system (Kawrakow I *et al.*, 2011) (development version: GitHub: Aug 2017). The simulation used a water phantom to represent the PMMA phantom, with water equivalence defined by scaling depth inversely with electron density. Dose was scored in slabs of 0.05 cm thick and 1 cm wide up to a depth of 2 cm.

The model of the  $^{60}\text{Co}$  beam was validated by performing air kerma measurements. A Physikalisch-Technische Werkstätten (PTW) Semiflex chamber (type 31010) was used to measure inline and crossline profiles at 128.2 cm from the source with an 8 cm  $\times$  8 cm field size, defined at the machine isocentre (80 cm). The thimble of chamber was positioned parallel to the radiation beam, its effective point of measurement was aligned to the measurement plane and scans were performed in air with the chamber's build-up cap being on.

Phase space files of the  $^{60}\text{Co}$  beam were generated using the BEAMnrc usercode<sup>8</sup>. The model of the experimental setup was constructed, and beam validation was performed at zero magnetic field. The BEAMDP tool, from EGSnrc code, was used to generate a scatter plot of the x-y dose values of particles from a phase space file. This plot was used for comparison with the experimental data.

### 3.2.5 Film response curve

Twelve pieces of EBT-3 films (3.5 cm  $\times$  3.5 cm), cut from one sheet of film, were used to generate a calibration curve. Each piece maintained the same orientation as the original short dimension of the film (landscape orientation) and placed parallel to the magnetic

---

<sup>8</sup> The cut-off energy for electrons (AE and ECUT) was set to 0.521 MeV and for photons (AP and PCUT) to 0.01 MeV.

field during irradiation and parallel to scanning direction during digitisation. The film orientation and alignment were kept consistent throughout the measurements.

The extent of the radiation field was chosen to match the gap between the two magnetic poles and the source-to-surface distance was set at 161 cm. Films were irradiated at a depth of 1 cm (a sufficient amount of PMMA was used to provide charged particle equilibrium) and the maximum dose given at each magnetic field was approximately 825 cGy. A region of interest of  $2.5\text{ cm} \times 2.5\text{ cm}$  was analysed for each film in order to obtain the netOD, where netOD is the difference between the optical density (OD) after and before irradiation. The film response curve is defined as netOD as a function of dose.

### 3.2.6 Film digitisation

Film were digitised following a protocol which is as follows: briefly, an EPSON Expression 10000XL Pro flat-bed colour scanner in transmission mode was used to scan the films. Coloured images were acquired with a spatial resolution of 150 dpi with 48 bit RGB and all scanner colour corrections turned off. A frame was used to position the films at an area of the scanner bed which could correct OD readings for scanner light non-uniformity (Saur and Frengen, 2008). The orientation of all films was kept constant and aligned within  $\pm 5^\circ$  to avoid any effect due to polarised light. A 3.5 mm PMMA sheet was placed on top of the films during digitisation in order to position the films flat on the scanner bed. The scanner warming-up effect was diminished by using ten repeated scans. Films were scanned before, to account for background correction, and 48 hours after irradiation in order to allow the film optical density to stabilise (Cheung *et al.*, 2005). More details of the protocol are described in Bouchard *et al.* (2009).

### 3.2.7 Film uncertainty

In a measurement of absorbed dose, the additional uncertainty<sup>9</sup> introduced by using film arises from two sources: (i) the variations in film response from pixel to pixel within each region of interest (ROI), which was determined using the method of Bouchard *et al.* (2009), and (ii) the variations in response between ROIs on different pieces of film (in particular, the film used for measurement, compared with the films used for calibration),

---

<sup>9</sup> That is, in addition to the uncertainty of the dosimeter against which the film is calibrated.

which was determined from a statistical analysis of repeated film measurements with 40 degrees of freedom.

### 3.3 Results

#### 3.3.1 Validation of the $^{60}\text{Co}$ beam model

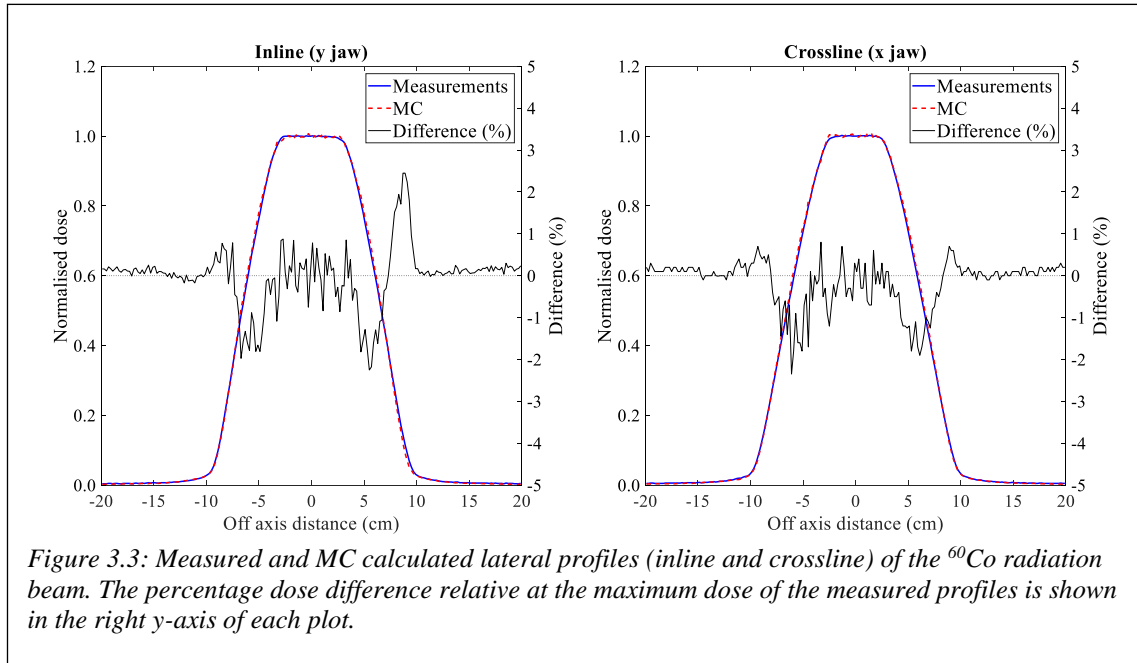


*Figure 3.3: Measured and MC calculated lateral profiles (inline and crossline) of the  $^{60}\text{Co}$  radiation beam. The percentage dose difference relative at the maximum dose of the measured profiles is shown in the right y-axis of each plot.*

The beam model was validated by comparing the MC calculated profiles along the x- and y-directions, provided from BEAMDP, with measured lateral profiles (inline and crossline), as shown in Figure 3.3. All data are normalised at central axis. To allow for this comparison MC data were interpolated to the measured off-axis distance points using a cubic Hermite polynomial function (which preserves the shape of the data). For both inline and crossline profiles, the dose agreement at each point is within  $\pm 1\%$ , except two regions confined to the steepest parts of the penumbra, where the dose difference is within  $\pm 2.5\%$ . It is fair to note that the penumbra on both profiles is greater compared to common  $^{60}\text{Co}$  profiles. This is because the trimmer bars are not installed on the gantry's head (which is not related with the current work, but this is how the machine is operated) and the phase space files were generated at 128.2 cm from the source.

### 3.3.2 Effect of magnetic field on absorbed dose to water at $^{60}\text{Co}$ beam quality

Figure 3.4 (a), left y-axis, shows the MC calculated  $^{60}\text{Co}$  depth-doses for 0 T and 1.5 T magnetic field strengths and the ratio, dose water of 1.5 T magnetic field ( $D_{w,Q_B}$ ) divided by the dose to water in zero magnetic field ( $D_{w,Q}$ ), on the right y-axis. It can be observed that for a magnetic field of 1.5 T the surface dose is enhanced by 13% and the depth of maximum dose ( $d_{max}$ ) is shifted closer to the surface by 0.05 cm. No effect was observed on the value of the dose at  $d_{max}$  between the two magnetic field strengths. Figure 3.4 (b) shows the ratios of calculated dose in water with and without magnetic field as a function of a magnetic field strength. The ratios were determined from the average ratios between the depths of 0.5 cm and 1.7 cm and it was found to change by  $-0.08\%$  per Tesla when a linear model is fitted. Based on this change, the dose values of the EBT-3 calibration curve at each magnetic field strength were adjusted to account for the effect of the magnetic field on dose to water. The electron return effect is visible after a depth of approximately 1.7 cm. It turns out that the dependence of this quantity, dose ratio with and without magnetic field, on magnetic field changes with energy and a more complicated model would be required at higher energies, see Figure 4.18 (b).

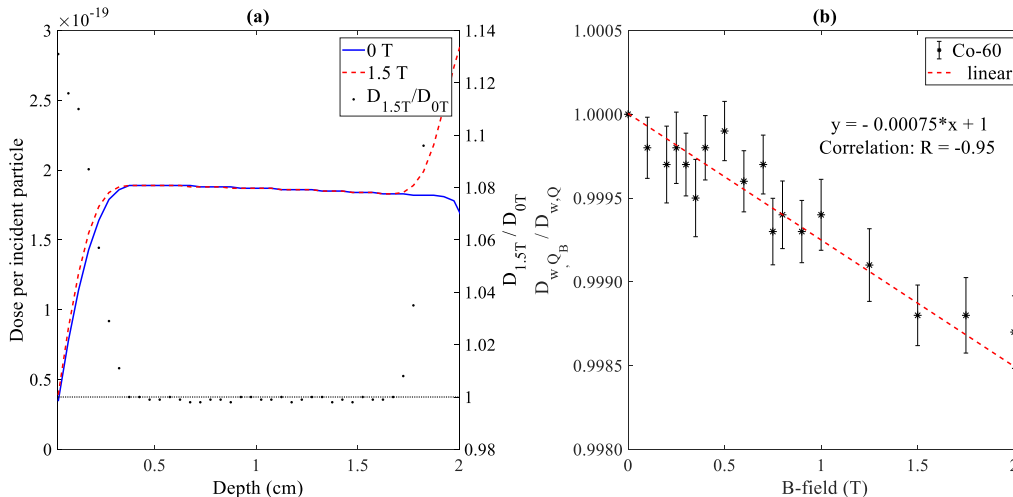


Figure 3.4: MC calculated  $^{60}\text{Co}$  depth doses for 0 T and 1.5 T and their dose ratio (shown on the right y-axis) (a). Ratios of dose with and without magnetic field at different strengths (b).

### 3.3.3 Beam uniformity at measurement plane

MC simulations were performed to calculate beam profiles, with zero magnetic field, in the measurement plane of the experimental setup: that is, between the magnetic poles. Figure 3.5 shows lateral profiles from left to right and from top to bottom of the magnet, in x- and y-axis, respectively, as shown in Figure 3.1. All data are normalised to the central axis. In the x-axis profile, the enhanced dose of the points at the edges is due to the contribution of the scattered electrons from the poles. Nevertheless, just after these two points, the profile takes the shape of the  $^{60}\text{Co}$  beam. Focusing in the distance of  $\pm 1.25$  cm, the ROI where film is analysed, radiation beam remains uniform within 99.85% and 99.88% for the x- and y-axis profiles, respectively.

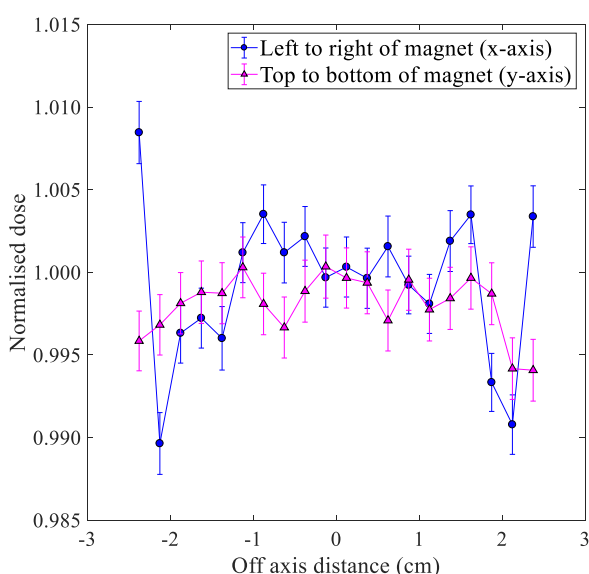


Figure 3.5: MC calculated beam profiles, for 0 T and 1.5 T, in the measurement plane of the experimental setup: that is, between the magnetic poles. Note that, because the data are ratios, there is a correlation between the data points, as the denominator is the same for all. Thus, uncertainties are partially correlated.

### 3.3.4 Effect of magnetic field on EBT-3 signal

In this work the red, green and blue channels are analysed. However, selected results in graphical form are presented, but mostly for the red channel only, as this is the channel which is usually used for single channel film dosimetry.

The EBT-3 film response curves (expressed in terms of netOD as a function of dose) for the red channel for all magnetic field strengths considered in this study is shown in Figure

3.6. The maximum spread between all the magnetic field strengths for the red channel is also presented on the right y-axis of the same figure. For dose values greater than 75 cGy the maximum spread is 2.6% for the red channel, 3.5% for the green channel and 4.2% for the blue channel.

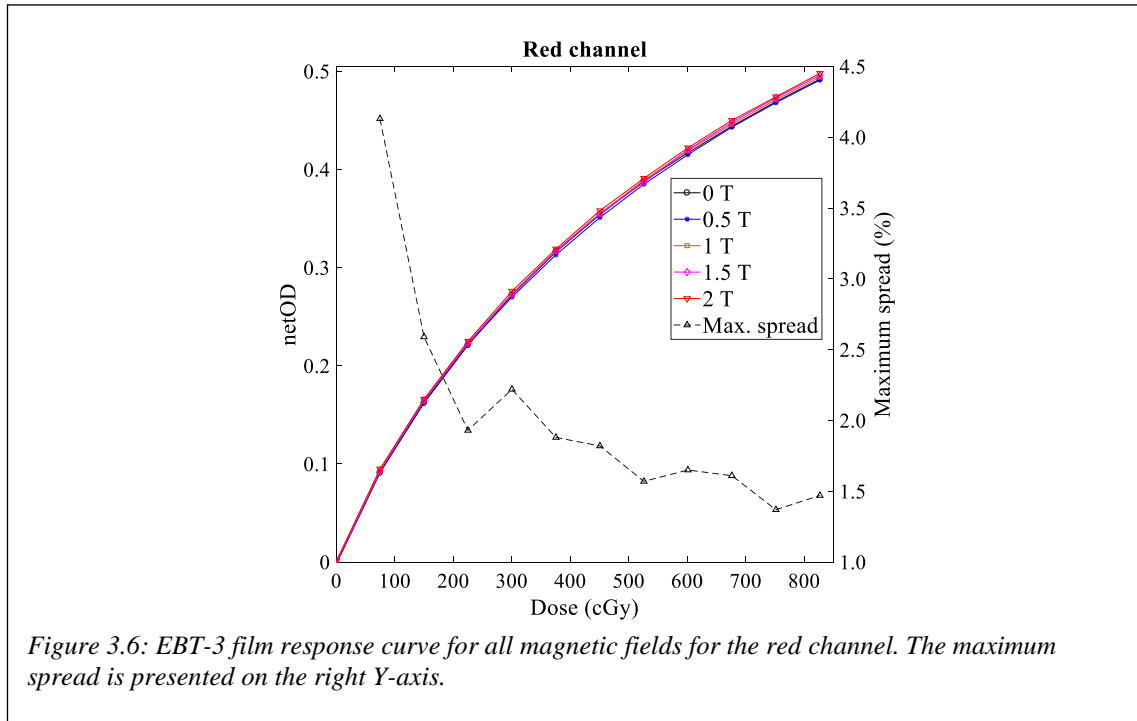


Table 3.1 shows the average absolute difference (in percent) of all dose levels between the response curves irradiated with and without a magnetic field. The difference is presented for each magnetic field strength and each colour channel.

Table 3.1. Average absolute difference for red, green and blue channel.

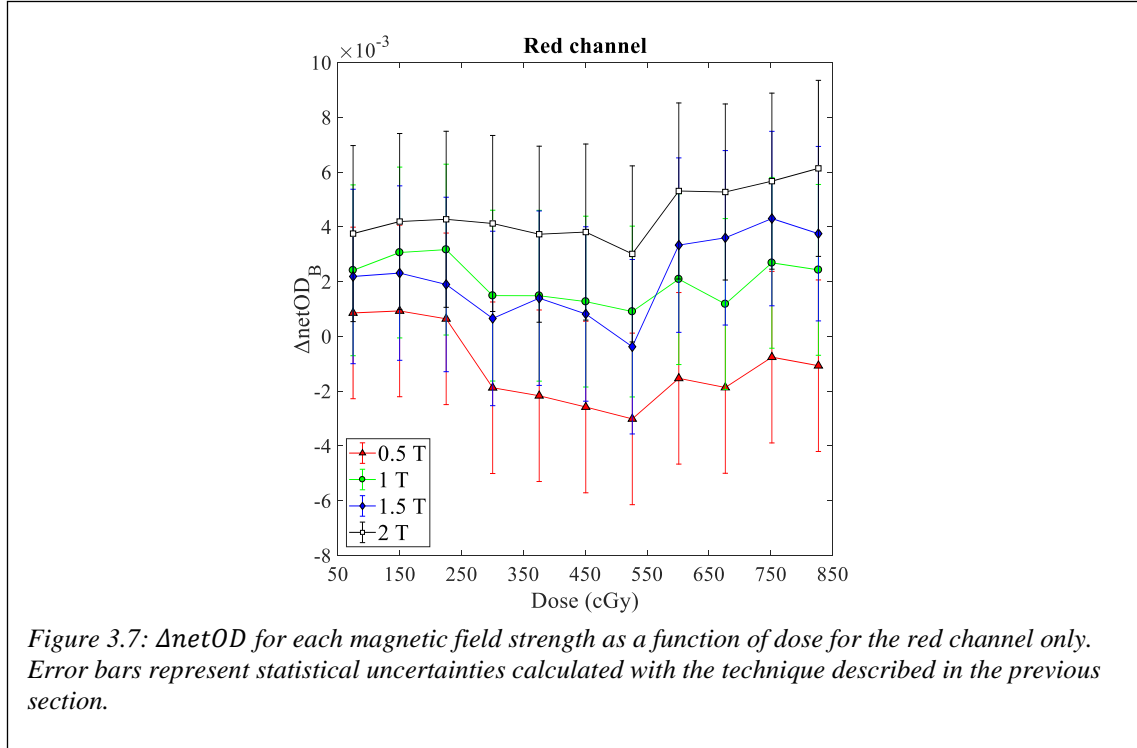
$$\left( \frac{|netOD_{B \neq 0}|}{|netOD_{B=0}|} - 1 \right) \cdot 100$$

Channel	0.5 T (%)	1.0 T (%)	1.5 T (%)	2.0 T (%)
Red	0.5	0.9	0.8	1.6
Green	0.8	1.2	1.2	2.1
Blue	1.2	1.6	0.8	0.7

$\Delta netOD_B$  is defined to be the difference between the netOD with and without a magnetic field:

$$\Delta netOD_B = netOD_{B \neq 0} - netOD_{B=0} \quad (3.1)$$

Figure 3.7 shows  $\Delta_{\text{netOD}} B$  as a function of dose, for each magnetic field and for the red channel only. The error bars denote the standard uncertainty in netOD. The maximum  $\Delta_{\text{netOD}} B$  was found to be 0.006 for the red and green channels and -0.003 for the blue channel. Figure 3.7 shows that  $\Delta_{\text{netOD}} B$  does not have a strong dependence on dose. Similar results were observed for the green and blue channels.



It appears that  $\Delta_{\text{netOD}} B$  does depend on the magnetic field strength, being typically negative at 0.5 T and positive at 1 T and above. This effect is shown more clearly in Figure 3.8, which depicts the average  $\Delta_{\text{netOD}} B$  over all dose levels,  $\langle \Delta_{\text{netOD}} B \rangle_{D_{\text{all}}}$ , as a function of magnetic field strength, for each channel.

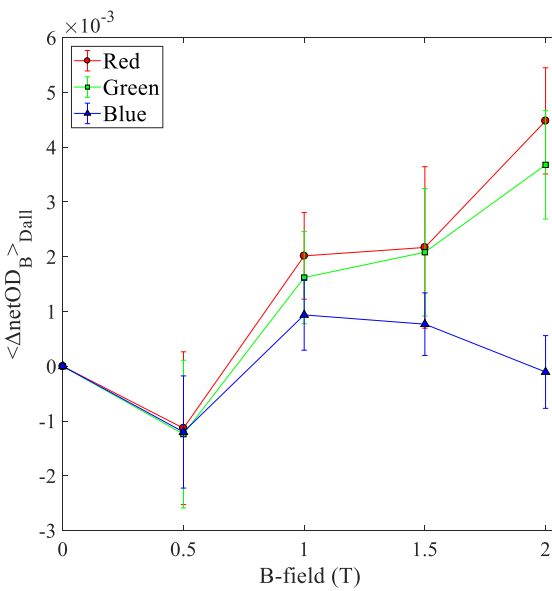
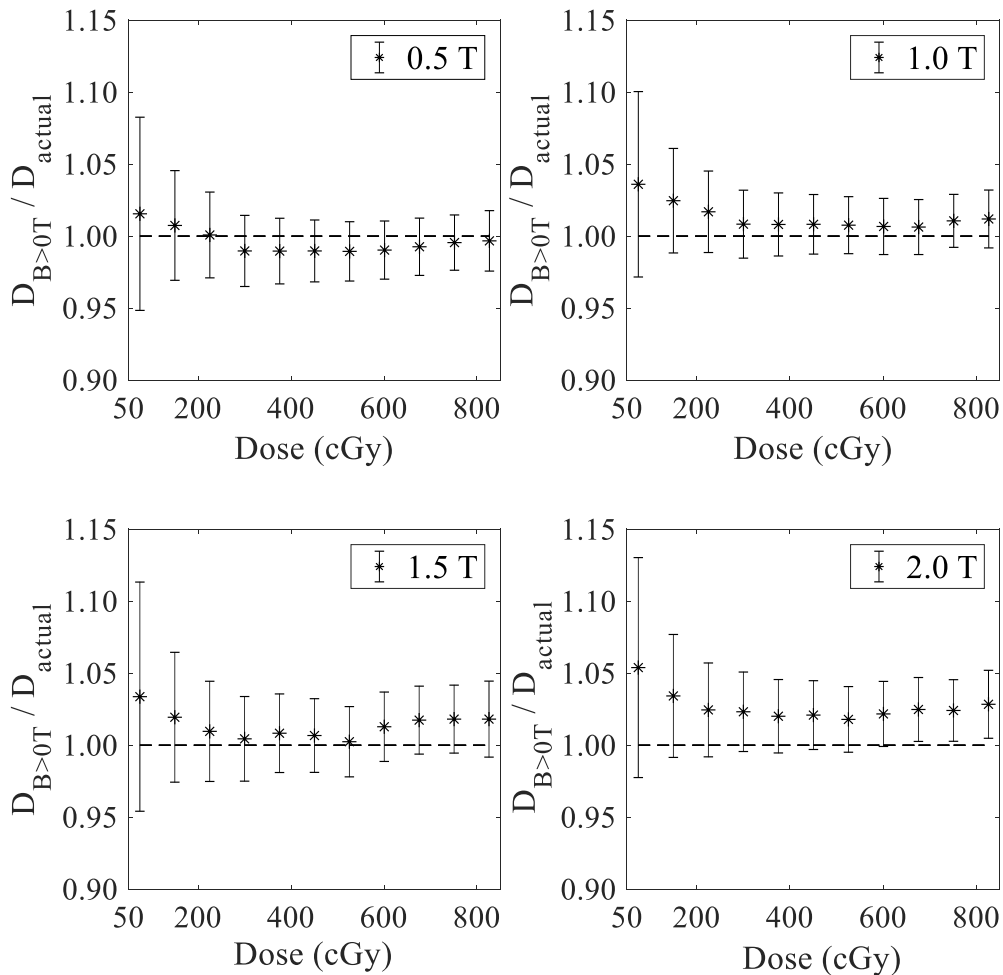


Figure 3.8.  $\langle \Delta_{\text{netOD}} \rangle_{\text{Dall}}$  as a function of magnetic field strength. Error bars represent the standard deviation of the distribution of the averaged  $\Delta_{\text{netOD}}$  values.

### 3.3.5 Effect of magnetic fields on dose determined with EBT-3 film

The effect of magnetic fields on dose measured using EBT-3 films is shown in Figure 3.9. The calibration curve, based on films irradiated at zero magnetic field, was used to obtain absorbed dose from films irradiated at non-zero magnetic field, which would be valid if the magnetic field has no effect on film response. Figure 3.9 shows the ratios, dose obtained from non-zero magnetic field films (using red channel) divided by the dose actually delivered. The delivered dose value takes account of the small effect of the magnetic field on dose to water, which was calculated by MC. The extent to which these ratios are significantly different from unity indicates the effect of the magnetic field on the film response. The apparent systematic behaviour of data points with increasing dose, across different field strengths, is also probably due (in part) to the use of the fourth order polynomial fit to the raw film dose response data. For values above 225 cGy, the ratios as a function of dose do not follow a simple trend and are somewhat scattered. Indeed, all ratios below 2 T are unity within the uncertainties.



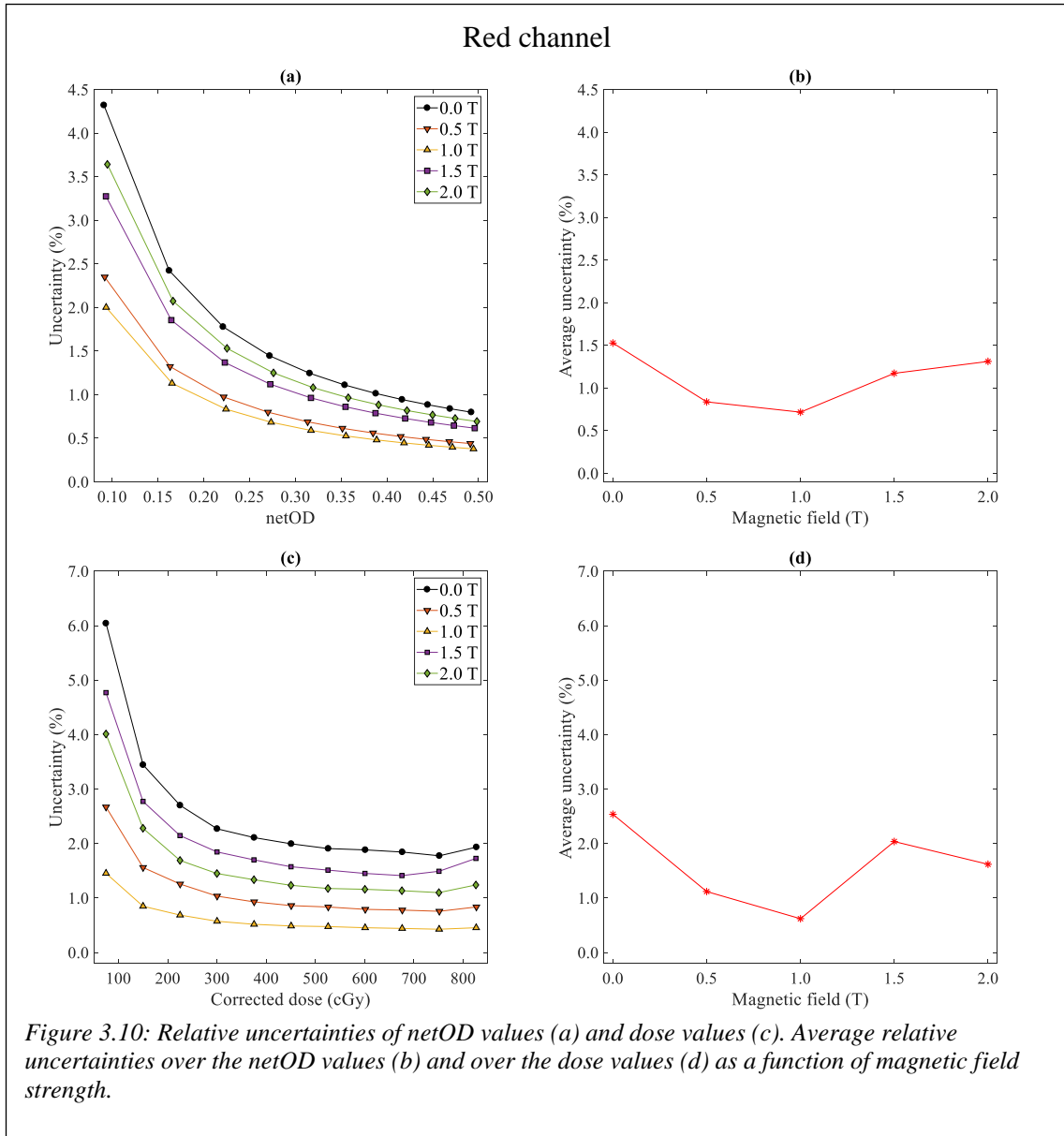
*Figure 3.9: Ratios of dose, with combined standard uncertainties, obtained (using the red channel) from films irradiated in non-zero magnetic field divided by the actual delivered dose.*

Taking averages over all dose values above 75 cGy, the mean ratios are  $0.994 \pm 0.024$  (0.5 T),  $1.011 \pm 0.023$  (1 T),  $1.012 \pm 0.028$  (1.5 T) and  $1.024 \pm 0.026$  (2 T).

### 3.3.6 Film uncertainty

The relative uncertainties of netOD and dose values, for the red channel, are shown on Figure 3.10 (a) and Figure 3.10 (c), respectively, for the five different magnetic field strengths. The average relative uncertainties over the netOD values, Figure 3.10 (b), and over the dose values, Figure 3.10 (d), as a function of magnetic field strength, do not follow a specific trend. This is an indication that film uncertainty is independent of the

magnetic field. The scatter distribution depicted on these figures, reflects the film variation between and within EBT-3 film sheets.



### 3.4 Discussion

The performance of the EBT-3 film in the presence of a magnetic field, has been investigated at different dose levels and over a range of magnetic field strengths. A  $^{60}\text{Co}$  unit was used to irradiate film pieces placed between the poles of an electromagnet and the film response as a function of dose was obtained at five different field strengths. MC simulations were performed to determine the effect of a magnetic field on dose to water at the position of the film, and this effect was included in the analysis. The uniformity of

the beam was evaluated by calculating a profile in x- and y-direction (as indicated in Figure 3.1) by means of MC simulation. The beam, within the ROI used for film analysis, was found to be 99.86% uniform, on average. The results show that there is at most a weak dependence of film sensitivity on magnetic field strength. At the smallest field strength (0.5 T), the film was found to under respond, while for field strengths of 1 T and above there was an over response. In terms of netOD (red channel) the under response was  $-0.0011$  and the over response was up to  $0.0045$  at 2.0 T, with a standard uncertainty of  $\pm 0.0030$ . Similar results were observed for the green and blue channels. If this effect remains uncorrected, the error in a film measurement of absorbed dose (using the red channel) would vary from  $-0.6\%$  at 0.5 T up to  $2.4\%$  at 2 T. The error at 1.5 T would be  $1.2\%$ . The standard uncertainty on this dose error is  $\pm 1.4\%$ , which is the contribution to a measurement of absorbed dose to water which arises from the use of film.

For the dose levels typically measured with EBT-3 film, and for the magnetic field strengths considered here, the actual values measured at different dose levels do not differ significantly from a magnetic field-dependent (but dose-independent) constant value.

Several studies have investigated the various sources of uncertainties on film dosimetry (Martisikova *et al.*, 2008, Saur and Frengen, 2008, Bouchard *et al.*, 2009, Garcia and Azorin, 2013), including film manufacturing, film manipulation, the irradiation and digitisation processes and film characterisation, leading to estimates of best uncertainty that range from 1% to 2%. The measurement uncertainties in the present work with EBT-3 (as explained in section 3.2.7) are consistent with this, ranging from 1.1% to 2.2% for dose levels above 75 cGy. This includes the small uncertainty related to the effect of the magnetic field on dose to water (0.05%). The magnitude of the effect of magnetic fields on EBT-3 film dosimetry observed in this study is comparable to the best achievable measurement uncertainty.

### 3.4.1 Comparison with different studies

The development of dosimetry in MRIgRT is still at a fairly early stage and it is essential that the performance of detectors used is well characterised. In the current literature on film dosimetry in magnetic fields, there remains some apparent inconsistency in the results reported from different studies. With the aim of resolving any consequent

confusion the results reported here, where possible, are compared with those already published.

Roed *et al.* (2017) examined the effect of a magnetic field (0 T and 1.5 T) on the response of EBT-3 film signal exposed in a  $^{60}\text{Co}$  radiation beam. Their experiment involved two different orientations of the reference film edge with respect to a) the magnetic field and b) to scanning direction: either parallel or perpendicular in both cases. In all possible combinations, when film analysed using red channel, they found an under-response (ranging from approximately 1% to 3%) on all examined dose levels with magnetic field strength of 1.5 T compared to zero magnetic field dose. However, they also state that when the film is left in the magnetic field for a duration of a) 6 min and 30 min the dose is over responding by less than 1% and b) 7 min and 10 min the dose is under responding by less than 1%. The relationship between the dose change and the time of the film left in magnetic field they do not follow a simple pattern. In the current study, the irradiation time of the films was ranging between 4 min to 15 min and the dose was found to over respond by an average of 1.2% at 1.5 T.

Reynoso *et al.* (2016) used a  $^{60}\text{Co}$  0.35 T MRIdian system to irradiate EBT-2 films. Their results indicate that the netOD of the red, green and blue channel is decreased by an average of 8.7%, 8% and 4.3%, respectively. This study concludes that magnetic fields affect crystal orientation and polymerization during irradiation, judging from films scanned with an electron microscope. Although that study evaluated a different type of film, they specifically state that similar behaviour can be expected for EBT-3 because of the identical composition of the active layer (see section 3.1). In the present work, the effect of a magnetic field on the netOD response of EBT-3 was found to be small. In the Reynoso *et al.* (2016) study they show an average under response of netOD of approximately 7% for data up to 8 Gy figure 2(b) in (Reynoso *et al.*, 2016). The reason for the difference between the results of these two studies is unclear.

A publication by Delfs *et al.* (2018) assessed the effect of the magnetic field on EBT-3 using a 6 MV conventional linac and irradiating films in an electromagnet at two different magnetic field strengths (0.35 T and 1.42 T). They report a decrease in the OD of up to 2.5% with an average, over all channels and over a range of dose values, of -0.8%. This effect was described by the authors as 2.1% increase in the dose values needed to produce

a given OD at a magnetic field of 1.42 T. The present study found that there is indeed a change on film sensitivity however in the opposite direction of Delfs findings: the net OD is increased by +0.8% (red channel, 1.5 T). The dose required to produce a given optical density is smaller by 1.2%. Part of this difference might be explained due to energy dependence of EBT-3 film.

A recent study by Barten *et al.* (2018) investigated the suitability of EBT-3 film for QA use in a 0.35 T  $^{60}\text{Co}$  MRIdian system. Their measurements involved irradiation of EBT-3 film with and without MR imaging and at different angles with respect to magnetic field. They also performed equivalent measurements at 0 T, but this time using a 6 MV conventional linac. Comparing calibration curves generated in  $^{60}\text{Co}$ , with magnetic field, and in 6 MV, without magnetic field, they found a maximum difference of 0.9%. In the present study the difference on dose measured using EBT-3 film with and without magnetic field in a  $^{60}\text{Co}$  beam and at 0.5 T (the closest strength to 0.35 T) was found to be 0.7%, which agrees with the findings from Barten *et al.* (2018).

The observed differences between the current study and the study by Roed *et al.* (2017) shown to be consistent within film uncertainties. Due to the nature of the film technique, any deviation can be explained because of the film perturbations influencing measurements uncertainties. However, this cannot explain the difference with the findings from Reynoso *et al.* (2016) as it exceeds uncertainty margins. Although different type of EBT film generations were used, consistency of published data is anticipated and that EBT-2 to have a similar behaviour to EBT-3 under the strength of magnetic field.

It is essential to take measurement uncertainty into account when assessing the degree of agreement between two investigations. The field strength used by Delfs *et al.* (2018) was 1.42 T. Assuming that it is fair to compare their result with our result for 1.5 T, and assuming that no correction is made for the possible effect of magnetic field on a film measurement of absorbed dose, then Delfs *et al.* (2018) would estimate the uncorrected error as +2.1%, and the present work would estimate the uncorrected error as -1.2%. The standard uncertainty on this error is quantified as 1.4%, while Delfs *et al.* (2018) merely assert that their 2.1% value “exceeds the uncertainty margin of the experiment” but without quantifying the uncertainty on dose measured by film in their paper. We would note, however, that the difference between our results could only be significant at the

level of two sigma if their standard uncertainty on dose is smaller than 0.8%, which is not plausible.

A good agreement was found between the current study and the study of Barten *et al.* (2018). Each of these studies (Barten *et al.*, 2018, Delfs *et al.*, 2018), however, used different beam quality, or a combination of beam qualities, to examine the effect of magnetic field on EBT-3 film response, compared to the present work.

### 3.5 Summary

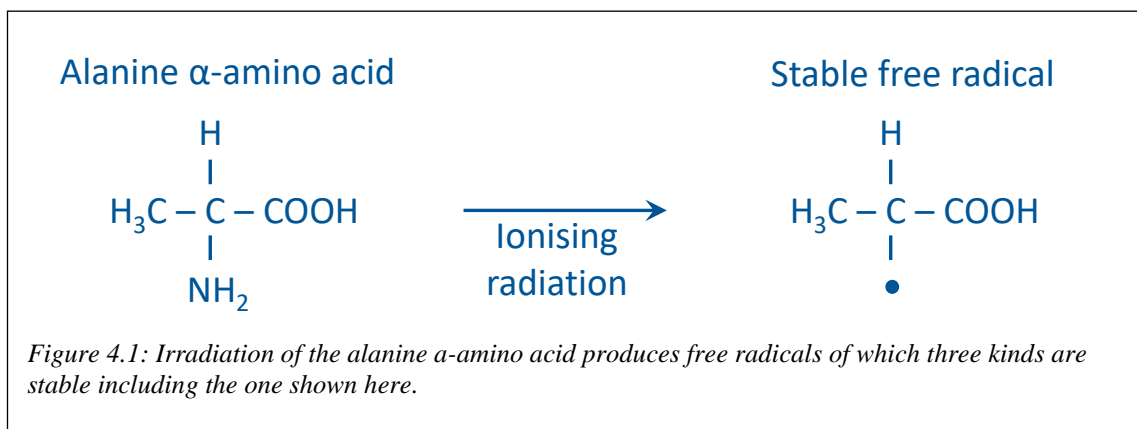
For the strongest magnetic field considered here (2 T), the sensitivity of Gafchromic EBT-3 film may be affected by the presence of a magnetic field at the time of irradiation. However, for MRI-linacs currently in use or under development, for which the field strength is at most 1.5 T, the effect of the magnetic field on EBT-3 film response was found to be zero within the best achievable measurement uncertainty. Results from this work agrees well with results presented by Roed *et al.* (2017), but significantly deviates from the results shown by Reynoso *et al.* (2016). A 3.3% different was found from Delfs *et al.* (2018) and a good agreement was observed with the findings by Barten *et al.* (2018). The outcome of the current work contributes on settling the contradiction of these studies and conclude that EBT-3 film is a suitable dosimeter for dosimetry in MRIgRT.

## Chapter 4 Alanine dosimetry in strong magnetic fields

Reference dosimetry in the presence of a strong magnetic field is challenging. Ionisation chambers, as it was shown on Chapter 2, are strongly affected by magnetic fields. There is a need for robust and stable detectors in MRIgRT. This chapter investigates the behaviour of the alanine dosimeter in magnetic fields and assess its suitability to act as a reference detector in MRIgRT.

### 4.1 Introduction

Alanine is an  $\alpha$ -amino acid with the chemical formula:  $\text{CH}_3\text{-CH}(\text{NH}_2)\text{-COOH}$ . When an alanine molecule is irradiated, undergoes radiolysis with the weakest chemical bond, C-N, being broken<sup>10</sup> (Stuglik, 2007). This process produces a stable free radical,  $\text{CH}_3\text{-C}\cdot\text{H-COOH}$ , as shown in Figure 4.1. Free radicals are known as paramagnetic substances, which consists of atoms that have unpaired electrons. These substances are expected to show electron spin resonance spectra, when analysed in a magnetic resonance spectroscopy, such as electron paramagnetic resonance (EPR), also known as electron spin resonance (ESR). The concentration of the radiation-induced stable free radicals can be measured as a signal using EPR spectroscopy and is proportional to the absorbed dose.



#### 4.1.1 Electron paramagnetic resonance spectroscopy

The basic principles of EPR spectroscopy focus on the interaction of a magnetic field with unpaired electrons and the induction of electromagnetic radiation. This method

<sup>10</sup> Note that the other chemical bonds may potentially break during irradiation. However, their initial configuration is restored, i.e. they do not form stable free radicals.

utilises electromagnetic radiation to a cavity with species of free radicals (unpaired electrons) in the presence of an external magnetic field to measure an EPR signal.

In quantum mechanics an electron has a magnetic moment and spin quantum number  $S = 1/2$ , with magnetic components  $m_S$ , which defines the spin of an electron,  $m_S = +1/2$  or  $m_S = -1/2$ . In the presence of a magnetic field  $B_0$  an electron exists in one of two discrete energy levels, i.e. its magnetic moment aligns either parallel ( $m_S = +1/2$ ) or antiparallel ( $m_S = -1/2$ ) to the field, with each alignment having a specific energy  $E$  due to *Zeeman effect*:

$$E = m_S \cdot g \cdot \mu_b \cdot B_0 \quad (4.1)$$

where,  $g$  is the electrons  $g$ -factor (*Lande* factor) and is a unitless measurement of the intrinsic magnetic moment of the electron, and its value for a free electron is 2.0023.  $\mu_b$  is the *Bohr magneton* ( $9.274 \cdot 10^{-24} J T^{-1}$ ).

In a diamagnetic substance, which consists of stable molecules held together by bonds, electrons are in pairs and their spins are orientated in opposite directions. Therefore, the electronic magnetic moment is cancelled and there is no interaction with an applied magnetic field. In contrast, in a paramagnetic substance, such as free radicals, the atoms consist of unpaired electrons. In such conditions the electron magnetic moment may interact with an external magnetic field, where its spin aligns either parallel or antiparallel to the field. The energy  $E$  of spin states as a function of magnetic field  $B_0$  is shown in Figure 4.2. As the magnetic field increases, the separation between the energy levels  $\Delta E$  increases too, and is given by:

$$\Delta E = g \cdot \mu_b \cdot B_0 \quad (4.2)$$

An incident electromagnetic radiation,  $h\nu$ , of an appropriate frequency can cause a transition from one spin state to the other. When the energy difference between the two electron spin states,  $\Delta E$ , equals the energy of the electromagnetic radiation, there is absorption of energy by the spins, which is known as resonance.

$$\Delta E = h\nu = g \cdot \mu_b \cdot B_0 \quad (4.3)$$

where  $h$  is Planck's constant ( $6.626 \cdot 10^{-34} \text{ J s}^{-1}$ ) and  $\nu$  is the frequency of radiation.

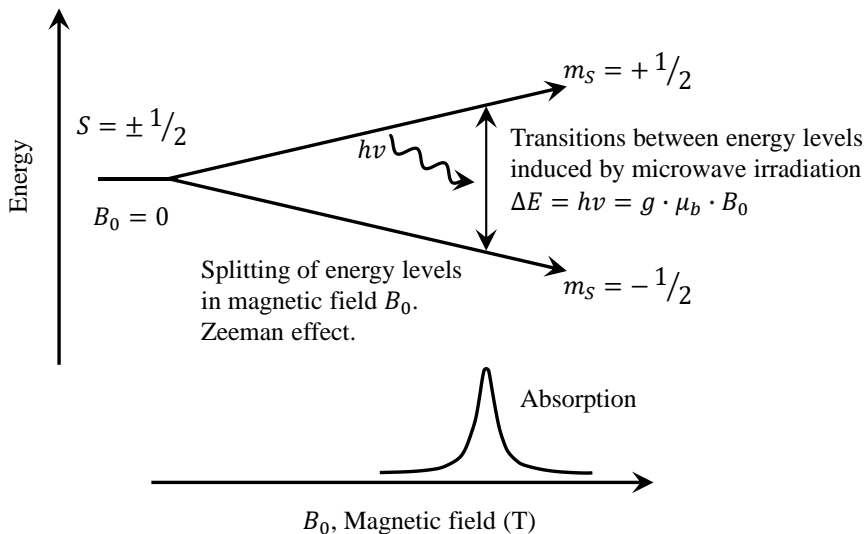


Figure 4.2: Energy levels of an electron spin ( $m_s = \pm 1/2$ ) in a magnetic field and absorption of photons.

Since both  $g$  and  $\mu_b$  are constants, the energy difference between the two spin states is directly proportional to the magnetic field strength and, therefore, there are two possible methods to determine the electron spin resonance spectra (Eaton *et al.*, 2010): 1) vary the electromagnetic radiation frequency (in forms of microwaves) and maintain the magnetic field constant or 2) maintain the electromagnetic radiation frequency constant and vary the magnetic field. Most EPR spectrometers are operated based on the latter approach with a frequency region between 9 to 10 GHz (X microwave band). In such frequency, to achieve a resonance condition for a  $g$  value of approximately 2.00, the magnetic field should be tuned to a strength of about 0.35 T. Note that  $g$ -factor is independent of the microwave frequency and is used to characterise signals and identify different compounds (Eaton *et al.*, 2010).

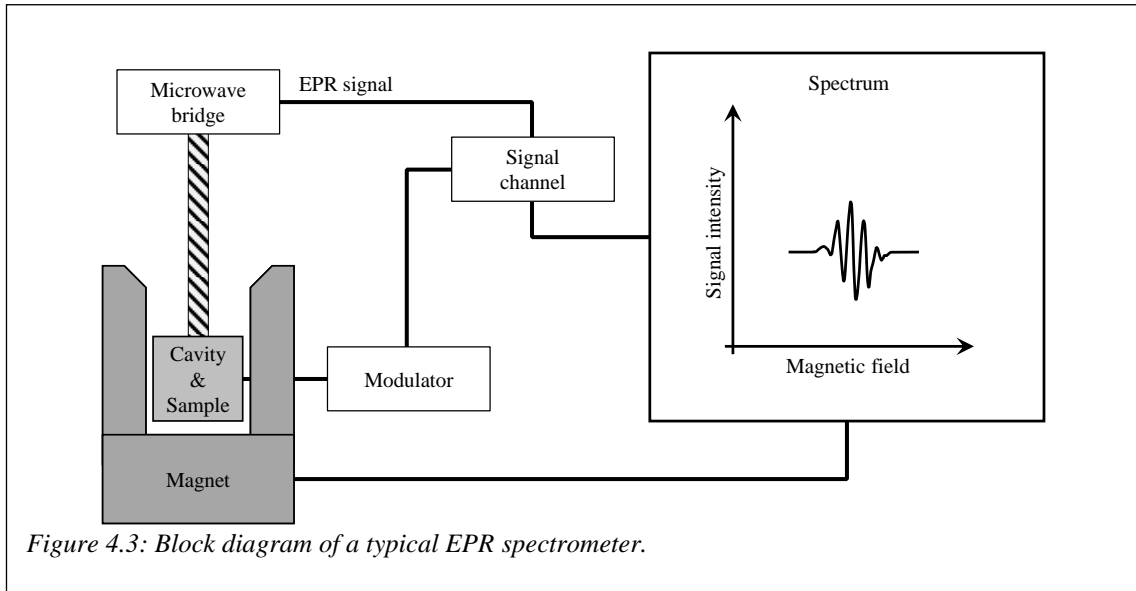
#### 4.1.2 EPR spectrometry system

A block diagram of a typical EPR spectrometer is shown on Figure 4.3 and the main components are:

- i. The microwave bridge: contains both the microwave source and the detector.
- ii. The microwave cavity: acts as a resonator for microwaves and holds the sample.

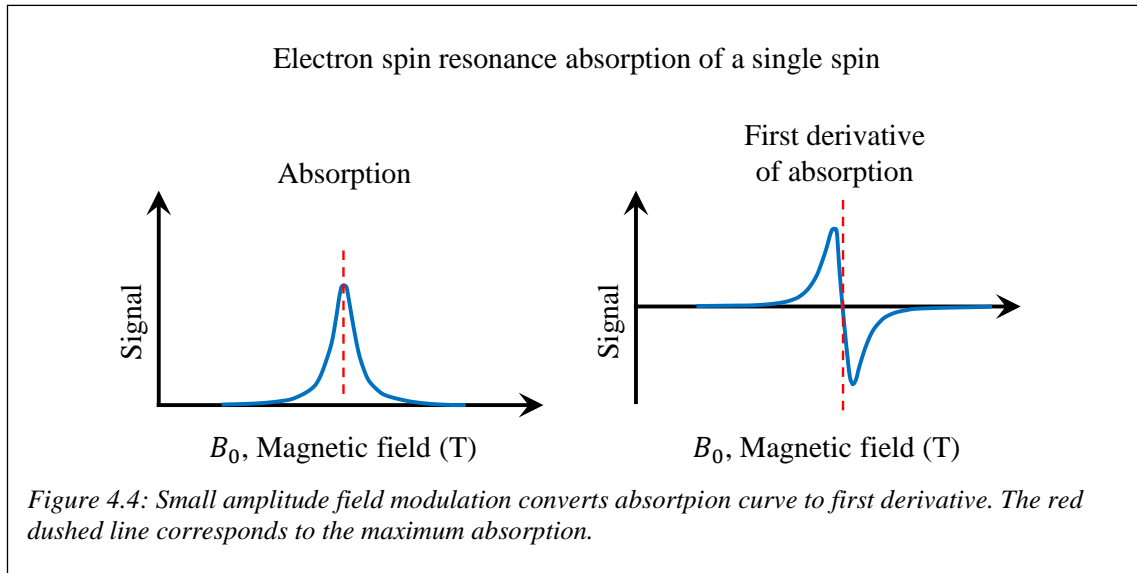
### iii. The magnet: application of a magnetic field.

The principles of EPR spectroscopy are well described in the literature (Schosseler, 1998, Jeschke, 2008, Eaton *et al.*, 2010). Here, its operation is briefly described.



In the microwave bridge, a source (klystron or Gunn diode) is used to generate a microwave irradiation, where their power level is adjusted and controlled with an attenuator. A circulator, which behaves like a traffic circle, routes the microwave irradiation into the cavity, via waveguides, where the sample is located. The cavity is a rectangular metal box which is designed to be exactly one wavelength in length (for X-band cavity the length is about 3 cm). Therefore, the microwave frequency from the source must be tuned to equal the resonance frequency of the cavity. In other words, the impedances of the cavity and the waveguides must be matched, such that the microwave power remains inside the cavity, i.e. the resonator is '*critically coupled*'. This is achieved via a hole called iris, which controls the amount of microwave power that enters to and reflected from the cavity. Once this is completed, the magnetic field, generated from the magnet, is swept to induce a spin transition in the sample, which absorbs microwave energy. This results in a change of impedance and the cavity being no longer critically coupled (the resonator is *detuned*), which means that microwave power is reflected to the bridge and directed through the circulator towards the detector (a diode). The detector produces a current which is proportional to the microwave power, reflected from the cavity. A technique known as phase sensitive detection is used to increase the signal-to-

noise ratio. This is achieved by introducing a small amplitude field modulation with a typical frequency of 100 kHz, which is applied in the same direction as the main magnetic field. When a resonance condition is fulfilled, the reflected from the cavity microwave is modulated at the same frequency. Therefore, the generated EPR signal (absorption curve) is transformed into a sine wave, where the amplitude is proportional to the slope of the signal. This is also responsible for the first derivative shape of the spectrum (Figure 4.4).



It must be noted that the shape of an EPR spectrum is more complex. What is presented on Figure 4.4, is the spectrum of a simple free particle. An unpaired electron, in addition to its interaction with the external magnetic field, will also interact with the magnetic moment of the nuclei found in the environment of the electron spin; this process is known as hyperfine interaction and leads to the splitting of the resonance peak in the EPR spectrum and provides additional information about the species of free radicals (such as identity and number of nuclei in a molecule). A typical alanine EPR spectrum is shown on Figure 4.5.

### 4.1.3 Alanine/EPR dosimetry

EPR spectroscopy of the *a*-alanine amino acid is used for absorbed dose measurements of ionising radiation. The methodology explained in the previous section, is used to determine the alanine/EPR signal. The intensity of the alanine/EPR signal, defined as the peak-to-peak (p-p) height of the central peak, as shown in Figure 4.5, is relative to the concentration of the free radicals, which is proportional to the absorbed dose. The

advantage of the free radicals generated in alanine after irradiation, is that they are stable for years. Based on that, an alanine/EPR dosimetry system can be established and used as reference and transfer standard in radiotherapy, but also in industrial dosimetry.

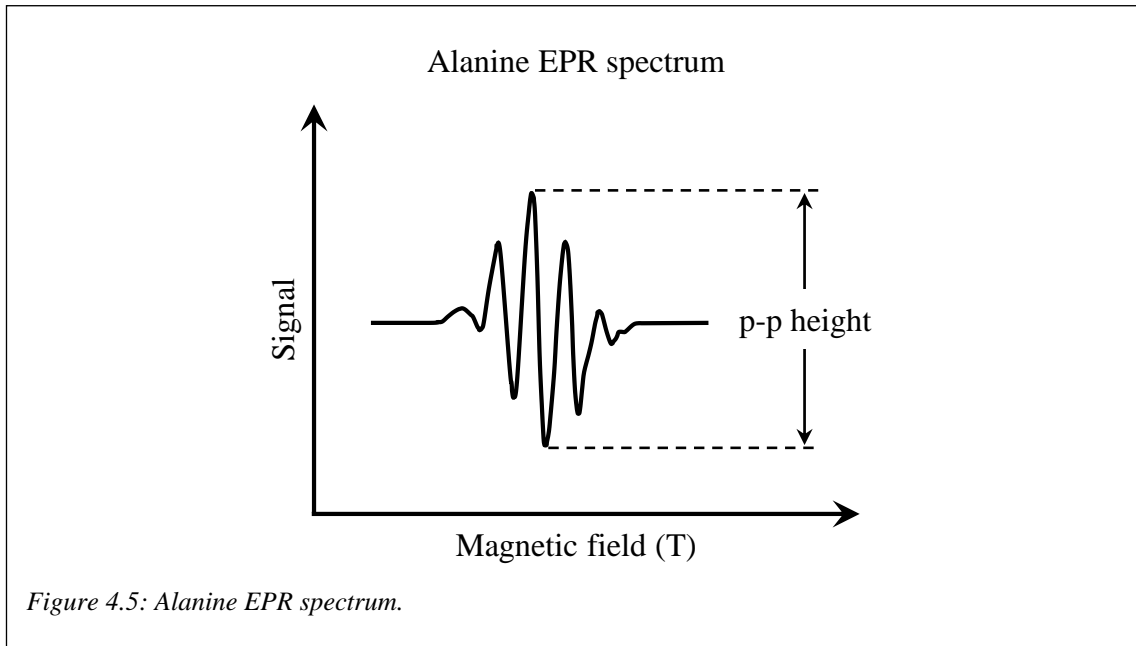


*Figure 4.5: Alanine EPR spectrum.*

In radiotherapy, alanine dosimeters provide an alternative to standard dosimetry systems, such as ionisation chambers. McEwen *et al.* (2015) has pinpointed the advantages of alanine dosimetry as a reference detector against an ionisation chamber in conventional radiotherapy. NPL provides an alanine reference dosimetry service (Sharpe *et al.*, 1996, Sharpe and Sephton, 2000, Sharpe and Sephton, 2006), which can be used to measure therapy level absorbed dose in reference and non-reference conditions. Alanine has been used as a transfer standard for comparison of the absorbed dose measured from national standards laboratories in a  $^{60}\text{Co}$  beam (Burns *et al.*, 2011) and in megavoltage electron beams (McEwen *et al.*, 2015) with a precision of 0.1%. The use of alanine in dosimetry audits for megavoltage photons and electrons under standard conditions has been proven by Thomas *et al.* (2003) to be an essential detector to ensure national consistency in radiotherapy dosimetry. In non-standard conditions, such as small field beams (Ramirez *et al.*, 2011, Massillon *et al.*, 2013, Dimitriadis *et al.*, 2017) and flattening filter free beams (Budgell *et al.*, 2016) alanine has been used for absolute dosimetry measurements transferring traceability to a primary standard.

A detailed description of alanine as a dosimeter has been given in the literature (Chu *et al.*, 2008, McEwen and Ross, 2009, Malinen, 2014) and some primary points have been emphasised by McEwen *et al.* (2015).

The alanine/EPR signal is affected from external influence quantities, such as irradiation temperature and relative humidity. The ICRU report 80 (Chu *et al.*, 2008), based on literature evaluation, reports that the irradiation temperature may increase the alanine response on a range from  $0.1\% \text{ }^{\circ}\text{C}^{-1}$  to  $0.3\% \text{ }^{\circ}\text{C}^{-1}$  for doses up to 50 kGy. On the other hand, relative humidity would decrease the alanine response over the time. Sleptchonok *et al.* (2000) showed that for a period of no more than half a year and for relative humidity above 60% (for dose values of 1 kGy to 10 kGy), the rate of the alanine/EPR signal fading increases with the relative humidity. However, below 60% the signal is stable within  $\pm 1\%$  of the initial dose value. The fading rate from the post-irradiation stability of the alanine/EPR signal, has been stated from the ICRU report 80 (Chu *et al.*, 2008) to range from 0.5% to 5% per year for dose values up to 10 kGy.

In practice, the effects from such external influence quantities should be considered and corrected by applying correction factors to the alanine response. These factors need to be considered either during irradiation or readout of the alanine detectors.

In the presence of magnetic fields, alanine/EPR offers an alternative to ionisation chamber-based reference dosimetry, in which the magnitude of the ERE, due to small air gaps created from the design of the alanine holder (explained in section 4.2.4), may be reduced compared to the effect in an air-filled ionisation chamber. Currently, the primary standards that can provide traceability for reference dosimetry in magnetic fields are the VSL's (Van Swinden Laboratory, which is the Dutch Metrology Institute) and PTB's (Physikalisch-Technische Bundesanstalt, which is the German Metrology Institute) water calorimeters. These MRI-safe primary standards have performed direct measurements of absorbed dose to water in an Elekta Unity™ (de Prez *et al.*, 2019a) and ViewRay MRIdian™ (Krauss *et al.*, 2020) MRI-linac systems and cross calibrated ionisation chambers to act as transfer standards. Nevertheless, as explained in Chapter 2, the strong magnetic field modifies the response of air-filled ionisation chambers, and the correction  $k_{Q_B,Q}$  for this effect may significantly increase the uncertainty of reference dosimetry.

The use of alanine as a transfer standard implies that it is used in the same conditions that it has been calibrated (primary condition). Where these conditions do not match the measurement conditions (i.e. alanine is irradiated in a different beam quality), a correction to account for changes in the response relative to those under calibration conditions need to be applied. For instance, the alanine/EPR signal depends on the energy spectrum of the radiation beam. Corrections for this effect have been well quantified in the literature (Bergstrand *et al.*, 2003, Sharpe, 2003, Zeng *et al.*, 2004, Bergstrand *et al.*, 2005, Anton *et al.*, 2013). When alanine is used to measure dose in the presence of a strong magnetic field (such as in MRI-linac systems), and an alanine calibration is available only in the absence of the magnetic field, then a correction factor that would account for the effect of the magnetic field needs to be applied. This factor will correct for both the effect of the magnetic field on dose to water and on alanine response.

In this chapter, alanine pellets are loaded in a waterproof holder, placed in an electromagnet and irradiated by  $^{60}\text{Co}$  and 6 MV and 8 MV linac beams over a range of magnetic field strengths. Monte Carlo simulations are performed to calculate the absorbed dose, to water and to alanine, with and without magnetic fields. Combining measurements with simulations, the effect of magnetic fields on alanine response is quantified and a correction factor for the presence of magnetic fields on alanine is determined. A statistical analysis and an investigation of the effect of the air gaps associated with the alanine holder, are also presented.

## 4.2 Materials and Methods

### 4.2.1 Alanine dosimetry at NPL

Typical NPL alanine pellets are shown on Figure 4.6 and their development for reference dosimetry at radiotherapy dose levels has been described in literature (Sharpe and Sephton, 1999, Sharpe and Sephton, 2000, Sharpe and Sephton, 2006). Alanine comprise of 90% L- $\alpha$ -alanine and 10% of binding agent of high melting point paraffin wax (m.p. 98 °C), by weight (Sharpe *et al.*, 1996). Alanine is near water-equivalent, but not waterproof, with a density of about 1.4 g/cm<sup>3</sup> and it has a linear response to dose. The mass of each alanine pellet varies slightly between different batches (nominal mass of a 2.3 mm × 5 mm pellet is 55 mg), but it is weighted before measurement. It also has good

reproducibility (0.3% variation between individual dosimeter pellets) and a small energy dependence, less than 1%, considering 4 MV to 15 MV photon beams relative to a  $^{60}\text{Co}$  beam (Bergstrand *et al.*, 2003, Sharpe, 2003, Zeng *et al.*, 2004, Bergstrand *et al.*, 2005, Anton *et al.*, 2013). EPR spectroscopy is used to detect and quantify the number of the stable free radicals that are created by the ionising radiation. The alanine/EPR signal is the corrected alanine peak-to-peak intensity per unit dosimeter mass, expressed in Gy to water, using a calibration curve derived from reading out alanine irradiated under reference conditions in  $^{60}\text{Co}$ . The corrections include effects such as temperature during irradiation and spectrometer sensitivity. If alanine is irradiated in some other conditions, then a correction may be needed to account for any change in the intrinsic sensitivity of alanine, which may be defined as the alanine/EPR signal per unit absorbed dose to alanine.

We would like to point out that in the work performed in this thesis, the readout of the alanine/EPR signal was performed by the chemical radiation dosimetry laboratory at NPL.

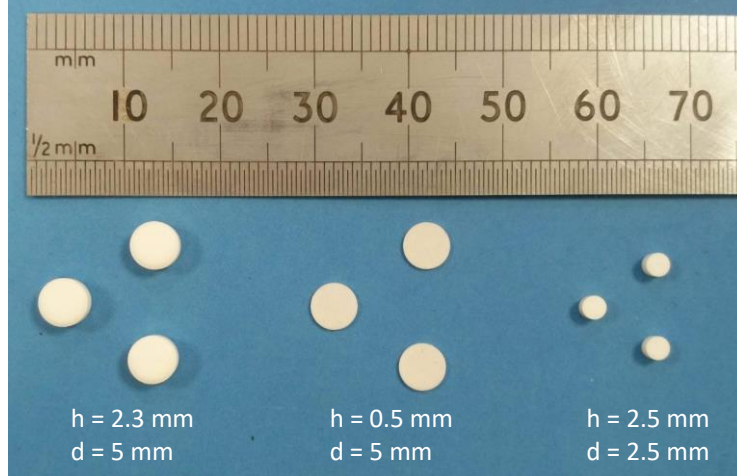


Figure 4.6: Typical NPL's alanine pellets.

#### 4.2.2 Alanine reference dosimetry in a magnetic field

The reference measurement of absorbed dose to water, in the presence of a magnetic field  $\mathbf{B}$ ,  $D_{w,Q_B}$ , using alanine, is given by:

$$D_{w,Q_B} = M_{al,Q_B} \cdot N_{D,w,Q_B} \quad (4.4)$$

where,  $M_{al,Q_B}$  and  $N_{D,w,Q_B}$  are the alanine/EPR signal and the calibration coefficient, respectively, of the alanine detector in the presence of magnetic field. The magnetic field affects the absorbed dose to water at the measurement point,  $D_{w,Q}$ , the absorbed dose to the alanine pellet,  $D_{al,Q}$ , and may also affect the intrinsic sensitivity of the alanine,  $R_{al,Q}$ , which is defined by:

$$R_{al,Q} = \frac{M_{al,Q}}{D_{al,Q}} \quad (4.5)$$

Note that this relation is analogous to the definition of detector dose response (or sensitivity) proposed by Bouchard and Seuntjens (2013).

If the alanine calibration is only available for a beam quality  $Q$  in the absence of any magnetic field,  $N_{D,w,Q}$ , then a correction factor for the effect of the magnetic field is needed:

$$D_{w,Q_B} = M_{al,Q_B} \cdot N_{D,w,Q} \cdot k_{Q_B,Q} \quad (4.6)$$

This correction factor is defined, by analogy with the usual quality dependent correction factor,  $k_{Q,Q_0}$  (Andreo *et al.*, 2000), by:

$$k_{Q_B,Q} = \frac{N_{D,w,Q_B}}{N_{D,w,Q}} = \frac{D_{w,Q_B}/M_{al,Q_B}}{D_{w,Q}/M_{al,Q}} = \frac{D_{w,Q_B}}{D_{w,Q}} \cdot \frac{M_{al,Q}}{M_{al,Q_B}} \quad (4.7)$$

The absorbed dose to water, with magnetic field,  $D_{w,Q_B}$ , and without magnetic field,  $D_{w,Q}$ , was calculated by using MC simulations. The alanine/EPR signal at a quality  $Q$ ,  $M_{al,Q}$ , can be derived from equation (4.5) as the product of the absorbed dose to alanine at a quality  $Q$ ,  $D_{al,Q}$ , and the alanine intrinsic sensitivity at the same quality  $Q$ ,  $R_{al,Q}$ . The effect of the magnetic field on the alanine intrinsic sensitivity may be represented by the ratio,  $F_{Q_B,Q}$ , and is defined as relative intrinsic sensitivity:

$$F_{Q_B,Q} = \frac{R_{al,Q_B}}{R_{al,Q}} \quad (4.8)$$

This was determined by combining measurements of the alanine/EPR signal with the absorbed dose to the alanine pellet, determined by MC simulation of the dosimeter setup:

$$F_{Q_B,Q} = \frac{M_{al,Q_B}}{M_{al,Q}} \cdot \frac{D_{al,Q}}{D_{al,Q_B}} = \frac{D_{w,Q_B}/D_{w,Q} \cdot D_{al,Q}/D_{al,Q_B}}{k_{Q_B,Q}} \quad (4.9)$$

#### 4.2.3 Experimental setup

Alanine pellets, of approximately 2.3 mm height and 5 mm diameter, were placed in a waterproof holder of polyether ether ketone (PEEK) material shaped like a Farmer-type ionisation chamber, in an electromagnet (GMW 3474-140) and irradiated by either a  $^{60}\text{Co}$  source or conventional 6 MV and 8 MV Elekta Synergy linac beams. A disassembled view of the NPL alanine holder is shown in Figure 4.7. The external dimensions of this holder are designed to match a PTW 30013 Farmer-type chamber. The holder has internal dimensions of 5.2 mm diameter (tolerance of 0.2 mm to allow the loading and unloading of the pellets) and a length of 20.5 mm. The measurement reference point of the PTW 30013 Farmer-type chamber is very close to the centre of the third pellet from the thimble tip of the holder. Thus, the first five pellets from the thimble tip of the holder were used for analysis.

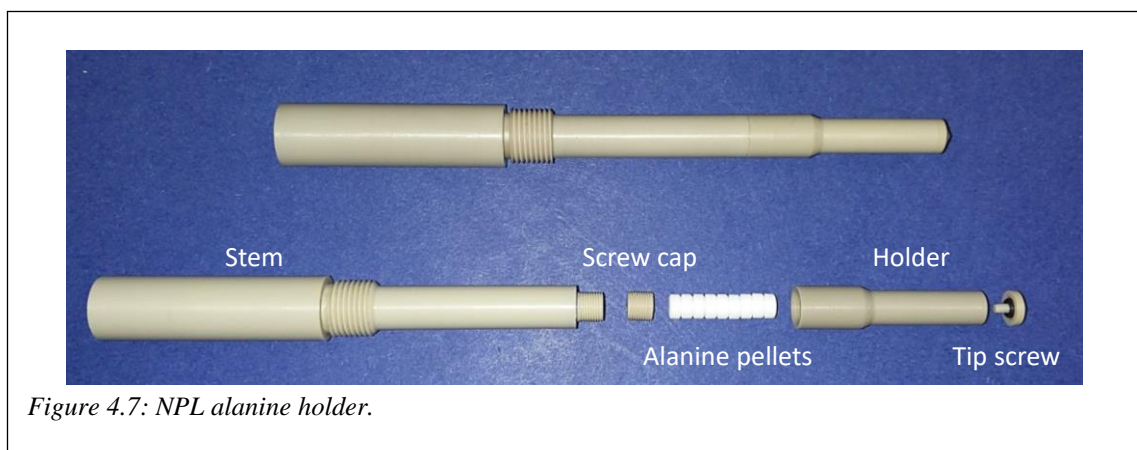
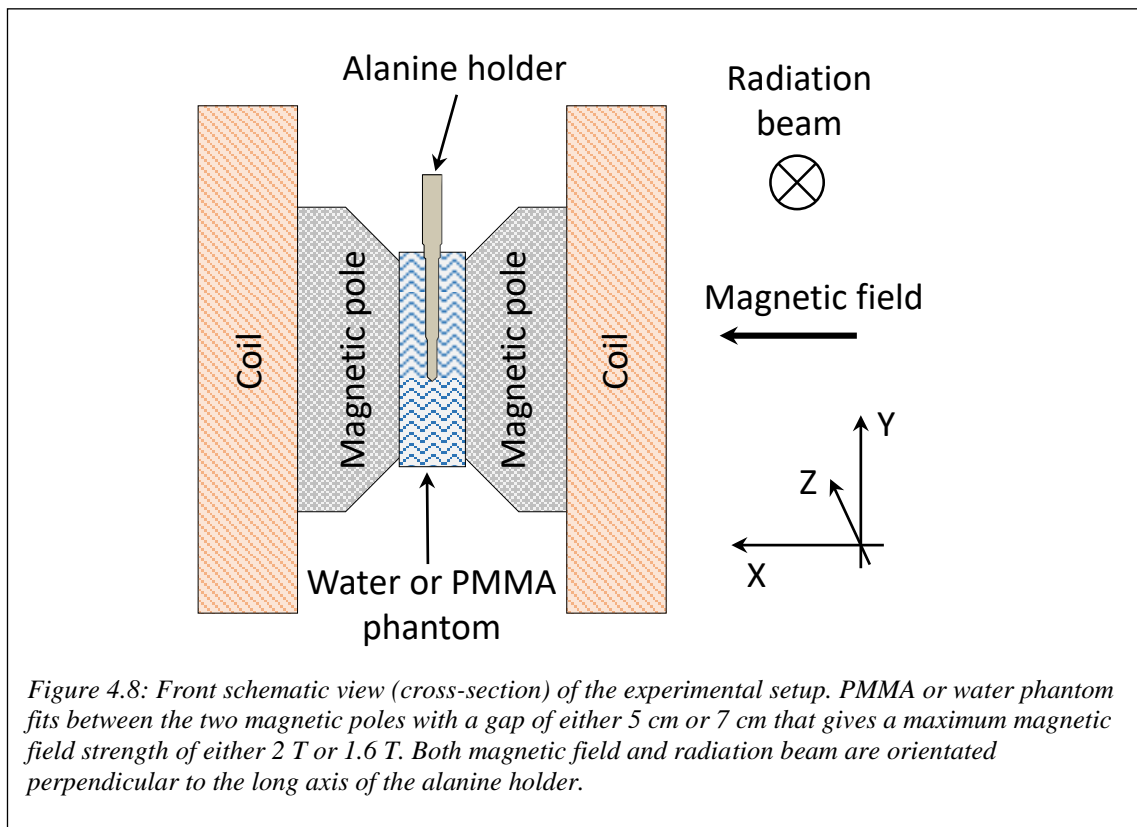


Figure 4.7: NPL alanine holder.

In  $^{60}\text{Co}$ , measurements were performed in a similar setup as explained in Chapter 3. The alanine dosimeters were irradiated in an in-house PMMA phantom, 2 cm  $\times$  5 cm  $\times$  26 cm, with a drilled insert to enable the alanine holder to fit in. Any air gap between the insert and the holder was carefully filled with water to mitigate the effects of the ERE. The

phantom was placed in the 5 cm gap between the two poles of the magnet and irradiated at a depth of 1 cm at five magnetic field strengths (0 T, 0.5 T, 1 T, 1.5 T and 2 T).

In the Elekta Synergy linac setup, a water phantom, 7 cm × 18 cm × 19 cm, was designed to place the alanine holder between the 7 cm gap of the magnetic poles (Figure 4.8), which provide a maximum magnetic field strength of 1.6 T. An insert frame-holder was built to set up the alanine holder in the water tank and between the two poles of the magnet. The surface to SSD was 305 cm, with alanine irradiated at a water equivalent depth of 5 cm and magnetic field strengths of 0 T, 0.35 T, 0.5 T, 1 T and 1.5 T.



In both  $^{60}\text{Co}$  and Elekta Synergy linac radiation beams, the long axis of the alanine holder was positioned in a) the centre of the two magnetic poles, b) perpendicular orientation to the radiation beam, along z-axis and c) perpendicular orientation to the magnetic field, along the x-axis. The radiation field was collimated to fill the gap between the two magnetic poles. A calibrated thermistor was placed close to the holder to record the ambient temperature needed to correct the effect of the alanine signal due to temperature.

#### 4.2.3.1 Magnetic field effect on photon beam symmetry

The effect of the magnetic field on the photon beam symmetry of the linac was evaluated. A Sun Nuclear IC Profiler was set at 100 cm iso-centre (using the same gantry angle as the experimental setup) and irradiated with a  $10\text{ cm} \times 10\text{ cm}$  beam field. With a magnetic field strength of 0 T, initial beam steering adjustment was performed to give zero tilt using the IC Profiler. The 2T (crossline) and 2R (inline) error values, which indicate if there is any asymmetry of the beam, were set to zero. The magnetic field strength was set to 1.5 T and it was found that symmetry was different by 1.5% compared to profiles without magnetic field (crossline and Inline profiles with magnetic field strengths set at 0 T and 1.5 T are shown on Figure 4.9). Beam steering was adjusted to eliminate the tilt (2T and 2R error values set back to zero) and the profile symmetry matched the beam without magnetic field. Therefore, it was concluded that zeroing the 2T and 2R error values was a good method to restore the symmetry of the photon beam when the magnetic field was on.

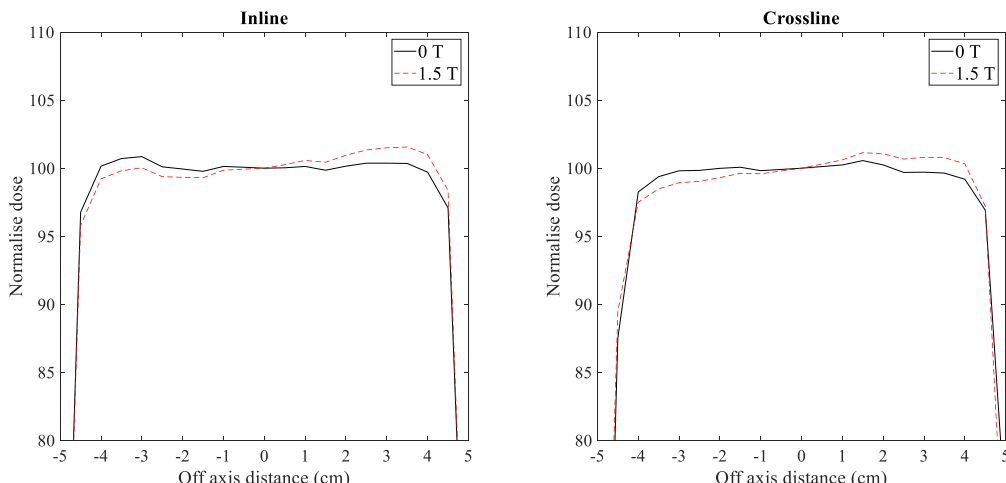


Figure 4.9: Inline and crossline profiles with 1.5 T and without magnetic field of a  $10\text{ cm} \times 10\text{ cm}$  at 8 MV linac beam.

Here, we must point out, that the magnetic field strength at the iso-centre was less than 0.05 mT, when the electromagnet was set up to give 1.5 T between the poles, and any effect on the IC profiler signal due to the magnetic field was found to be negligible.

#### 4.2.3.2 Magnetic field uniformity

The magnetic field uniformity for a pole gap of 7 cm was evaluated by measuring the magnetic field at different strengths in z- (front to rear of the magnet) and y-axis (top to bottom of the magnet) as shown in Figure 4.8. Measurements were performed with a gaussmeter (HIRST GM07) positioned in the centre of the gap between the two poles, as in x-axis of Figure 4.8. Figure 4.10 shows magnetic field data normalised at 0 cm, of 0.35 T, 0.5 T, 1.0 T and 1.5 T strengths, as a function of position along the centre of two magnetic poles: front to rear and top to bottom. Data from the GMW electromagnet user manual (GMW, 2009), for a pole gap of 7 cm, are also included. On average, the uniformity within  $\pm 3$  cm was found to be 99.83% and 99.82% for the front to rear and the top to bottom directions, respectively. The uniformity of the magnetic field from the (GMW, 2009) user manual is 99.83%. Note that the GMW (2009) user manual provides data for the front to rear direction only. However, assuming that the field would be symmetrical along the circular poles, the same data may be used for comparison with the measured top to bottom data.

It can be noticed that in the top to bottom direction in Figure 4.10, the measured data are more noisy compared to the front to rear direction. This is due to the method used for the readings of the magnetic field, which was not as stable as the one used for the front to rear direction.

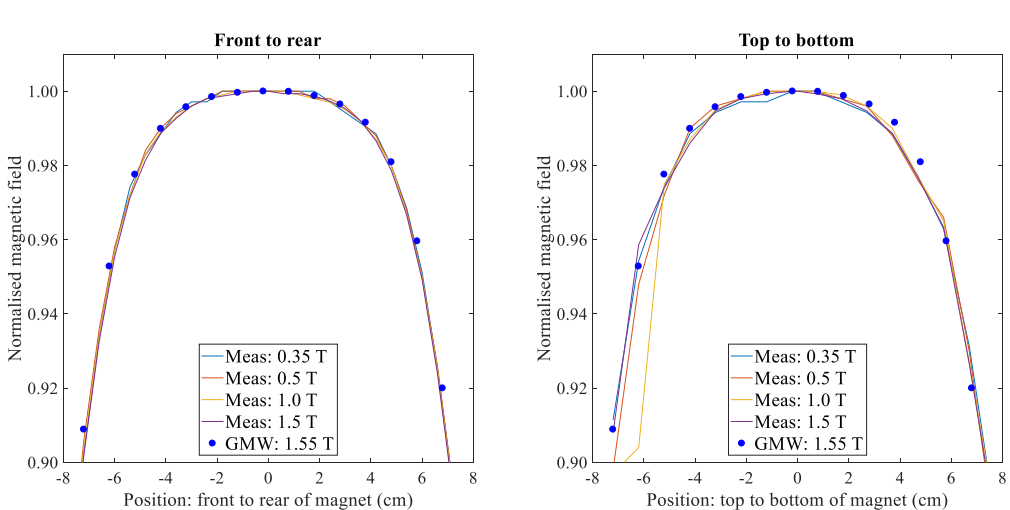


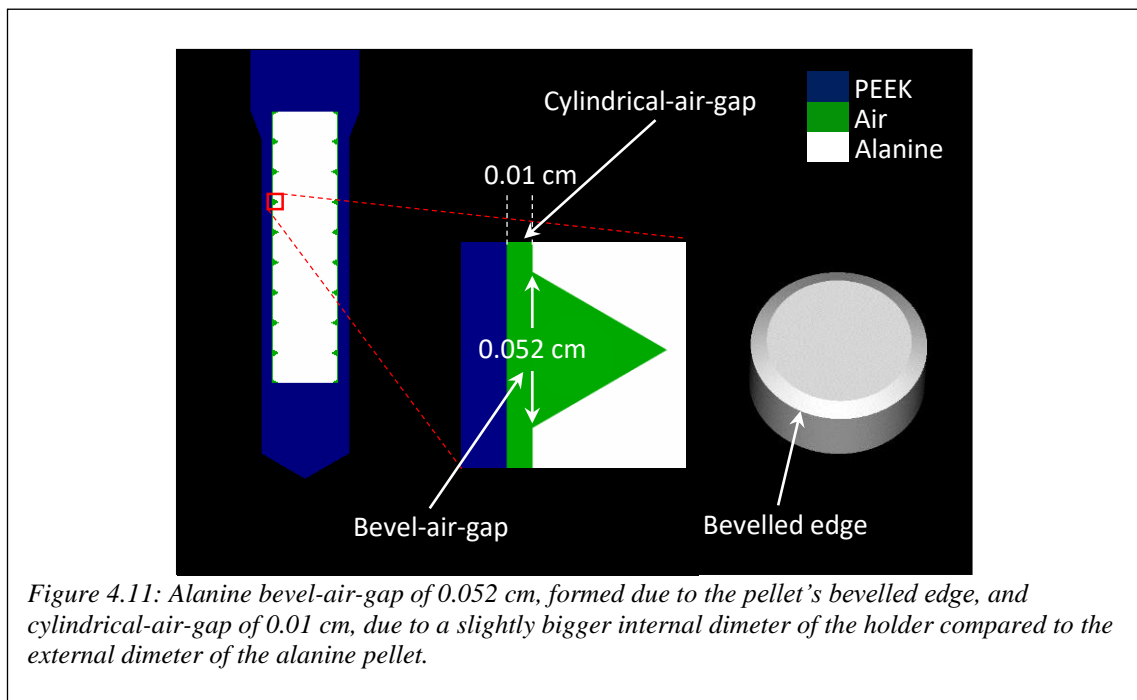
*Figure 4.10: Measured magnetic field uniformity at different strengths for a pole gap of 7 cm. Plots also show the magnetic field uniformity retrieved from the GMW electromagnet user manual (GMW, 2009), Filename: SC7955 Uniformity Plot 6.507, pole gap: 7 cm, magnet operated at 140 A with the magnetic field strength being 1.55 T at 0 cm. All data are normalised at a position of 0 cm.*

#### 4.2.4 Air gaps on the farmer compatible alanine holder

Alanine is a non-waterproof solid-state detector and the pellets has to be located in a watertight holder. Air gaps exist inside the holder and two cases were identified and investigated:

- i. Bevel-air-gap: alanine pellets do not have a flat surface, but instead they form a bevelled edge (Figure 4.11), which introduces air gaps when loaded in the holder. This creates a maximum of 0.052 cm air gap around the bevelled edge between the two pellets. The first (close to the thimble tip) and the last (close to the stem) pellet form the half of this air gap (0.026 cm).
- ii. Cylindrical-air-gap: the internal diameter of the holder has a tolerance of 0.02 cm to allow the pellets to be loaded and unloaded in the holder. This forms an air gap between the inner holder wall and the pellets of 0.01 cm (Figure 4.11).

MC simulations were performed for both cases to investigate the effect of air gaps on the alanine signal. This effect must be included as a component in the measurement uncertainty, when alanine is used as a dosimeter in the presence of the magnetic field. This is further explained in section 4.3.8.2. In any case, any effect (including the fluence perturbation by the PEEK holder) will be part of the alanine magnetic field correction factor, explained in section 4.2.2.



#### 4.2.5 Monte Carlo simulations

In this study, MC simulations were performed to include calculations of absorbed dose to water and to alanine, the investigation on the effect of the air gaps around the alanine pellets and the uncertainty estimation due to the random position of the alanine pellets inside the holder.

The user code *cavity* that forms part of the EGSnrc code system (Kawrakow I *et al.*, 2011) (development version: GitHub: Aug 2017) was used. An accurate model of the experimental setup consisting of the two magnetic poles, the bespoke water tank, the holder and the alanine pellets was first constructed. The dimensions and material specifications used were taken from the associated manuals, test certificates and in-house dimensional measurements. In the MC simulation, the pellet medium was set to be a 90:10 mixture of alanine and paraffin wax binder. The medium density was set to the measured pellet bulk density ( $1.23 \text{ g/cm}^3$ ), and the alanine stopping power density effect correction was based on the crystalline density ( $1.42 \text{ g/cm}^3$ ). Following Zeng *et al.* (2005) the alanine/EPR signal was replaced by dose to the pellet mixture since, over the relevant range of electron energy, variations in the paraffin/alanine stopping power ratio are confined within a range of  $\pm 0.15\%$ . The effect of this approximation on the calculation of the dose to alanine ratio, with and without the magnetic field, is expected to be negligible.

The cut-off energy for electrons (AE and ECUT) was set to 0.521 MeV and for photons (AP and PCUT) to 0.01 MeV. For the simulations of the external magnetic field, the default electromagnetic field macros (EMF\_MACROS) were enabled, in which each electron step is adjusted to include the effect of the Lorentz force in a way that preserves the loss of kinetic energy per unit path length, and EM ESTEPE was set to 0.01. All other parameters were set to their default values.

Phase space data of the 6 MV and 8 MV Elekta Synergy x-ray beams were generated at 270 cm from the target, using the BEAMnrc usercode, for the purpose of the detector simulations. For beam validation at 0 T, depth dose and profile measurements were performed at 279 cm from the target. The radiation field size, at the machine isocentre, was 1.9 cm (crossline)  $\times$  4.4 cm (inline). A parallel plate chamber (NACP-02) was placed in a water tank for depth dose measurements, and profiles were measured by irradiating

EBT-3 films with a 5 cm build-up. Films were processed and analysed using a method developed by Bouchard *et al.* (2009).

The same  $^{60}\text{Co}$  beam model used in Chapter 3, is used in this chapter as well.

The following three sections (4.2.5.1, 4.2.5.2, 4.2.5.3) will describe the MC simulations that were performed to support investigations in this study.

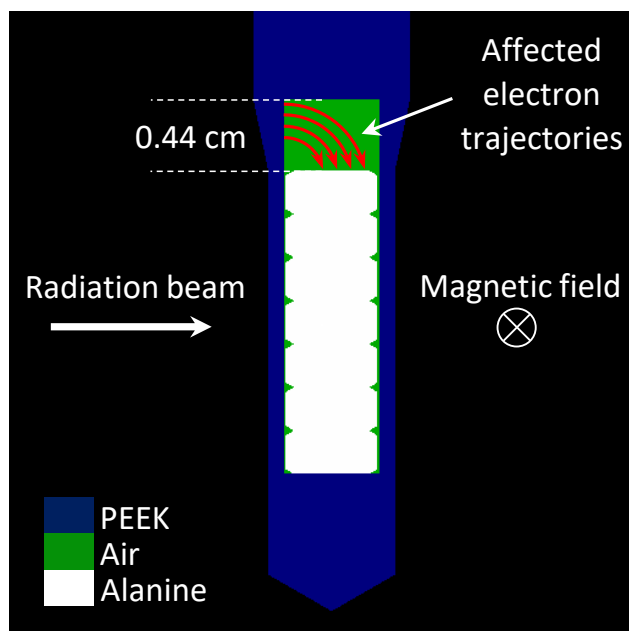


*Figure 4.12: Alanine holder filled with pellets for the purpose of experimental setup validation. The direction of the magnetic field (pointing into the plane of the paper) and radition beam (lying in the plane of the paper) with respect to the holder are shown together with the affected electron trajectories.*

#### 4.2.5.1 Experimental setup model validation

For the model validation of the experimental setup, including the electromagnet, alanine and holder, measurements were performed using the setup explained in section 4.2.3. In this case, measurement and MC simulations were performed with the holder partially loaded with alanine pellets, so that an air gap of nominal 0.44 cm occurs between the stem and the first pellet (Figure 4.12). In this air gap, the electrons follow on average a curved trajectory in accordance with the Lorentz force by increasing the dose on the first pellet, which are distributed along the long axis of the holder towards the thimble tip. The magnetic field strength was 1.5 T and alanine pellets were irradiated with 6 MV and 8 MV delivering 20 Gy in each case. In the simulations, the total dose per incident particle was scored in each pellet. Unfortunately, it was not possible to perform similar

measurements to validate the experimental setup at 1.5 T in the  $^{60}\text{Co}$  beam during the study. Nevertheless, the characteristics of the  $^{60}\text{Co}$  beam model, have been benchmarked Chapter 3.

#### 4.2.5.2 Monte Carlo model for the air gap effect

MC simulations were performed to determine the effect of the air gaps around the alanine pellets. A model of the holder loaded with alanine pellets was used and three sets of simulations were performed: a) full model including both air gaps (bevel and cylindrical), b) full model with the air gaps created from the bevelled edge of the alanine pellets (bevel-air-gaps only) filled with alanine medium and c) full model with no air gaps (both air gaps filled with alanine medium). Figure 4.13 depicts the three models. Simulations were performed for all beam qualities at all examined magnetic field strengths. For each combination, the total dose per incident particle was scored to the first five pellets from the thimble tip of the holder.

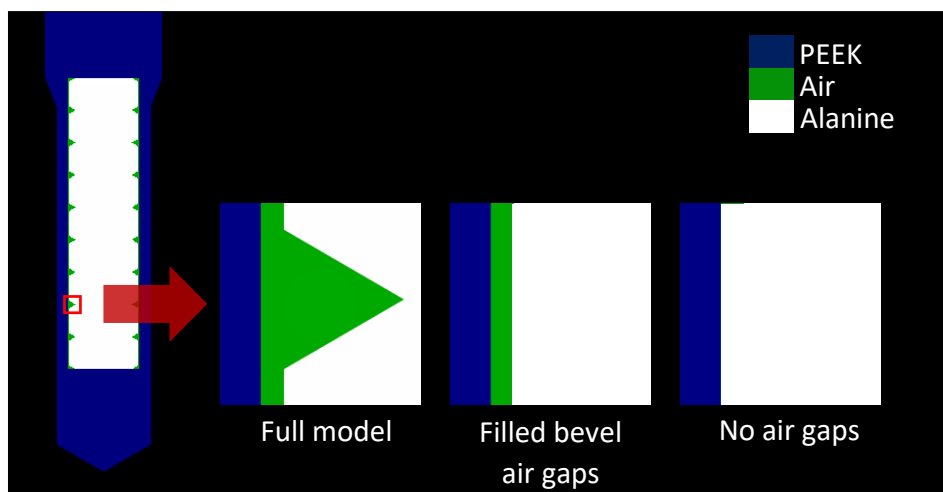
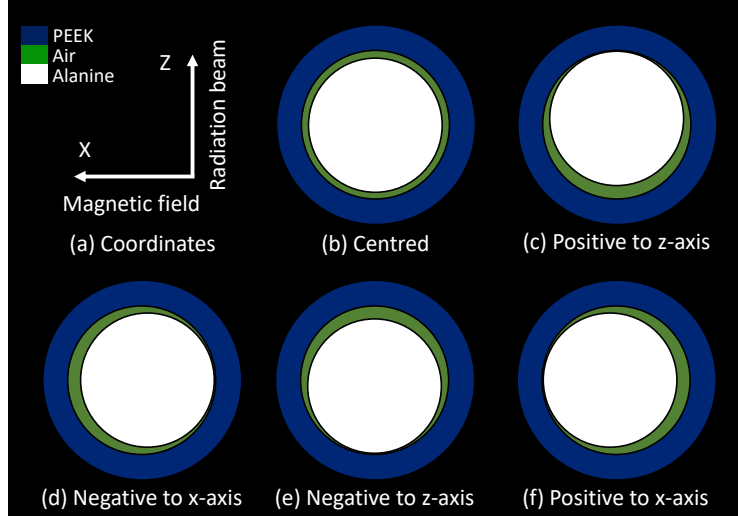


Figure 4.13: MC models for the investigation of the effect of the air gaps around the alanine pellets.

#### 4.2.5.3 Uncertainty due to the air gaps

When alanine pellets are loaded inside the holder, they will not be located symmetrically but rather randomly due to the air gap of 0.02 cm (see section 4.2.4). Depending on the position of the air gaps inside the holder with respect to the magnetic field, the ERE will either increase or decrease the dose in each alanine pellet. Due to the unpredictable location of the pellets, it is difficult to calculate what the effect would be and correct for it. However, known air gaps of 0.02 cm, which is the maximum between the holder and

the alanine pellets, can be modelled by MC simulations to estimate the effect and include it in the uncertainties (see section 4.3.8.2). For that purpose, a model of the holder loaded with nine alanine pellets was built and MC simulations were performed by shifting the pellets in the x- and z-axis as shown in Figure 4.14 (dimensions not to scale), allowing the maximum achievable air-gap (0.02 cm). The total dose per incident particle was scored to the first five pellets from the thimble tip of the holder for each of the three beam energies, for all magnetic field strengths and all five combinations.



*Figure 4.14: MC models to evaluate uncertainties due to air gaps. (a) coordinates indicating the direction of magnetic field and radiation beam with respect to the alanine holder, (b) model of the centred alanine pellets in the holder and (c, d, e, f) offset alanine pellets along the short axis (x- and z-axis) creating an air gap of 0.02 cm. Dimensions not to scale.*

## 4.3 Results

### 4.3.1 Validation of the beam models

The 6 MV and 8 MV beam models were validated by comparing the simulated lateral and depth dose profiles with the measured data as shown in Figure 4.15. For each plot, the data were normalised to the integral of the curve to minimise the effect of point-to-point variations in film sensitivity. Piecewise cubic Hermite polynomial functions (which preserves the shape of the data) were used to interpolate the MC calculated data to the measured depth and off-axis distance points. This will enable a comparison in terms of dose points differences between the MC and the measured data.

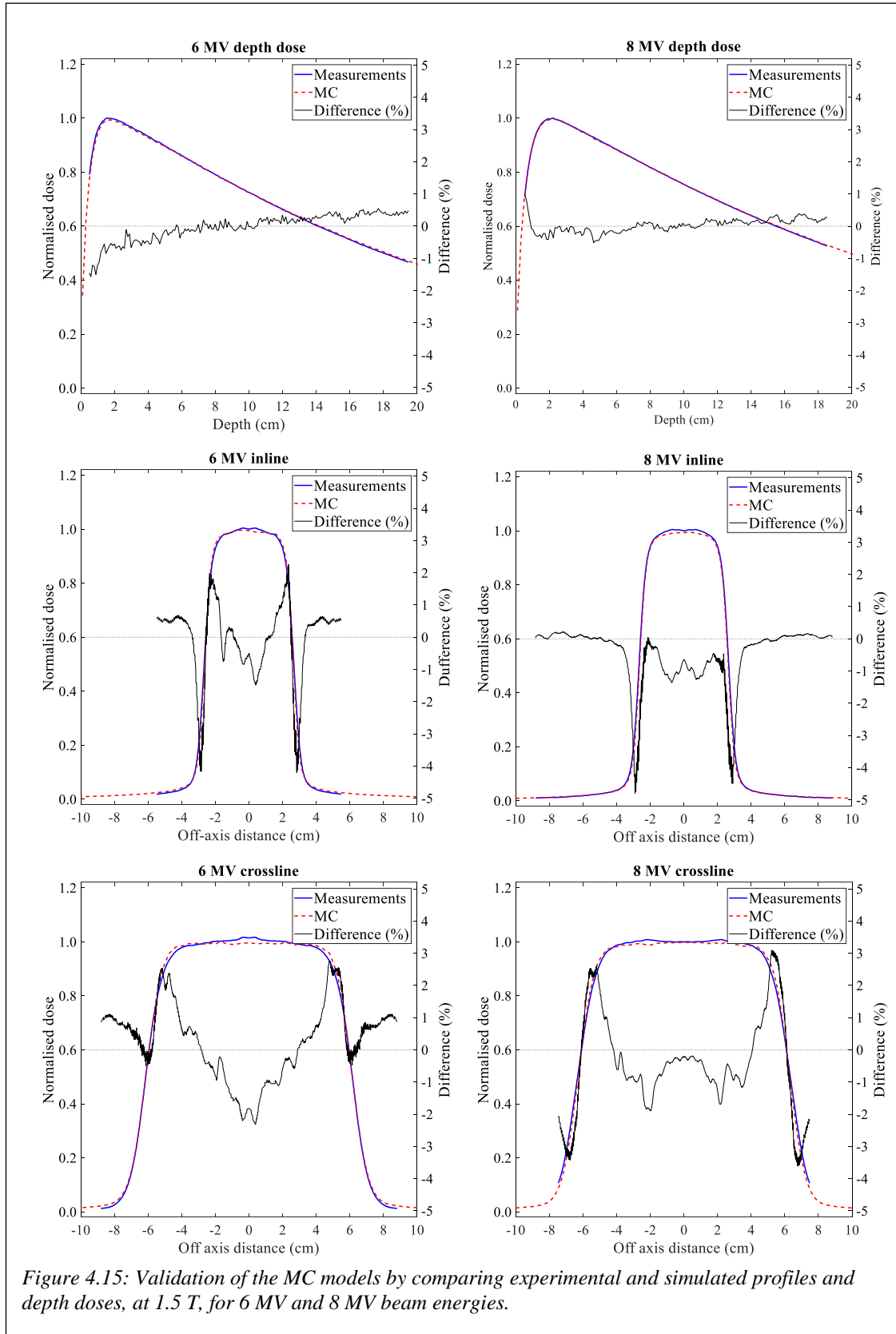


Figure 4.15: Validation of the MC models by comparing experimental and simulated profiles and depth doses, at 1.5 T, for 6 MV and 8 MV beam energies.

In the right y-axis of the plots in Figure 4.15, the percentage dose difference is shown. The dose difference between the MC calculated profiles and the film measurements diverge over a range of 3%. Part of this difference is accounted to the uncertainty of the single channel analysis made of the film data, which was estimated to be 2%. In the two regions confined to the steepest parts of the penumbra, the dose difference varied over a range of 6%.

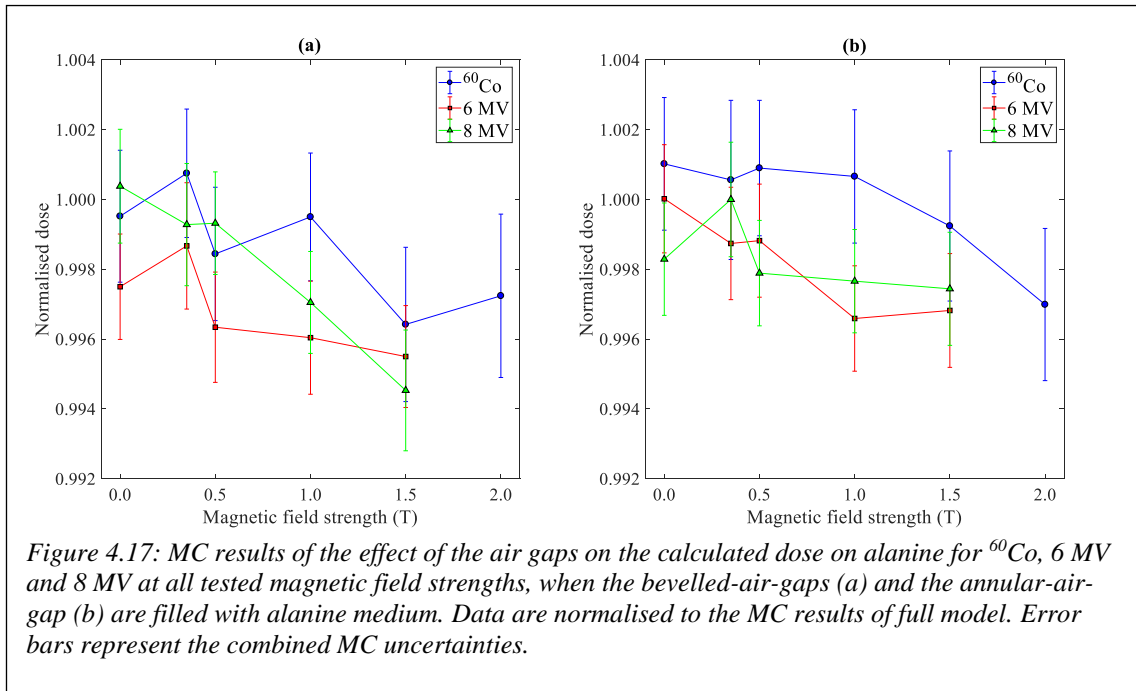
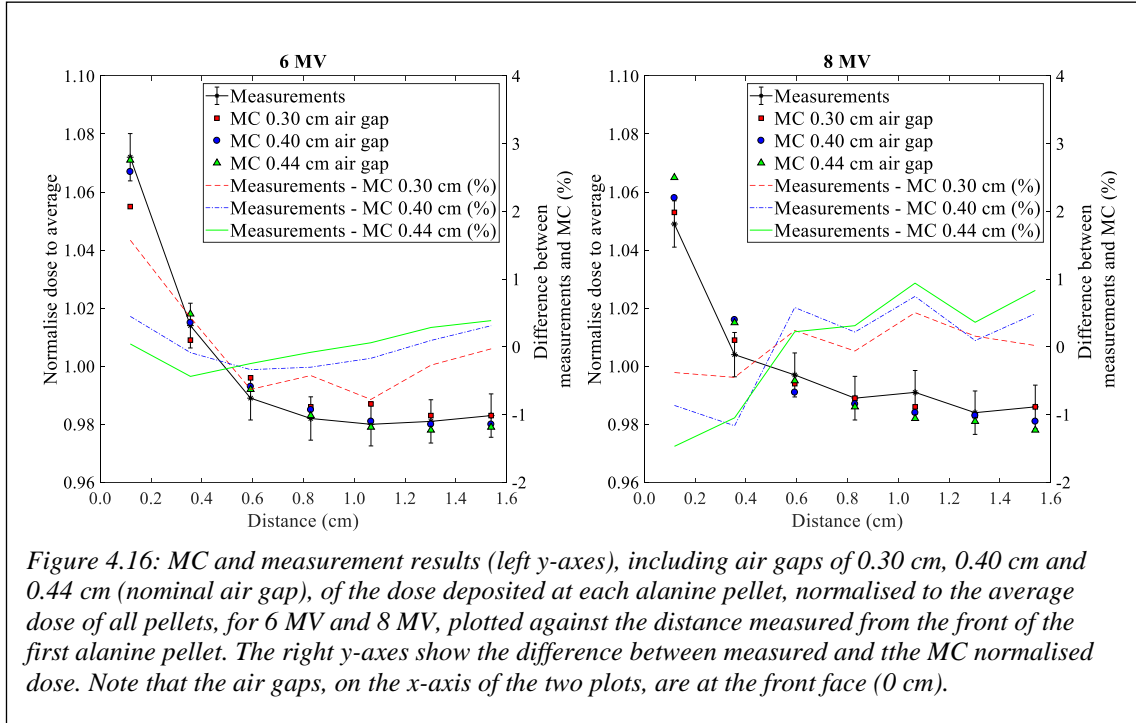
### **4.3.2 Alanine model and experimental setup validation in a magnetic field**

The validation of the experimental setup model for 6 MV and 8 MV with experiments was performed at a magnetic field strength of 1.5 T. It was found that the thickness of the air gap between the PEEK stem and the first alanine pellet, depends on the force that is applied to adjust the screw cap shown in Figure 4.7, which is used to secure the pellets inside the holder. Further measurements of five actual holders and pellets showed typical variations of the air gap in the order of  $0.35 \pm 0.02$  cm, and so additional simulations with air gaps of 0.30 cm and 0.40 cm were made. Figure 4.16 shows the MC results (for three different air gaps) and the measurement results of the dose deposited at each alanine pellet, normalised to the average dose of all pellets, for 6 MV and 8 MV. The same plot, on the right y-axes, shows differences between the measured and the MC normalised doses for the three air gaps. The experimental data points for both energies agree with the MC calculated points of the two additional simulations, of 0.30 cm and 0.40 cm air gaps, within the measurement uncertainties. The error bars on the experimental data represent the combined standard uncertainty of an alanine pellet (0.3%) and the uncertainty due to the air gaps as explained in section 4.3.8.2. The uncertainty on the MC data is in the order of 0.15%. For clarity, error bars are not included on the MC data.

### **4.3.3 Effect of air gaps on alanine in a magnetic field**

Figure 4.17 shows the effect of the air gaps on the calculated dose-to-alanine for the three beam energies and all tested magnetic field strengths, based on the three sets of simulations described in section 4.2.5.2. Calculated data show how the dose to alanine changes when the air gaps created from the bevelled edge are simulated with alanine replacing the air, Figure 4.17 (a), and when both bevel and cylindrical air gaps are replaced with alanine medium, i.e. full model with no air gaps, Figure 4.17 (b). In both

cases, data were normalised to the MC results of the full model (including both air gaps). In Figure 4.17 (b), the maximum deviation from the full model was found to be 0.45% and 0.55% for 6 MV and 8 MV, respectively, at 1.5 T. In Figure 4.17 (a), the maximum deviation was found to be at 1 T and 1.5 T and was less than 0.4% for both 6 MV and 8 MV. For the  $^{60}\text{Co}$  beam all data from both figures were found to be less than 0.4%.



#### 4.3.4 Effect of the magnetic field on absorbed dose to water

The effect of the magnetic field on absorbed dose to water at the measurement point,  $D_{w,Q}$ , is needed to determine the alanine magnetic field quality correction factor and its relative intrinsic sensitivity, as explained in section 4.2.2. For that purpose, depth doses in water for each beam energy and at magnetic field strengths up to 3 T were calculated by using MC simulations. Figure 4.18 (a) shows depth doses, of the 8 MV energy beam, without and with 1.5 T magnetic field (left y-axis) and the ratio  $D_{w,Q_B}/D_{w,Q}$  at each dose point (right y-axis). After  $d_{max}$ , for all beam energies, depth doses in the presence of a magnetic field, although systematically lower compared to 0 T, were found to be similar. Therefore, the  $D_{w,Q_B}/D_{w,Q}$  ratios at each magnetic field strength were determined from the average ratios after  $d_{max}$ , which results in a level of standard uncertainty of 0.04%. Figure 4.18 (b) shows the MC calculated  $D_{w,Q_B}/D_{w,Q}$  ratios as a function of magnetic field strength for the three beam energies.

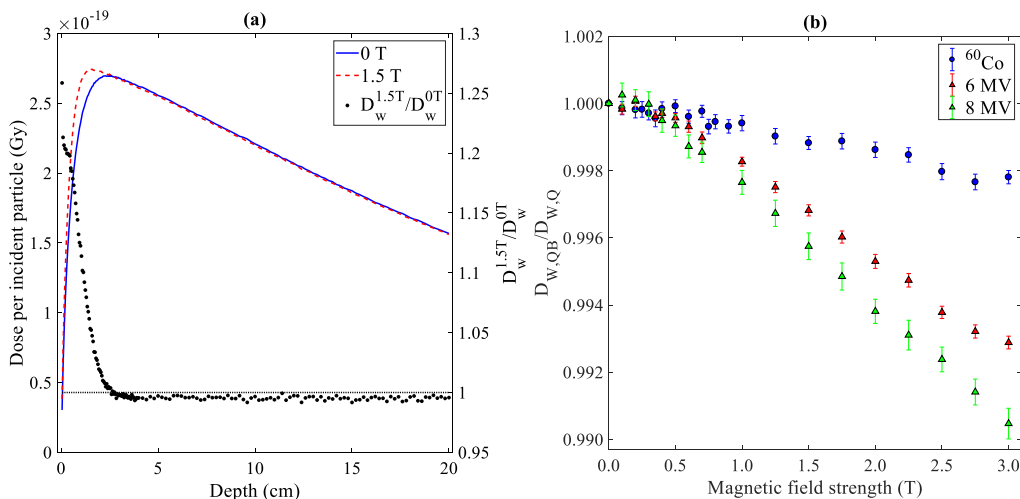


Figure 4.18: a) Depth doses, of the 8 MV energy beam, for 0 T and 1.5 T (left y-axis) and the ratio  $D_{w,Q_B}/D_{w,Q}$  at each dose point (right y-axis). b) MC calculated  $D_{w,Q_B}/D_{w,Q}$  ratios as a function of magnetic field strength for  $^{60}\text{Co}$ , 6 MV and 8 MV.

#### 4.3.5 Alanine response in a magnetic field

Dose delivered to each alanine pellet in a Farmer-type holder was investigated as a function of position within the holder. The pellets are labelled 1 – 5, with 1 being closest to the stem of the alanine holder. Figure 4.19 shows results of the dose data of the three energy beams, for each individual pellet, for all tested magnetic field strengths. Each line

represents data of the five readouts from the stack of the pellets in one holder, which are normalised to the average dose over all pellets in each holder. The error bars represent uncorrelated part of the uncertainties of the dose to water measured with alanine. It may be observed that for all cases there is not any systematic trend, but rather, data are randomly scatter. This figure shows that the value (dose per pellet normalised to the mean of all pellet in the stack) does not vary with pellet position in the stack.

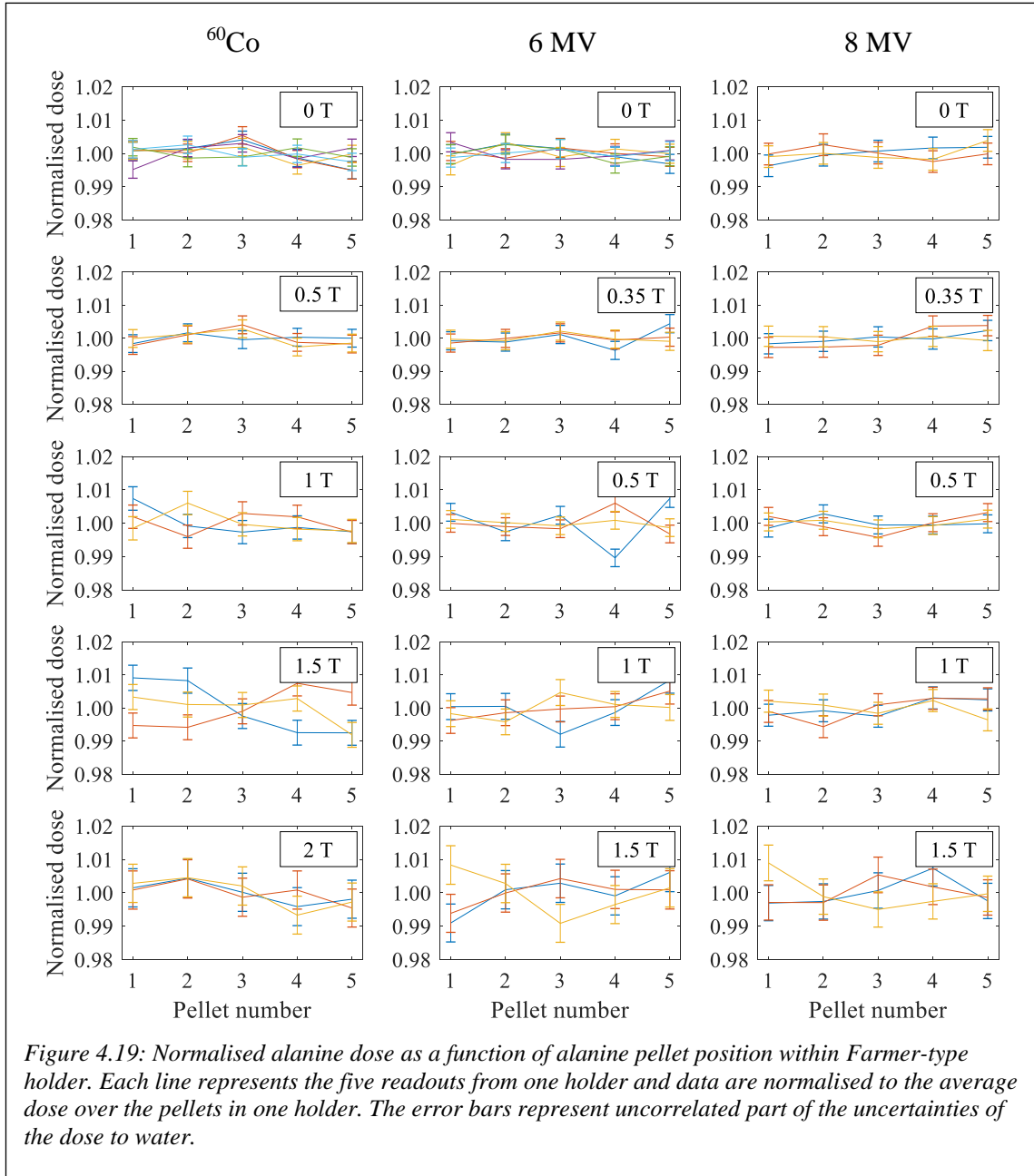
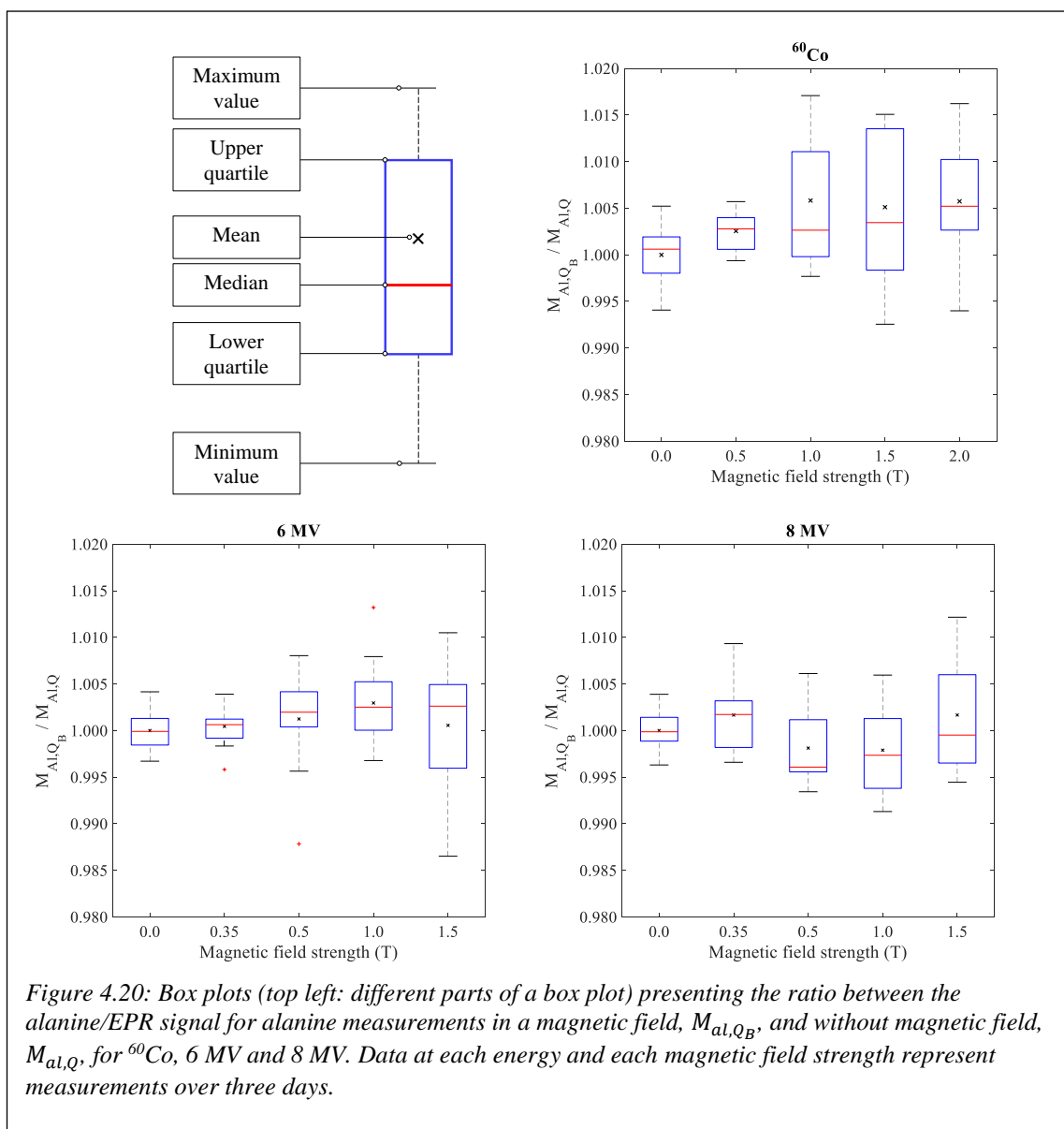


Figure 4.20 summarises the alanine/EPR signal for measurements in a magnetic field,  $M_{al,Q_B}$ , normalised to the signal at zero magnetic field,  $M_{al,Q}$ , as a function of magnetic

field strength for the three beam energies. For each plot and each strength, data represent measurements over three days and their distribution is displayed in a form of box plot. Note that crosses ( $\times$ ) on each box plot indicate the mean value of the normalised alanine signal for each magnetic field strength over three days.

For zero magnetic field and for each energy, the pellet-to-pellet variation of the signal has a standard deviation of up to 0.52%. This results in a standard uncertainty of the mean of 0.13% or better, considering the number of the pellets used in this study. However, as the magnetic field strength is increased, for each energy, the standard deviation also increases, up to 0.85% (standard uncertainty of the mean of 0.22%).



*Figure 4.20: Box plots (top left: different parts of a box plot) presenting the ratio between the alanine/EPR signal for alanine measurements in a magnetic field,  $M_{\text{al},Q_B}$ , and without magnetic field,  $M_{\text{al},Q}$ , for  $^{60}\text{Co}$ , 6 MV and 8 MV. Data at each energy and each magnetic field strength represent measurements over three days.*

### 4.3.6 Quality correction factor for the presence of a magnetic field on alanine

The alanine quality correction factors as a function of a magnetic field strength,  $k_{Q_B,Q}$ , are shown in Figure 4.21 and Table 4.1, for the three beam energies. The error bars denote the overall combined standard uncertainty (ranging from 0.2% to 0.6%), as quoted in section 4.3.8, and include the effects of measurement repeatability, air gaps, linac drift and MC uncertainties. Figure 4.21 shows how the correction factor for each energy decreases with increasing magnetic field strength. Except for the data point at 0.5 T (1.0014) for 8 MV, all the remaining data points lie below unity, ranging from 0.9933 to 0.9998 with an average of  $0.9967 \pm 0.0027$ . Note that this correction includes both the effect of the magnetic field on absorbed dose to water and its effect on alanine intrinsic sensitivity. The latter effect is isolated in the following.

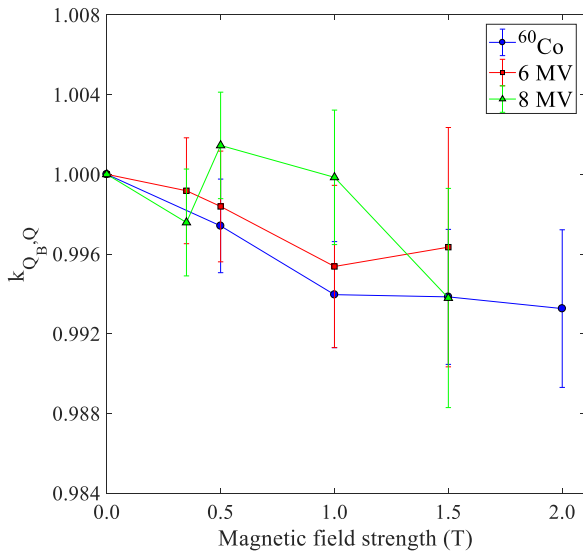


Figure 4.21: Alanine quality correction factors for the presence of magnetic field,  $k_{Q_B,Q}$ , for all examined magnetic field strengths for  $^{60}\text{Co}$ , 6 MV and 8 MV. The error bars denote the standard combined uncertainties estimated in section 4.3.8.

*Table 4.1: Alanine quality correction factors for the presence of a magnetic field,  $k_{Q_B,Q}$ , for all examined magnetic field strengths for the three beam energies. Standard uncertainties estimated in section 4.3.8.*

Magnetic field strength (T)	$^{60}\text{Co}$	6 MV	8 MV
0.35	-	$0.9992 \pm 0.0026$	$0.9976 \pm 0.0027$
0.50	$0.9974 \pm 0.0024$	$0.9984 \pm 0.0027$	$1.0014 \pm 0.0026$
1.00	$0.9940 \pm 0.0027$	$0.9954 \pm 0.0040$	$0.9998 \pm 0.0034$
1.50	$0.9939 \pm 0.0034$	$0.9964 \pm 0.0060$	$0.9938 \pm 0.0055$
2.00	$0.9933 \pm 0.0039$	-	-

#### 4.3.7 The effect of the magnetic field on alanine response

The magnetic field effect on alanine intrinsic sensitivity may be represented by the quantity  $F_{Q_B,Q}$ , relative intrinsic sensitivity, which is defined as the ratio of the alanine intrinsic sensitivity with and without magnetic field (equations (4.8) and (4.9) in section 4.2.2). This was obtained by combining measurements with MC simulations and is shown in Figure 4.22 and Table 4.2, for the three beam energies. The alanine over-response tends to increase with magnetic field strength, up to 1.0099 at 8 MV in 1.5 T, but without any obvious trend as a function of energy.

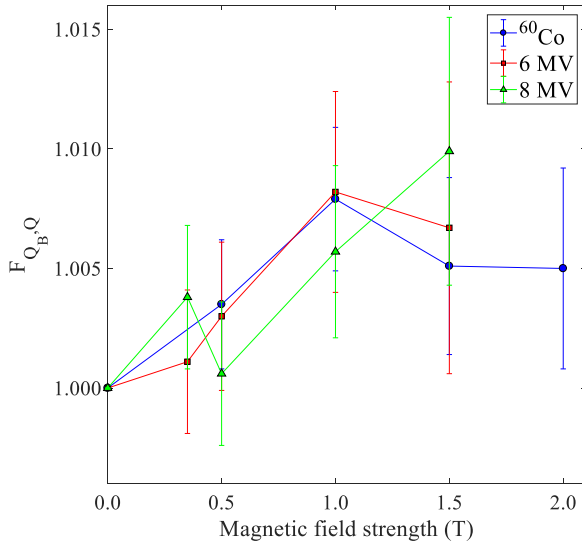


*Figure 4.22: Alanine relative intrinsic sensitivity,  $F_{Q_B,Q}$ , for all examined magnetic field strengths for  $^{60}\text{Co}$ , 6 MV and 8 MV. The error bars denote the standard combined uncertainties estimated in section 4.3.8.*

Table 4.2: Alanine relative intrinsic sensitivity,  $F_{Q_B,Q}$ , for all examined magnetic field strengths for the three beam energies. Standard uncertainties estimated on section 4.3.8.

Magnetic field strength (T)	$^{60}\text{Co}$	6 MV	8 MV
0.35	-	$1.0011 \pm 0.0030$	$1.0038 \pm 0.0030$
0.50	$1.0035 \pm 0.0027$	$1.0030 \pm 0.0031$	$1.0006 \pm 0.0030$
1.00	$1.0079 \pm 0.0030$	$1.0082 \pm 0.0042$	$1.0057 \pm 0.0036$
1.50	$1.0051 \pm 0.0037$	$1.0067 \pm 0.0061$	$1.0099 \pm 0.0056$
2.00	$1.0050 \pm 0.0042$	-	-

### 4.3.8 Uncertainties

The analysis of uncertainty here follows the Joint Committee for Guides in Metrology (JCGM) Guide to the Expression of Uncertainty in Measurement (JCGM, 2008). Uncertainties evaluated by statistical analysis are grouped as type A and the rest are grouped as type B. These are added in quadrature to give a combined standard uncertainty with coverage factor  $k = 1$ .

The quoted relative standard uncertainties are shown in Table 4.3. This includes the overall combined relative standard uncertainties in  $k_{Q_B,Q}$  at 0.35 T and 1.5 T for 6 MV and 8 MV. For  $^{60}\text{Co}$ , uncertainties are presented at 0.5 T and 1.5 T. For the rest of the magnetic field strengths at all three energy beams, the relative standard uncertainties are between the stated uncertainties in Table 4.3. For  $^{60}\text{Co}$  and 2 T, the uncertainty was found to be 0.56%.

Table 4.3: Uncertainty budget for the determination of the quality correction factor for the presence of magnetic field on alanine,  $k_{Q_B,Q}$ .

<b>Uncertainty component</b>	Type	Relative standard uncertainty (%)					
		$^{60}\text{Co}$		6 MV		8 MV	
		0.5 T	1.5 T	0.35 T	1.5 T	0.35 T	1.5 T
Measurement repeatability	A	0.06	0.22	0.06	0.20	0.08	0.11
Air gaps	B	0.11	0.29	0.13	0.52	0.19	0.47
Linac output correction	A	-	-	0.07	0.07	0.10	0.10
Monte Carlo	A+B	0.15	0.15	0.15	0.15	0.15	0.15
<b>Overall combined relative standard uncertainty on <math>k_{Q_B,Q}</math></b>		0.20	0.39	0.22	0.58	0.27	0.52

#### **4.3.8.1 Measurement uncertainty and repeatability**

The uncertainty on the repeatability of the measurements is evaluated by considering the behaviour of the averaged signal over the alanine pellets at each magnetic field strength for each energy, over all experiments. The standard deviation of the mean was found to be ranging from 0.05% to 0.22%.

#### **4.3.8.2 Uncertainty due to air gaps**

Uncertainties due to the unknown spatial distribution of the alanine pellets in the PEEK holder were estimated using MC simulations as explained in section 4.2.5.3. Figure 4.23 (a) shows the MC calculated dose to alanine for each energy, when pellets are shifted in the x- and z-axis inside the alanine holder (see Figure 4.14). For clarity, Figure 4.23 (a), only includes data for 1.5 T, which are normalised with respect to when the pellets are centrally-located in the holder. This figure shows how the ERE is varying the dose to alanine at the different positions. The type A uncertainties were based on the root mean square (RMS) error of the four different distributions of the alanine pellets inside the holder. The uncertainties, for each energy, were found to increase with magnetic field strength up to 0.52% and 0.47% for 6 MV and 8 MV at 1.5 T, respectively. For  $^{60}\text{Co}$  it was 0.52% at 2 T. For the other magnetic field strengths and for all beam energies the determined uncertainties were below 0.30%. The rise in uncertainties as a function of magnetic field strength is reflected by the length of the error bars in Figure 4.23 (b), (c) and (d). These figures show the average normalised dose over the four shifted alanine positions, as per Figure 4.23 (a), for each energy beam at all examined magnetic field strengths. It can be observed that the error bars, at each energy beam, increases with magnetic field strength. The uncertainty due to the air gaps is the dominant component in the uncertainty budget and is applicable to the absorbed dose to water measured with the alanine detector, in the presence of a magnetic field using the holder designed for this study.

#### **4.3.8.3 Uncertainty due to linac output**

The short term (over one day) behaviour of the output from the Elekta Synergy linac beams was investigated during the alanine irradiation. The output was measured several times in-between the alanine irradiations using an ionisation chamber with the same experimental set up and always at 0 T. For each day of irradiation, the output (dose rate) was found to diverge by an average of -0.07% per hour. This deviation was considered,

and used to correct the alanine signal, based on a linear fit between the ionisation chamber signal and the time. The uncertainty was estimated from the gradient of the residuals of the fit (RMS error) and estimated to be less than 0.1%, on average.

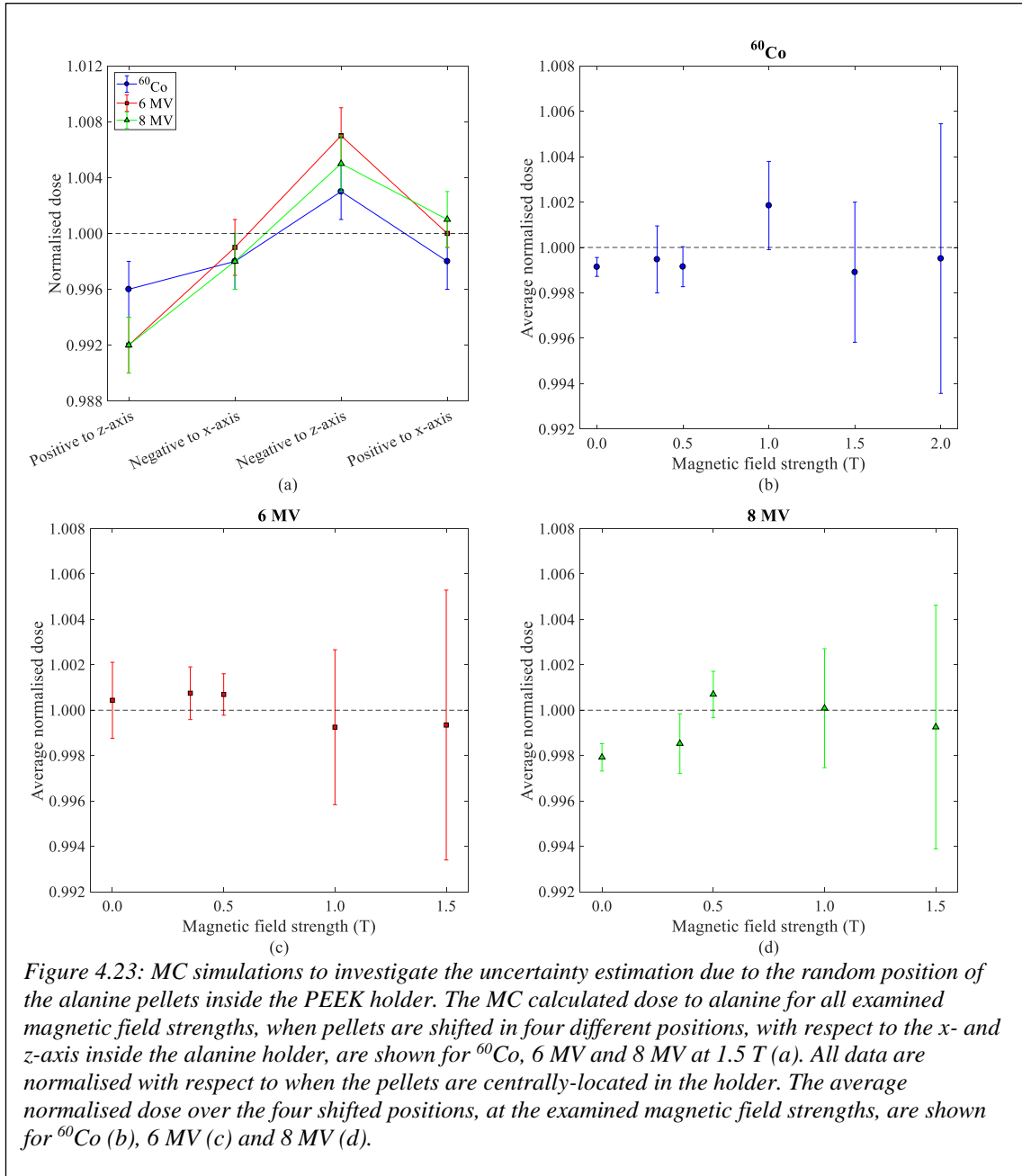


Figure 4.23: MC simulations to investigate the uncertainty estimation due to the random position of the alanine pellets inside the PEEK holder. The MC calculated dose to alanine for all examined magnetic field strengths, when pellets are shifted in four different positions, with respect to the x- and z-axis inside the alanine holder, are shown for  $^{60}\text{Co}$ , 6 MV and 8 MV at 1.5 T (a). All data are normalised with respect to when the pellets are centrally-located in the holder. The average normalised dose over the four shifted positions, at the examined magnetic field strengths, are shown for  $^{60}\text{Co}$  (b), 6 MV (c) and 8 MV (d).

#### 4.3.8.4 Monte Carlo uncertainties

In the MC simulations, the Type A uncertainties in the determination of the absorbed dose to water, and of the absorbed dose to alanine, with and without magnetic field, were typically 0.1%. For self-consistency and transport parameters we estimated a Type B

uncertainty of 0.1% (Kawrakow, 2000, Malkov and Rogers, 2016). The combined standard uncertainty on the MC simulations resulted in 0.15%.

## 4.4 Discussion

The performance of the alanine dosimeter in the presence of a magnetic field has been investigated at three different photon beam energies over a range of magnetic field strengths. Alanine pellets were placed in a waterproof PEEK holder, developed in-house and shaped to match a Farmer-type chamber, in an electromagnet and irradiated by either a  $^{60}\text{Co}$  source or conventional 6 MV and 8 MV Elekta Synergy linac beams. The long axis of the alanine holder was positioned in the centre of the magnetic poles of the electromagnet and in perpendicular orientation relative to both radiation beam and the magnetic field.

### 4.4.1 MC simulations and air gap effects

MC simulations were performed to: a) investigate the effect of the air gaps on dose to alanine (found around the pellets when loaded in the PEEK holder), b) investigate the uncertainty due to the random position of the pellets inside the holder and c) calculate the absorbed dose to water and absorbed dose to alanine at the three beam qualities, with and without magnetic field, for the determination of the quality correction factor for the presence of magnetic field on alanine.

The linac 6 MV and 8 MV photon beam MC models were validated by comparing simulated with experimental beam profiles and depth doses. For both energies a very good agreement was found between the simulations and the measurements. In validating the MC simulations of the experimental set up, for both energies at 1.5 T, the holder was loaded with alanine pellets, creating an air gap between the holder's stem and the first pellet. It became apparent that the thickness of the air gap varies with respect to the force that is applied on the screw cap (Figure 4.7) to secure the pellets in the holder. Thus, MC simulations were performed for different air gaps and it was demonstrated that at least two of the MC models reproduced well the deviated behaviour of the dose along the pellets towards the thimble tip of the holder.

The results of the MC simulations show that the air gaps affect the alanine response, due to the ERE caused by the magnetic field, by as much as 0.45% and 0.55% for 6 MV and

8 MV, respectively, and less than 0.40% for  $^{60}\text{Co}$  over all the magnetic field strengths. The air gaps around other dosimeters, such as ionisation chambers, will increase the variation on the dose measurement, which can be as much as 3.8% for a Farmer-type chamber (Agnew *et al.*, 2017). This can be eliminated by immersing the dosimeters in water (if waterproof). Alanine, however, is not waterproof and needs to be placed in a watertight holder for dose measurements in water. Due to the structure of the alanine pellets (they form bevelled edges) and the possible asymmetry in the positions of them inside the holder, it is difficult to avoid the effect caused by the existing air gaps. However, we can include this effect as a component in the measurement uncertainty, which increases with magnetic field strength and reaches 0.52% for 6 MV and 0.47% for 8 MV at 1.5 T. For  $^{60}\text{Co}$  the highest uncertainty was 0.52% at 2 T (0.29% at 1.5 T).

The maximum pellet-to-pellet variation of the measured alanine EPR/signal at 0 T, based on the number of the pellets considered in this study for the three energies, was found to be 0.52%, which results in a standard uncertainty of the mean of 0.13% or less. This is in line with previous studies (Anton, 2006, Sharpe and Sephton, 2006, McEwen *et al.*, 2015), which investigated alanine dosimetry at therapy level energy beams. Nevertheless, for each energy, the variation was found to increase with the magnetic field strength up to 0.85%, reaching a standard uncertainty of the mean of 0.22% at 1.5 T. The increase in variation is mainly attributable to the air gaps, which vary in size, based on the random locations of the pellets inside the holder. In this case, the ERE will diverge the alanine EPR/signal, as the path length of the secondary electrons will follow a curved trajectory due to the Lorentz force. These affected electrons will either deposit their energy to alanine or will curve back ‘exiting’ the holder.

#### **4.4.2 Quality correction factor for the presence of a magnetic field on alanine**

The alanine quality correction factor for the presence of a magnetic field was determined by combining measurements of the alanine/EPR signal with calculations of the absorbed dose, to water and to alanine, in the presence of a magnetic field, by MC simulations. Figure 4.21 shows that the correction factor tends to decrease with increasing magnetic field strength. For each energy the correction, averaged over all non-zero magnetic field strengths, is  $0.9946 \pm 0.0019$  for  $^{60}\text{Co}$ ,  $0.9973 \pm 0.0018$  for 6 MV and  $0.9982 \pm 0.0033$

for 8 MV. Although the change in the average correction factor with energy is monotonic, the uncertainties are too large to allow a more precise conclusion regarding energy dependence. The overall correction factor,  $k_{Q_B,Q}$ , takes account of all the effects of the magnetic field, on dose to water, dose to alanine, alanine sensitivity, and the fluence perturbation by the PEEK holder and by the air gaps. These effects are built in the  $k_{Q_B,Q}$ , which can be used to correct the dose to water measured with alanine in the presence of a magnetic field, when alanine is calibrated in the absence of a magnetic field. If a different holder was used (holder material, air gap details, etc.), it would be necessary to recalculate the  $k_{Q_B,Q}$  correction factor. This correction factor is holder-dependent.

#### 4.4.3 The effect of the magnetic field on alanine response

The effect on the alanine intrinsic sensitivity due to the magnetic field,  $F_{Q_B,Q}$ , can be calculated by using the experimental data and the MC simulations as defined in equation (3.1). The intrinsic sensitivity describes the yield of stable free radicals per unit dose to alanine. It can be seen from Figure 4.22, that the alanine intrinsic sensitivity increases with magnetic field strength for all examined beam energies, without any obvious energy dependence. All  $F_{Q_B,Q}$  values lie above unity with the highest being  $1.0099 \pm 0.0056$  at 8 MV and at 1.5 T. A common linear fit, formula (4.10), was made to the data, for all energies, and this indicates that the effect of a magnetic field on alanine is to increase its relative intrinsic sensitivity by  $a = 0.0047 \pm 0.0005$  per Tesla.

$$F_{Q_B,Q} \sim (1 + aB) \quad (4.10)$$

This value,  $a$ , may be used to estimate the required correction factor,  $k_{Q_B,Q}$ , for different field strengths,  $B$ , by combining the fit value of  $F_{Q_B,Q}$  with MC simulations of absorbed dose, to water and to alanine.

This work investigated the possibility of an effect (with the aim of determining the correction for any such effect) which is at the limit of measurement capability. As a consequence, and looked at in isolation, the measurement results shown are noisy and often appear consistent with there being no effect. However, as will be discussed on Chapter 6, the measurement results and the uncertainty on those measurement results will

both be improved by including a correction factor for alanine response in the presence of a magnetic field.

## 4.5 Summary

In this chapter, the performance of alanine irradiated in the presence of a magnetic field was successfully characterised. It was found that the effect of the magnetic field on an alanine/EPR signal is energy independent and the best estimate would be that the signal is increased by 0.2% at 0.35 T and by 0.7% at 1.5 T. However, the uncertainty on this estimate is such that the effect of the magnetic field may be zero. If the effect is not zero, neglecting to correct for it would introduce a systematic error in the measured absorbed dose to water in commercially available MRI linacs. Therefore, if alanine is calibrated in the absence of any magnetic field, a correction factor,  $k_{Q_B,Q}$ , may need to be applied in order to minimise the uncertainty in a determination of the absorbed dose to water in the presence of a magnetic field. This correction factor, which depends on the geometry and material of the alanine holder, would vary with magnetic field strength. Not applying this correction factor would result in an overestimation of the dose to water and tends to reduce the measured dose. Alanine is an MR safe, robust and stable dosimeter with comparable uncertainties to a Farmer-type chamber, and suitable for use as a reference class detector for MRIgRT. The inclusion of the correction factor  $k_{Q_B,Q}$  will be determined by an analysis of uncertainty in Chapter 5 and in section 6.4.

## **Chapter 5 Experimental reference dosimetry measurements in MRIgRT using alanine: calibration and magnetic field correction factors of ionisation chambers**

MRIgRT falls outside the scope of existing high energy photon therapy dosimetry protocols, because those protocols do not consider the effects of the magnetic field on detector response and on absorbed dose to water. The aim of this chapter is to evaluate and demonstrate the traceable measurement of absorbed dose in MRIgRT systems using alanine, made possible by the characterisation of alanine sensitivity to magnetic fields reported in chapter 4, in a way which is compatible with existing standards and calibrations available for conventional radiotherapy.

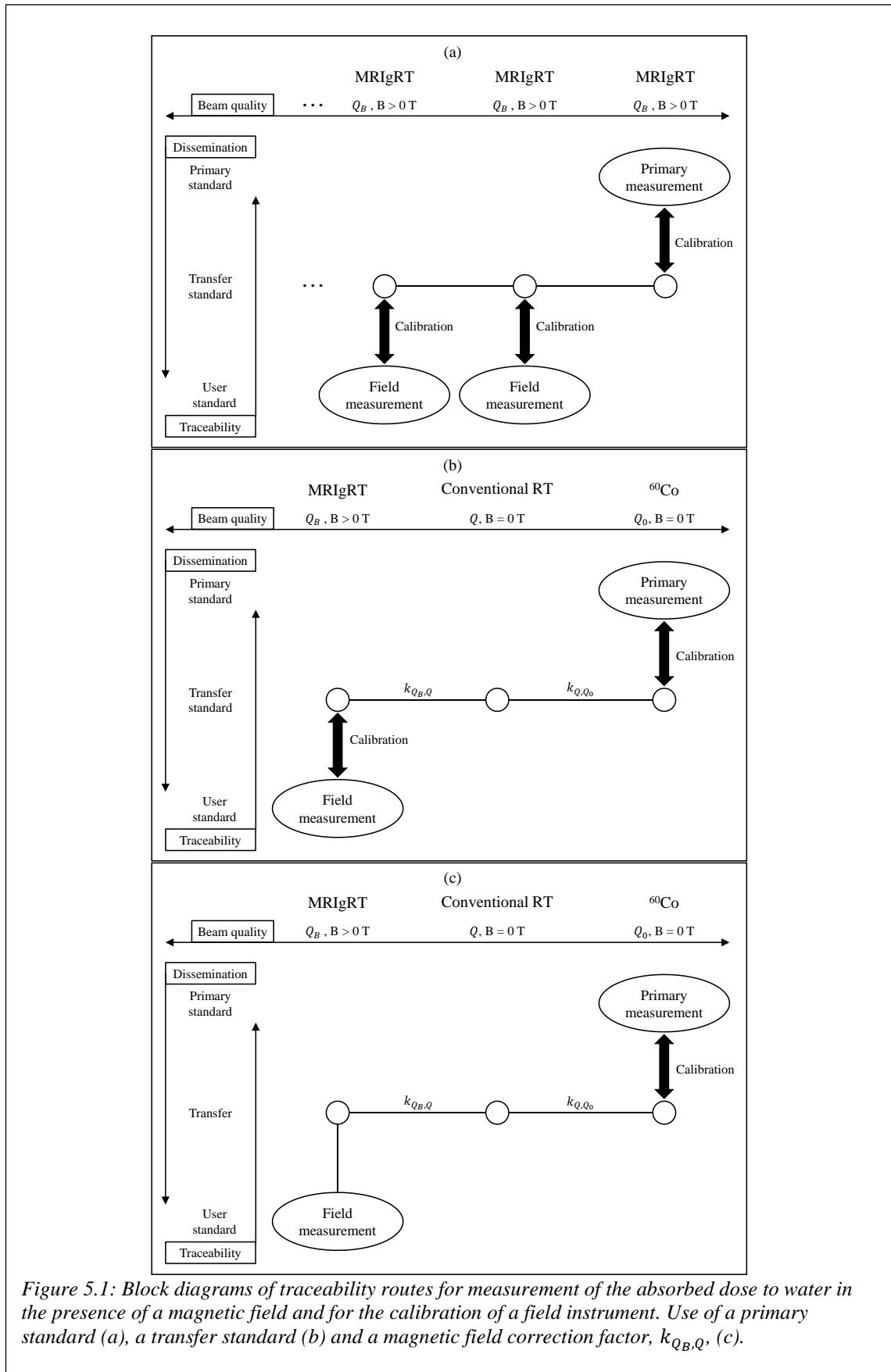
### **5.1 Introduction**

In achieving traceable dosimetry for MRIgRT, a choice must be made between:

- i. realising absorbed dose to water directly, in a beam, in the magnetic field (using a primary standard), Figure 5.1 (a), and
- ii. transferring absorbed dose to water to the beam in a magnetic field (using a transfer standard), from a realisation in a beam in zero magnetic field, Figure 5.1(b).

In both options, the user's chamber is calibrated in the user's beam, in the presence of the magnetic field. Either way, there is no need for a magnetic field correction factor for the user's chamber. However, both options require an adequate understanding of how detector response may be affected by the magnetic field, whether that detector is (i) the primary standard, whose correction factors may be magnetic field dependent, or (ii) the transfer standard, whose absorbed dose sensitivity may be magnetic field dependent. There is a third choice, if a magnetic field correction factor is available for the user's chamber, in which:

- iii. absorbed dose is realised, and the user's chamber is calibrated, in a beam with no magnetic field, Figure 5.1 (c).



Subsequent measurements in the MRIgRT system with the user's chamber are then traceable, even in option (iii) provided its magnetic field correction factor is valid.

The realisation of the physical quantity absorbed dose to water is achieved by a primary standard, which makes an absolute measurement, based on the definition of the quantity, and which is tied into the metrology infrastructure of international comparisons of equivalent standards.

Several studies suggested a formalism (O'Brien *et al.*, 2016, van Asselen *et al.*, 2018, Malkov and Rogers, 2019, Cervantes *et al.*, 2020) that can be used for the determination of the absorbed dose to water. This formalism introduces a magnetic field strength-dependent correction factor to modify the detector calibration coefficient from zero magnetic field. This factor is applicable for option (iii), which ensures traceability on the measurements of the absorbed dose to water. Data sets of correction factors are accessible from published studies, which may be integrated into existing conventional protocols for the improvement of the dosimetry in MRIgRT. Nevertheless, as pointed out in a recent review paper (de Pooter *et al.*, 2021), the performance of ionisation chambers in magnetic fields is still yet to be fully understood. It has become clear that the magnetic field enhances the sensitivity of ionisation chamber response to some aspects of design that in conventional conditions were less important. The presence of small air gaps (Hackett *et al.*, 2016, Agnew *et al.*, 2017), the dead volume (Malkov and Rogers, 2017, Pojtinger *et al.*, 2019, Cervantes *et al.*, 2020), manufacturing tolerances (Cervantes *et al.*, 2020) and intra-type variability, especially in small cavity chambers, all tend to increase the uncertainty of ionisation chamber-based dose measurements. Although values for the magnetic field correction factor have been published for various ionisation chamber types, there remains a need for more data and a better understanding, of all of these effects. As mentioned in de Pooter *et al.* (2021), early publications on dosimetry in magnetic fields have some *flaws*, as the importance of some potential effects was not yet appreciated. Correction factors from such studies must be carefully assessed before combining them with values determined more recently.

This chapter aims to demonstrate the validity of using alanine as the transfer standard in the second option, identified above as (ii), and to provide further data for the magnetic field correction factor, to support the third option (iii), to achieve traceability in dosimetry

for MRIgRT systems which is compatible with the existing standards and calibrations available for conventional radiotherapy. Both options avoid the requirement for the widespread use of primary standards directly in users' MRIgRT systems. Alanine dosimetry, as shown in Chapter 4, has only a modest sensitivity to the presence of a magnetic field at the time of irradiation, and the magnetic field dependence is less strong than for reference class ionisation chambers. The alanine is calibrated in a  $^{60}\text{Co}$  beam at zero magnetic field, its calibration coefficient converted to conventional linac by the application of a beam quality correction factor and its absorbed dose response is then corrected for the effect of the magnetic field.

My investigations reported in this chapter were carried out in the currently commercial MRIgRT systems, i.e. Elekta Unity™ and ViewRay MRIdian™, known as perpendicular systems, and in the under development Australian MRI-linac, known as an inline system. Comprehensive measurements for the determination of the absorbed dose to water in a magnetic field, including the investigation of the influence quantities on the detector signal, were performed. The alanine magnetic field correction factors, for the Elekta Unity™, the ViewRay MRIdian™ and the Australian MRI-linac beam qualities, were obtained, and the effect of the air gaps were assessed, by means of MC simulations. Two methods of obtaining the magnetic field correction factor are presented and a rigorous analysis of the uncertainties is performed. The values of Farmer-type chamber magnetic field correction factors obtained in this work are compared with values from other studies, and may be used to support and extend existing data sets of correction factors, all with the aim of reducing the uncertainty in the measurement of absorbed dose to water for MRIgRT systems.

The work in the Australian MRI-linac is not as comprehensive as in the other two commercial MRI-linac systems. However, the results for the Australian MRI-linac, will highlight differences of the ionisation chamber dose responses when compared to the standard commercial systems, where the radiation beam is orientated perpendicular to a magnetic field. The methodology followed in this work, and the results presented, may be included in potential future code of practice to support traceable reference dosimetry in inline MRI-linac systems.

## 5.2 Materials and Methods

### 5.2.1 Traceable measurements of absorbed dose to water in magnetic fields

Traceability for measurements of the absorbed dose to water is usually achieved through utilization of a transfer standard. A transfer standard is acting as a reference for calibrating secondary detectors (user detectors). The calibration is performed under reference conditions (i.e. SDD, depth in water, field size, environmental conditions, etc.), which are the same conditions under which the absolute absorbed dose to water has been realised from a primary standard. If detectors are irradiated in some other conditions, then a correction should be applied to account for the resulting change in the detector signal.

A magnetic field will affect the value of the absorbed dose to water at the reference point. The magnetic field can also affect the detector signal, and these two effects are inseparable experimentally. Instead it is necessary to determine the effect on absorbed dose to water by other means, such as MC simulation, and to combine this effect with the empirically observed change in the detector signal, to obtain the magnetic field correction factor for the detector. The result is that the corrected detector signal relates to the value absorbed dose to water at the reference point, in the presence of the magnetic field.

The dissemination of the physical quantity absorbed dose to water, in the presence of a magnetic field, requires the use of a transfer standard, whose response has been corrected for any effects of the magnetic field, with an acceptably small uncertainty. The route in option (ii) has been followed in this work, which uses alanine as a transfer detector, whose calibration is traceable to the NPL's primary standard of absorbed dose to water. A diagram of the route is adopted for alanine and is given in Figure 5.2, which shows the dissemination of absorbed dose to water from the primary standard to the end user of MRIgRT. First, alanine is calibrated against the NPL's primary standard (graphite calorimeter) at a  $^{60}\text{Co}$  beam energy, under reference conditions and zero magnetic field. A beam quality correction factor,  $k_{Q,Q_0}^{al}$ , allows the use of alanine in different energy beams (e.g. clinical linac beams in conventional RT) and a magnetic field correction factor,  $k_{Q_B,Q}^{al}$ , allows for alanine measurements of absorbed dose to water in the presence of a magnetic field (i.e. MRIgRT). The result is a calibration of the user detector (field

instrument) in terms of absorbed dose to water determined by direct comparison with the alanine detector, under reference conditions, in an MRI-linac. The use of  $k_{Q_B,Q}^{al}$  is described in section 5.2.4 and the  $k_{Q,Q_0}^{al}$  correction factor is explained in the following.

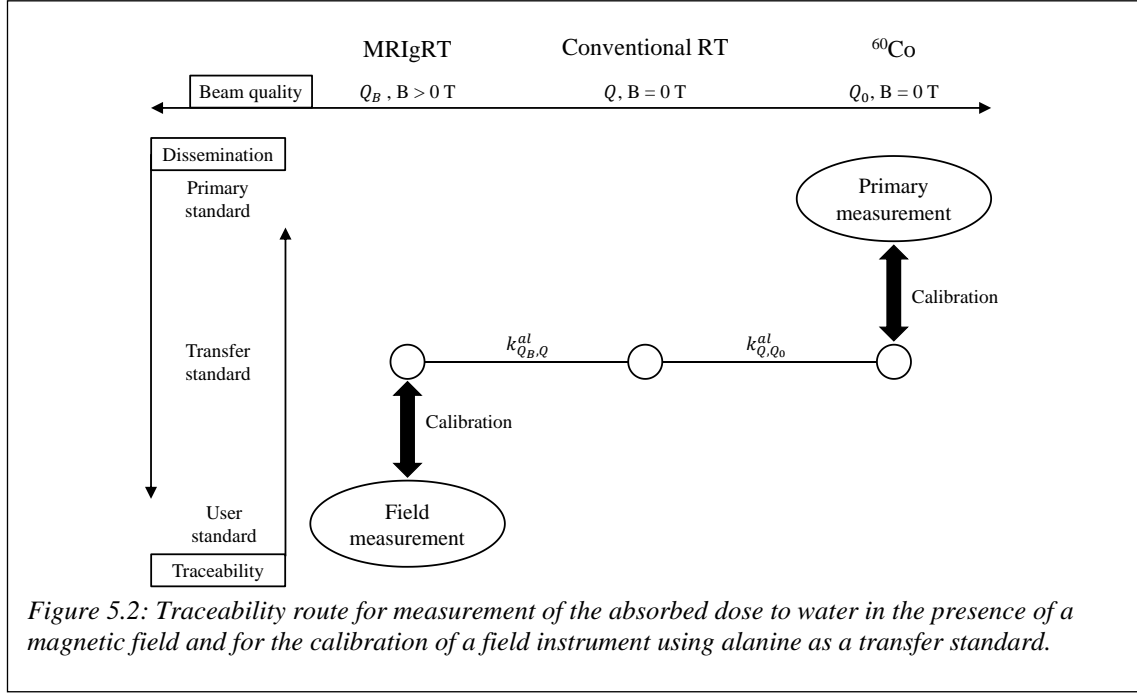


Figure 5.2: Traceability route for measurement of the absorbed dose to water in the presence of a magnetic field and for the calibration of a field instrument using alanine as a transfer standard.

The absorbed dose to water response of alanine has a weak dependence on beam quality and alanine produces a slightly smaller EPR signal for a given dose when irradiated by megavoltage x-rays compared to  $^{60}\text{Co}$  radiation. Investigation by various researchers (Bergstrand *et al.*, 2003, Sharpe, 2003, Zeng *et al.*, 2004, Bergstrand *et al.*, 2005, Anton *et al.*, 2013) reported an average reduction of alanine response up to 0.8%. A study by Thomas *et al.* (2014), which uses the alanine used in this study, has shown a correction of  $1.004 \pm 0.006$ , and this is the value applied to correct the alanine energy dependence in this work.

### 5.2.2 Ionisation chamber calibration coefficient in magnetic fields

The calibration coefficient,  $N_{D,w,Q_B}$ , in terms of absorbed dose to water,  $D_w$ , for a beam quality  $Q$ , of an ionisation chamber in the presence of a magnetic field  $B$ , is given by:

$$N_{D,w,Q_B} = \frac{D_{w,Q_B}}{M_{Q_B}} \quad (5.1)$$

where,  $M_{Q_B}$  and  $D_{w,Q_B}$  are the corrected ionisation chamber signal and the absorbed dose to water, respectively, in the presence of a magnetic field. In this study, the absorbed dose to water under reference conditions, in the presence of a magnetic field,  $D_{w,Q_B}$ , is measured by using alanine (*al*) as a transfer standard:

$$D_{w,Q_B} = M_{Q_B}^{al} \cdot k_{Q_B,Q}^{al} \cdot k_{Q,Q_0}^{al} \cdot N_{D,w,Q_0}^{al} \cdot k_{vol}^{al} \quad (5.2)$$

where,  $M_{Q_B}^{al}$  is the alanine/EPR signal in the presence of a magnetic field,  $k_{Q_B,Q}^{al}$  is the alanine magnetic field correction factor,  $k_{Q,Q_0}^{al}$  is the alanine beam quality correction factor,  $N_{D,w,Q_0}^{al}$  is the calibration coefficient of the alanine detector at a  $^{60}\text{Co}$  beam energy in the absence of a magnetic field and  $k_{vol}^{al}$  is the volume averaging correction factor on the alanine/EPR signal.

Equation (5.1) can be rewritten as follows, to consider the influence quantities that will perturb the signal from an ionisation chamber:

$$N_{D,w,Q_B} = \frac{M_{Q_B}^{al} \cdot k_{Q_B,Q}^{al} \cdot k_{Q,Q_0}^{al} \cdot N_{D,w,Q_0}^{al} \cdot k_{vol}^{al}}{M_{Q_B raw} \cdot k_{elec} \cdot k_{Tp} \cdot k_{ion} \cdot k_{vol}} \quad (5.3)$$

where:

$M_{Q_B raw}$	is the displayed chamber signal on the electrometer
$k_{elec}$	is the correction factor for the electrometer
$k_{Tp}$	is the correction factor for temperature and pressure
$k_{ion}$	is the correction factor for ion recombination
$k_{vol}$	is the correction factor for volume averaging

In this work all readings are taken with the ionisation chamber operated at negative polarity, and these are the conditions under which the resulting calibration coefficients have been used. Previous work has shown that the polarity effect is small and independent of the magnetic field (de Prez *et al.*, 2019b).

### 5.2.3 Determination of the quality correction factor for the presence of a magnetic field on a radiation detector

The magnetic field correction factor,  $k_{Q_B,Q}$ , is required for the determination of the absorbed dose to water in the presence of a magnetic field, if the detector calibration

coefficient is only available in the absence of any magnetic field. This factor corrects for the effect of the magnetic field on dose to water and also for the effect on the detector's response and is defined as:

$$k_{Q_B,Q} = \frac{N_{D,w,Q_B}}{N_{D,w,Q}} \quad (5.4)$$

where,  $N_{D,w,Q}$  is the calibration coefficient in the absence of a magnetic field:

$$N_{D,w,Q} = \frac{D_{w,Q}}{M_Q} \quad (5.5)$$

In this work,  $k_{Q_B,Q}$  was determined based on two different methods: one indirect and one direct, and are explained in the following sections.

### 5.2.3.1 Indirect determination of $k_{Q_B,Q}$

The experimental determination of the calibration coefficient at both 0 T and the MRI-linac field strength, implies that the magnetic field of the MRI scanner is off. However, the process of ramping down, and up, a superconducting magnet solely for the purpose of this measurement, is time consuming, expensive and impractical. An alternative, indirect, way to determine a calibration coefficient at zero magnetic field and at a beam quality of an MRI-linac, is described. Provided that the chamber is calibrated at a range of megavoltage x-ray beams from a conventional linac and in  $^{60}\text{Co}$ , for zero magnetic field, the calibration coefficient can be determined as a function of beam quality index, Tissue Phantom Ratio ( $\text{TPR}_{20,10}$ ), and interpolated to the value measured in the MRI-linac. Figure 5.3 shows an example of an absorbed dose to water calibration coefficient as a function of  $\text{TPR}_{20,10}$  for a Farmer-type chamber. A quadratic fit is applied and the interpolated calibration coefficients of an Elekta Unity™, a ViewRay MRIdian™ and the Australian MRI-linac beam quality are shown with a filled square, a triangle and a rhombus marker, respectively. The calibration coefficient in the presence of a magnetic field can be obtained based on the method described in section 5.2.1.

Note that  $\text{TPR}_{20,10}$  has been shown to be independent of the magnetic field (O'Brien *et al.*, 2016, van Asselen *et al.*, 2018, Begg *et al.*, 2019), and as long as the field size is 10 cm  $\times$  10 cm at the measurement plane, then  $\text{TPR}_{20,10}$  is also independent of the SDD.

Consequently, the  $TPR_{20,10}$  measured in MRI-linacs, with the magnet switched on, may be used to determine the calibration coefficient, at 100 cm SDD, at zero magnetic field as explained above. It is possible that the  $TPR_{20,10}$  is affected by the magnetic field, but from the limited measurements performed in this study, this change cannot be quantified precisely. Instead, a contribution from this influence quantity has been included in the uncertainty analysis.

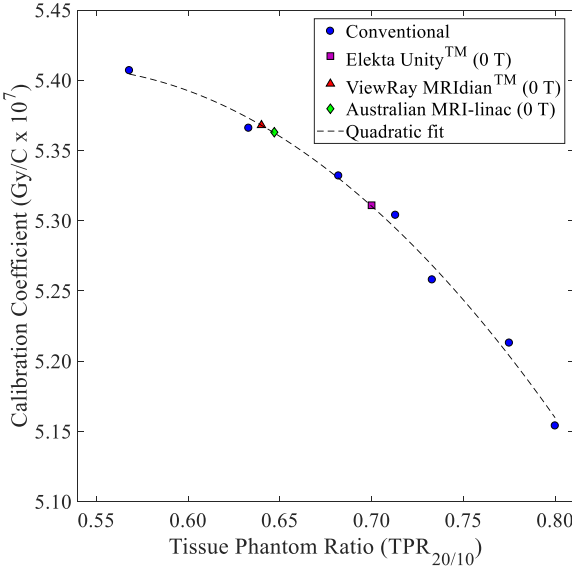


Figure 5.3: PTW 30013 Farmer-type chamber with serial number 3981 calibration coefficients as a function of beam quality ( $TPR_{20,10}$ ) in a conventional linac. The interpolated calibration coefficients of the Elekta Unity™, the ViewRay MRIdian™ and the Australian MRI-linac, at 0 T, are also presented with a filled square, triangle and rhombus markers, respectively.

### 5.2.3.2 Direct determination of $k_{Q_B,Q}$

In this work, the direct determination of  $k_{Q_B,Q}$ , was performed based on the calibration of the detectors directly in an MRI-linac environment in the presence and the absence of the magnetic field. The traceability route described in section 5.2.1 was used to obtain both calibration coefficients, but, when the magnet was switched off, the alanine magnetic field correction factor was omitted.

### 5.2.3.3 Measurements and experimental setup

I made measurements at six radiotherapy treatment centres that employ commercial MRI-linac systems (Elekta Unity™ and ViewRAY MRIdian™) and in the Australian MRI-linac facility at Liverpool, Australia (Table 5.1). Dose measurements were also performed while the constant magnetic field of the MRI scanner was off (0 T) at four of the seven

visited centres (Table 5.1). The experimental setup, for all cases, includes irradiation of Farmer-type chambers (a Physikalisch-Technische Werkstätten (PTW) type 30013 and an Ion Beam Applications (IBA) type FC65-G) and alanine dosimeter, which was acting as a transfer standard. Dose measurements were performed in water, at the machine isocentre (143.5 cm for the Elekta Unity™, 90 cm for the ViewRay MRIdian™ and 284 cm for the Australian MRI-linac), at a water-equivalent depth of 10 cm and a radiation field size of 10 cm × 10 cm at the measurement plane. The Farmer-type chamber long axis was orientated either parallel ( $\uparrow\uparrow$ )<sup>11</sup>, anti-parallel ( $\uparrow\downarrow$ )<sup>12</sup> or perpendicular ( $\perp$ )<sup>13</sup> to the magnetic field and alanine always parallel (Figure 5.4). The gantry angle was either 0° or 90° with the detector long axis always perpendicular to the radiation beam. The Australian MRI-linac was operated at an energy of 6 MV flattening filter free (FFF). The Elekta Unity™ and the ViewRay MRIdian™ at their standard energy beams, 7 MV FFF and 6 MV FFF, respectively.

*Table 5.1: The radiotherapy treatment centres that I visited, their operating MRI-linac systems and centres where measurements were performed at 0 T, while the magnet of the MRI scanner was switched off.*

Radiotherapy centre	MRI-linac system			Measurement at 0 T in MRI-linac	Measurement days $B \neq 0 T$
	Elekta Unity™ 1.5 T	ViewRAY MRIdian™ 0.35 T	Australian MRI-linac 1.0 T		
NKI	✓				2
RMH/ICR	✓			✓	2
Christie	✓			✓	3*/2†
Odense	✓			✓	1
IPC		✓		✓	1
GCUK		✓			1
Australia			✓		3

NKI: Netherlands Cancer Institute, The Netherlands

RMH/ICR: The Royal Marsden Hospital and The Institute of Cancer Research, UK

Christie: The Christie NHS Foundation Trust, UK

Odense: Odense University Hospital, Denmark

IPC: Institute Paoli Calmettes, Marseille, France

GCUK: GenesisCare, Oxford, UK

Australia: Liverpool Hospital, Australia

\*1<sup>st</sup> visit in 2017

†2<sup>nd</sup> visit in 2019

<sup>11</sup>Parallel ( $\uparrow\uparrow$ ): detector is pointing towards the front of the machine for Elekta Unity™ and towards the back of the machine for ViewRay MRIdian™.

<sup>12</sup>Anti-parallel ( $\uparrow\downarrow$ ): detector is pointing towards the back of the machine for Elekta Unity™ and towards the front of the machine for ViewRay MRIdian™.

<sup>13</sup>Perpendicular ( $\perp$ ): detector is pointing towards the bottom of the machine for both Elekta Unity™ and ViewRay MRIdian™ and towards the side of the MRI-scanner for the Australian MRI-linac.

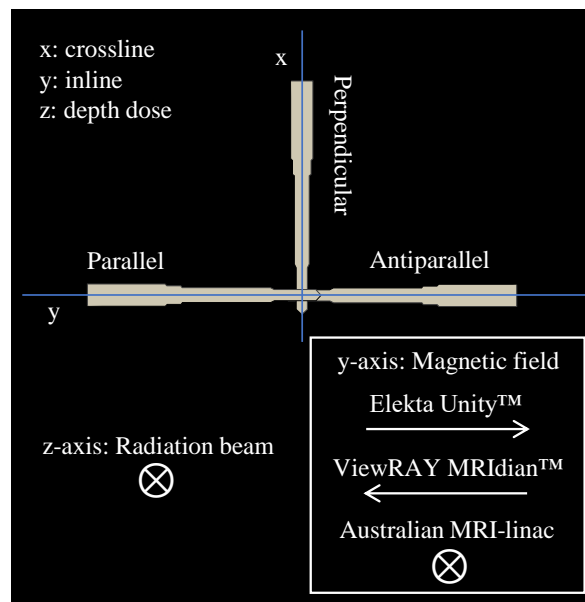


Figure 5.4: Orientations of a Farmer-type chamber and an alanine holder (shaped as a Farmer-type chamber) with respect to the magnetic field and the radiation beam. The crossline and inline profiles are across x- and y-axis, respectively, and depth dose in z-axis. Symbol  $\otimes$  indicate magnetic field pointing into the plane.

The use of seven different MRI-linacs enabled an assessment of the consistency of the methodology followed in this work. The linac-to-linac variation may also be assessed, at least for the Elekta Unity™ system, since more than two machines were visited.

Alanine pellets were loaded in a waterproof holder of PEEK material shaped like a Farmer-type ion chamber. The measurement reference point of a Farmer-type chamber is very close to the centre of the third pellet from the thimble tip of the holder. So, the average of five alanine pellets from the thimble tip of the holder was used for the measurement of the absorbed dose to water.

Measurements were performed using a water tank, which was placed on the patient couch (Figure 5.6) inside the bore of the MRI scanner. Three different water tanks were used throughout the measurements at the seven radiotherapy centres:

1. A PTW MP1 1D manual water tank was used for measurements at NKI and The RMH/ICR. A PMMA holder that could accommodate the detectors was fixed to a manual stepping mechanism enabling the crossline movement. For this setup, measurements were performed with the detector long axis orientated anti-parallel to the magnetic field and perpendicular to the radiation beam.

2. An NPL in house developed water tank (Figure 5.5), with dimensions of 33 cm width, 33 cm length and 21.5 cm height, was used for measurements at The Christie, Odense, IPC and GCUK. The water tank consists of PMMA and includes a square frame, which is constructed such that the detector long axis is orientated either parallel, anti-parallel or perpendicular to the magnetic field, by maintaining the same chamber reference point. In all three orientations the chamber long axis was perpendicular to the radiation beam.

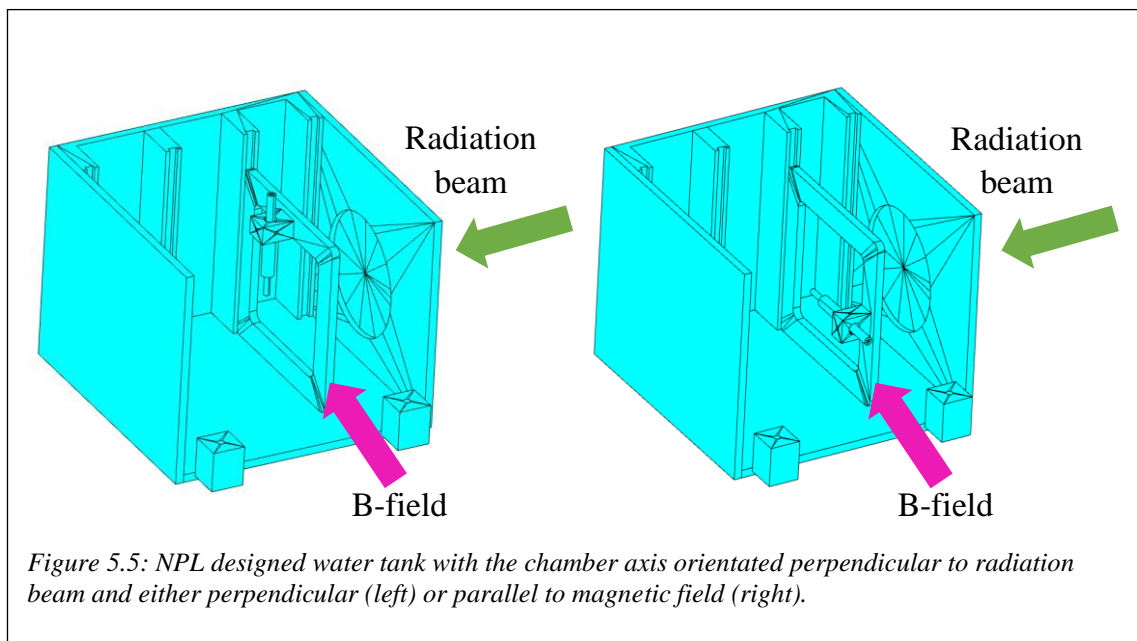


Figure 5.5: NPL designed water tank with the chamber axis orientated perpendicular to radiation beam and either perpendicular (left) or parallel to magnetic field (right).

3. A water tank (Medtec MT-DDA), with dimensions of 40 cm width, 39 cm height and 32 cm depth, was used for measurements in the Australian MRI-linac. A PMMA holder that could accommodate the detectors was fixed to a manual stepping mechanism enabling the crossline movement. Fixed PMMA rods (machined at NPL) were used to set up the detectors in the inline position at the reference depth. In this setup, the detector long axis was perpendicular to both radiation beam and magnetic field.

In the Elekta Unity™ system, the machine isocentre was defined based on the central pixel (iso-pixel) of 2D MV planar images using an electronic portal imaging device. Images were acquired with the gantry angle being 0° and 90°. The chamber cavity was aligned so that the iso-pixel, in images from both gantry angles, is shown at the measurement reference point of the chamber. In the ViewRay MRIdian™ system, a

practical isocentre was defined based on room lasers outside of the bore, which is positioned approximately 155 cm from the machine isocentre. In the Australian MRI-linac, following local practice, the water tank was set up to an isocentre indicated by the three wall-mounted room lasers and had a distance of 284 cm from the target. The water tank was aligned and located so that the reference point of the detector would coincide with the indicated isocentre.



Figure 5.6: Experimental setup on the Elekta Unity™ (left), the ViewRay MRIdian™ (middle) and the Australian MRI-linac (right).

Each Farmer-type chamber was connected to a calibrated electrometer and measurements were performed with beam deliveries of 200 MU, collecting negative charge (between -30 nC to -40 nC, depending on the MRI-linac system and chamber orientation). Before each measurement, the electrometer was warmed-up, as required, and zeroed to account for any background noise. The relative humidity was monitored to be between 20% and 70% and the collected charge was corrected to standard environmental conditions (20 °C and 1013.25 mbar). Ambient air pressure was measured by using a calibrated barometer and temperature was measured with a calibrated alcohol thermometer placed in the water tank.

A correction for the incomplete collection of charge due to ion recombination,  $k_{ion}$ , was measured and applied, for all three chamber orientations with respect to the magnetic field. By assuming that the ion recombination is less than 3%, the two-voltage method (Boag and Currant, 1980) was a good approximation (within 0.1%) to determine  $k_{ion}$  (Andreo *et al.*, 2000). To further validate this method, Jaffé plots for a PTW 30013 and an IBA FC65-G chamber were performed directly in an Elekta Unity™ at 1.5 T.

Correction factors due to volume averaging,  $k_{vol}$ , for alanine and Farmer-type chambers were determined, considering the dimensions of their collecting volume and the FFF

beams of the MRI-linac systems. Correction factors were defined based on TRS 483 (Palmans *et al.*, 2017).

The measurement sequence includes a set of five irradiations for each Farmer-type chamber. The readings of each set were examined to confirm no trend and that the standard deviation of the mean was less than 0.05%. Several alanine dosimeters were irradiated to a nominal dose of 20 Gy in between the chamber irradiations. In the commercial MRI-linacs, the behaviour of the linac output was monitored by including a chamber (acting as a monitor) several times in between the detectors irradiation and always in one orientation. Any deviation that occurred was used to correct the absorbed dose to water, measured with alanine, at the chamber irradiation time. In the Australian MRI-linac, due to the non-stability of the linac output, an Exradin type A1SL ionisation chamber was used as an external monitor. The chamber was located outside of the magnetic field, between the target and the multileaf collimator, for all the measurement days.

The beam quality index was based on TPR<sub>20,10</sub> measurements in water. As recommended by TRS 398 (Andreo *et al.*, 2000) water-equivalent depths of 10 g/cm<sup>2</sup> and 20 g/cm<sup>2</sup> were used, with the source-to-chamber distance being fixed and always at one orientation. Chamber readings were corrected for ion recombination and to standard air density.

The alanine dosimetry system, as well as the PTW 30013 and IBA FC65-G Farmer-type chambers, used in this study were calibrated at NPL based on the Code of Practice for high-energy photon therapy dosimetry (Lillicrap *et al.*, 1990, Eaton *et al.*, 2020). The calibration was performed in a conventional Elekta Synergy linac (zero magnetic field), for a range of megavoltage x-ray beams between 4 MV and 18 MV, and in <sup>60</sup>Co radiation, collecting negative charge (for the chambers), traceable to the NPL primary standard of absorbed dose to water. The PTW 30013 and IBA FC65-G Farmer-type chambers calibration coefficients obtained at NPL, together with those of an MRI-linac, could indirectly determine magnetic field correction factors, as explained in section 5.2.3.1.

#### **5.2.4 Alanine magnetic field correction factor, $k_{Q_B,Q}^{al}$**

The magnetic field affects the determination of absorbed dose to water using alanine in multiple ways: it modifies the dose to water, but it also modifies the absorbed dose

sensitivity to the alanine itself. By considering the intrinsic sensitivity of the alanine, i.e. its response relative to the absorbed dose to alanine, rather than to the absorbed dose to water, the alanine sensitivity was shown in Chapter 4 to be independent of the beam energy. This alanine intrinsic sensitivity, previously determined, was combined with Monte Carlo simulations of absorbed dose to water and of absorbed dose to alanine for the experimental setups used in the present study, to obtain the required magnetic field correction factor for alanine,  $k_{Q_B,Q}^{al}$ .

In perpendicular orientation of the magnetic field to the energy beam, the effect of the magnetic field on the absorbed dose, to water and to alanine, depends on the field strength and on the beam energy. Therefore, MC simulations were performed to calculate the absorbed dose, to water and to alanine, with and without a magnetic field for the beam energies and magnetic field strengths of the Elekta Unity™ and the ViewRay MRIdian™ systems. Simulations were also performed for the uncertainty estimation due to the air gaps associated with the alanine holder. Detailed explanation on the MC simulations and the transport parameters (i.e. models of the alanine pellet and its holder, ECUT, PCUT, EM ESTEPE, etc.) can be found in Chapter 4. The sections 5.2.4.1 and 5.2.4.2 describe the MC simulations of the beam models of the Elekta Unity™ and the ViewRay MRIdian™ systems and the experimental setup performed to validate them. The cavity and the BEAMnrc user codes, that forms part of the EGSnrc code system (Kawrakow I *et al.*, 2011), were used for the MC simulations in this work.

In parallel orientation of the magnetic field to the energy beam, the absorbed dose to water at the reference point is magnetic field independent, provided that there is a lateral electron equilibrium (Bielajew, 1993), and energy dependent. Therefore, for the Australian MRI-linac the ratio of  $D_{w,Q_B}/D_{w,Q}$  is unity. The ratio of  $D_{al,Q}/D_{al,Q_B}$  is, however, magnetic field and energy dependent, as the irradiation is performed in heterogeneous medium, where the full alanine holder is included. In this case, the air gaps inside the holder will affect the dose to the alanine pellets. This effect is considered by performing MC calculations of the absorbed doses to alanine, with 0 T and 1 T field strengths, at three different beam energies of  $^{60}\text{Co}$ , 6 MV and 8 MV. Simulations were based on the setup as described in Chapter 4 (section 4.3.4), but with the magnetic field parallel to the radiation beam (which replicate the configuration of the Australian MRI-

linac). The  $D_{al,Q}/D_{al,Q_B}$  ratio can be determined as a function of TPR<sub>20,10</sub> of the three beam energies and interpolated to the value measured in the Australian MRI-linac. This method was followed as information and data were not available to perform simulations directly with the Australian MRI-linac beam energy.

The uncertainty due to the air gaps, in the inline MRI-linac, is estimated based on the average uncertainties, as defined in Chapter 4 (section 4.3.8.2), of the three energy beams (<sup>60</sup>Co, 6 MV and 8 MV) and for a magnetic field strength of 1 T, which configure perpendicular orientation to the energy beam. Given the lack of information on the Australian MRI-linac beam model, this is the best approach, in which the uncertainty, if not similar, might be overestimated, as the ERE will have higher impact on the dose to alanine in perpendicular compared to the parallel orientation of the energy beam to the magnetic field.

#### ***5.2.4.1 MC simulations of the Elekta Unity™ and the ViewRay MRIdian™ MRI-linac beam models***

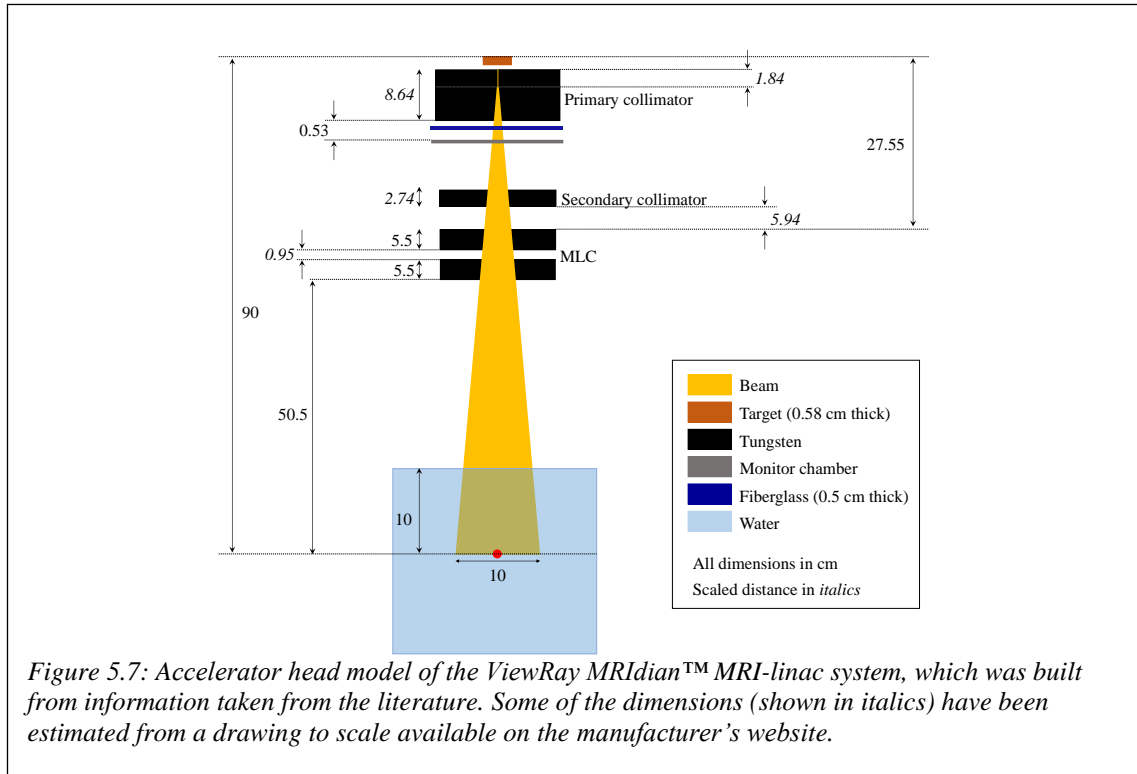
An accurate beam model will determine the quality and the accuracy of the calculated alanine magnetic field correction factor, which is needed for the determination of the absorbed dose in the presence of a magnetic field. Phase space data of the Elekta Unity™ were provided from Elekta. The beam was modelled to generate phase space files at a distance plane of 130.5 cm from the source. This provides a 10 cm × 10 cm radiation field at the isocentre plane (143.5 cm).

An accelerator head model of the ViewRay MRIdian™ was built using the BEAMnrc user code. Taking the best approach, the model was constructed by using dimensional details and material specifications taken from the literature (Mutic and Dempsey, 2014, Kluter, 2019) and information found on the manufacturer's website. The model is shown in Figure 5.7. Important features which are critical for an effective beam model are:

- the distance from the source to isocentre, 90 cm, and the distance from the isocentre to the distal side of the multi-leaf collimator (MLC), 50.5 cm
- the double-stack and double-focus MLC (without additional jaws) which comprises of 34 leaf pairs on the upper stack and 35 leaf pairs on the lower stack, with each leaf having a physical width and height of 0.4 cm and 5.5 cm, respectively

- the minimum,  $0.2\text{ cm} \times 0.415\text{ cm}$ , and the maximum,  $24.1\text{ cm} \times 27.4\text{ cm}$ , radiation field sizes at the isocentre

There was no need to model any of the MRI components (i.e. cryostat, gradient coil, etc.), as the beam is passing through the 28 cm gap, between the two superconducting magnet halves, and only attenuated by a 0.5 cm thick connecting fiberglass panel (Kluter, 2019).



On simulating the ViewRay MRIidian™ beam, the BEAMnrc model was compiled as a shared library and used as a direct input for dose calculations in the cavity user code.

The elliptical beam with gaussian distribution in x and y (ISOURCE = 19) was used to simulate the primary electron beam. The ellipse was specified by the full width at half maxima (FWHM's) of the energy distributions in x ( $= 0.11\text{ cm}$ ) and y ( $= 0.11\text{ cm}$ ). An electron energy spectrum from an in house 6 MV FFF beam model was used for the simulations. The energy tuning was performed by simulating a  $10\text{ cm} \times 10\text{ cm}$  radiation field using the electron spectrum with varying mean energies in the range of 5.3 MeV to 7.7 MeV in steps of 0.4 MeV.

#### 5.2.4.2 Validation of the virtual beams

The phase space file provided by Elekta to represent the beam from a Unity™ MRI-linac, and the beam model developed to represent ViewRay MRIdian™, were validated by comparing MC calculated lateral and depth dose profiles with measured data (see Figure 5.4 for the direction of the profiles with respect to the magnetic field and the radiation beam). The experimental set up involves a scan of a 10 cm × 10 cm radiation field, in a water tank, using a PTW 60019 microdiamond detector. The detector was positioned vertically (parallel to the radiation beam), the source-to-surface distance was 133.5 cm (Elekta Unity™) and 80 cm (ViewRay MRIdian™) and the inline and crossline profiles at a mass depth of 10 g/cm<sup>2</sup> were acquired. For the Elekta Unity™ the measurements were performed in Odense and for the ViewRay MRIdian™ data were provided from GCUK.

### 5.3 Results

#### 5.3.1 Alanine magnetic field correction factor, $k_{Q_B,Q}^{al}$

Table 5.2, contains results for the  $F_{Q_B,Q}$  values, the MC calculated ratios of absorbed dose to water (with and without magnetic field) and absorbed dose to alanine (without and with magnetic field), and the alanine magnetic field correction factors,  $k_{Q_B,Q}^{al}$ , for the three MRI-linac systems. The combined standard uncertainties on the  $k_{Q_B,Q}^{al}$  values include the uncertainty due to the air gaps.

The validation of the virtual beams and the MC simulations performed for the uncertainty estimation due to the air gaps, are described in sections 5.3.1.1 to 5.3.1.3.

##### 5.3.1.1 Validation of the virtual beams

The Elekta Unity™ phase space file and the ViewRay MRIdian™ beam model were validated by comparing MC calculated lateral (inline and crossline) and depth dose profiles with measured data, as shown in Figure 5.8. To enable a comparison in terms of dose differences the MC calculated data were interpolated to the measured depth and off-axis distance points using piecewise cubic Hermite polynomial functions (which preserves the shape of the data). The measured and the MC fit lateral dose profiles were normalised to the central axis and the depth dose profiles at 10 cm depth. In the right y-

axis of the plots in Figure 5.8Figure 5.8, the percentage dose difference relative at the maximum dose of the measured profiles is shown.

*Table 5.2: Alanine magnetic field correction factor,  $k_{Q_B,Q}^{al}$ , for the Elekta Unity™, the ViewRay MRIdian™ and the Australian MRI-linac systems together with the alanine relative intrinsic sensitivity,  $F_{Q_B,Q}$ , and the calculated ratios of absorbed dose, to water (with and without magnetic field) and absorbed dose to alanine (without and with magnetic field). The uncertainties shown are standard uncertainties ( $k = 1$ ).*

MRI-linac system	$F_{Q_B,Q}$	$D_{w,Q_B}/D_{w,Q}$	$D_{al,Q}/D_{al,Q_B}$	$k_{Q_B,Q}^{al}$
Elekta Unity™	$1.0071 \pm 0.0008$	$0.9950 \pm 0.0012$	$1.0077 \pm 0.0017$	$0.9957 \pm 0.0059$
ViewRay MRIdian™	$1.0016 \pm 0.0002$	$1.0001 \pm 0.0012$	$1.0012 \pm 0.0017$	$0.9997 \pm 0.0028$
Australian MRI-linac	$1.0047 \pm 0.0005$	1.0000	$1.0018 \pm 0.0017$	$0.9971 \pm 0.0032$

For the Elekta Unity™, the dose agreement at each point is generally within  $\pm 1\%$ , except two regions confined to the steepest parts of the penumbra, where the dose difference varied over a range of 5%. It should be possible to substantially reduce these differences by making a very small adjustment to the collimator setting, however, for the present investigation in which the reference dose measurements are all close to the central axis, this adjustment is not essential.

For fine tuning the energy on the ViewRay MRIdian™ beam model, depth dose profiles were calculated by MC simulations, for various electron energies in the range from 5.3 MeV to 7.7 MeV. The electron energy was chosen to optimise the agreement between MC calculated and measured normalised depth doses, based on the statistics of the absolute value of their difference. The mean and standard deviation are shown in Table 5.3 for the seven energies simulated, and 6.5 MeV is the energy which produces the best agreement. Figure 5.8 shows MC calculated and measured lateral and depth dose profiles of the ViewRay MRIdian™ with this optimum electron energy of 6.5 MeV. There is a small discrepancy outside the primary beam, beyond the steep part of the penumbra, between the calculated and the measured lateral dose profiles. This might be due to an incompleteness (i.e. missing components) in the linac geometry used to generate beams for this study. Another aspect of the observed difference in the inline profiles is a lack of symmetry, predominantly of the measured profile (the MC simulation is symmetric, and any asymmetry should only be the result of random uncertainty). Nevertheless, restricting

the comparison in the area where the alanine simulations take place (within  $\pm 4.5$  cm from the central axis), the calculated inline and crossline profile data agree very well with measurements with the dose agreement at each point being less than  $\pm 1.4\%$ . Note that practical limitations in the experimental setup meant that the crossline profile could only be accurately measured up to approximately 5 mm beyond the central axis.

*Table 5.3: Statistics of the absolute value of the difference between the measured and MC normalised depth doses of the different electron energies, for the ViewRay MRIdian™.*

Electron energy (MeV)	Absolute difference in normalised depth dose	
	Standard deviation	Mean
5.3	0.0293	0.0230
5.7	0.0189	0.0135
6.1	0.0107	0.0073
6.5	0.0088	0.0055
6.9	0.0145	0.0124
7.3	0.0209	0.0185
7.7	0.0285	0.0254

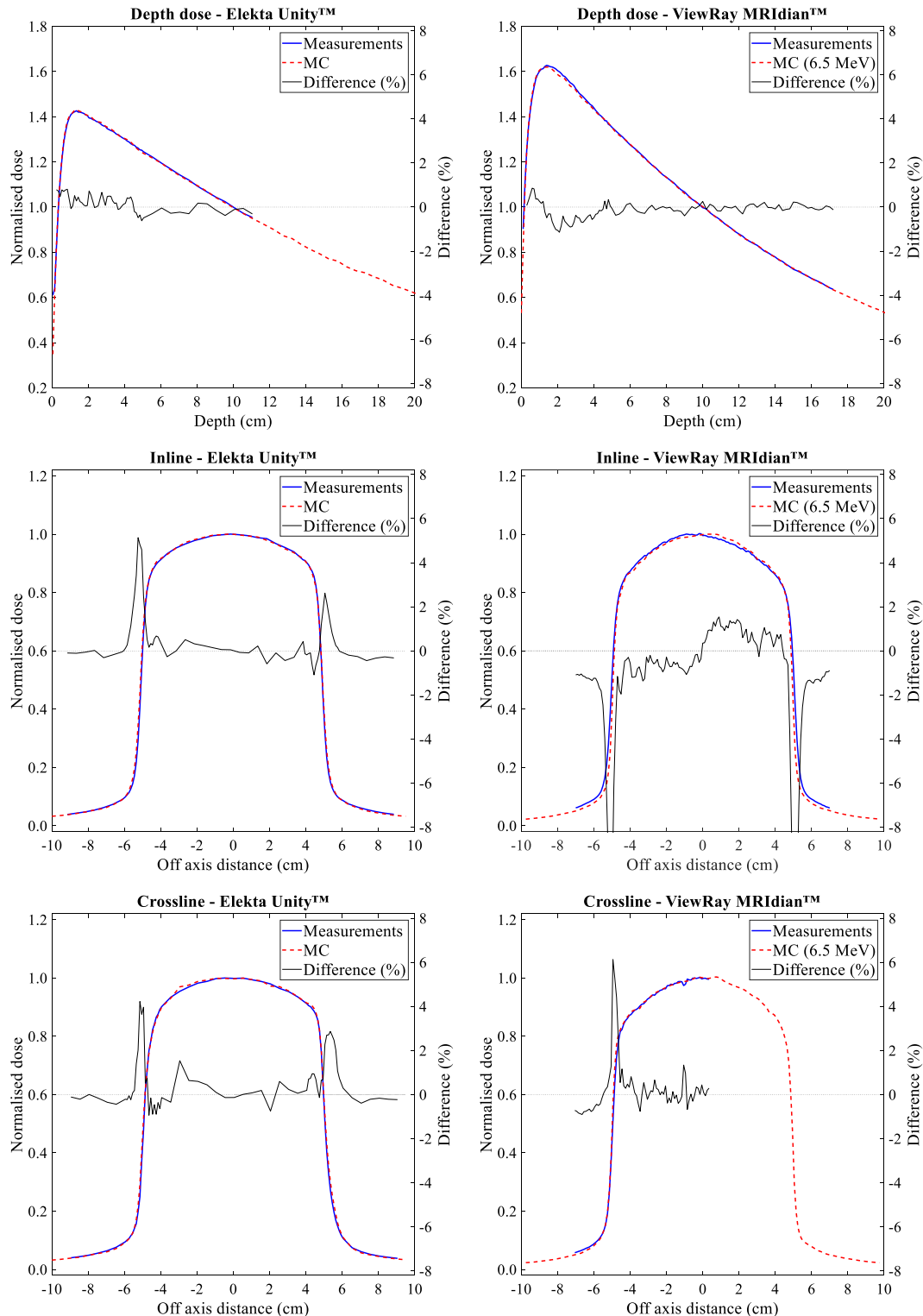
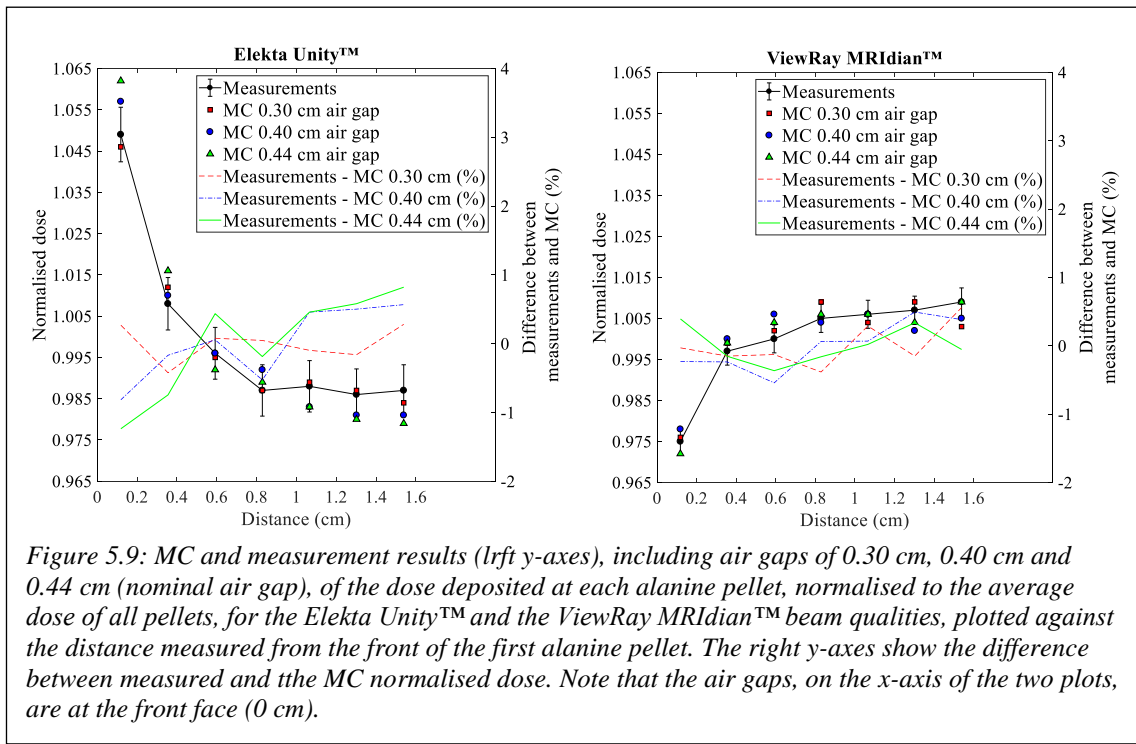


*Figure 5.8: Measured and MC calculated lateral dose profiles (inline and crossline) and depth doses of the Elekta Unity™ and the ViewRay MRIdian™ (electron energy of 6.5 MeV) radiation beams. The percentage dose difference relative at the maximum dose of the measured profiles is shown in the right y-axis of each plot. Note that for the benefit of enhancing the percentage dose difference on the right y-axis of each plot, the scale is set to  $\pm 8\%$ . The value of the Inline - ViewRay MRIdian™ reaches down to  $-16\%$ .*

### 5.3.1.2 Alanine dosimeter model and experimental setup validation in MRI-linacs

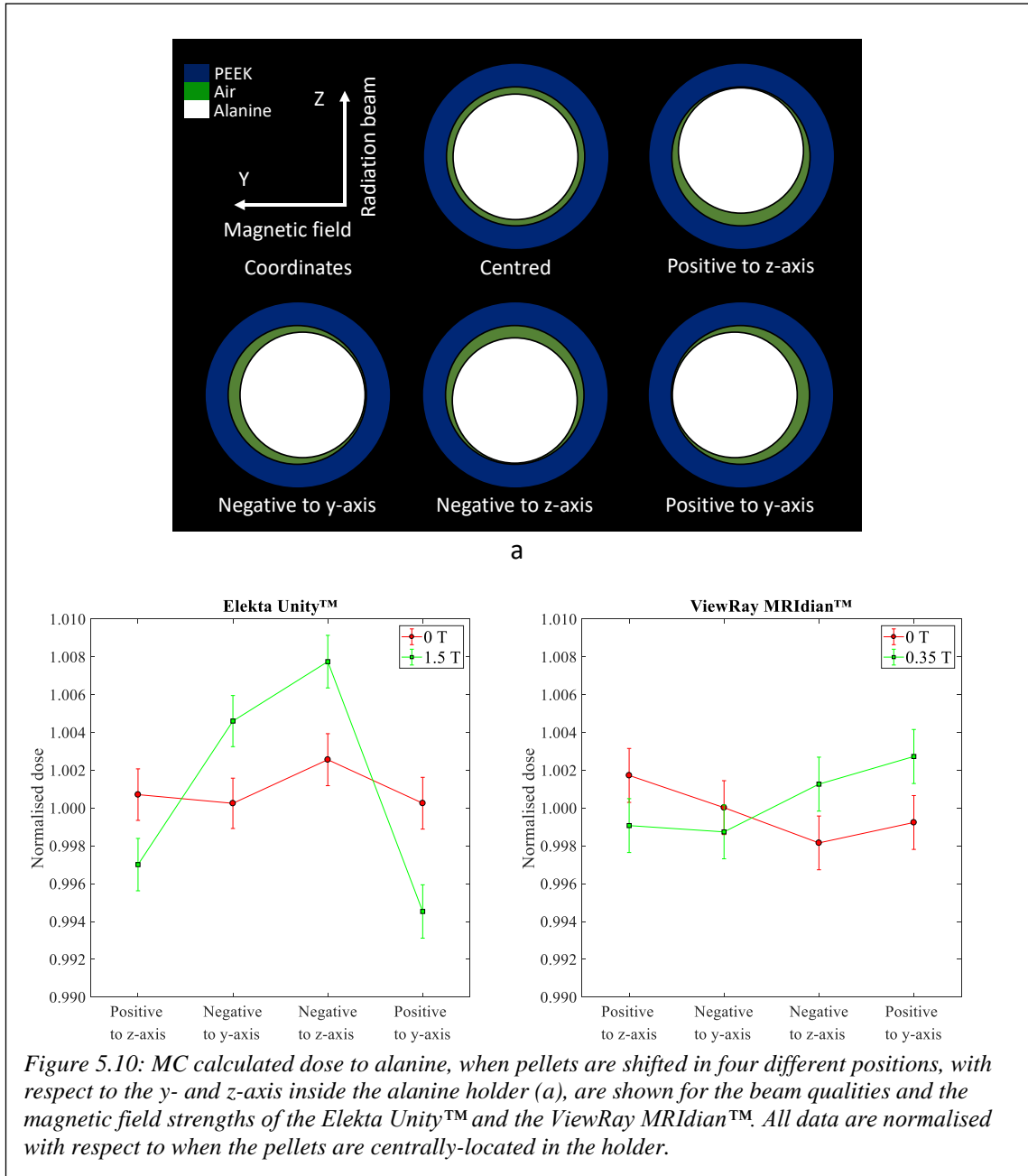
The validation of the experimental setup model for Elekta Unity™ and ViewRay MRIdian™ systems with experiments was performed in a similar way as was performed in Chapter 4. Briefly, the alanine holder was partially loaded with pellets creating a nominal air gap of 0.44 cm between the stem and the first pellet, see Figure 4.12. In both Elekta Unity™ and ViewRay MRIdian™ systems, the alanine was setup perpendicular to the magnetic field and the radiation beam, at the machine isocentre and at a depth of 10 cm. MC simulations include two additional models with air gaps of 0.30 cm and 0.40 cm to consider air gap variation. Figure 5.9 shows the MC results, from the three different air gaps, and the measurement results of the dose deposited at each alanine pellet. Data are normalised to the average dose of all pellets for each case. The same plot, on the right y-axes, shows differences between the measured and the MC normalised doses for the three air gaps. The MC calculated data points of the three models agree very well with the measured points (always with one of the points of the three models), within the measurement uncertainties, in both MRI-linac systems. From the figures, an opposite effect is observed between the two MRI-linac systems, which is related to the direction of the magnetic field in the two systems. The magnitude of the effect is smaller in the ViewRay MRIdian™ due to the lower magnetic field strength compared to the Elekta Unity™.



### ***5.3.1.3 Effect of air gaps on alanine response***

MC simulations were performed to investigate the effect of the air gaps formed due to the unknown spatial distribution of the pellets in the holder. This effect will be included as a component in the uncertainty budget. Similar simulations were also performed in Chapter 4, but here simulations include beam energies of the Elekta Unity™ and the ViewRay MRIdian™ systems and reflect the experimental setup: the holder orientated parallel to the magnetic field and perpendicular to the radiation beam. Figure 5.10 shows the MC calculated dose to alanine for the two MRI-linac systems, with and without magnetic field, when pellets are shifted in the y- and z-axis inside the holder, as shown in Figure 5.10 (a). Data are normalised to the dose of the pellets centrally located in the holder. The RMS variation of the four different distributions of the alanine pellets inside the holder was found to be 0.55% and 0.17% for the Elekta Unity™ and the ViewRay MRIdian™, respectively.

For the Australian MRI-linac the uncertainty was estimated to be 0.27%. This is based on the average uncertainties of the three energy beams ( $^{60}\text{Co}$ , 6 MV and 8 MV), as described in section 4.3.8.2, at 1 T.



### 5.3.2 Output stability of MRI-linacs

The output stability and setup repeatability of the three MRI-Linac systems are presented in Figure 5.11, which shows the normalised chamber signals to the signal of the first measurement. Data are shown for the chamber irradiated in the Elekta Unity™, the ViewRay MRIdian™ and the Australian MRI-linac. In the latter, figure includes data for the field chamber, the external monitor chamber and the ratio between the field and the external monitor. Data are shown for a period of the visited days at each centre (see Table 5.1) and their distribution is displayed in a form of box plots.

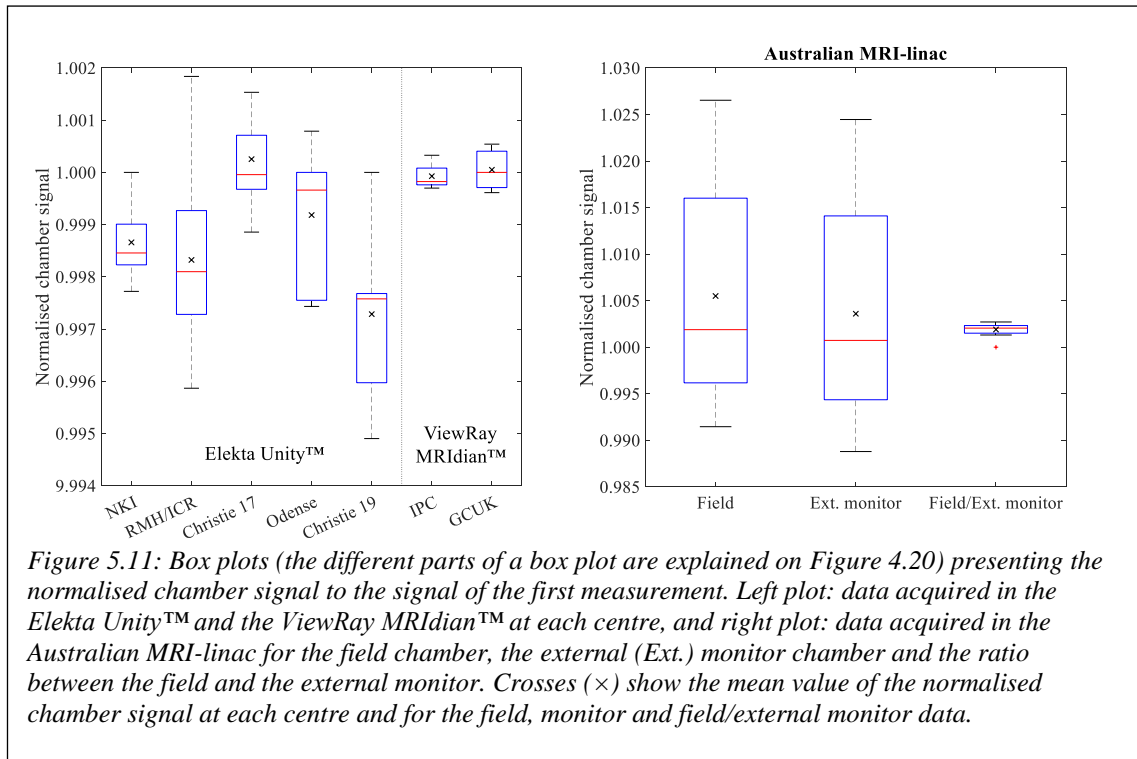


*Figure 5.11: Box plots (the different parts of a box plot are explained on Figure 4.20) presenting the normalised chamber signal to the signal of the first measurement. Left plot: data acquired in the Elekta Unity™ and the ViewRay MRIdian™ at each centre, and right plot: data acquired in the Australian MRI-linac for the field chamber, the external (Ext.) monitor chamber and the ratio between the field and the external monitor. Crosses ( $\times$ ) show the mean value of the normalised chamber signal at each centre and for the field, monitor and field/external monitor data.*

### 5.3.3 TPR<sub>20,10</sub> of MRI-linacs

The measured beam quality index values, based on TPR<sub>20,10</sub>, for all MRI-linacs are shown in Table 5.4, which also includes TPR<sub>20,10</sub> values for 0 T. On average, TPR<sub>20,10</sub> for the Elekta Unity™ machines was found to be  $0.700 \pm 0.002$  and  $0.697 \pm 0.003$  for 0 T and 1.5 T, respectively. The TPR<sub>20,10</sub> of the ViewRay MRIdian™ was 0.645 for 0 T and 0.642 for 0.35 T (average of two values).

In the Elekta Unity™ and the ViewRay MRIdian™, there is a difference of 0.003 between the TPR<sub>20,10</sub> values without and with a magnetic field. Based on the Elekta Unity™ measurements, TPR<sub>20,10</sub> can vary up to 0.5% between different machines of the same type at 1.5 T. This variation will also include the setup repeatability on TPR<sub>20,10</sub> measurements. In this study, any difference observed between the TPR<sub>20,10</sub> without and with a magnetic field, may be within the variation of the TPR<sub>20,10</sub> between the different MRI-linac machines.

*Table 5.4: Measured  $TPR_{20,10}$  of the Elekta Unity™ and the ViewRay MRIdian™ (without and with magnetic fields) and the Australian MRI-linac.*

Radiotherapy centres	Elekta Unity™		ViewRay MRIdian™		Australian MRI-linac
	0 T	1.5 T	0 T	0.35 T	1 T
NKI (Dec 16)		0.694			
RMH (Mar 17)	0.699	0.694			
RMH (May 17)	0.699				
Christie (Sep 17)		0.699			
Christie (Oct 18)	0.700				
Odense (Jun 18)	0.702	0.701			
Christie (Mar 19)		0.698			
IPC (Sep 18)			0.645		
IPC (May. 19)				0.640	
GCUK (Dec 19)				0.643	
Australia (Jun 17)					0.647

### 5.3.4 Ion recombination correction factors, $k_{ion}$

The impact of the magnetic field on the ion recombination correction is typically small and is indicated in Figure 5.12, which shows the ratio of the correction with, and without, the magnetic field. Results are shown for the chambers at the users' normal operating voltages: the ratio is generally slightly larger than unity, but with a noticeable intra-type variation for both MRI-linac systems. Data include results from two different chamber orientations with respect to the magnetic field, parallel and perpendicular. The correction factors are the results of measurements from one machine for each system (Odense for Elekta Unity™ and IPC for ViewRay MRIdian™), when the constant magnetic field was off and on. Uncertainties represent the combined standard uncertainty of the collected charge at the normal operating polarising voltage and the collected charge at a lower voltage. The two-voltage technique used in this study was validated by performing Jaffé plots for a PTW 30013 and an IBA FC65-G in an Elekta Unity™ at 1.5 T. A linear dependence of  $1/M$  on  $1/V$ , for both chambers is demonstrated in Figure 5.13.

It was not possible to perform  $k_{ion}$  measurements at 0 T in the Australian MRI-linac. For 1 T the  $k_{ion}$  values of three Farmer-type ionisation chambers are shown in Table 5.5.

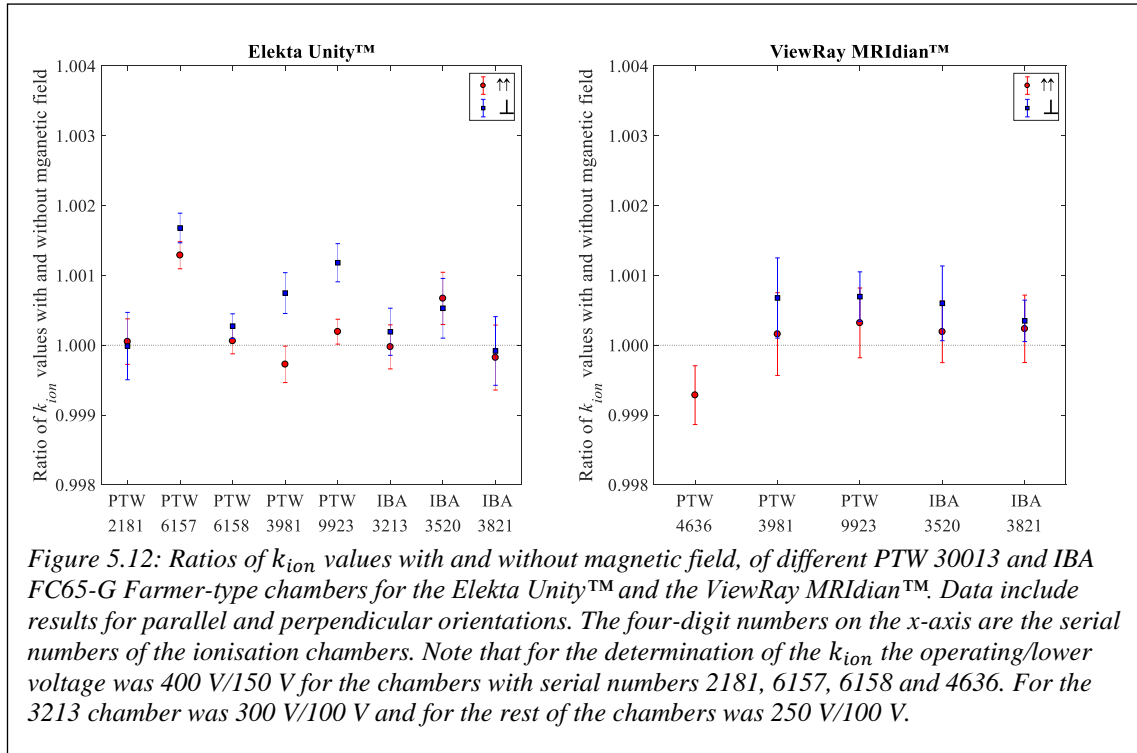
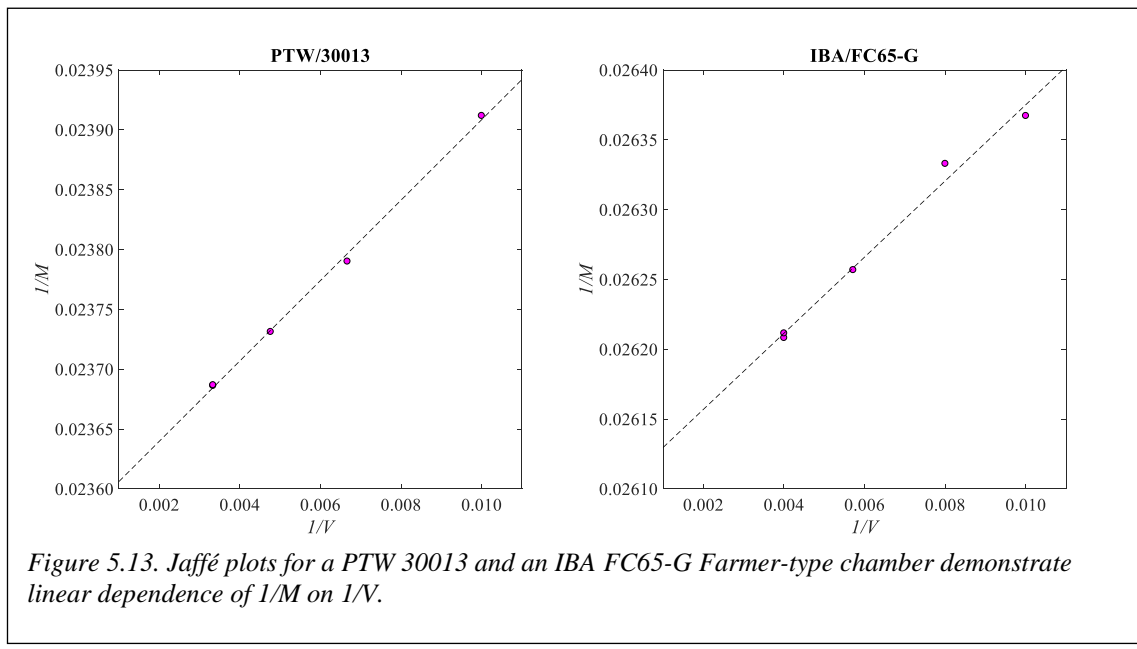


**Table 5.5:** Ion recombination correction factors,  $k_{ion}$ , of three Farmer-type ionisation chambers measured in the Australian MRI-linac at 1 T.

Chamber (type/sn)	Voltage (operating/lower)	$k_{ion}$ at 1 T
PTW/03981	250 V/100 V	$1.0013 \pm 0.0007$
IBA/3520	250 V/100 V	$1.0017 \pm 0.0006$
IBA/819	300 V/100 V	$1.0012 \pm 0.0004$



### 5.3.5 Volume averaging correction factors, $k_{vol}$

Figure 5.14 shows the measured lateral inline profiles of the Elekta Unity™, the ViewRay MRIdian™ and the Australian MRI-linac of a 10 cm × 10 cm radiation field at the measurement plane. In the two commercial systems, profiles were acquired with a PTW 60019 microdiamond detector, as described in section 5.2.4.2, while in the Australian MRI-linac an EBT3 film was used and placed at a depth of 10 cm of water-equivalent solid water. Profiles are focused in an area of ±3.5 cm to show the non-uniformity of the three profiles, where quadratic fits (solid lines) are also applied. The collecting volume of the alanine and the Farmer-type chamber, on their long axis, is also depicted and is indicating how the dose is distributed along their collecting volume. Following recommendations from TRS 483 (Palmans *et al.*, 2017),  $k_{vol}$  values for both alanine and Farmer-type chamber, at each MRI-linac, were determined using the line approximation and are shown on Table 5.6. The type B standard uncertainty for all values was estimated to be 0.05%.

A study by de Prez *et al.* (2019b) found a difference of 0.02% on the  $k_{vol}$  values with and without a magnetic field and no significant difference between the  $k_{vol}$  values determined using the inline and the crossline profiles, in a magnetic field (Elekta Unity™). Therefore, where applicable, the present study used the  $k_{vol}$  values as obtained in Table 5.6 to correct the alanine/EPR and Farmer-type chamber signals.

Table 5.6:  $k_{vol}$  values for alanine and Farmer-type chamber, at each MRI-linac. The uncertainty for all values was estimated to be 0.05%.

MRI-linac system	$k_{vol}$	
	Alanine	Farmer-type chamber
Elekta Unity™	1.0005	1.0019
ViewRay MRIdian™	1.0007	1.0028
Australian MRI-linac	1.0001	1.0003

### 5.3.6 Reference dosimetry measurements and calibration coefficients of Farmer-type chambers

Reference dosimetry measurements were performed at the visited centres (Table 5.1) using the traceability route developed in this work. Absorbed dose to water was measured with alanine and the relative standard deviation of the pellet dose values was found, on

average, to be 0.50% and 0.29% for Elekta Unity™ and ViewRay MRIdian™ machines, respectively. For the Australian MRI-linac the variation was 0.45%. The difference in repeatability between the three machine types is in accord with the magnetic field strength dependence of the air gap uncertainty reported on Chapter 4.

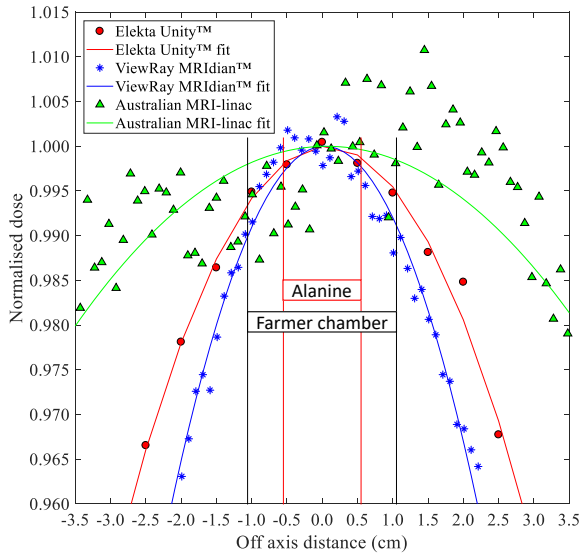


*Figure 5.14: Measured lateral inline profiles of the Elekta Unity™, the ViewRay MRIdian™ and the Australian MRI-linac of a 10 cm × 10 cm radiation field at the measurement plane (focus in an area of ±3.5 cm). A fit between the measured data points is applied and the collecting volume of the alanine and the Farmer-type chamber, on their long axis, is also depicted.*

Figure 5.15 shows the calibration coefficients of two Farmer-type chambers, a PTW 30013 (sn 3981) and an IBA FC65-G (sn 3520). These two chambers were calibrated at different Elekta Unity™ machines at three (or more) different centres, for the three orientations. Differences between the calibration coefficients, for each chamber orientation, are consistent within the standard uncertainties shown. Each calibration coefficient is plotted with its standard uncertainty, but the contributions to uncertainty that would be correlated have been removed for the purpose of this comparison. Excluding correlations in this way reduces the combined standard uncertainty for each calibration coefficient from 1.06% to 0.58%. Results also indicate the degree of consistency of the reference dosimetry measurements performed in this work.

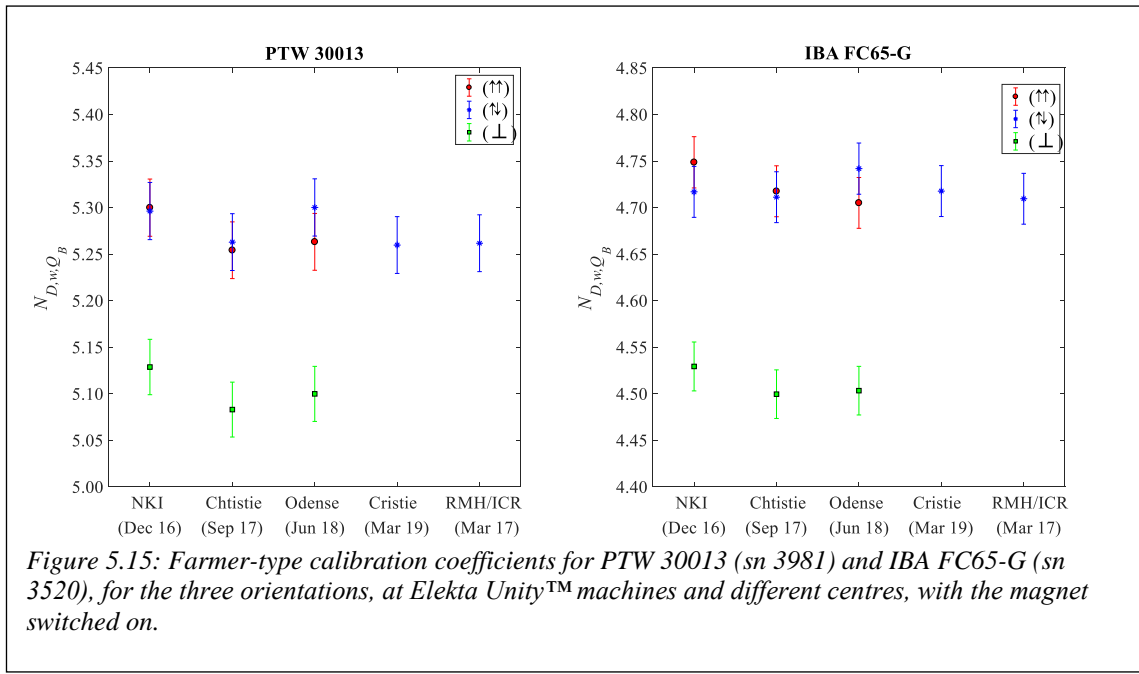


Figure 5.15: Farmer-type calibration coefficients for PTW 30013 (sn 3981) and IBA FC65-G (sn 3520), for the three orientations, at Elekta Unity™ machines and different centres, with the magnet switched on.

### 5.3.7 Farmer-type chamber magnetic field correction factors, $k_{Q_B,Q}$

Figure 5.16 shows results (and Table 5.7 summarises these results) of the indirect determination of the magnetic field correction factors,  $k_{Q_B,Q}$ , of the PTW 30013 and the IBA FC65-G Farmer-type chambers at different MRI-linac centres. Results are shown when the chamber long axis is orientated parallel, anti-parallel and perpendicular to the magnetic field of the Elekta Unity™ and the ViewRay MRIdian™ systems. Each plot also includes  $k_{Q_B,Q}$  values determined for the Australian MRI-linac, where the chamber long axis is orientated only perpendicular to the magnetic field (magnetic field is parallel to the radiation beam). The error bars represent the combined standard uncertainties of the calibration coefficients, of each chamber, with and without the magnetic field. Any correlated uncertainty related with the primary standard has been omitted. In Appendix A, the indirect (Table A.1 and Table A.3) and the direct (Table A.2)  $k_{Q_B,Q}$  values of the PTW 30013 and the IBA FC65-G Farmer-type chambers for all visited centres, for the three MRI-linac systems, are shown. Results are presented for the three orientations of the chamber with respect to the magnetic field ( $\uparrow\uparrow$ ,  $\uparrow\downarrow$ ,  $\perp$ ). The standard uncertainty of each  $k_{Q_B,Q}$  value is 0.88% for the Elekta Unity™, 0.71% for the ViewRay MRIdian™ and 0.74% for the Australian MRI-linac in the indirect method. For the direct method, the uncertainty is reduced to 0.62% and 0.34% for Elekta Unity™ and the ViewRay MRIdian™, respectively. This is because, in these two MRI-linac systems, the chambers

were calibrated against alanine in the presence and the absence of a magnetic field, and any correlated uncertainties were not included.

*Table 5.7: Indirect and direct  $k_{QB,Q}$  values, determined from Elekta Unity™, ViewRay MRIdian™ and the Australian MRI-linac machines, for the PTW 30013 and the IBA FC65-G Farmer-type chambers in parallel ( $\parallel$ ), anti-parallel ( $\uparrow\downarrow$ ) and perpendicular ( $\perp$ ) orientations. The Elekta Unity™  $k_{QB,Q}$  values are the average over the values obtained at different Elekta Unity™ machines, and their uncertainties reflect the variation between the  $k_{QB,Q}$  values. The remaining quoted uncertainties are standard uncertainties ( $k = 1$ ) as described in this section (5.3.7).*

MRI-linac system	Method	Centre/chamber sn	$k_{QB,Q}$		
			$\parallel$	$\uparrow\downarrow$	$\perp$
PTW 30013	Elekta Unity™	Indirect	-	$0.9926 \pm 0.0038$	$0.9913 \pm 0.0030$
		Direct	-	$0.9954 \pm 0.0050$	$0.9942 \pm 0.0046$
	ViewRay MRIdian™	IPC/3981	$0.9993 \pm 0.0072$	$0.9992 \pm 0.0072$	$0.9724 \pm 0.0070$
			$1.0009 \pm 0.0072$	$1.0002 \pm 0.0072$	$0.9764 \pm 0.0070$
		GCUK/9923	$0.9951 \pm 0.0072$	$0.9939 \pm 0.0072$	$0.9718 \pm 0.0070$
			$0.9965 \pm 0.0034$	$0.9963 \pm 0.0034$	$0.9696 \pm 0.0033$
	Australian MRI-linac	Indirect	IPC/3981	$0.9976 \pm 0.0034$	$0.9969 \pm 0.0034$
		Indirect	GCUK/9923	$0.9973 \pm 0.0033$	$0.9732 \pm 0.0033$
IBA FC65-G	Elekta Unity™	Indirect	Liverpool/3981	-	-
		Indirect	-	$0.9970 \pm 0.0038$	$0.9963 \pm 0.0027$
		Direct	-	$1.0014 \pm 0.0039$	$0.9994 \pm 0.0056$
	ViewRay MRIdian™	Indirect	IPC/3520	$0.9977 \pm 0.0072$	$0.9994 \pm 0.0072$
		Direct	IPC/3520	$0.9914 \pm 0.0034$	$0.9931 \pm 0.0034$
	Australian MRI-linac	Indirect	Liverpool/3520	-	-
			Liverpool/915	-	-

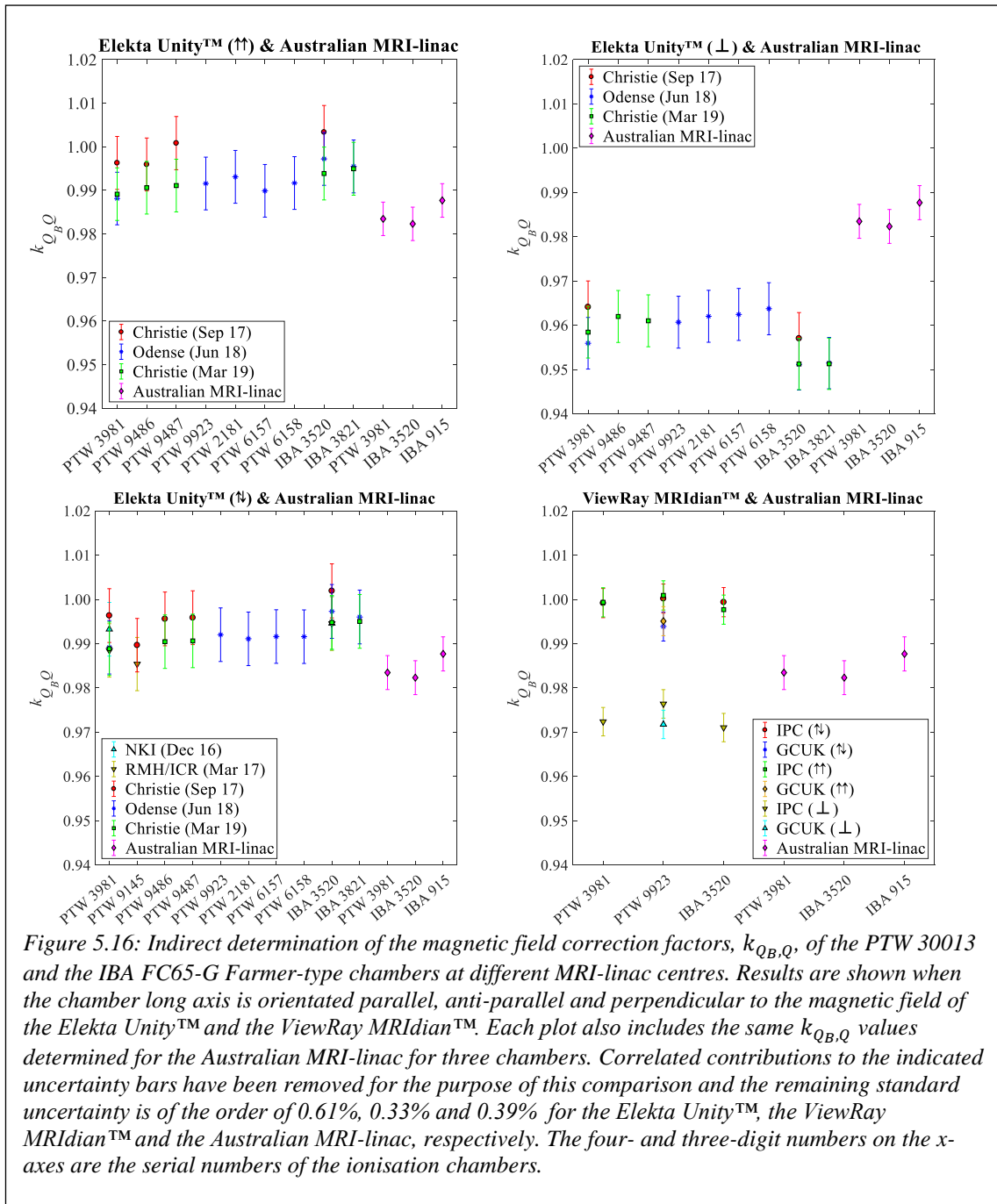


Figure 5.16: Indirect determination of the magnetic field correction factors,  $k_{Q_B,Q}$ , of the PTW 30013 and the IBA FC65-G Farmer-type chambers at different MRI-linac centres. Results are shown when the chamber long axis is orientated parallel, anti-parallel and perpendicular to the magnetic field of the Elekt Unity™ and the ViewRay MRIdian™. Each plot also includes the same  $k_{Q_B,Q}$  values determined for the Australian MRI-linac for three chambers. Correlated contributions to the indicated uncertainty bars have been removed for the purpose of this comparison and the remaining standard uncertainty is of the order of 0.61%, 0.33% and 0.39% for the Elekt Unity™, the ViewRay MRIdian™ and the Australian MRI-linac, respectively. The four- and three-digit numbers on the x-axes are the serial numbers of the ionisation chambers.

### 5.3.8 Uncertainty budget

The analysis of uncertainty here follows the Joint Committee for Guides in Metrology (JCGM) Guide to the Expression of Uncertainty in Measurement (JCGM, 2008). Uncertainties evaluated by statistical analysis are grouped as type A and the rest are grouped as type B. These are added in quadrature to give a combined standard uncertainty with coverage factor  $k = 1$ .

Where it is not specifically stated (i.e. footnotes 14, 15 and 16 cross-reference to the Elekta Unity™, the ViewRay MRIdian™ and the Australian MRI-linac, respectively), uncertainties are the same for all three MRI-linac systems.

The quoted relative standard uncertainties are shown in Table 5.8. The overall combined relative standard uncertainty in the chamber calibration coefficient in the presence of a magnetic field,  $N_{D,w,Q_B}$ , was found to be 1.06% for the Elekta Unity™, 0.92% for the ViewRay MRIdian™ and 0.94% for the Australian MRI-linac, with a coverage factor of  $k = 1$ . The uncertainty budget also reports uncertainties for the alanine magnetic field correction factor,  $k_{Q_B,Q}^{al}$ , ( $0.59\%^{14} / 0.28\%^{15} / 0.35\%^{16}$ ) and the absorbed dose to water in the presence of the magnetic field,  $D_{w,Q_B}$ , ( $1.04\%^{14} / 0.90\%^{15} / 0.92\%^{16}$ ).

The short-term behaviour of the output from the beams of each commercial MRI-linac system was recorded during the measurements over one day (see section 5.2.3.3). For each day of irradiation, the output (dose per MU) was found to decrease by 0.03%, or less, per hour. This deviation was considered, and used to correct the absorbed dose to water, measured with alanine, based on a linear fit between the ionisation chamber signal and the irradiation time. The uncertainty was estimated from the gradient of the residuals of the fit (RMS variation) and found to be 0.06%, on average.

In the MC simulations, the Type A uncertainties in the determination of the absorbed dose to water and to alanine, with and without a magnetic field, were less than 0.1%. For self-consistency and transport parameters a Type B uncertainty of 0.1% was estimated (Kawrakow, 2000, Malkov and Rogers, 2016). The combined standard uncertainty on the MC simulations resulted in less than 0.15%.

---

<sup>14</sup> Elekta Unity™

<sup>15</sup> ViewRay MRIdian™

<sup>16</sup> Australian MRI-linac

*Table 5.8. Uncertainty budget for the Farmer-type chamber calibration coefficient in the presence of a magnetic field for the Elekta Unity™, the ViewRay MRIdian™ and the Australian MRI-linac systems. Where it is not specifically stated (i.e. footnotes 14, 15 and 16 cross-reference to the Elekta Unity™, the ViewRay MRIdian™ and the Australian MRI-linac, respectively), uncertainties are the same for all three MRI-linac systems.*

Uncertainty component	Relative standard uncertainties	
	Type A (%)	Type B (%)
Uncertainties of the correction factors and quantities for the determination of absorbed dose to water in magnetic field, $D_{w,Q_B}$ , using alanine as a transfer standard.		
Alanine air gap effect	0.55 <sup>14</sup> / 0.17 <sup>15</sup> / 0.27 <sup>16</sup>	-
Alanine relative intrinsic sensitivity, $F_{Q_B,Q}$		0.08 <sup>14</sup> / 0.02 <sup>15</sup> / 0.05 <sup>16</sup>
Ratio of MC calculated absorbed dose to water with and without magnetic field, $D_{w,Q_B}/D_{w,Q}$	0.07	0.10
Ratio of MC calculated absorbed dose to alanine without and with magnetic field, $D_{al,Q}/D_{al,Q_B}$	0.14	0.10
Combined standard uncertainty in $k_{Q_B,Q}^{al}$	0.59 <sup>14</sup> / 0.28 <sup>15</sup> / 0.32 <sup>16†</sup>	
Alanine/EPR signal, $M_{Q_B}^{al}$	-	0.08
Alanine beam quality correction factor, $k_{Q,Q_0}^{al}$	-	0.60
Alanine calibration coefficient at 0 T in a $^{60}\text{Co}$ energy beam	-	0.60
Alanine volume averaging correction factor, $k_{vol}^{al}$		0.05
Correction due to linac drift	0.06	-
Combined standard uncertainty in $D_{w,Q_B}$	1.04 <sup>14</sup> / 0.90 <sup>15</sup> / 0.92 <sup>16</sup>	
Uncertainties of the correction factors and quantities on the obtained chamber signal		
Raw chamber readings, $M_{Q_B raw}$	0.03	-
Electrometer correction factor, $k_{elec}$	-	0.10
Temperature	-	0.10
Pressure	-	0.02
Ion recombination correction factor, $k_{ion}$	0.04	-
Farmer-type chamber volume averaging correction factor, $k_{vol}$		0.05
Combined standard uncertainty in chamber signal, $M_{Q_B}$	0.16	
Measurement repeatability	0.10	-
Overall combined relative standard uncertainty in the Farmer-type chamber calibration coefficient in the presence of a magnetic field, $N_{D,w,Q_B}$		1.06 <sup>14</sup> / 0.92 <sup>15</sup> / 0.94 <sup>16</sup>

<sup>†</sup>The uncertainty from the MC calculated dose to water, with and without magnetic field, is omitted for the Australian MRI-linac, as  $D_{w,Q_B}/D_{w,Q}$  ratio is assumed to be unity.

The uncertainty associated with the calibration of the alanine dosimeters in  $^{60}\text{Co}$  energy beam,  $N_{D,w,Q_0}^{al}$ , and the uncertainty associated with the variation between individual dosimeter pellets have been determined by statistical methods, from the NPL chemical dosimetry laboratory, and are 0.6% and 0.3%, respectively. The latter, results in a standard uncertainty of the mean alanine/EPR signal of 0.08%, considering fifteen pellets (irradiation of three alanine holders per measurement day). The uncertainty of the alanine beam quality correction factor,  $k_{Q,Q_0}^{al}$  (0.6%), together with the uncertainty of  $N_{D,w,Q_0}^{al}$  are the dominant components in the uncertainty budget.

The average charge over five irradiations for each Farmer-type chamber (for the Australian MRI-linac this was based on the ratio between the field and the monitor chamber) was used for the determination of each calibration coefficient. The standard deviation of the mean of the five charge readings (and field/monitor ratio), results in 0.03%, or less.

The uncertainty on the ion recombination correction factor,  $k_{ion}$ , was estimated to be 0.04%. This is based on the combined standard uncertainties of the chamber signal at the normal operating voltage and the chamber signal at a reduced voltage.

## 5.4 Discussion

A methodology for the traceable measurement of the absorbed dose to water and calibration of ionisation chambers in the presence of a magnetic field has been developed. This approach uses alanine to calibrate ionisation chambers directly in MRI-linac systems. Alanine is calibrated against the NPL primary standard in zero magnetic field and its response is corrected for use in a magnetic field. This procedure was followed in seven different centres that have MRI-linac systems and the results were presented. Correction factors to realise the absorbed dose to water in the presence of a magnetic field have been evaluated and applied for both alanine and ionisation chambers. A new indirect determination of the magnetic field correction factor for ionisation chambers, described in section 5.2.3.1, is also presented in detail.

### 5.4.1 MC simulations

MC simulations were performed to support the determination of the alanine magnetic field correction factor for the two commercial MRI-linac systems. The Elekta Unity™ phase space files (provided by Elekta) and the ViewRay MRIdian™ accelerator model (constructed by using dimensional details and material specifications found in the literature) were validated by comparing MC calculated lateral and depth dose profiles with measured data. The comparison was quantified by analysing point dose differences between the measured and the calculated lateral and depth dose profiles.

In the Elekta Unity™ and the ViewRay MRIdian™ the experimental setup and the alanine (with its holder) models, were validated by considering the same approach as used in Chapter 4. The effect of the air gaps, associated with the structure of the alanine pellets and the possible asymmetry of their positions inside the holder and for parallel orientation, in the two MRI-linac environments, were investigated. The results were used as the basis for estimating one component in the measurement uncertainty, which was found to be 0.55% and 0.17% for the Elekta Unity™ and the ViewRay MRIdian™ beam qualities, respectively. For the Australian MRI-linac the uncertainty was estimated to be 0.27%.

### 5.4.2 Measurements and influence quantities on the detectors' signals

The measurement repeatability at the visited commercial MRI-linac systems was found to be 0.1%, on average, based on the standard deviation from the readings (signal per MU) of an individual chamber, which was used repeatedly during the calibration of the secondary chambers at each centre (with the magnet ramped up). The variation in the linac beam output (machine stability), was found to be very stable for both MRI-linac systems during the measurements. The linac-to-linac variation, on the Elekta Unity™, may be reflected in the variation in the TPR<sub>20,10</sub> measurements. This was found to be 0.003 and 0.002 when the magnet was either on or off, respectively. In the Australian MRI-linac, the use of the external monitor chamber reduced the beam output variation from 1.2% to 0.1%.

The effect of the magnetic field on the chamber signal depends on the chamber orientation and is smaller for the parallel orientation. The change in signal might be expected to lead

to a proportional change in the volume recombination: measurements show that any change in ion recombination is small, and also subject to intra-type variation.

On average, the  $TPR_{20,10}$  value in the presence of a magnetic field was found to differ by 0.003 from the value at zero magnetic field, for both MRI-linac systems. This difference is within the variation of the measured  $TPR_{20,10}$  at different Elekta Unity™ machines. We did not have enough data to make a similar conclusion for the ViewRay MRIdian™ system, but, a change of 0.003 in the  $TPR_{20,10}$  at 0 T, would result in a change in the chamber magnetic field correction factor of only 0.03% (on average), determined indirectly. This has been included in the uncertainty budget. We must also note that the distance between the source and the detector in the Australian MRI-linac is 284 cm. Measurements at NPL with 6 MV conventional energy beam show a change of 0.001 between the TPR at 100 cm and 300 cm. This has a negligible effect on magnetic field correction factor.

The volume averaging correction factors, due to the non-uniform lateral beam profiles of the 10 cm  $\times$  10 cm radiation field in the FFF beams of the Elekta Unity™ and the ViewRay MRIdian™, were determined for the alanine and the Farmer-type chambers. The  $k_{vol}$  value of the ViewRay MRIdian™, for both alanine and Farmer-type chamber, was found to be higher compared the Elekta Unity™ and the Australian MRI-linac. This is because the lateral profile of the two latter machines is somewhat flatter, compared to the ViewRay MRIdian™, which can be attributed to the difference in focal distance, partially offset by the difference in beam energy.

Note that, in Chapter 4, a volume average correction was not applied to the alanine/EPR signal as the beams were flattened and the SDD was approximately 300 cm. Thus, any effect due to volume averaging would be negligible. Even if there was any correction, this would not have any effect on the alanine relative intrinsic sensitivity,  $F_{Q_B,Q}$ , used in the current chapter to determine the alanine magnetic field correction factors.  $F_{Q_B,Q}$  is obtained as a ratio of data with and without a magnetic field, and any effect due to volume averaging would have been cancelled.

### **5.4.3 Validation of alanine as a transfer standard in zero magnetic field and Farmer-type chamber calibration coefficients**

The process of the absorbed dose to water measurements was validated at zero magnetic field. The dose measured with alanine was compared to the dose measured with a Farmer-type chamber at 0 T in an MRI-linac. On average, the ratio between the alanine-measured dose and the chamber-measured dose was found to be  $0.9989 \pm 0.0006$ . This difference from unity, of  $-0.11\%$ , is consistent with the combined standard uncertainty of the ratio, which is  $0.62\%$ . Note that the uncertainty of the ratio includes correlated contributions, such as the uncertainty of the NPL primary standard of absorbed dose to water. These correlated contributions cancel in the uncertainty of the ratio.

The present work successfully calibrated Farmer-type chambers (PTW 30013 and IBA FC65-G), by using alanine as a transfer standard, in an Elekta Unity<sup>TM</sup> and a ViewRay MRIdian<sup>TM</sup> systems when the constant magnetic field was switched off and on. A detailed explanation of the uncertainty budget is also provided. It was found that the overall combined standard uncertainty of the ionisation chamber calibration coefficient,  $N_{D,w,Q_B}$ , in the presence of a magnetic field, was  $1.06\%$  and  $0.92\%$  for the Elekta Unity<sup>TM</sup> and the ViewRay MRIdian<sup>TM</sup>, respectively.

The accuracy of the developed traceability route for reference dosimetry measurements and calibration of ionisation chambers in the presence of a magnetic field can be checked in a consistency test. The test was based on the variation of an ion chamber calibration coefficient,  $N_{D,w,Q_B}$ , for the different orientations, for different Elekta Unity<sup>TM</sup> systems. Variations were found of between  $0.32\%$  and  $0.48\%$  (average of  $0.41\%$ ), which is within the standard uncertainty, even after the removal of correlated contributions, which reduces that standard uncertainty from  $1.06\%$  to  $0.58\%$ .

### **5.4.4 Farmer-type chamber magnetic field correction factors, $k_{Q_B,Q}$**

In the two commercial MRI-linac systems, the Farmer-type chamber magnetic field correction factors were determined for three different orientations of the chamber long axis with respect to the magnetic field. Two different methods were applied: an indirect (section 5.2.3.1) and a direct (section 5.2.3.2). The absolute average difference between the  $k_{Q_B,Q}$  values determined indirectly and directly (between all three orientations at both

MRI-linac systems) was found to be 0.36%. This is consistent within the stated standard uncertainties. Further comparison of the two methods of this study is presented in Table 5.7.

On average, the  $k_{Q_B,Q}$  values in the anti-parallel orientation appears to be smaller compared with the values in the parallel orientation for both MRI-linac beam qualities. However, the uncertainties are too large to allow a more precise conclusion on this small difference. On the other hand, the  $k_{Q_B,Q}$  values for the perpendicular orientation are known (de Pooter *et al.*, 2021) to differ from the values for the parallel/anti-parallel orientations, for a field strength of 1.5 T, by up to 5%. In this work we found this difference, averaging over all chambers of each type, to be 3.4% (PTW 30013) and 4.7% (IBA FC65-G) for the Elekta Unity<sup>TM</sup>. From our measurements in the ViewRay MRIdian<sup>TM</sup> this difference decreases to 2.6% (PTW 30013) and 2.8% (IBA FC65-G).

In the Australian MRI-linac system,  $k_{Q_B,Q}$  values of one PTW 30013 and two IBA FC65-G chambers were presented. In all chambers, the values differ by approximetly - 1.5% from unity.

In the inline MRI-linac systems, although the absorbed dose to water in the central axis of a broad parallel beam (i.e.  $10 \times 10 \text{ cm}^2$  as used for reference dosimetry) is independent to the magnetic field, the magnetic field correction factor of an ionisation chamber is still significantly affected. This was shown in this study and reported by other studies in the literature (Reynolds *et al.*, 2013, Spindeldreier *et al.*, 2017, Malkov and Rogers, 2018).

From this study it is understood that the level of the effect of the magnetic field in ionisation chamber-based dosimetry in the perpendicular (in the case where the chamber is orientated parallel to a magnetic field) and the inline MRI-linacs, is comparable. The methodology followed in this work for reference dosimetry should be applicable for both perpendicular and inline MRI-linac systems. There is nothing to suggest that reference dosimetry in the two systems should be performed differently.

#### 5.4.5 Uncertainties

Future improvement of alanine holder to minimise the air gaps between the inner wall and the alanine pellets would reduce the uncertainties on the measurements of absorbed dose to water. This is the best that this study could do. Nevertheless, even if air gaps are

eliminated the standard uncertainty will never drop below 0.85%, in any given magnetic field strength, as the uncertainty of the alanine beam quality correction factor and the uncertainty of the alanine calibration coefficient are the dominant components in the uncertainty budget. These uncertainties are type B and cannot be controlled by the present work.

## 5.5 Summary

This study established an alternative, robust and practical traceable reference dosimetry for, and calibration of, MRIgRT machines. An alanine dosimeter, calibrated with the NPL's primary standard in a conventional linac and corrected for the effect of magnetic fields, is used as a transfer standard for reference dosimetry measurements and calibration of secondary detectors. The developed traceability route may be applied to calibrate ionisation chambers in the two commercial MRIgRT systems, Elekta Unity™ and ViewRay MRIdian™, and in the under development inline MRIgRT system, Australian MRI-linac, with a standard uncertainty of 1.06%, 0.92% and 0.94%, respectively. In this chapter, values of magnetic field correction factors are determined for Farmer-type chambers (PTW 30013 and IBA FC65-G), at three different orientations with respect to the magnetic field, for the two commercial MRI-linac systems, and for perpendicular orientation for the Australian MRI-linac. These values, which are reported in Appendix A, should be considered for inclusion in new data sets of correction factors for the development of the future protocols for reference dosimetry in MRIgRT.

## Chapter 6 Validation of alanine-based reference dosimetry on MRIgRT

The application of work described in Chapter 5 includes an alanine dosimetry service, for MRI-linac systems. This allows the calibration of ionisation chambers either by a site visit to radiotherapy centres or as a postal dosimetry service. In the first case, NPL performs measurements with its own fully calibrated instruments to determine absorbed dose to water and calibrate the user's ionisation chamber(s). In this case, traceability to the national standard is confirmed by an NPL calibration report. For the postal dosimetry service, alanine pellets loaded in Farmer-type holders are posted to the users of MRI-linacs, where they irradiate the alanine and post them back to NPL. NPL reports only the absorbed dose to water, which is traceable to the NPL primary standard. The validation and the implementation of both cases are described in the current Chapter 6.

### 6.1 Dose comparison with VSL

The suitability of alanine/EPR for reference dosimetry in MRI-linacs was assessed by comparison with three Farmer-type chambers (two of PTW 30013 and one of IBA FC65-G). The chambers had previously been calibrated using the VSL water calorimeter in another Elekta Unity™ MRI-linac (de Prez *et al.*, 2019a). The alanine/EPR dosimetry was traceable to the NPL graphite calorimeter following the route described in section 5.2.1. Absorbed dose measurements were performed in the Elekta Unity™ at The Christie and Odense with the experimental setup being the same as in section 5.2.3.3 and with magnetic field of 0 T (only in Odense) and 1.5 T.

Figure 6.1 shows the dose rate (cGy/MU) values, measured with alanine and an IBA FC65-G chamber, with a serial number 3213, at Odense (0 T and 1.5 T) and The Christie (1.5 T) for parallel orientation as a function of time. The error bars represent the standard uncertainty on dose output, which is 1.04% for the alanine and 0.37% (de Prez *et al.*, 2019a) for the chamber. In the same figure, dose rate values measured with the IBA FC65-G chamber in parallel and perpendicular orientation are shown. The repeatability of the dose rate measured with the chambers is within 0.1% for all the chambers and both orientations. A systematic difference of 0.3% (average over the three chambers) between the dose measured with the chamber being parallel and perpendicular was observed (i.e.

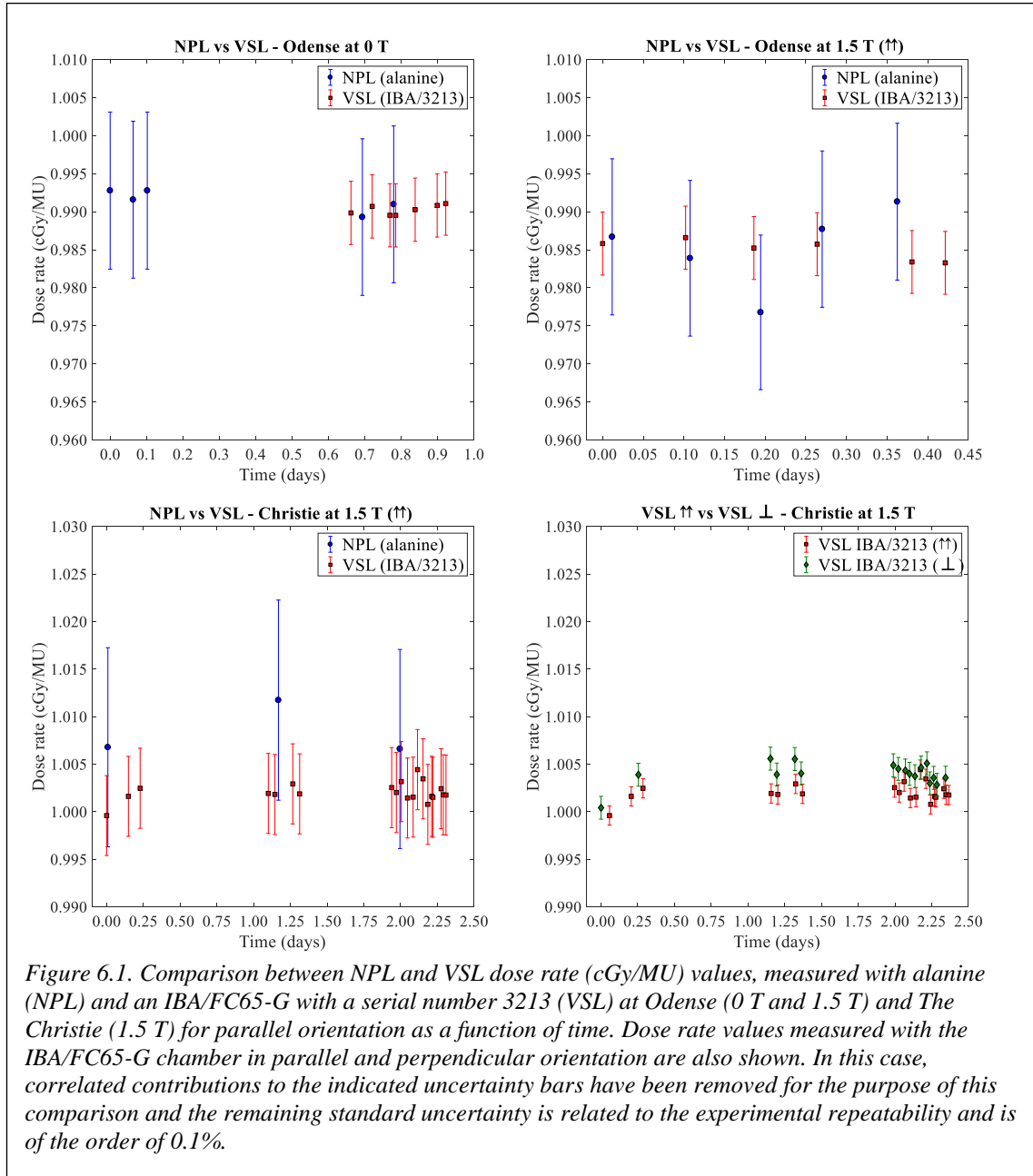
the dose measured with chamber in perpendicular orientation is higher, for all three chambers).

*Table 6.1: Ratios, R, on measured dose outputs between alanine and the three Farmer-type chambers and between the three Farmer-type chambers. The four-digit numbers on the numerators and denominators are the serial numbers of the ionisation chambers.*

Magnetic field strength (chamber orientation)		$R_{NPL/VSL}$			Farmer-type chamber ratios			
		Odense		Christie		Christie		
		Alanine IBA/3213	Alanine IBA/3213	Alanine PTW/7120	Alanine PTW/8377	PTW/7120 IBA/3213	PTW/8377 IBA/3213	PTW/7120 PTW/8377
0 T	1.0012	-	-	-	-	-	-	-
With alanine correction	1.5 T ( $\uparrow\uparrow$ )	1.0003	1.0063	1.0069	1.0087	0.9994	0.9976	1.0018
	1.5 T ( $\perp$ )	0.9985	1.0044	1.0057	1.0037	0.9987	1.0007	0.9980
Without alanine correction	1.5 T ( $\uparrow\uparrow$ )	1.0046	1.0107	1.0113	1.0131	-	-	-
	1.5 T ( $\perp$ )	1.0029	1.0087	1.0101	1.0080	-	-	-

For brevity, Figure 6.1 includes data only from one chamber and one orientation, but similar variation on dose rate values is observed with the other chambers and orientations. Table 6.1 shows the level of agreement in absorbed dose measurements using alanine/EPR and the three Farmer-type chambers for 0 T, and for perpendicular and parallel orientation at 1.5 T (ratio of the averaged doses measured with alanine and chamber). Results are shown when the dose is measured with alanine, including the correction for the effect of the magnetic field and not including this correction. A comparison between the three chambers is also presented. The observed deviations from unity, of the ratios alanine/chamber, is partly accounted for by the degree of equivalence of the NPL and VSL primary standards, in which the ratios of the NPL and the VSL are 1.0041 for both 6MV and 10MV (Picard *et al.*, 2015, Picard *et al.*, 2017). This means that a dose measured traceable to the NPL primary standard could be expected to be 0.41% higher compared to a dose measured traceable to the VSL primary standard, under conventional conditions.

The application of the alanine magnetic field correction factor,  $k_{Q_B,Q}$ , improves the dose agreement with VSL to 0.43% from 0.87%, on average, and improves the uncertainty by 0.2%. In the case that the alanine  $k_{Q_B,Q}$  is not applied, the uncertainty must account for the possible uncorrected effect of the magnetic field on alanine intrinsic sensitivity, and this extra contribution increases the combined standard uncertainty from 1.04% to 1.25% (for 1.5 T).



## 6.2 Comparison with other studies

The indirect and the direct determination of  $k_{QB,Q}$  values of the Farmer-type chambers of this study, determined for the Elekta Unity™ and the ViewRay MRIdian™, are compared with values found in the literature (van Asselen *et al.*, 2018, de Prez *et al.*, 2019b, Krauss *et al.*, 2020). Only studies that have performed measurements in MRI-linac systems are considered for comparison in this work. The review by de Pooter *et al.* (2021) points out that early publications on the determination of the  $k_{QB,Q}$  did not consider fully the potential difficulties of dosimetry in magnetic fields. As a result, the uncertainty of those determinations is underestimated and, for this reason, in comparing results reported here with previous results, some studies have been excluded. We have excluded from our comparison studies where:

- a)  $k_{QB,Q}$  is determined in a non-MRI-linac environment, so that an MRI-linac beam quality cannot be achieved (and quality-dependent aspects of the magnetic field correction factor, including the effect of the magnetic field on the absorbed dose to water in homogeneous water, would increase the uncertainty),
- b) the effective collection volume, in MC calculations of  $k_{QB,Q}$ , is not considered (such  $k_{QB,Q}$  values may lead to errors of up to 1.4% (Pojtinger *et al.*, 2019), on Farmer-type chambers) and
- c)  $k_{QB,Q}$  is expressed as a ratio of chamber readings only, ignoring the effect of the magnetic field on absorbed dose to water in homogeneous water.

Table 6.2 and Table 6.3 present the  $k_{QB,Q}$  values determined from Elekta Unity™ and ViewRay MRIdian™ machines, respectively. Results from this study (indirect and direct methods) are compared with results from de Prez *et al.* (2019b) and van Asselen *et al.* (2018) (Table 6.2) and from Krauss *et al.* (2020) (Table 6.3), for the PTW 30013 and IBA FC65-G Farmer-type chamber in parallel, anti-parallel and perpendicular orientations. Any difference between the  $k_{QB,Q}$  values of the present work and the three studies, is consistent within the standard uncertainties.

*Table 6.2:  $k_{QB,Q}$  values, determined from Elekta Unity™ machines, of the studies from van Asselen et al. (2018) and de Prez et al. (2019b) and of this study (indirect and direct methods for the PTW 30013 and the IBA FC65-G Farmer-type chambers in parallel ( $\uparrow\uparrow$ ), anti-parallel ( $\uparrow\downarrow$ ) and perpendicular ( $\perp$ ) orientations. The quoted uncertainties are standard uncertainties ( $k = 1$ ).*

	Study	$k_{QB,Q}$		
		$\uparrow\uparrow$	$\uparrow\downarrow$	$\perp$
PTW 30013	van Asselen et al. (2018)	-	$0.9920 \pm 0.0020$	$0.9630 \pm 0.0020$
	de Prez et al. (2019b)	-	$0.9850 \pm 0.0060$	$0.9630 \pm 0.0040$
	This study indirect	$0.9926 \pm 0.0038$	$0.9913 \pm 0.0030$	$0.9612 \pm 0.0027$
	This study direct	$0.9954 \pm 0.0050$	$0.9942 \pm 0.0046$	$0.9626 \pm 0.0030$
IBA FC65-G	van Asselen et al. (2018)	-	$0.9970 \pm 0.0030$	$0.9520 \pm 0.0020$
	de Prez et al. (2019b)	-	$0.9950 \pm 0.0040$	$0.9560 \pm 0.0040$
	This study indirect	$0.9970 \pm 0.0038$	$0.9963 \pm 0.0027$	$0.9524 \pm 0.0027$
	This study direct	$1.0014 \pm 0.0039$	$0.9994 \pm 0.0056$	$0.9566 \pm 0.0026$

*Table 6.3:  $k_{QB,Q}$  values, determined from ViewRay MRIdian™ machines, of the study from Krauss et al. (2020), with standard uncertainty of 0.78%, and of this study (indirect and direct methods with standard uncertainties of 0.72% and 0.34%, respectively) for the PTW 30013 and the IBA FC65-G Farmer-type chambers in parallel ( $\uparrow\uparrow$ ), anti-parallel ( $\uparrow\downarrow$ ) and perpendicular ( $\perp$ ) orientations.*

	Study	Centre/ chamber sn	$k_{QB,Q}$		
			$\uparrow\uparrow$	$\uparrow\downarrow$	$\perp$
PTW 30013	Krauss et al. (2020)	-	0.9936	-	0.9706
		IPC/3981	0.9993	0.9992	0.9724
	This study indirect	IPC/9923	1.0009	1.0002	0.9764
		GCUK/9923	0.9951	0.9939	0.9718
IBA FC65-G	This study direct	IPC/3981	0.9965	0.9963	0.9696
		IPC/9923	0.9976	0.9969	0.9732
	Krauss et al. (2020)	-	0.9936	-	0.9668
	This study indirect	IPC/3520	0.9977	0.9994	0.9710
	This study direct	IPC/3520	0.9914	0.9931	0.9650

Notes:

1. the parallel orientation in van Asselen et al. (2018) has the same orientation as the anti-parallel in the present and the de Prez et al. (2019b) work.
2. the  $k_{QB,Q}$  values from this study in Table 6.2, are the average over the values obtained at different Elekta Unity™ machines, for each chamber type, orientation and method. Uncertainties reflect the variation between the  $k_{QB,Q}$  values.

3. in Table 6.3, the determination of  $k_{Q_B,Q}$  in the study of Krauss *et al.* (2020), involves a beam quality correction factor,  $k_{Q,Q_0}$ , taken from Andreo *et al.* (2020). The uncertainty on their  $k_{Q_B,Q}$  values results in 0.78%, which is the combination of the uncertainties on  $k_{Q,Q_0}$  (0.62%) and their results (0.48%). In the present study, the uncertainties have been estimated to be 0.72% and 0.34% for the indirect and the direct method, respectively.

For the Australian MRI-linac,  $k_{Q_B,Q}$  values may also be compared with values found in the literature. To the best of our knowledge, only two studies (Reynolds *et al.*, 2013, Spindeldreier *et al.*, 2017) were found to report  $k_{Q_B,Q}$  values (MC calculated) of Farmer-type ionisation chambers (PTW 30013 and NE2571) similar to our setup (beam orientated parallel to a 1 T magnetic field, with the chamber being perpendicular). However, none of these studies satisfy all the conditions (identified above as a, b and c) as applied in the perpendicular MRI-linac systems to ensure comparison with studies that will not introduce unnecessary uncertainties. As the literature is lacking works on dosimetry in inline MRI-linac, some assumptions are made on the way that the magnetic field correction factors have been obtained. Table 6.4 shows  $k_{Q_B,Q}$  values of the present study (determined indirectly), the Reynolds *et al.* (2013) and Spindeldreier *et al.* (2017). These two studies used a flatten 6 MV energy beams (with a TPR<sub>20,10</sub> of approximately 0.674) compared to the 6 MV FFF (TPR<sub>20,10</sub> of 0.647) used in the Australian MRI-linac. Therefore, the observed differences between our values and those of Reynolds *et al.* (2013) and Spindeldreier *et al.* (2017) is partly accounted for to the different beam quality used.

To ensure a reasonable comparison, the results from the investigation on  $k_{Q_B,Q}$  energy dependence by Malkov and Rogers (2018) were used. This study performed MC calculations of  $k_{Q_B,Q}$  at different energies, for a set of different ionisation chamber types and at 0.35 T and 1.5 T. Their setup included an orientation of the magnetic field parallel to the beam and perpendicular to the chamber, which complement the setup in the Australian MRI-linac. Their findings show that, the magnetic field correction factor for ionisation chambers at 1.5 T, increases with beam quality. We used the data from figure 10 in Malkov and Rogers (2018) ( $k_{Q_B,Q}$  as a function of TPR<sub>20,10</sub> at 1.5 T), for the NE2571, and interpolated  $k_{Q_B,Q}$  values based on the TPR<sub>20,10</sub> in the present work, and

from the studies in Reynolds *et al.* (2013) and Spindeldreier *et al.* (2017). It was found that the interpolated  $k_{Q_B,Q}$  values of these two studies could differ by +0.2% compared to the interpolated value of the Australian MRI-linac. Consequently, considering the energy dependence on  $k_{Q_B,Q}$ , the difference from the values reported in our work with those of Reynolds *et al.* (2013) and Spindeldreier *et al.* (2017) will be reduced.

The sensitive volume is one of the criteria that needs to be considered in a MC calculated  $k_{Q_B,Q}$ . The work by Spindeldreier *et al.* (2017) and Malkov and Rogers (2018) also investigated the effect of the dead volume in the MC calculated ionisation chamber dose response when the magnetic field is parallel to the radiation beam. They report that any effect is negligible. Therefore, the dead volume is not considered as a potential source of error that will affect the comparison between the calculated and the our measured  $k_{Q_B,Q}$  values.

*Table 6.4:  $k_{Q_B,Q}$  values, determined from the inline MRI-linac configuartion (beam parallel to magnetic field), of the studies from Reynolds *et al.* (2013), Spindeldreier *et al.* (2017) and of this study (indirect method) for the PTW 30013 and the IBA FC65-G Farmer-type chambers in parallel perpendicular ( $\perp$ ) orientation. The quoted uncertainties are standard uncertainties ( $k = 1$ ).*

Study	Chamber type (sn)	$k_{Q_B,Q}$
This study indirect	PTW 30013 (3981)	$0.9835 \pm 0.0073$
This study indirect	IBA FC65-G (3520)	$0.9823 \pm 0.0073$
This study indirect	IBA FC65-G (915)	$0.9877 \pm 0.0073$
Reynolds <i>et al.</i> (2013)	NE2571	$0.9872 \pm 0.0070$
Spindeldreier <i>et al.</i> (2017)	PTW 30013	$0.9935^\dagger \pm 0.0030$

<sup>†</sup>Average of values for 90° and 270° orientations

It also has to be noted that, Reynolds *et al.* (2013) report chamber response relative to 0 T. The ratio between 1T and 0 T is  $1.0130 \pm 0.007$  (retrieved from figure 2 in Reynolds *et al.* (2013)). Bielajew (1993) demonstrated that the absorbed dose to water at the central axis of the beam is magnetic field independent, assuming a broad photon beam. Reynolds *et al.* (2013) performed MC simulation with an energy of 6 MV and field size of 4 cm × 10 cm. With these parameters, electron equilibrium occurs in the central axis, and the ratio of the dose to water with and without magnetic field is unity. Therefore, the  $k_{Q_B,Q}$  would result in  $0.9872 \pm 0.007$  (which is the inverse value of 1.0130), and this is the value presented in Table 6.4.

### 6.3 Pilot study of alanine postal dosimetry service for MRI-linac machines

A pilot study of alanine postal dosimetry audit for MRI-linac was performed. The methodology for traceable measurements of the absorbed dose to water and calibration of ionisation chambers that was described and established in Chapter 5, it was adopted for use as an alanine postal dosimetry service. The pilot study included two radiotherapy centres that employ an Elekta Unity™ system. Work instructions (shown in Appendix B), together with the alanine dosimeters, were sent to the participant centres. The presented work instructions are these after the feedback received from the two centres.

NPL also performed measurements in these two radiotherapy centres following the methodology described in Chapter 5. Comparison between the results of the postal dosimetry audits and the results of the measurements completed by NPL, are reported in section 6.4.

### 6.4 Comparison

The comparison of the NPL measurements with Odense and The Christie are presented in Table 6.5 and Table 6.6. Both tables show ionisation chamber calibration coefficients (two for Odense) and  $TPR_{20,10}$  values. Each participant (including NPL) performed measurements with different instruments (i.e. water tank, electrometer, thermometer, alanine pellets and holders, etc.). Only the users' ionisation chambers and the MRI-linac machine were common between NPL and each centre.

*Table 6.5: Calibration coefficients of two ionisation chambers and  $TPR_{20,10}$  determined from NPL and Odense at the same Elekta Unity™ system.*

Chamber type (s.n.)	$N_{D,W,Q_B} \text{ (cGy/nC)}$		Difference to NPL
	Odense	NPL	
PTW/30006 (0534)	5.082	5.041	0.82%
PTW/30013 (2181)	5.252	5.234	0.34%
$TPR_{20,10}$	0.703	0.701	0.24%

*Table 6.6: Calibration coefficients of an ionisation chamber and TPR<sub>20,10</sub> determined from NPL and the Christie at the same Elekta Unity™ system.*

Chamber type (s.n.)	$N_{D,W,Q_B}$ (cGy/nC)		
	Christie	NPL	Difference to NPL
PTW/30013 (9486)	5.241	5.233	0.16%
TPR <sub>20,10</sub>	0.702	0.698	0.60%

## 6.5 Summary

The methodology for the traceable reference dosimetry in the presence of a magnetic field, described in Chapter 5, was compared with an approach that achieves traceability directly to an MRI-linac through ionisation chambers (calibrated using the VSL’s water calorimeter). Any difference on dose output measurements with different detectors were consistent within the combined standard uncertainties. Comparison was also performed between published  $k_{Q_B,Q}$  values and those determined in this study. All values show agreement within the stated standard uncertainties.

The alanine postal dosimetry service for MRI-linac systems was tested at two different radiotherapy centres. Experiences gained during these two pilot studies, improved the written work instructions provided in Appendix B.

## Chapter 7 General discussion and conclusion, and future work

Technology is evolving with rapid steps, especially in the last 150 years. This is also reflected into the health science. With the invention of x-rays, back in 1895, it was realised that this high energy electromagnetic radiation can be used for medical diagnosis. The use of x-ray did not stop there. Not long after it was discovered that ionising radiation could treat diseases, such as cancer. Doses of radiation delivered daily over several weeks, greatly improved the patient's chance for a cure. Soon after it was realised that radiation could significantly damage healthy tissues. Since then, the methods and the systems that delivers radiation therapy have substantially improved. Despite the progress on delivering a radiation more precisely, this is not enough to ensure that the right amount of radiation dose is delivered to the tumour. Metrology and dosimetry are essential parts on the evolution of radiotherapy. Dosimetry protocols have been developed, adjusted and adapted based on the need of each radiotherapy modality. New metrological capabilities and dosimetry systems need to be included in these protocols to establish a well calibrated machine that deliver radiotherapy. This will allow for the safe clinical implementation and ensure that the patient is treated with a physical dose which can be reproducibly and accurately measured worldwide.

The new cancer treatment modality of MRIgRT, discussed in this thesis, is expected to transform radiotherapy in the next decade and beyond. However, as in most cases where a new modality is introduced, technical challenges need to be addressed. One of these challenges is the effect of the magnetic field, associated with the MRI, on the dose delivered to the patient. This is critical, as the therapeutic dose must be delivered as accurately as possible and its uncertainty should be comparable to this in conventional radiotherapy. Therefore, the effect of the magnetic field on the existing dosimetry systems must be understood and quantified.

In this thesis, I have investigated various fundamental aspects of dosimetry in the presence of magnetic fields, with the aim to establish utmost confidence and reproducibility for dose standards and measurements as required for safe cancer treatments with MRI-linacs. Within my work I investigated the performance of Gafchromic EBT-3 film and alanine dosimeters in the presence of magnetic fields. The

suitability of these two detectors was assessed for relative and absolute dosimetry in MRI-linac systems. Next, I aimed to achieve traceability to existing primary standards of absorbed dose to water. I devised and evaluated respective routes, with the inclusion of a rigorous analysis of the uncertainties. Finally, I recommend guidelines for combining reference dosimetry measurements in MRI-linacs to achieve traceability to the NPL primary standard.

Dose calculations are the key component of every TPS used in radiotherapy. The TPS provides the interface between the patient anatomy and the dose delivery system. It is critical that the TPS can accurately predict the dose to be delivered, and it therefore requires that the respective dose calculation is adequately commissioned and validated. The process of commissioning and validation of the used dosimetry systems is equivalently important.

In conventional radiotherapy, it has been shown that film is an important dosimeter for the verification of treatment plans and the commissioning of the TPS. It is a robust detector that can measure dose in simple block phantoms and in more advanced anthropomorphic phantoms. One of the aims of this thesis was to investigate the effect of the magnetic field on the response of the Gafchromic EBT-3 film. In a first investigation, I could establish a small effect of the magnetic field on the dose measured with EBT-3 films, which exceeds the acceptable uncertainties at field strength above 2 T. Nevertheless, for currently available MRI-linacs, with a maximal field strength of 1.5 T, EBT-3 was assessed to be a suitable detector for dosimetry in MRIgRT. This finding is important as it supports the continued use of this dosimetry system for treatment verification and TPS commissioning also for MRIgRT.

The development of dosimetry in MRIgRT is still at an early stage and it is crucial that the performance of detectors used is documented and well understood. The results derived in this thesis, were instrumental to resolve apparent inconsistencies in reported effects of magnetic field on radiochromic film sensitivity in earlier works from different research teams (section 3.4.1).

Clinical medical physicists in radiotherapy rely on dosimetry protocols that provide traceable reference dosimetry for, and calibration of, MRIgRT machines. These dosimetry protocols needed to be newly established, because existing protocols do not

account for the effects of the magnetic field on detector response and of the modified electron transport on absorbed dose in phantoms or patients. The lack of any standard for reference dosimetry and the need for robust and stable detectors in MRIgRT, was the key motivation for the investigations of this thesis. I studied the response of alanine dosimeters in magnetic fields and assessed their suitability to act as reference detectors in MRIgRT. I could demonstrate that, with the inclusion of a magnetic field correction factor, alanine can be used as a suitable reference dosimeter for measurements in MRIgRT. Based on this finding, a methodology that describes the calibration of secondary standard ionisation chambers (user's detectors) in an MRI-linac, in terms of absorbed dose to water traceable to the NPL primary standard by using NPL alanine as a transfer standard, has been established. This traceability route is applicable to all currently available commercial MRI-linacs (Elekta Unity™ and ViewRay MRIdian™) and the under-development Australian MRI-linac, with an uncertainty which is comparable to the routes used for conventional radiotherapy.

I furthermore established a traceability route that introduces a magnetic field correction factor to adjust the detector calibration coefficient from zero magnetic field. Values of this factor generated in this work, should be included into existing data sets of correction factors, for the development of future protocols for reference dosimetry in MRIgRT.

My work on the suitability of alanine for dosimetry in the presence of magnetic fields also enables novel dosimetry audits for adaptive MRIgRT. For instance a recent work by Axford *et al.* (2021) used the methodology developed in this thesis for the design of an end-to-end assessment procedure in adaptive MRIgRT.

A further application of my results on alanine dosimetry is the establishment of a national alanine reference dosimetry service, for MRI-linac systems at NPL. This would allow a dosimetry audit (i.e., checking dose output and  $TPR_{20,10}$ ) and the calibration of ionisation chambers (but also other dosimeters), either by a site visit to radiotherapy centres or as a postal dosimetry service. As a direct result of this thesis work, the on-site service is now available and, at the time of writing, has been successfully delivered to three radiotherapy centres.

For the postal dosimetry service, alanine pellets loaded in Farmer-type holders, together with written work instructions, are posted to the users of MRI-linacs, where they

irradiate the alanine and post them back to NPL. NPL reports only the absorbed dose to water, which is traceable to the NPL primary standard. The implementation of this case has been evaluated with two radiotherapy centres, but not offered as a service yet. Importantly since the advent of Covid-19, this remote audit may also support the radiotherapy centres during a pandemic, where an in-person service is not possible.

The development of these services will improve the consistency of MRIgRT dosimetry between different radiotherapy centres, as medical physicists can measure the absorbed dose to water in MRIgRT systems directly traceable to the UK primary standard of absorbed dose to water.

The knowledge gained and the accurate metrological capabilities demonstrated in this thesis work should be used by the medical physics community (i.e. clinicians, stakeholders, national laboratories, etc.), in the implementation of future dosimetry protocols. This will enable reliable dosimetry in MRIgRT traceable to primary standards.

## 7.1 Future work

The proof-of-principle on disseminating the quantity of absorbed dose to water in the presence of magnetic fields using alanine as a transfer standard, under reference conditions, has been delivered by this thesis work. One of the advantages of MRIgRT is the superior image quality that can provide, but the bore of the MRI constrains patient positioning and forces increased use of off-axis fields in treatment. Thus, investigations in this dosimetry aspect is inevitable. Future work will build on further development of alanine and film detectors to support non-standard off-axis field dosimetry in magnetic fields. Both detectors have been proven to be capable for relative and absolute dosimetry in standard and non-standard beams, and their inclusion in this modality deserves further research.

A complete end-to-end audit in MRI-linac systems is of major importance to provide consistency between radiotherapy centres. Such an audit would verify both the dosimetry aspects, associated with the delivery system, and the quality and reliability of the imaging, associated with the MRI scanner. This requires the incorporation of dosimeters, where their magnetic susceptibility have a zero or a minimal effect on the MR image distortion, are versatile to *exotic* setup in anthropomorphic phantoms and can measure dose with acceptable uncertainties. Alanine and film are promising candidates, since they are

adaptable and near water equivalent detectors, and their feasibility on dosimetry in the presence of magnetic fields was demonstrated in the present thesis work.

The integration of MRI with a photon therapy delivery system has been successful. It is expected that the integration of a similar system but with a proton therapy machine, MRIgPT, will follow-up (Oborn *et al.*, 2017, Hoffmann *et al.*, 2020). Dosimetry in such system is still at an early stage and the feasibility of dose delivery with MRIgPT must be demonstrated. Therefore, it is of great importance that future work includes the development of traceable dosimetry methods for MRIgPT. Compared to MRI photon therapy, it is expected, however, that in MRIgPT the effect of the magnetic field on detector response to be smaller, as the generated electrons from the protons will have lower energy. The traceability route, established in this thesis work, can be adapted for use in such systems and is worth of investigation.

## Appendix A Summary of magnetic field correction factors of ionisation chambers

Table A.1 and Table A.2 show the indirect and the direct, respectively,  $k_{Q_B,Q}$  values of the PTW 30013 and the IBA FC65-G Farmer-type chambers for all visited centres, for the Elekta Unity™ and the ViewRay MRIdian™ systems. Results are presented for the three orientations of the chamber with respect to a magnetic field: parallel ( $\uparrow\uparrow$ ), anti-parallel ( $\uparrow\downarrow$ ) and perpendicular ( $\perp$ ). Table A.3 shows the indirect,  $k_{Q_B,Q}$  values of the PTW 30013 and the IBA FC65-G Farmer-type chambers determine in the Australian MRI-linac in perpendicular orientation.

**Table A.1: Indirect determination of the  $k_{QB,Q}$  values of the PTW 30013 and the IBA FC65-G Farmer-type chambers for all visited centres, for both the Elekta Unity™ and the ViewRay MRIdian™ systems, with uncertainties for each value of 0.88% and 0.71%, respectively. Results are presented for the three orientations of the chamber**

	Chamber (type/sn)	Elekta Unity™						ViewRay MRIdian™						
		PTW 3981	PTW 9145	PTW 9486	PTW 9487	PTW 9923	PTW 2181	PTW 6157	PTW/6 6158	IBA 3520	IBA 3821	PTW 3981	PTW 9923	IBA 3520
††	Christie (Sep 17)	0.9963		0.9959	1.0008					1.0034			IPC (May 19)	0.9993
	Odense (Jun 18)	0.9881				0.9916	0.9931	0.9899	0.9917	0.9972	0.9955			1.0009
	Christie (Mar 19)	0.9891				0.9906	0.9911			0.9939	0.9950		GCUK (Dec 19)	0.9951
†‡	NKI (Dec 16)	0.9933								0.9946			IPC (May 19)	0.9992
	RMHICR (Mar 17)	0.9885	0.9854							0.9945				1.0002
	Christie (Sep 17)	0.9963	0.9897	0.9956	0.9959					1.0019				0.9994
‡	Odense (Jun 18)	0.9892				0.9920	0.9911	0.9916	0.9916	0.9973	0.9960		GCUK (Dec 19)	0.9939
	Christie (Mar 19)	0.9889		0.9905	0.9906					0.9948	0.9950			
	Christie (Sept 17)	0.9641								0.9570			IPC (May 19)	0.9724
⊥	Odense (Jun 18)	0.9559				0.9607	0.9620	0.9624	0.9637	0.9512	0.9514			0.9764
	Christie (Mar 19)	0.9584		0.9620	0.9610					0.9513	0.9513		GCUK (Dec 19)	0.9718

*Table A.2: Direct determination of the  $k_{QBQ}$  values of the PTW 30013 and the IBA FC65-G Farmer-type chambers for all visited centres, for both the Elekta Unity™ and the ViewRay MRIdian™ systems, with uncertainties for each value of 0.62% and 0.34%, respectively. Results are presented for the three orientations of the chamber with respect to a magnetic field (T, fl., /).*

		Elekta Unity™							ViewRay MRIdian™						
Chamber (type/sn)		PTW 3981	PTW 9145	PTW 9486	PTW 9487	PTW 9923	PTW 2.81	PTW 32.3	PTW 6157	PTW 6158	IBA 3520	IBA 3821	PTW 3981	PTW 9923	IBA 3520
↑↑	Christie (Sep 17)	0.9988		0.9953	1.0067					1.0073					
	Odense (Jun 18)	0.9937				0.9952	0.9939	1.0015	0.9908	0.9900	1.0031	0.9999	IPC (May 19)	0.9965	0.9976
	Christie (Mar 19)	0.9919		0.9903	0.9972					0.9981	0.9984				0.9914
↑↓	RMH/ICR (Mar 17)	0.9878	0.9892									0.9896			
	Christie (Sep 17)	0.9988		0.9950	1.0017							1.0059			
	Odense (Jun 18)	0.9948				0.9956	0.9919	1.0029	0.9925	0.9898	1.0031	1.0005	IPC (May 19)	0.9963	0.9969
	Christie (Mar 19)	0.9916		0.9902	0.9967						0.9990	0.9985			0.9931
	RMH/ICR (Mar 17)	0.9878	0.9892								0.9896				
⊥	Christie (Sep 17)	0.9665									0.9608				
	Odense (Jun 18)	0.9614				0.9642	0.9628	0.9557	0.9633	0.9620	0.9567	0.9557	IPC (May 19)	0.9696	0.9732
	Christie (Mar 19)	0.9611		0.9617	0.9669						0.9553	0.9546			0.9650

*Table A.3: Indirect  $k_{Q_B,Q}$  values of the PTW 30013 and the IBA FC65-G Farmer-type chambers determined at the Australian MRI-linac. The uncertainties for each value is 0.74%.*

Chamber (type/sn)	$k_{Q_B,Q}$
PTW/3981	0.9835
IBA/3520	0.9823
IBA/915	0.9877

## Appendix B Work instructions for user's chamber calibration in an MRI-linac

### B.1 Summary

The user's waterproof ionisation chamber is calibrated in an MRI-Linac, in terms of absorbed dose to water traceable to the NPL primary standard, by using NPL alanine/EPR as a transfer standard. The alanine dosimeters are provided in PTW Farmer chamber-compatible holders, designed to facilitate chamber calibration by substitution. After irradiation, the alanine dosimeters are returned for EPR readout at NPL, who will report the absorbed dose to water at the point of measurement in water. The user obtains the calibration coefficient as the ratio of this absorbed dose divided by the fully corrected ionisation measured with their ionisation chamber.

### B.2 Equipment provided by NPL

- Three alanine dosimeters for measurement, one dummy dosimeter for imaging during setup. All dosimeters are pre-loaded in waterproof PTW Farmer-compatible holders.

### B.3 Equipment provided by the user

- Farmer-type waterproof ionisation chamber(s)
- Thermometer, barometer, humidity meter and electrometer
- Water phantom (MR safe), and distilled water

### B.4 Materials and Methods

The measurements **must** be performed in water. The Farmer chamber and the alanine holder should be oriented with the alanine holder and Farmer symmetry axes parallel to the magnetic field. Make sure no air bubbles are attached to the outer surface of the detectors before irradiation.

- The field size should be  $10 \times 10 \text{ cm}^2$  at the plane of measurement, with the detector reference point at the machine isocentre.
- If possible, a horizontal beam should be used for the measurements, having verified that the reference point of the chamber is located at the isocentre.

- Recommendations: in an Elekta Unity™ system the isocentre may be defined based on the central pixel (iso-pixel) of 2D MV planar images using an electronic portal imaging device, at gantry angles 0 and 90 degrees (within 1 mm in each of the three directions is recommended). In the ViewRay MRIdian™ system, a practical iso-centre may be defined based on room lasers outside of the bore.
- Otherwise, in both systems, local procedures may be followed.
  - It is recommended to measure TPR<sub>20,10</sub> first, keeping the chamber at the machine isocentre and setting the measurement depths 10 g.cm<sup>-2</sup>, 20 g.cm<sup>-2</sup>, 10 g.cm<sup>-2</sup> to check chamber setup repeatability.
  - The Farmer chamber should be irradiated to a nominal dose of 2 Gy at depth 10 g.cm<sup>-2</sup>. At least three irradiations at each setup are recommended.
  - The user must ensure a robust setup procedure of the alanine holders with negligible uncertainties.
  - The calibration measurements should be made, by substitution, in the sequence

chamber / alanine / chamber / alanine / chamber / alanine / chamber

so that the chamber readings can be used to monitor any drift in linac output. Each alanine dosimeter should be irradiated to a nominal dose of 20 Gy, which may conveniently be delivered in three equal fractions. The water temperature at the time of irradiation must be recorded and reported to NPL with an estimated delivery dose.

- Ion chamber readings must be corrected for temperature and pressure, and the relative humidity should be within the range 20% to 70% at the time of measurement. Readings should be corrected to zero ion recombination.

## B.5 Result

The absorbed dose calibration coefficient is given by

$$N_{D,w,Q_B} = \frac{D_{w,Q_B}}{M_{Q_B}} \quad (B.1)$$

where  $D_{w,Q_B}$  is the absorbed dose to water measured in beam quality  $Q = \text{TPR}_{20,10}$  and magnetic field  $B$  using alanine/EPR and reported by NPL, and  $M_{Q_B}$  is the user's ion

chamber reading scaled to the same nominal doses as for alanine, corrected to standard air density (20°C, 1013.25 mbar) and zero ion recombination.

## References

- Acharya, S., Fischer-Valuck, B. W., Kashani, R., Parikh, P., Yang, D., Zhao, T., Green, O., Wooten, O., Li, H. H., Hu, Y., Rodriguez, V., Olsen, L., Robinson, C., Michalski, J., Mutic, S. & Olsen, J. 2016. Online Magnetic Resonance Image Guided Adaptive Radiation Therapy: First Clinical Applications. *International Journal of Radiation Oncology\*Biology\*Physics*, 94, 394-403.
- Agnew, J., O'Grady, F., Young, R., Duane, S. & Budgell, G. J. 2017. Quantification of static magnetic field effects on radiotherapy ionization chambers. *Physics in Medicine and Biology*, 62, 1731-1743.
- Alfonso, R., Andreo, P., Capote, R., Huq, M. S., Kilby, W., Kjall, P., Mackie, T. R., Palmans, H., Rosser, K., Seuntjens, J., Ullrich, W. & Vatnitsky, S. 2008. A new formalism for reference dosimetry of small and nonstandard fields. *Medical Physics*, 35, 5179-5186.
- Almond, P. R., Biggs, P. J., Coursey, B. M., Hanson, W. F., Huq, M. S., Nath, R. & Rogers, D. W. O. 1999. AAPM's TG-51 protocol for clinical reference dosimetry of high-energy photon and electron beams. *Medical Physics*, 26, 1847-1870.
- Andreo, P., Burns, D. T., Hohlfeld, K., Huq, M. S., Kanai, T., Laitano, F., Smyth, V. & Vynckier, S. 2000. Absorbed dose determination in external beam radiotherapy: an international Code of Practice for dosimetry based on standards of absorbed dose to water. *IAEA Technical Reports Series no 398* (Vienna: International Atomic Energy Agency).
- Andreo, P., Burns, D. T., Kapsch, R. P., McEwen, M., Vatnitsky, S., Andersen, C. E., Ballester, F., Borbinha, J., Delaunay, F., Francescon, P., Hanlon, M. D., Mirzakhanian, L., Muir, B., Ojala, J., Oliver, C. P., Pimpinella, M., Pinto, M., de Prez, L. A., Seuntjens, J., Sommier, L., Teles, P., Tikkanen, J., Vijande, J. & Zink, K. 2020. Determination of consensus k Q values for megavoltage photon beams for the update of IAEA TRS-398. *Physics in Medicine & Biology*, 65, 095011.
- Anton, M. 2006. Uncertainties in alanine/ESR dosimetry at the Physikalisch-Technische Bundesanstalt. *Physics in Medicine and Biology*, 51, 5419-5440.
- Anton, M., Kapsch, R. P., Krauss, A., von Voigts-Rhetz, P., Zink, K. & McEwen, M. 2013. Difference in the relative response of the alanine dosimeter to megavoltage x-ray and electron beams. *Physics in Medicine and Biology*, 58, 3259-3282.
- Antypas, C. & Pantelis, E. 2008. Performance evaluation of a CyberKnife (R) G4 image-guided robotic stereotactic radiosurgery system. *Physics in Medicine and Biology*, 53, 4697-4718.
- Arjomandy, B., Tailor, R., Anand, A., Sahoo, N., Gillin, M., Prado, K. & Vicic, M. 2010. Energy dependence and dose response of Gafchromic EBT2 film over a wide range of photon, electron, and proton beam energies. *Medical Physics*, 37, 1942-1947.

- Axford, A., Dikaios, N., Roberts, D. A., Clark, C. H. & Evans, P. M. 2021. An end-to-end assessment on the accuracy of adaptive radiotherapy in an MR-linac. *Phys Med Biol*, 66, 055021.
- Banwell, C. N. 1983. *Fundamentals of Molecular Spectroscopy*, London, McGraw-Hill Inc.
- Barten, D. L. J., Hoffmans, D., Palacios, M. A., Heukelom, S. & van Battum, L. J. 2018. Suitability of EBT3 GafChromic film for quality assurance in MR-guided radiotherapy at 0.35 T with and without real-time MR imaging. *Physics in Medicine and Biology*, 63.
- Begg, J., Alnaghy, S. J., Causer, T., Alharthi, T., George, A., Glaubes, L., Dong, B., Goozee, G., Keall, P., Jelen, U., Liney, G. & Holloway, L. 2019. Technical Note: Experimental characterization of the dose deposition in parallel MRI-linacs at various magnetic field strengths. *Medical Physics*, 46, 5152-5158.
- Berbeco, R. I., Jiang, S. B., Sharp, G. C., Chen, G. T. Y., Mostafavi, H. & Shirato, H. 2004. Integrated radiotherapy imaging system (IRIS): design considerations of tumour tracking with linac gantry-mounted diagnostic x-ray systems with flat-panel detectors. *Physics in Medicine and Biology*, 49, 243-255.
- Bergstrand, E. S., Bjerke, H. & Hole, E. O. 2005. An experimental investigation of the electron energy dependence of the EPR alanine dosimetry system. *Radiation Measurements*, 39, 21-28.
- Bergstrand, E. S., Shortt, K. R., Ross, C. K. & Hole, E. O. 2003. An investigation of the photon energy dependence of the EPR alanine dosimetry system. *Physics in Medicine and Biology*, 48, 1753-1771.
- Bhushan, C., Haldar, J. P., Joshi, A. A. & Leahy, R. M. 2012. Correcting Susceptibility-Induced Distortion in Diffusion-Weighted MRI using Constrained Nonrigid Registration. *Signal Inf Process Assoc Annu Summit Conf APSIPA Asia Pac*, 2012.
- Bielajew, A. F. 1993. The effect of strong longitudinal magnetic fields on dose deposition from electron and photon beams. *Medical Physics*, 20, 1171-1179.
- Billas, I., Bouchard, H., Subiel, A., Silvestre, I. & Duane, S. A characterisation of EBT3 Gafchromic film for relative and absolute dosimetry (PO-0781). ESTRO 36, 2017 Vienna, Austria.
- Boag, J. W. & Currant, J. 1980. CURRENT COLLECTION AND IONIC RECOMBINATION IN SMALL CYLINDRICAL IONIZATION CHAMBERS EXPOSED TO PULSED RADIATION. *British Journal of Radiology*, 53, 471-478.
- Bouchard, H. & Bielajew, A. 2015. Lorentz force correction to the Boltzmann radiation transport equation and its implications for Monte Carlo algorithms. *Physics in Medicine and Biology*, 60, 4963-4971.

- Bouchard, H., de Pooter, J., Bielajew, A. & Duane, S. 2015. Reference dosimetry in the presence of magnetic fields: conditions to validate Monte Carlo simulations. *Physics in Medicine and Biology*, 60, 6639-6654.
- Bouchard, H., Lacroix, F., Beaudoin, G., Carrier, J. F. & Kawrakow, I. 2009. On the characterization and uncertainty analysis of radiochromic film dosimetry. *Medical Physics*, 36, 1931-1946.
- Bouchard, H. & Seuntjens, J. 2013. Applications of Monte Carlo to radiation dosimetry. In: SECO, J. & VERHAEGEN, F. (eds.) *Monte Carlo Techniques in Radiation Therapy*. 1 ed. Boca Raton: CRC Press.
- Boyer, A. L., Butler, E. B., DiPetrillo, T. A., Engler, M. J., Fraass, B., Grant, W., Ling, C. C., Low, D. A., Mackie, T. R., Mohan, R., Purdy, J. A., Roach, M., Rosenman, J. G., Verhey, L. J., Wong, J. W., Cumberlin, R. L., Stone, H., Palta, J. R. & Intensity Modulated Radiation, T. 2001. Intensity-modulated radiotherapy: Current status and issues of interest. *International Journal of Radiation Oncology Biology Physics*, 51, 880-914.
- Budgell, G., Brown, K., Cashmore, J., Duane, S., Frame, J., Hardy, M., Paynter, D. & Thomas, R. 2016. IPEM topical report 1: guidance on implementing flattening filter free (FFF) radiotherapy. *Physics in Medicine and Biology*, 61, 35.
- Burns, D. T., Allisy-Roberts, P. J., Desrosiers, M. F., Sharpe, P. H. G., Pimpinella, M., Lourenco, V., Zhang, Y. L., Miller, A., Generalova, V. & Sochor, V. 2011. Supplementary comparison CCRI(I)-S2 of standards for absorbed dose to water in Co-60 gamma radiation at radiation processing dose levels. *Metrologia*, 48, 18.
- Cancer Research UK 2020. <https://www.cancerresearchuk.org/health-professional/cancer-statistics-for-the-uk#heading-Two>, Accessed December 2020.
- Cervantes, Y., Billas, I., Shipley, D., R, Duane, S. & Bouchard, H. 2020. Small-cavity chamber dose response in megavoltage photon beams coupled to magnetic fields. *Physics in Medicine & Biology*.
- Chandarana, H., Wang, H., Tijssen, R. H. N. & Das, I. J. 2018. Emerging role of MRI in radiation therapy. *J Magn Reson Imaging*, 48, 1468-1478.
- Cheung, T., Butson, M. J. & Yu, P. K. N. 2005. Post-irradiation colouration of Gafchromic EBT radiochromic film. *Physics in Medicine and Biology*, 50, N281-N285.
- Chu, R. D. H., McLaughlin, W. L., Miller, A. & Sharpe, P. H. G. 2008. Report 80. *Journal of the International Commission on Radiation Units and Measurements*, 8, NP-NP.
- Clark, C. H., Aird, E. G. A., Bolton, S., Miles, E. A., Nisbet, A., Snaith, J. A. D., Thomas, R. A. S., Venables, K. & Thwaites, D. I. 2015. Radiotherapy dosimetry audit: three decades of improving standards and accuracy in UK clinical practice and trials. *British Journal of Radiology*, 88.

- Costa, F., Doran, S. J., Hanson, I. M., Nill, S., Billas, I., Shipley, D., Duane, S., Adamovics, J. & Oelfke, U. 2018. Investigating the effect of a magnetic field on dose distributions at phantom-air interfaces using PRESAGE (R) 3D dosimeter and Monte Carlo simulations. *Physics in Medicine and Biology*, 63, 10.
- Court, L., Rosen, I., Mohan, R. & Dong, L. 2003. Evaluation of mechanical precision and alignment uncertainties for an integrated CT/LINAC system. *Medical Physics*, 30, 1198-1210.
- Cremers, F., Frenzel, T., Kausch, C., Albers, D., Schonborn, T. & Schmidt, R. 2004. Performance of electronic portal imaging devices (EPIDs) used in radiotherapy: Image quality and dose measurements. *Medical Physics*, 31, 985-996.
- Crijns, S. P. M., Kok, J. G. M., Lagendijk, J. J. W. & Raaymakers, B. W. 2011. Towards MRI-guided linear accelerator control: gating on an MRI accelerator. *Physics in Medicine and Biology*, 56, 4815-4825.
- Crijns, S. P. M., Raaymakers, B. W. & Lagendijk, J. J. W. 2010. Real-time correction of magnetic field inhomogeneity-induced image distortions for MRI-guided conventional and proton radiotherapy. *Physics in Medicine and Biology*, 56, 289-297.
- Crijns, S. P. M., Raaymakers, B. W. & Lagendijk, J. J. W. 2012. Proof of concept of MRI-guided tracked radiation delivery: tracking one-dimensional motion. *Physics in Medicine and Biology*, 57, 7863-7872.
- de Pooter, J., A., Billas, I., de Prez, L. A., Duane, S., Kapsch, R.-P., Karger, C., van Asselen, B. & Wolthaus, J., W. H. 2021. Reference dosimetry in MRI-linacs: evaluation of available protocols and data to establish a code of practice. *Physics in Medicine & Biology*, 66, 05TR02.
- de Pooter, J. A., de Prez, L. A. & Bouchard, H. 2015. Application of an adapted Fano cavity test for Monte Carlo simulations in the presence of B-fields. *Physics in Medicine and Biology*, 60, 9313-9327.
- de Prez, L., de Pooter, J., Jansen, B., Woodings, S., Wolthaus, J., van Asselen, B., van Soest, T., Kok, J. & Raaymakers, B. 2019a. Commissioning of a water calorimeter as a primary standard for absorbed dose to water in magnetic fields. *Physics in Medicine and Biology*, 64, 12.
- de Prez, L., Woodings, S., de Pooter, J., van Asselen, B., Wolthaus, J., Jansen, B. & Raaymakers, B. 2019b. Direct measurement of ion chamber correction factors,  $k(Q)$  and  $k(B)$ , in a 7 MV MRI-linac. *Physics in Medicine and Biology*, 64, 11.
- Delfs, B., Schoenfeld A A , Popping D, Kapsch R P, Jiang P, Harder D, Poppe B & Looe H K 2018. Magnetic fields are causing small, but significant changes of the radiochromic EBT3 film response to 6 MV photons. *Physics in Medicine and Biology*, 63, 035028.
- Deming, W. & David, M. D. 2005. Geometric Distortion in Structural Magnetic Resonance Imaging. *Current Medical Imaging*, 1, 49-60.

- Devic, S., Seuntjens, J., Hegyi, G., Podgorsak, E. B., Soares, C. G., Kirov, A. S., Ali, I., Williamson, J. F. & Elizondo, A. 2004. Dosimetric properties of improved GafChromic films for seven different digitizers. *Medical Physics*, 31, 2392-2401.
- Devic, S., Tomic, N. & Lewis, D. 2016. Reference radiochromic film dosimetry: Review of technical aspects. *Physica Medica-European Journal of Medical Physics*, 32, 541-556.
- Dimitriadis, A., Palmer, A., Thomas, R., Nisbet, A. & Clark, C. 2017. Adaptation and validation of a commercial head phantom for cranial radiosurgery dosimetry end-to-end audit.
- Doran, S. J., Charles-Edwards, L., Reinsberg, S. A. & Leach, M. O. 2005. A complete distortion correction for MR images: I. Gradient warp correction. *Phys Med Biol*, 50, 1343-61.
- Eaton, D. J., Bass, G., Booker, P., Byrne, J., Duane, S., Frame, J., Grattan, M., Thomas, R. A. S., Thorp, N. & Nisbet, A. 2020. IPEM code of practice for high-energy photon therapy dosimetry based on the NPL absorbed dose calibration service. *Physics in Medicine & Biology*, 65, 195006.
- Eaton, G. R., Eaton, S. S., Barr, D. P. & Weber, R. T. 2010. *Quantitative EPR*, Vienna, Springer.
- Fallone, B. G. 2014. The Rotating Biplanar Linac-Magnetic Resonance Imaging System. *Seminars in Radiation Oncology*, 24, 200-202.
- Fischer-Valuck, B. W., Henke, L., Green, O., Kashani, R., Acharya, S., Bradley, J. D., Robinson, C. G., Thomas, M., Zoberi, I., Thorstad, W., Gay, H., Huang, J., Roach, M., Rodriguez, V., Santanam, L., Li, H., Li, H., Contreras, J., Mazur, T., Hallahan, D., Olsen, J. R., Parikh, P., Mutic, S. & Michalski, J. 2017. Two-and-a-half-year clinical experience with the world's first magnetic resonance image guided radiation therapy system. *Advances in Radiation Oncology*, 2, 485-493.
- Fransson, A., Andreo, P. & Pötter, R. 2001. Aspects of MR image distortions in radiotherapy treatment planning. *Strahlenther Onkol*, 177, 59-73.
- Garcia, L. I. R. & Azorin, J. F. P. 2013. Improving the calibration of radiochromic films by the use of uncertainties in optical density and dose. *Medical Physics*, 40, 7.
- Gargett, M., Oborn, B., Metcalfe, P. & Rosenfeld, A. 2015. Monte Carlo simulation of the dose response of a novel 2D silicon diode array for use in hybrid MRI-LINAC systems. *Medical Physics*, 42, 856-865.
- Girard, F., Bouchard, H. & Lacroix, F. 2012. Reference dosimetry using radiochromic film. *Journal of Applied Clinical Medical Physics*, 13, 339-353.
- GMW 2009. Model 3474 User's Manual, Retrived from: <https://gmw.com/wp-content/uploads/2019/03/GMW-MAN-3474-RevH-July2009.pdfFile>. In: ASSOCIATES, G. (ed.) No:M3474h.407.doc 955 Industrial Road, San Carlos, CA 94070: GMW Associates.

- Hackett, S. L., van Asselen, B., Wolthaus, J. W. H., Kok, J. G. M., Woodings, S. J., Lagendijk, J. J. W. & Raaymakers, B. W. 2016. Consequences of air around an ionization chamber: Are existing solid phantoms suitable for reference dosimetry on an MR-linac? *Medical Physics*, 43, 3961-3968.
- Haus, A. G., Pinsky, S. M. & Marks, J. E. 1970. TECHNIQUE FOR IMAGING PATIENT TREATMENT AREA DURING A THERAPEUTIC RADIATION EXPOSURE. *Radiology*, 97, 653-&.
- Herman, M. G., Balter, J. M., Jaffray, D. A., McGee, K. P., Munro, P., Shalev, S., Van Herk, M. & Wong, J. W. 2001. Clinical use of electronic portal imaging: Report of AAPM radiation therapy committee Task Group 58. *Medical Physics*, 28, 712-737.
- Hoffmann, A., Oborn, B., Moteabbed, M., Yan, S., Bortfeld, T., Knopf, A., Fuchs, H., Georg, D., Seco, J., Spadea, M. F., Jäkel, O., Kurz, C. & Parodi, K. 2020. MR-guided proton therapy: a review and a preview. *Radiation Oncology*, 15, 129.
- Hohlfeld, K., Andreo, P., Mattsson, O. & Simoen, J. P. 2001. Report 64. *Journal of the International Commission on Radiation Units and Measurements*, 1, NP-NP.
- JCGM 2008. Evaluation of measurement data – Guide to the expression of uncertainty in measurement. JCGM 100:2008 (GUM 1995 with minor corrections).
- Jeschke, G. 2008. Electron Spin Resonance. Analysis and Interpretation. By Philip H. Rieger. *Angewandte Chemie International Edition*, 47, 2913-2913.
- Jette, D. 2000. Magnetic fields with photon beams: Monte Carlo calculations for a model magnetic field. *Med Phys*, 27, 2726-38.
- Kalach, N. I. & Rogers, D. W. O. 2003. Which accelerator photon beams are "clinic-like" for reference dosimetry purposes? *Medical Physics*, 30, 1546-1555.
- Kawrakow, I. 2000. Accurate condensed history Monte Carlo simulation of electron transport. II. Application to ion chamber response simulations. *Medical physics*, 27, 499-513.
- Kawrakow I, Mainegra-Hing E, Rogers D W O, Tessier F & B, W. B. R. 2011. The EGSnrc code system: Monte Carlo simulation of electron and photon transport National Research Council of Canada (NRCC) Report PIRS-701.
- Keall, P. J., Barton, M., Crozier, S. & Australian, M. R. I. L. P. 2014. The Australian Magnetic Resonance Imaging-Linac Program. *Seminars in Radiation Oncology*, 24, 203-206.
- Kirkby, C., Stanescu, T., Rathee, S., Carlone, M., Murray, B. & Fallone, B. G. 2008. Patient dosimetry for hybrid MRI-radiotherapy systems. *Med Phys*, 35, 1019-27.
- Kluter, S. 2019. Technical design and concept of a 0.35 T MR-Linac. *Clinical and Translational Radiation Oncology*, 18, 98-101.

- Korhonen, J., Kapanen, M., Keyriläinen, J., Seppälä, T. & Tenhunen, M. 2014. A dual model HU conversion from MRI intensity values within and outside of bone segment for MRI-based radiotherapy treatment planning of prostate cancer. *Medical Physics*, 41, 011704.
- Krauss, A., Spindeldreier, C. K. & Klüter, S. 2020. Direct determination of  $k_B \gamma, Q, Q_0$  for cylindrical ionization chambers in a 6 MV 0.35 T MR-linac. *Physics in Medicine & Biology*.
- Kuriyama, K., Onishi, H., Sano, N., Komiyama, T., Aikawa, Y., Tateda, Y., Araki, T. & Uematsu, M. 2003. A new irradiation unit constructed of self-moving gantry-CT and linac. *International Journal of Radiation Oncology Biology Physics*, 55, 428-435.
- Lagendijk, J. J. W., Raaymakers, B. W., Raaijmakers, A. J. E., Overweg, J., Brown, K. J., Kerkhof, E. M., van der Put, R. W., Hardemark, B., van Vutpen, M. & van der Heide, U. A. 2008. MRI/linac integration. *Radiotherapy and Oncology*, 86, 25-29.
- Lagendijk, J. J. W., Raaymakers, B. W., Van den Berg, C. A. T., Moerland, M. A., Philippens, M. E. & van Vulpen, M. 2014a. MR guidance in radiotherapy. *Physics in Medicine and Biology*, 59, R349-R369.
- Lagendijk, J. J. W., Raaymakers, B. W. & van Vulpen, M. 2014b. The Magnetic Resonance Imaging-Linac System. *Seminars in Radiation Oncology*, 24, 207-209.
- Largent, A., Barateau, A., Nunes, J.-C., Lafond, C., Greer, P. B., Dowling, J. A., Saint-Jalme, H., Acosta, O. & de Crevoisier, R. 2019. Pseudo-CT Generation for MRI-Only Radiation Therapy Treatment Planning: Comparison Among Patch-Based, Atlas-Based, and Bulk Density Methods. *International Journal of Radiation Oncology\*Biology\*Physics*, 103, 479-490.
- Leu, S. C., Huang, Z. & Lin, Z. 2020. Generation of Pseudo-CT using High-Degree Polynomial Regression on Dual-Contrast Pelvic MRI Data. *Scientific Reports*, 10, 8118.
- Lillicrap, S. C., Owen, B., Williams, J. R. & Williams, P. C. 1990. Code of Practice for high-energy photon therapy dosimetry based on the NPL absorbed dose calibration service. *Physics in Medicine and Biology*, 35, 1355-1360.
- Liney, G. P., Dong, B., Begg, J., Vial, P., Zhang, K., Lee, F., Walker, A., Rai, R., Causer, T., Alnaghy, S. J., Oborn, B. M., Holloway, L., Metcalfe, P., Barton, M., Crozier, S. & Keall, P. 2016. Technical Note: Experimental results from a prototype high-field inline MRI-linac. *Medical Physics*, 43, 5188-5194.
- Litzenberg, D. W., Fraass, B. A., McShan, D. L., O'Donnell, T. W., Roberts, D. A., Beccchetti, F. D., Bielajew, A. F. & Moran, J. M. 2001. An apparatus for applying strong longitudinal magnetic fields to clinical photon and electron beams. *Physics in Medicine and Biology*, 46, N105-N115.

- Low, D. A., Moran, J. M., Dempsey, J. F., Dong, L. & Oldham, M. 2011. Dosimetry tools and techniques for IMRT. *Medical Physics*, 38, 1313-1338.
- Malinen, E. 2014. EPR Dosimetry in Clinical Applications. In: LUND, A. & SHIOTANI, M. (eds.) *Applications of EPR in Radiation Research*. 1 ed.: Springer International Publishing.
- Malkov, V. & Rogers, D. 2016. Charged particle transport in magnetic fields in EGSnrc. *Medical physics*, 43, 4447-4458.
- Malkov, V. N. & Rogers, D. W. O. 2017. Sensitive volume effects on Monte Carlo calculated ion chamber response in magnetic fields. *Medical Physics*, 44, 4854-4858.
- Malkov, V. N. & Rogers, D. W. O. 2018. Monte Carlo study of ionization chamber magnetic field correction factors as a function of angle and beam quality. *Medical Physics*, 45, 908-925.
- Malkov, V. N. & Rogers, D. W. O. 2019. Monte Carlo study of ionization chamber magnetic field correction factors as a function of angle and beam quality (vol 45, pg 908, 2018). *Medical Physics*, 46, 5367-5370.
- Martisikova, M., Ackermann, B. & Jakel, O. 2008. Analysis of uncertainties in Gafchromic (R) EBT film dosimetry of photon beams. *Physics in Medicine and Biology*, 53, 7013-7027.
- Massillon, G., Cueva-Procel, D., Diaz-Aguirre, P., Rodriguez-Ponce, M. & Herrera-Martinez, F. 2013. Dosimetry for Small Fields in Stereotactic Radiosurgery Using Gafchromic MD-V2-55 Film, TLD-100 and Alanine Dosimeters. *Plos One*, 8, 8.
- McEwen, M., DeWerd, L., Ibbott, G., Followill, D., Rogers, D. W., Seltzer, S. & Seuntjens, J. 2014. Addendum to the AAPM's TG-51 protocol for clinical reference dosimetry of high-energy photon beams. *Med Phys*, 41, 041501.
- McEwen, M. & Ross, C. 2009. Fricke and alanine dosimeters. In: ROGERS, D. W. O. & CYGLER, J. E. (eds.) *Clinical Dosimetry Measurements in Radiotherapy*. Madison, WI: Medical Physics.
- McEwen, M., Sharpe, P. & Vörös, S. 2015. Evaluation of alanine as a reference dosimeter for therapy level dose comparisons in megavoltage electron beams. *Metrologia*, 52, 272-279.
- Meijsing, I., Raaymakers, B. W., Raaijmakers, A. J. E., Kok, J. G. M., Hogeweg, L., Liu, B. & Lagendijk, J. J. W. 2009. Dosimetry for the MRI accelerator: the impact of a magnetic field on the response of a Farmer NE2571 ionization chamber. *Physics in Medicine and Biology*, 54, 2993-3002.
- Moerland, M. A., Beersma, R., Bhagwandien, R., Wijrdeman, H. K. & Bakker, C. J. G. 1995. ANALYSIS AND CORRECTION OF GEOMETRIC DISTORTIONS IN

- 1.5-T MAGNETIC-RESONANCE IMAGES FOR USE IN RADIOTHERAPY TREATMENT PLANNING. *Physics in Medicine and Biology*, 40, 1651-1664.
- Moylan, R., Aland, T. & Kairn, T. 2013. Dosimetric accuracy of Gafchromic EBT2 and EBT3 film for in vivo dosimetry. *Australasian Physical & Engineering Sciences in Medicine*, 36, 331-7.
- MRgRT 2019. Metrology for MR guided Radiotherapy. *Report retrieved from: [https://www.euramet.org/download/?tx\\_eurametfiles\\_download%5Bfiles%5D=38931&tx\\_eurametfiles\\_download%5Bidentifier%5D=%252Fdocs%252FEMRP%252FJRP%252FJRP\\_Summaries\\_2015%252FHealth%252F15HLT08\\_Final\\_Publishable\\_Report.pdf&tx\\_eurametfiles\\_download%5Baction%5D=download&tx\\_eurametfiles\\_download%5Bcontroller%5D=File&cHash=dfac0395f1b2ad3be7388fdeda93ae8](https://www.euramet.org/download/?tx_eurametfiles_download%5Bfiles%5D=38931&tx_eurametfiles_download%5Bidentifier%5D=%252Fdocs%252FEMRP%252FJRP%252FJRP_Summaries_2015%252FHealth%252F15HLT08_Final_Publishable_Report.pdf&tx_eurametfiles_download%5Baction%5D=download&tx_eurametfiles_download%5Bcontroller%5D=File&cHash=dfac0395f1b2ad3be7388fdeda93ae8)*
- Munro, P. & Bouius, D. C. 1998. X-ray quantum limited portal imaging using amorphous silicon flat-panel arrays. *Medical Physics*, 25, 689-702.
- Mutic, S. & Dempsey, J. F. 2014. The ViewRay System: Magnetic Resonance-Guided and Controlled Radiotherapy. *Seminars in Radiation Oncology*, 24, 196-199.
- Niroomand-Rad, A., Blackwell, C. R., Coursey, B. M., Gall, K. P., Galvin, J. M., McLaughlin, W. L., Meigooni, A. S., Nath, R., Rodgers, J. E. & Soares, C. G. 1998. Radiochromic film dosimetry: Recommendations of AAPM Radiation Therapy Committee Task Group 55. *Medical Physics*, 25, 2093-2115.
- O'Brien, D. J., Roberts, D. A., Ibbott, G. S. & Sawakuchi, G. O. 2016. Reference dosimetry in magnetic fields: formalism and ionization chamber correction factors. *Medical Physics*, 43, 4915-4927.
- O'Brien, D. J. & Sawakuchi, G. O. 2017. Monte Carlo study of the chamber-phantom air gap effect in a magnetic field. *Medical Physics*, 44, 3830-3838.
- Oborn, B. M., Dowdell, S., Metcalfe, P. E., Crozier, S., Mohan, R. & Keall, P. J. 2017. Future of medical physics: Real-time MRI-guided proton therapy. *Med Phys*, 44, e77-e90.
- Oborn, B. M., Kolling, S., Metcalfe, P. E., Crozier, S., Litzenberg, D. W. & Keall, P. J. 2014. Electron contamination modeling and reduction in a 1 T open bore inline MRI-linac system. *Medical Physics*, 41, 051708.
- Oborn, B. M., Metcalfe, P. E., Butson, M. J. & Rosenfeld, A. B. 2010. Monte Carlo characterization of skin doses in 6 MV transverse field MRI-linac systems: effect of field size, surface orientation, magnetic field strength, and exit bolus. *Med Phys*, 37, 5208-17.
- Owrangi, A. M., Greer, P. B. & Glide-Hurst, C. K. 2018. MRI-only treatment planning: benefits and challenges. *Phys Med Biol*, 63, 05tr01.
- Palmans, H., Andreo, P., Huq, S., Seuntjens, J., Christaki, K. & Meghzifene, A. 2017. *Dosimetry of Small Static Fields Used in External Beam Radiotherapy*, Vienna, INTERNATIONAL ATOMIC ENERGY AGENCY.

- Palmer, A. L., Diez, P., Gandon, L., Wynn-Jones, A., Bownes, P., Lee, C., Aird, E., Bidmead, M., Lowe, G., Bradley, D. & Nisbet, A. 2015a. A multicentre 'end to end' dosimetry audit for cervix HDR brachytherapy treatment. *Radiotherapy and Oncology*, 114, 264-271.
- Palmer, A. L., Dimitriadis, A., Nisbet, A. & Clark, C. H. 2015b. Evaluation of Gafchromic EBT-XD film, with comparison to EBT3 film, and application in high dose radiotherapy verification. *Physics in Medicine and Biology*, 60, 8741-8752.
- Pawlicki, T., Scanderbeg, D. J. & Starkschall, G. 2016. *Hendee's Radiation Therapy Physics*, Wiley.
- Picard, S., Burns, D. T., Roger, P., de Prez, L. A., Jansen, B. J. & de Pooter, J. A. 2017. Key comparison BIPM.RI(I)-K6 of the standards for absorbed dose to water of the VSL, Netherlands and the BIPM in accelerator photon beams. *Metrologia*, 54, 1A.
- Picard, S., Burns, D. T., Roger, P., Duane, S., Bass, G. A., Manning, J. W. & Shipley, D. R. 2015. Key comparison BIPM.RI(I)-K6 of the standards for absorbed dose to water at 10 g cm<sup>-2</sup> of the NPL, United Kingdom and the BIPM in accelerator photon beams. *Metrologia*, 52, 1A.
- Pojtinger, S., Dohm, O. S., Kapsch, R. P. & Thorwarth, D. 2018. Ionization chamber correction factors for MR-linacs. *Physics in Medicine and Biology*, 63, 8.
- Pojtinger, S., Kapsch, R. P., Dohm, O. S. & Thorwarth, D. 2019. A finite element method for the determination of the relative response of ionization chambers in MR-linacs: simulation and experimental validation up to 1.5 T. *Physics in Medicine and Biology*, 64, 7.
- Pollard, J. M., Wen, Z., Sadagopan, R., Wang, J. & Ibbott, G. S. 2017. The future of image-guided radiotherapy will be MR guided. *The British Journal of Radiology*, 90, 20160667.
- Popescu, C. C., Olivotto, I. A., Beckham, W. A., Ansbacher, W., Zavgorodni, S., Shaffer, R., Wai, E. S. & Otto, K. 2010. VOLUMETRIC MODULATED ARC THERAPY IMPROVES DOSIMETRY AND REDUCES TREATMENT TIME COMPARED TO CONVENTIONAL INTENSITY-MODULATED RADIOTHERAPY FOR LOCOREGIONAL RADIOTHERAPY OF LEFT-SIDED BREAST CANCER AND INTERNAL MAMMARY NODES. *International Journal of Radiation Oncology Biology Physics*, 76, 287-295.
- Prior, P., Chen, X., Botros, M., Paulson, E. S., Lawton, C., Erickson, B. & Li, X. A. 2016. MRI-based IMRT planning for MR-linac: comparison between CT- and MRI-based plans for pancreatic and prostate cancers. *Physics in Medicine and Biology*, 61, 3819-3842.
- Raaijmakers, A. J. E., Raaymakers, B. W. & Lagendijk, J. J. W. 2005. Integrating a MRI scanner with a 6 MV radiotherapy accelerator: dose increase at tissue-air interfaces in a lateral magnetic field due to returning electrons. *Physics in Medicine and Biology*, 50, 1363-1376.

- Raaijmakers, A. J. E., Raaymakers, B. W. & Lagendijk, J. J. W. 2007a. Experimental verification of magnetic field dose effects for the MRI-accelerator. *Physics in Medicine and Biology*, 52, 4283-4291.
- Raaijmakers, A. J. E., Raaymakers, B. W., van der Meer, S. & Lagendijk, J. J. W. 2007b. Integrating a MRI scanner with a 6 MV radiotherapy accelerator: impact of the surface orientation on the entrance and exit dose due to the transverse magnetic field. *Physics in Medicine and Biology*, 52, 929-939.
- Raaymakers, B. W., Jürgenliemk-Schulz, I. M., Bol, G. H., Glitzner, M., Kotte, A. N. T. J., van Asselen, B., de Boer, J. C. J., Bluemink, J. J., Hackett, S. L., Moerland, M. A., Woodings, S. J., Wolthaus, J. W. H., van Zijp, H. M., Philippens, M. E. P., Tijssen, R., Kok, J. G. M., de Groot-van Breugel, E. N., Kiekebosch, I., Meijers, L. T. C., Nomden, C. N., Sikkes, G. G., Doornaert, P. A. H., Eppinga, W. S. C., Kasperts, N., Kerkmeijer, L. G. W., Tersteeg, J. H. A., Brown, K. J., Pais, B., Woodhead, P. & Lagendijk, J. J. W. 2017. First patients treated with a 1.5 T MRI-Linac: clinical proof of concept of a high-precision, high-field MRI guided radiotherapy treatment. *Physics in Medicine & Biology*, 62, L41-L50.
- Raaymakers, B. W., Lagendijk, J. J. W., Overweg, J., Kok, J. G. M., Raaijmakers, A. J. E., Kerkhof, E. M., van der Put, R. W., Meijsing, I., Crijns, S. P. M., Benedosso, F., van Vulpen, M., de Graaff, C. H. W., Allen, J. & Brown, K. J. 2009. Integrating a 1.5 T MRI scanner with a 6 MV accelerator: proof of concept. *Physics in Medicine and Biology*, 54, N229-N237.
- Raaymakers, B. W., Raaijmakers, A. J. E., Kotte, A., Jette, D. & Lagendijk, J. J. W. 2004. Integrating a MRI scanner with a 6 MV radiotherapy accelerator: dose deposition in a transverse magnetic field. *Physics in Medicine and Biology*, 49, 4109-4118.
- Ramirez, J. L. V., Chen, F., Nicolucci, P. & Baffa, O. 2011. Dosimetry of small radiation field in inhomogeneous medium using alanine/EPR minidosimeters and PENELOPE Monte Carlo simulation. *Radiation Measurements*, 46, 941-944.
- Reinhardt, S., Hillbrand, M., Wilkens, J. J. & Assmann, W. 2012. Comparison of Gafchromic EBT2 and EBT3 films for clinical photon and proton beams. *Medical Physics*, 39, 5257-5262.
- Reisz, J. A., Bansal, N., Qian, J., Zhao, W. & Furdui, C. M. 2014. Effects of ionizing radiation on biological molecules--mechanisms of damage and emerging methods of detection. *Antioxidants & redox signaling*, 21, 260-292.
- Reynolds, M., Fallone, B. G. & Rathee, S. 2013. Dose response of selected ion chambers in applied homogeneous transverse and longitudinal magnetic fields. *Medical Physics*, 40, 7.
- Reynoso, F. J., Curcuru, A., Green, O., Mutic, S., Das, I. J. & Santanam, L. 2016. Technical Note: Magnetic field effects on Gafchromic-film response in MR-IGRT. *Medical Physics*, 43, 6552-6556.

- Roed, Y., Lee, H., Pinsky, L. & Ibbott, G. Characterizing the response of Gafchromic EBT3 film in a 1.5 T magnetic field (PO-0763). ESTRO 36, 2017 Vienna, Austria.
- Sankar, A., Kurup, P., Murali, V., Ayyangar, K., Nehru, R. & Velmurugan, J. 2006. Evaluation of gafchromic EBT film for intensity modulated radiation therapy dose distribution verification. 31, 78-82.
- Saur, S. & Frengen, J. 2008. GafChromic EBT film dosimetry with flatbed CCD scanner: A novel background correction method and full dose uncertainty analysis. *Medical Physics*, 35, 3094-3101.
- Schenck, J. F. 1996. The role of magnetic susceptibility in magnetic resonance imaging: MRI magnetic compatibility of the first and second kinds. *Med Phys*, 23, 815-50.
- Schosseler, P. M. 1998. *Electron paramagnetic resonance study of the copper(II) complexation with carbonate ligands in aqueous solution and at calcium carbonate surfaces*. ETH Zürich.
- Sempau, J. & Andreo, P. 2006. Configuration of the electron transport algorithm of PENELOPE to simulate ion chambers. *Phys Med Biol*, 51, 3533-48.
- Seuntjens, J., Kawrakow, I., Borg, J., Hobeila, F. & Rogers, D. 2002. Calculated and measured air-kerma response of ionization chambers in low and medium energy photon beams. In: Seuntjens J, Mobit PN, editors. *Recent Developments in Accurate Radiation Dosimetry: Proc. Int. Workshop*. Madison: Medical Physics Publishing; . Retrieved from: <https://people.physics.carleton.ca/~drogers/pubs/papers/Se02.pdf>.
- Sevilla, M. D., Becker, D., Kumar, A. & Adhikary, A. 2016. Gamma and Ion-Beam Irradiation of DNA: Free Radical Mechanisms, Electron Effects, and Radiation Chemical Track Structure. *Radiation physics and chemistry (Oxford, England : 1993)*, 128, 60-74.
- Shan, S. S., Liney, G. P., Tang, F. F., Li, M. Y., Wang, Y. H., Ma, H., Weber, E., Walker, A., Holloway, L., Wang, Q. L., Wang, D. M., Liu, F. & Crozier, S. 2020. Geometric distortion characterization and correction for the 1.0 T Australian MRI-linac system using an inverse electromagnetic method. *Medical Physics*, 47, 1126-1138.
- Sharpe, P. H. G. 2003. Report on Radiation Dosimetry at NPL. Report No. CCRI(I)/03-14.
- Sharpe, P. H. G., Rajendran, K. & Sephton, J. P. 1996. Progress towards an alanine/ESR therapy level reference dosimetry service at NPL. *Applied Radiation and Isotopes*, 47, 1171-1175.
- Sharpe, P. H. G. & Sephton, J. 2000. An automated system for the measurement of alanine/EPR dosimeters. *Applied Radiation and Isotopes*, 52, 1185-1188.

- Sharpe, P. H. G. & Sephton, J. 2006. Therapy level alanine dosimetry at the NPL. *Proceedings of 216th PTB Seminar "Alanine Dosimetry for Clinical Application"*, PTB, Braunschweig, PTB-Dos-51.
- Sharpe, P. H. G. & Sephton, J. P. 1999. Alanine dosimetry at NPL - the development of a mailed reference dosimetry service at radiotherapy dose levels. International Atomic Energy Agency (IAEA).
- Shipley, D., Billas, I. & Duane, S. Experimental benchmarking of Monte Carlo based detector response simulations in magnetic fields. nd International Conference on Monte Carlo Techniques for Medical Applications, 2019 Montreal, CA.
- Sleptchonok, O., Nagy, V. & Desrosiers, M. 2000. Advancements in accuracy of the alanine dosimetry system. Part 1. The effects of environmental humidity. *Radiation Physics and Chemistry*, 57, 115-133.
- Smit, K., Kok, J. G. M., Lagendijk, J. J. W. & Raaymakers, B. W. 2014. Performance of a multi-axis ionization chamber array in a 1.5 T magnetic field. *Physics in Medicine and Biology*, 59, 1845-1855.
- Smit, K., van Asselen, B., Kok, J. G. M., Aalbers, A. H. L., Lagendijk, J. J. W. & Raaymakers, B. W. 2013. Towards reference dosimetry for the MR-linac: magnetic field correction of the ionization chamber reading. *Physics in Medicine and Biology*, 58, 5945-5957.
- Spindeldreier, C. K., Schrenk, O., Bakenecker, A., Kawrakow, I., Burigo, L., Karger, C. P., Greilich, S. & Pfaffenberger, A. 2017. Radiation dosimetry in magnetic fields with Farmer-type ionization chambers: determination of magnetic field correction factors for different magnetic field strengths and field orientations. *Physics in Medicine and Biology*, 62, 6708-6728.
- Stuglik, Z. 2007. Alanine-EPR dosimetry system. Why we like it? IAEA Training Course, 3-7 December 2007, Warsaw. Retrieved from: [https://inis.iaea.org/collection/NCLCollectionStore/\\_Public/39/066/39066524.pdf?r=1](https://inis.iaea.org/collection/NCLCollectionStore/_Public/39/066/39066524.pdf?r=1).
- Thomas, R. A. S., Duane, S., McEwen, M. R. & Rosser, K. E. 2003. *Role of the National Physical Laboratory in monitoring and improving dosimetry in radiotherapy in the United Kingdom*, International Atomic Energy Agency (IAEA), IAEA.
- Thomas, S. J., Aspradakis, M. M., Byrne, J. P., Chalmers, G., Duane, S., Rogers, J., Thomas, R. A. S., Tudor, G. S. J., Twyman, N. & Party, I. W. 2014. Reference dosimetry on TomoTherapy: an addendum to the 1990 UK MV dosimetry code of practice. *Physics in Medicine and Biology*, 59, 1339-1352.
- Trachsel, M. A., Pojtinger, S., Meier, M., Schrader, M., Kapsch, R.-P. & Kottler, C. 2020. Chemical radiation dosimetry in magnetic fields: characterization of a Fricke-type chemical detector in 6 MV photon beams and magnetic fields up to 1.42 T. *Physics in Medicine & Biology*, 65, 065005.
- Uematsu, M., Shioda, A., Suda, A., Fukui, T., Ozeki, Y., Hama, Y., Wong, J. R. & Kusano, S. 2001. Computed tomography-guided frameless stereotactic

- radiotherapy for Stage I non-small-cell lung cancer: A 5-year experience. *International Journal of Radiation Oncology Biology Physics*, 51, 666-670.
- van Asselen, B., Woodings, S. J., Hackett, S. L., van Soest, T. L., Kok, J. G. M., Raaymakers, B. W. & Wolthaus, J. W. H. 2018. A formalism for reference dosimetry in photon beams in the presence of a magnetic field. *Physics in Medicine and Biology*, 63, 9.
- ViewRay™ 2014. ViewRay™ Announces World's First Patients Treated Using MRI-Guided Radiation Therapy. Announcement retrieved from: <https://investors.viewray.com/static-files/ec503013-2aa9-4832-8e8c-3212d2ca4d5f>.
- Western, C., Hristov, D. & Schlosser, J. 2015. Ultrasound Imaging in Radiation Therapy: From Interfractional to Intrafractional Guidance. *Cureus*, 7, e280.
- World Health Organization 2020. *Global Cancer Observatory*. <https://gco.iarc.fr/>. Accessed December 2020.
- Yorke, E. D., Ling, C. C. & Rustgi, S. 1985. AIR-GENERATED ELECTRON CONTAMINATION OF 4 AND 10 MV PHOTON BEAMS - A COMPARISON OF THEORY AND EXPERIMENT. *Physics in Medicine and Biology*, 30, 1305-1314.
- Zeng, G. G., McEwen, M. R., Rogers, D. W. O. & Klassen, N. V. 2004. An experimental and Monte Carlo investigation of the energy dependence of alanine/EPR dosimetry: I. Clinical x-ray beams. *Physics in Medicine and Biology*, 49, 257-270.
- Zeng, G. G., McEwen, M. R., Rogers, D. W. O. & Klassen, N. V. 2005. An experimental and Monte Carlo investigation of the energy dependence of alanine/EPR dosimetry: II. Clinical electron beams. *Physics in Medicine and Biology*, 50, 1119-1129.